UNIVERSITÀ DEGLI STUDI DI SIENA
FACOLTÀ DI SCIENZE MATEMATICHE, FISICHE E NATURALI
DIPARTIMENTO DI FISICA

# Very High Energy emission from *blazars* interpreted through simultaneous multiwavelength observations

*Relatore/Supervisor:*
Dr. Antonio Stamerra

*Tutore/Tutor:*
Prof. Riccardo Paoletti

*Candidato/Candidate:*
Giacomo Bonnoli

Ph.D. School in Physics
Cycle XXI
December 2010

# Abstract

In the framework of Astroparticle Physics the understanding of the particle acceleration process and related high energy electromagnetic emission within astrophysical sources is an issue of fundamental importance to unravel the structure and evolution of many classes of celestial objects, on different scales from micro–*quasars* to active galactic nuclei. This has an important role not only for astrophysics itself, but for many related topics of cosmic ray physics and High Energy physics, such as the search for dark matter. Also cosmology is interested, as deepening our knowledge on Active Galactic Nuclei and their interaction with the environment can help to clarify open issues on the formation of cosmic structures and evolution of universe on large scales. The present view on sources emitting high energy radiation is now gaining new insight thanks to multiwavelength observations. This approach allows to explore the spectral energy distribution of the sources all across the electromagnetic spectrum, therefore granting the best achievable understanding of the physical processes that originate the radiation that we see, and their mutual relationships. Our theories model the sources in terms of parameters that can be inferred from the observables quantities measured, and the multiwavelength observations are a key instrument in order to rule out or support some selected models out of the many that compete in the effort of describing the processes at work. Amongst the various instruments, VHE and X–ray telescopes play a crucial role, as these bands sample the most energetic and variable part or the spectrum of this kind of source, likely related to the high energy tail of the particle distribution that produce the emission and therefore the most sensitive probe currently at hand for the study of the relativistic jets in Active Galactic Nuclei. The variability on scales of hours and below observed in the high energy band imposes to perform simultaneous multiwavelength campaigns, ensuring that all the observations refer to an unique state of the source and thus fully constrain the broadband emission model. Such an approach has been first exploited in the seminal work by Maraschi et al. (1999) on the Active Galactic Nucleus Markarian 421, and hereinafter has been followed by other authors with different instruments. The increased sensitivity of present generation of ground–based Very High Energy $\gamma$–ray detectors allows to explore the hourly or even sub–hour variability, and the correlation with measurements at lower

energies, with unprecedented accuracy.

This thesis reports on the multiwavelength campaigns on two different *blazars*, OJ 287 and Markarian 421, involving instruments sensitive in the optical, UV, X–ray and $\gamma$–ray bands. The detection of Mrk 421 with the Cherenkov telescope MAGIC has been used to derive the physical properties of the emission in the jet and fully constrain the homogeneous leptonic Synchrotron Self–Compton model proposed by Tavecchio et al. (1998). The results achievable from such broadband observations with the present instruments are outlined.

This research has been carried on during my PhD studentship at Università degli Studi di Siena, working within the research group of the Department of Physics led by Professor Riccardo Paoletti and involved in the MAGIC Collaboration. The MAGIC Collaboration is an international consortium of Universities and Research Institutes, mostly European, with relevant contribution by German, Italian, Spanish and Swiss institutes. The Collaboration, gathering $\sim$ 200 scientists and technicians from all over the world, planned, built and currently runs a frontier experiment in the field of Gamma–ray Astronomy, based at the time of the observations studied here on a 17 meter wide, single dish Imaging Air Cherenkov Telescope, that is currently sided by a twin telescope, MAGIC-II, and forms with it an Imaging Air Cherenkov stereo system. The telescope, capable of observing from the ground $\gamma$–rays with energies in the approximate range 0.1–10 TeV, is located in the Canary Island of La Palma and since 2004 is used by the Collaboration itself to perform observations of known or potential astrophysical sources of $\gamma$–rays, delivering to the scientific community original knowledge relevant to astrophysics, cosmology and fundamental physics.

After a brief, general introduction to the field of High Energy Astronomy (Chapter 1), the Active Galactic Nuclei are introduced and summarized, and the subclass of *blazars* is described (Chapter 2), together with the models of their emission mechanism assumed in this work and their connection with observations in the VHE band (Chapter 3). Then the Imaging Air Cherenkov detection technique (Chapter 4) and the MAGIC telescope (Chapter 5) are reviewed, and the data analysis chain used for extracting from the raw data the physically relevant results is presented in some detail (Chapter 6). Then the observational campaigns on the *blazars* OJ 287 (Chapter 7) and Mrk 421 (Chapter 8) are summarized, the MAGIC results reported together with the data obtained in the other bands, and the modeling of the sources allowed by these datasets is presented and discussed. In the last chapter the results are reviewed and some general conclusions are derived.

# Contents

# Chapter 1

# Very High Energy Astronomy

The quest for a unified picture of the known interactions in the modern physics, pursued by particle and cosmic ray Physics through the studies on the innermost structure of matter, and the intimate connection to the cosmic evolution and structure formation, led naturally to the study of the particle acceleration and emission processes in astrophysical objects, and gave birth to the field of Astroparticle physics, somehow lying at the border among astronomy, particle physics and cosmology.

The main research topics in the field deal with cosmic rays, neutrinos, gravitational waves, search for dark matter and $\gamma$–ray astronomy.

Present state–of–the art instruments tackle the theoretical and observational issues of such apparently heterogeneous areas. A variety of different detection techniques, operating at different energy bands, have been exploited. The work described in this thesis will focus mainly on the Very High energy (VHE) emission from astrophysical sources, anyway keeping into account fruitful contribution coming from different instruments, sensitive in different energy bands. In the framework of Astroparticle physics, a brief overview of VHE astronomy will be now outlined.

To fix some definitions, Table 1.1 reports the common classification of the bands of the electromagnetic spectrum, that is also graphically illustrated in Figure 1.1.

## 1.1 Cosmic rays

After Becquerel accidental discovery of radioactivity, while studying fluorescence in uranium in 1896, widespread interest arose on the subject, and many natural minerals producing ionizing radiations were discovered. Early studies on natural background radioactivity were performed, following some

| Band Name | Abbreviation | Range of photon energies |
|---|---|---|
| Radio | – | $E_\nu < 10^{-2}\,\mathrm{eV}$ |
| Infra–Red | IR | $10^{-2}\,\mathrm{eV} < E_\nu < 1\,\mathrm{eV}$ |
| Optical | – | $1\,\mathrm{eV} < E_\nu < 4\,\mathrm{eV}$ |
| Ultra–Violet | UV | $4\,\mathrm{eV} < E_\nu < 100\,\mathrm{eV}$ |
| X–rays (soft) | soft–X | $0.1\,\mathrm{keV} < E_\nu < 10\,\mathrm{keV}$ |
| X–rays (hard) | hard–X | $10\,\mathrm{keV} < E_\nu < 500\,\mathrm{keV}$ |
| Low Energy $\gamma$ rays | LE | $0.5\,\mathrm{MeV} < E_\nu < 50\,\mathrm{MeV}$ |
| High Energy $\gamma$ rays | HE | $50\,\mathrm{MeV} < E_\nu < 50\,\mathrm{GeV}$ |
| Very High Energy $\gamma$ rays | VHE | $50\,\mathrm{GeV} < E_\nu < 10\,\mathrm{TeV}$ |
| Ultra High Energy $\gamma$ rays | UHE | $10\,\mathrm{TeV} < E_\nu$ |

Table 1.1: Conventional nomenclature of electromagnetic bands. The quantitative definition must be taken as loose and tentative, as the separation is mostly based on a combination of historical reasons and operating energy ranges of the different classes of detectors sensitive in each band.

hints pointing towards the existence of highly penetrative ionizing radiations.

It was actually seen that a charged gold–foil electroscope discharged spontaneously, and that could be ascribed to some ionizing radiation pervading the atmosphere. Nevertheless, a detector could detect some signal even if heavily shielded, so that this radiation had to be extremely penetrating as well. At first, it was thought that this radiation arose from the earth surface, and from contamination of radioactive elements in the air. Experiments performed on the sea surface and at some depth by Domenico Pacini (Pacini 1912, also in Pacini & De Angelis 2010) showed that the count rate didn't show the drop that was expected, due to the shielding effect of water. This was not in agreement with the ground origin of the radioactivity. Balloon-borne experiments from Victor Hess (Hess, 1913) confirmed that the count rate in detectors increased with heigh, implying that a substantial contribution to the natural radioactive background came from the space.

This discovery (that led Hess to the Nobel Prize in 1936) was of paramount importance and can be considered the starting point for the High energy branch of astrophysics.

Since then, the knowledge on "cosmic rays"[1] has increased a lot. The Earth is continuously bombarded by many kinds of high energy particles, neutral or charged, originated in the Sun (solar wind) in the galaxy, and from extragalactic sources. On average[2] the main contribution ($\sim 98\%$, averaging on the energies) comes from charged protons, and from a distribution of heavier charged nuclei[3].

[1] As Millikan subsequently defined them.

[2] Actually, the composition is different at different energies.

[3] Some current experiments, e.g. the CREAM balloon–borne experiment (Beatty, 1999)

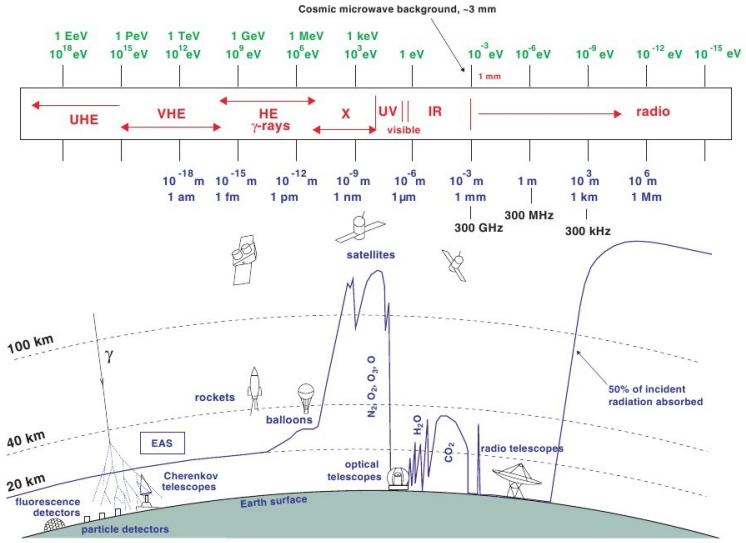


Figure 1.1: Sketch of the observational windows across the whole electromagnetic spectrum. In the upper box, the conventional name of the energy bands are reported (in red), with reference wavelengths (in blue) and corresponding energies in eV (in green). Below, cartoons of the peculiar detectors for each band are represented. The continuous blue line marks the height above sea level where the photon flux at each wavelength is halved by atmospheric absorption. Except for windows at optical, near–IR and radio frequencies, observation must be performed from great altitudes or from the space. Instead, Cherenkov detectors allow observation of VHE $\gamma$–rays from the ground as well. Picture from Mazin (2007), adapted from Longair (1992).

Electrons and photons together account for $\sim 2\%$ of the total flux. For these particles, the energy distribution is well described by a broken power law,

$$F(E) \propto E^{-\alpha} \quad , \quad \alpha \sim 2.7 \tag{1.1}$$

The spectrum spans more than 10 decades, from $10^{-1}$ to $10^{11}$ GeV, and the power index is slightly changing with energy, as it can be seen from the "knee" at $\sim 10^{15}$ eV and "ankle" at even higher energies.

This kind of distribution clearly accounts for non-thermal phenomena, as particle populations at thermal equilibrium should follow different, less dispersed distributions, such as Planck distribution in the case of photons.

led in Antarctica, aim to an exact determination of the mass distribution of cosmic rays and of the antimatter fraction.

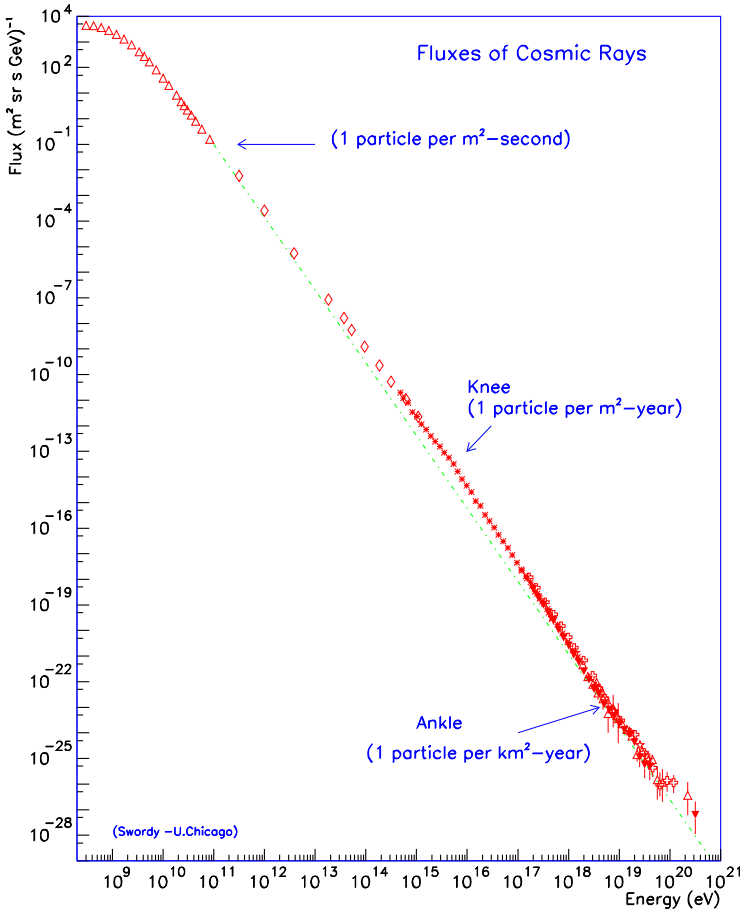


Figure 1.2: The energy spectrum of cosmic rays, as shown in Cronin et al. (1997). The green line represents a simple power law fit to the low energy slope, that clearly shows the changing power index of the measured distribution. The plot is built from data taken from $\sim$ 20 different experiments, ranging the whole $10^8$–$10^{20}$ eV energy band and more than 20 years of observations, with remarkable agreement.

### 1.1.1 Why photons?

Even if charged particles are dominant in the composition of the cosmic rays, they are of little use in all those studies of astronomy and astrophysics that rely on the association between the detected particles and the position of their sources in the sky. This is due to the presence in the Universe, on various scales, of magnetic fields that bend the trajectories of charged particles (Zeldovich et al., 1983). This is not always an issue, and many interesting experiments devoted to cosmic rays are operated or planned in the field of Astroparticle physics: on board of satellites such as PAMELA (PAMELA Collaboration, 1999) or the soon to be launched Alpha Magnetic Spectrometer (Chung & AMS Collaboration, 2006; Kounine, 2010), from balloons such as CREAM (Beatty, 1999) or ATIC (Guzik et al., 2004) or from the ground like the Pierre Auger Observatory (Zavrtanik, 2000). In most of these cases, the flux of cosmic rays is considered as a whole, regardless of incoming direction or of the possible individual emitting sources. In the case of Auger, that is sensitive to cosmic rays of the utmost energy and coming from local sources, a guess of the source can still be made as the bending induced by weak magnetic fields on high momentum protons along relatively short paths is relatively small.

But in many researches, including the present one, interest is devoted to peculiar point sources, and the connection between the observed events and the emitter must be mandatorily established. Photons become then the privileged vectors of information as, being electrically neutral, they travel across the Universe along straight lines, that can be traced back to the source of emission.

## 1.2 Instruments for $\gamma$–ray astronomy with photons

High Energy phenomena in the universe span many decades of energy. This naturally makes impossible for a single detector to cover all the interested bands. Even considering only photon–oriented detectors, from soft X–rays (e.g. the 0.2 keV accessible to the X–ray satellite ROSAT) to the 100 TeV energies accessible to MILAGRO (Goodman et al., 1993), the detection principle is very different. This leads to instruments of different concept, structure, dimensions, collection area, sensitivity, and each characterized by different advantages, weaknesses, systematics.

### 1.2.1 Interaction processes of photons with matter

Detection of photon relies on the interaction with some sensitive device. The dominant interaction processes of photons with matter, depending on the energy of the incoming photon and on the atomic number $Z$ of the target

element, are shown in Figure 1.3, adapted form Longair (1992). Photons and matter interact in three ways: photoelectric absorption, Compton scattering and pair production.

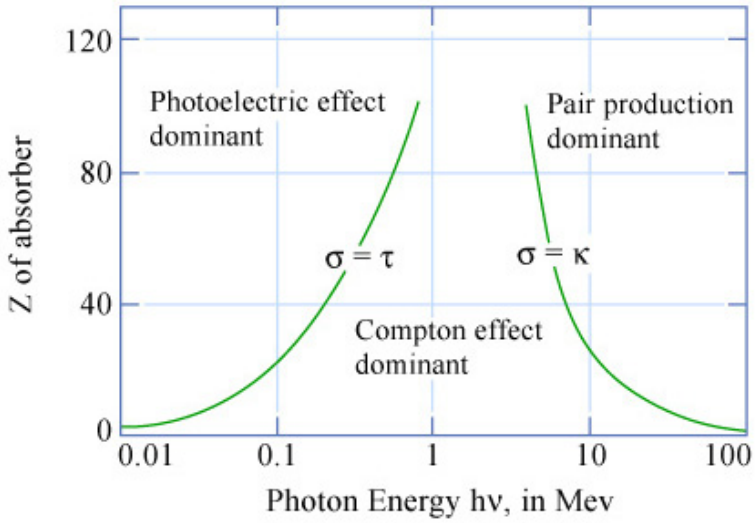


Figure 1.3: Diagram showing the dominant photon–matter interaction processes at different energies. The green lines are determined by the equivalence of the cross sections of the concurrent processes, namely photoelectric absorption, Compton scattering and pair production. In the range $0.5 < 5$ MeV all three processes contribute for any absorber, making the design of a detector difficult. Above a few MeV, the dominant process is pair production.

### 1.2.2 Satellites for HE: CGRO/EGRET and *Fermi*/LAT

The main contribution to the knowledge of the universe in the HE band until the *Fermi*[4] mission started its operations in 2008, has come from the Arthur Holly Compton Gamma–Ray Observatory (CGRO). This NASA mission, launched in 1991 and operative until 2000, hosted 4 instrument:

- BATSE, a full sky hard X–ray/LE (0.05–1 MeV) detector devoted to alert the other instruments in case of Gamma–Ray Bursts (GRB);
- OSSE, a scintillation spectrometer sensitive in the 0.1–10 MeV band;
- the *Compton Telescope* (COMPTEL, Schönfelder et al. 1984), sensitive in the 1–30 MeV range, with 1 sr FOV;)

[4]Renamed after the launch in honor of Enrico Fermi; formerly *Gamma–Ray Large Area Space Telescope* (GLAST).

- the *Energetic Gamma–Ray Experiment* (EGRET Kanbach et al. 1988; Gehrels et al. 1994))

The latter, consisted of a spark chamber tracker combined with a calorimeter and anti–coincidence shield. This setup allowed detection of photons in the range 20 MeV – 30 GeV with energy resolution of ∼25% in a 45° wide FOV.

The last catalog of the sources detected by EGRET (Third EGRET Catalog, Hartman et al. 1999a,b), numbered 271 $\gamma$–ray sources:

- 170 unidentified sources;
- 66 *blazars*(see Section 2.2.4), while other 27 out of the unidentified sources had a tentative association with *blazars* as well;
- the radiogalaxy Cen A;
- 5 *pulsars*;
- the Little Magellan Cloud;
- a Solar flare.

Even if many of the detections have been questioned based on a revision of the Galactic interstellar background (Casandjian & Grenier, 2008a,b) and both the total number and the number of the unidentified sources had to be lowered, the richness of the $\gamma$–ray sky had been unveiled. It's also worth noticing that many of these sources don't cross–correlate with any known source of the classes foreseen as potential $\gamma$–ray emitters, paving the way to many research routes, ranging from further observations to theoretical speculations.

A sky map of the sources included in the 3rd EGRET catalog is reported in Figure 1.2.2.

After a gap until 2007 when no $\gamma$–ray satellite was in operation, the ASI[5] satellite AGILE (Tavani et al., 2008), a light payload mission hosting a detector (GRID) capable of performances similar to CGRO/EGRET and, since August 2008, the NASA satellite *Fermi* (formerly GLAST) are currently in operation. The latter is a state of the art mission, with major contribution from italian institutes, such as the INFN[6]. It hosts two instruments:

- the Gamma–ray Burst Monitor (GBM), an all–sky monitor in the 8 keV – 40 MeV band;
- the Large Area Telescope (LAT);

[5]Agenzia Spaziale Italiana.
[6]Istituto Nazionale di Fisica Nucleare.

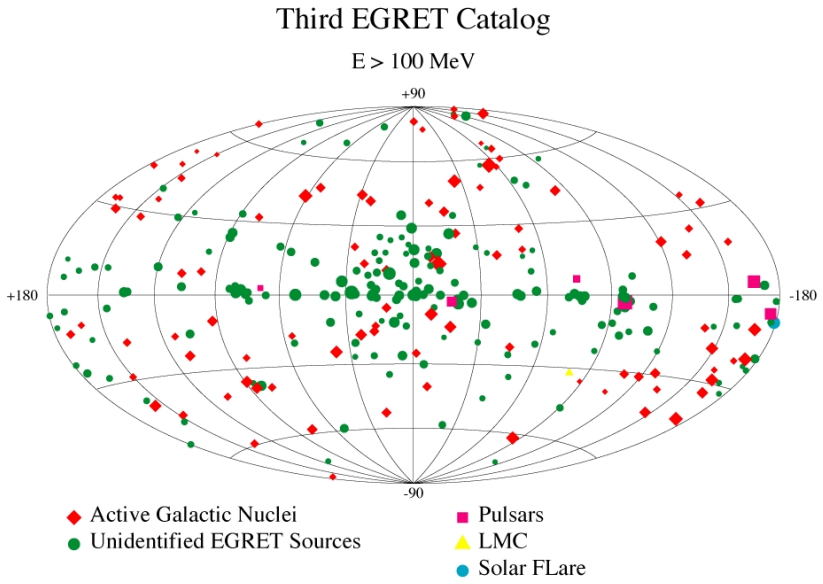


Figure 1.4: The third EGRET catalog of Gamma–ray sources, plotted in Aitoff–Hammer projection.

This one can be considered an evolution of the EGRET telescope, based on a silicon stripe tracker. The performance is highly improved under many respects, mainly the Field Of View (FOV), collection area, energy and angular resolution.

This telescope, scanning the whole sky every 3 hours, granted after only 11 months of operation a catalog (1FGL, Abdo et al. 2010) rich of 1451 sources detected and characterized in the 0.1–100 GeV range.

A comparison of the CGRO/EGRET and *Fermi*/LAT photon maps is displayed in Figure 1.5, clearly showing the improvement in sensitivity and angular resolution of the latter.

### 1.2.3 Ground telescopes for VHE $\gamma$ rays

At energies above $\sim 0.1$ TeV the performance of satellites degrades, due to a few concurring factors:

- fluxes of $\gamma$–rays decrease with power law at increasing energies, therefore the event rates are constrained by the limited collection area of the detectors;
- photons above a certain energy threshold produce showers that are not fully contained in the calorimeter, therefore spoiling the accuracy

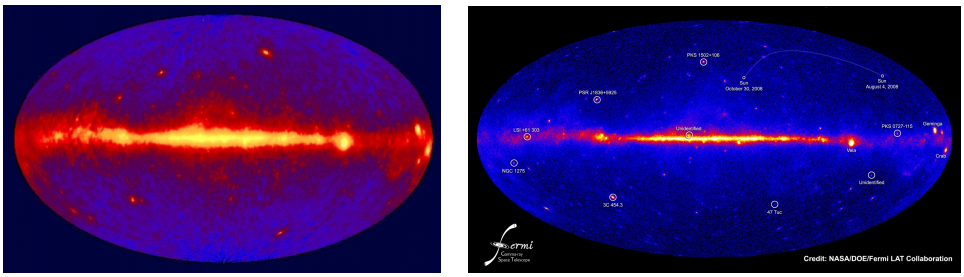


Figure 1.5: A comparison between the all–sky photon maps (plotted in Aitoff–Hammer projection) built with CGRO/EGRET (left) and *Fermi*/LAT (right). The improved sensitivity and angular resolution of the latter are easily noticed.

of the energy measurement;

- the anti–coincidence shield can be misled by high energy protons, therefore contamination by misinterpreted charged particles becomes an issue.

This limitations can be overridden with ground–based detectors that observe following a fully different concept: not the direct detection of the primary photons, but the detection of the products of its interaction with atmosphere, for instance by means of the optical–UV Cherenkov light cone that the charged secondary particles produce when traveling faster than light in a transparent dielectric such as air or water.

There are many different arrangements, such as:

- Water Cherenkov detectors (Yodh, 1996), such as MILAGRO (Goodman et al., 1993);
- Solar concentrator arrays, originally proposed by Danaher et al. (1982) (see Smith, 2006, for a review); an example is STACEE (Chantell et al., 1998)
- Ground detector arrays, such as ARGO-YBL (De Mitri, 2007);
- Imaging Air Cherenkov Telescopes, (IACT, see e.g. Weekes, 2005);

The class of greatest interest here is that of Imaging Air Cherenkov Telescopes, as MAGIC is one of those. The peculiar feature that distinguish them from the other air shower detetors is that actual *imaging* of the showers is performed. A more detailed introduction to this detection technique, will be given in Chapter 4, while chapter 5 will be devoted to the description of the MAGIC telescope.

### 1.2.4 Examples of IACT

#### The pioneer: Whipple

The first instrument of the IACT class in operation was the Whipple telescope, with a 10 m wide mirror and a single photodetector, inaugurated in 1968. It was therefore capable of detecting the air showers, but not of performing the background rejection that is the key of the sensitivity of the currently working instruments.

#### The second generation: Whipple and HEGRA

In the late seventies the detector system of Whipple was upgraded with a multi–channel photomultiplier camera (Weekes & Turver, 1977). This allowed imaging of the showers and background discrimination. This way, Whipple discovered the Crab Nebula as a source of VHE $\gamma$–ray (Weekes et al., 1989), opening the path for astronomical observation in a new energy band. The Whipple telescope is still in operation nowadays, as a monitoring instrument for bright and variable VHE sources.

The *High Energy Gamma Ray Astronomy* (HEGRA) telescope array (see e.g. Mirzoyan et al., 1994; Daum et al., 1997) was located at the same site now occupied by the MAGIC Telescope. In its final arrangement it was made of an array of 5 telescopes, each 3.4 m wide. Exploiting the powerfulness of the stereoscopic reconstruction of showers, it reached an angular resolution of 0.1° at 0.5 TeV (Pühlhofer et al., 2003). The energy resolution was $\sim 15\%$ and the flux sensitivity allowed detection of sources as weak as 3% of Crab Nebula in 100 h of observations.

#### The third generation: HESS, VERITAS and MAGIC

The *High Energy Stereoscopic System* (HESS, HESS Collaboration, 2000) currently consists of 4 telescopes, each 10 m wide, allowing detection of VHE $\gamma$ rays in the 0.1–10 TeV energy range. An additional single dish with 26 m diameter and 600 $m^2$ of surface is under construction (HESS–II, Vincent, 2005), aiming to lower the energy threshold of the system. HESS is located in Namibia; thus due to its latitude ($\sim 23°$ S) has access to the less explored Southern sky. Moreover, the Galactic Center is visible ad low zenith angles from this location and this, added to the good angular resolution and wide field of view arising from the design of the stereoscopic system, allowed a deep scan of the Galactic Plane (Funk, 2005) and high quality observations of the Galactic Center (Aharonian et al., 2006b).

The *Very Energetic Radiation Imaging Telescope Array System* (VERITAS, Krennrich et al., 2004) is an array of four 12 m optical reflectors, located at the same site of the Whipple Telescope. Its performance figures are similar to HESS.

MAGIC is an acronym for *Major Air Gamma–ray Imaging Cherenkov* [telescope]. This definition condenses the fundamental features that the telescope shares with the others of the IACT type, and a transient one, "major", that concerns being, with its 17 m wide mirror, the biggest single–dish telescope in operation; an important feature with a deep impact on its performance, mainly on the energy threshold (see Section 4.5). This primacy lives on still now, but may expire in the next future, due to IACTs of wider diameter such as the aforementioned HESS–II, or the *Cherenkov Telescope Array* (CTA, CTA Consortium, 2010, in its design phase) or, if we take a glimpse outside of the VHE band, to the construction of the *Extremely Large Telescope* and *OverWhelmingly Large* optical telescopes[7].

The telescope is currently sided by its twin telescope, MAGIC–II, and has therefore been renamed as MAGIC–I, while MAGIC currently refers to the stereo system of both. The two telescopes are routinely operated in stereoscopic mode since mid 2009. This allows observations with improved background rejection, sensitivity, angular and energy resolution and lower energy threshold with respect to the stand–alone MAGIC–I telescope. MAGIC–II was in commissioning phase when the observations considered in the thesis were performed. A description of MAGIC–I will be given in Chapter 5.

### 1.2.5 The VHE sky

The VHE sky is populated by many classes of objects, and other have been speculated and investigated but still lack any discovery, such as Dark Matter.

#### Galactic sources of VHE $\gamma$ rays

As far as Galactic sources are concerned, a summary list can include: Supernova Remnants, Pulsar Wind Nebulae, Pulsars, X–ray binaries, Micro–quasars and the Galactic Center. Moreover, there are sources of unidentified classes and also diffuse emission from the Galactic Plane has been claimed. A recent review can be found in (Torres, 2009).

#### Extra–galactic sources of VHE $\gamma$ rays

The extragalactic VHE sources discovered until 2010 October are reported in Figure 1.6.

They also belong to some different classes:

[7]Relying on active and adaptive optics in order to bypass the limitations induced by atmospheric *seeing*, these telescopes will be supplied with tessellated main mirrors up to 50–100 m in diameter

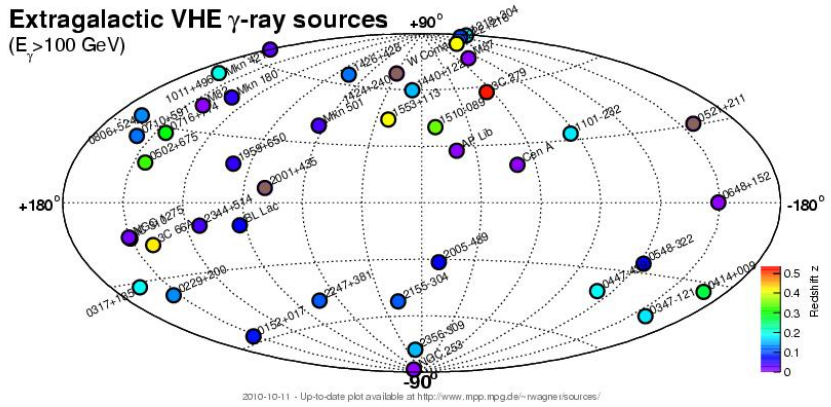


Figure 1.6: An Aitoff–Hammer projection of the distribution of extragalactic VHE sources in the sky, including all the sources known until October 2010.

- Active Galactic Nuclei, that will be presented in Chapter 2; amongst these, almost all are *blazars*, nearly all from the HBL subclass (see Section 2.2.4 for the AGN taxonomy). Exceptions are: some LBLs, such as BL Lac (Albert et al., 2007d), S5 0716+714 (Anderhub et al., 2009a); a few FSRQs such as 3C 279 (MAGIC Collaboration, 2008), PKS B1222+216 (Mariotti, 2010b); and radiogalaxies, such as M87, NGC 1275 (Mariotti, 2010c), the head–tail radiogalaxy IC 310 (Mariotti, 2010a));
- *Starburst* galaxies, such as M82 (Karlsson et al., 2009);
- Gamma Ray Bursts, observed at HE but still not detected at VHE (see e.g. Albert et al., 2007e).

# Chapter 2

# Active Galactic Nuclei

*"Twinkle, twinkle quasi-star*
*Biggest puzzle from afar*
*How unlike the other ones*
*Brighter than a billion suns*
*Twinkle, twinkle, quasi-star*
*How I wonder what you are."*
- George Gamow, "*Quasar*" 1964.

## 2.1 Stars, galaxies, and something else

It is since Hubble observation of Cepheid stars in M31, also known as the Andromeda Nebula, Hubble (1929a) and M33 (Hubble, 1926) that we know for sure that our Galaxy is not alone in the Universe, and it is not peculiar or special at all, but just one out of many "island–universes" . Thereafter, by many means, mainly (and formerly) optical photometry and spectroscopy, astronomers acquired a somehow robust discrimination of optical sources belonging to our galaxy (stars, planetary nebulae, gaseous nebulae) and external galaxies, with their own main classification in spirals, elliptical, irregulars, with further, finer subdivisions in each category (see van den Bergh 1998 for an exhaustive review).

### Stars and diffuse nebulae

Basically, stars are pointlike sources for optical photometry, and their spectra show a continuum, that follows quite well a blackbody distribution with temperature $2 \times 10^3 \lesssim T_{BB} \lesssim 4 \times 10^4$ K, except for superimposed features (atomic lines, molecular bands) that for some stellar types can be intense. Galactic nebulae are instead extended optical sources, cannot be resolved in stars (the emission is truly diffuse) and the spectra show bright emission

lines, often associated to forbidden atomic transitions; the continuum here is absent or, at most, very weak.

### Galaxies

Galaxies are instead extended sources (but single stars can be resolved, provided the distance is small enough) that show spectra with both continuum and absorption and (perhaps) emission lines. The continuum comes from the sum of contributions of the single stars in the galaxies, which are a population of blackbodies with a distribution in $T_{BB}$ that can be very different from a galaxy to another. The absorption lines originate from the stellar athmospheres and from the gas clouds in the galaxy. The emission lines galaxies are produced by the diffuse interstellar material (present mainly in late and intermediate type galaxies, such as irregular and spirals[1]) the absorption lines and the breaks from the stellar atmospheres and again from the interstellar gas and dust present in the galaxy. As example, two templates of optical spectra of galaxies taken from Kinney et al. (1996) are plotted in Figure 2.1. In ellipticals (E) the old, red star population and absence of gas produces a red spectrum with prominent absoption features (CaH,CaK, Balmer break) but no emission lines (upper panel). In spirals, young blue stars and dffuse gas (HI, HII) clouds are present, originating a bluer spectrum whit less evident absorption features but also bright emission lines ($H_\alpha$, $H_\beta$ of the Balmer series, [OII], [OIII] forbidden lines) Osterbrock & Ferland (2006). All become dimmer bluewards of the Balmer and Lyman limits, where only the hotter blue stars could emit and moreover strong absorption intervenes due to ionization of neutral H.

### .... what else?

In this more or less clear picture, some classes of peculiar sources have to be considered. On one side, many stars showed variability, that can be periodic (such as in Cepheids) or aperiodic, and may show different scales of amplitude and time.

On the other side, some point–like sources showed propertuies that puzzled the observers. The most peculiar features were the strong UV excess and the severe broadening of lines in optical spectra. Sometimes, the photometry indicated strong variability, usually irregular and aperiodic; in these cases, such sources were for long time believed to belong to some kind of irregular variable stars. For example, an historical light curve of Mrk 421 all across the XXth century is reported in Figure 2.1, taken from Liu et al. (1997). The observed luminosity spans nearly 5 magnitudes, from 16 when

[1] Ellipticals are also said *early–type*.

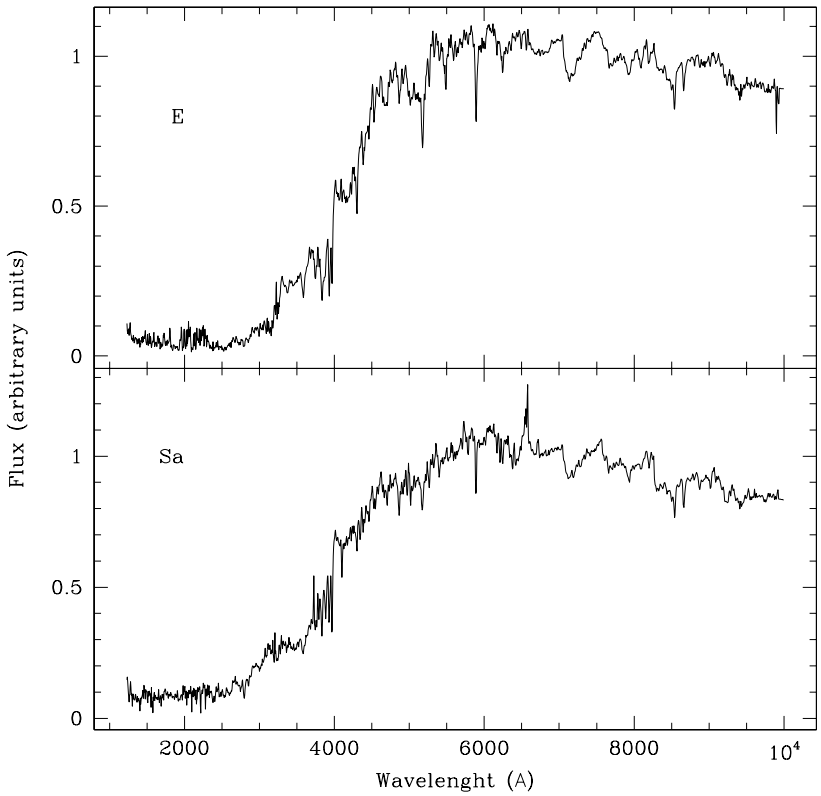


Figure 2.1: Example templates of optical spectra of standard galaxies, from Kinney et al. (1996). Upper panel: spectrum of an elliptical galaxy, charactherized by old red stellar populations, and lack of diffuse gas; no emission lines are present, while absorption features due to the stellar athmospheres are evident. Lower panel: template of a spiral galaxy (subclass Sa), where the absorption features are weaker, but emission lines due to allowed and forbidden transitions in diffuse gas shined by young blue stars are evident. In both classes, the UV portion of the spectrum is dim.

quiescent to 11.4 during major outbursts. These elements could hardly be matched with standard stars.

Other puzzles came from radio data: counterparts of bright radio sources were identified in some of these peculiar point–like sources: The now well known *quasar* 3C 273 was indeed a radio source from the Cambridge catalog of radio sources (Bennett, 1962), that was spatially coincident (Hazard et al., 1963) with a "variable star" of roughly $M_R \sim 13$. Great turmoil followed the amazing measurement of its redshift (z=0.123, Schmidt 1963)

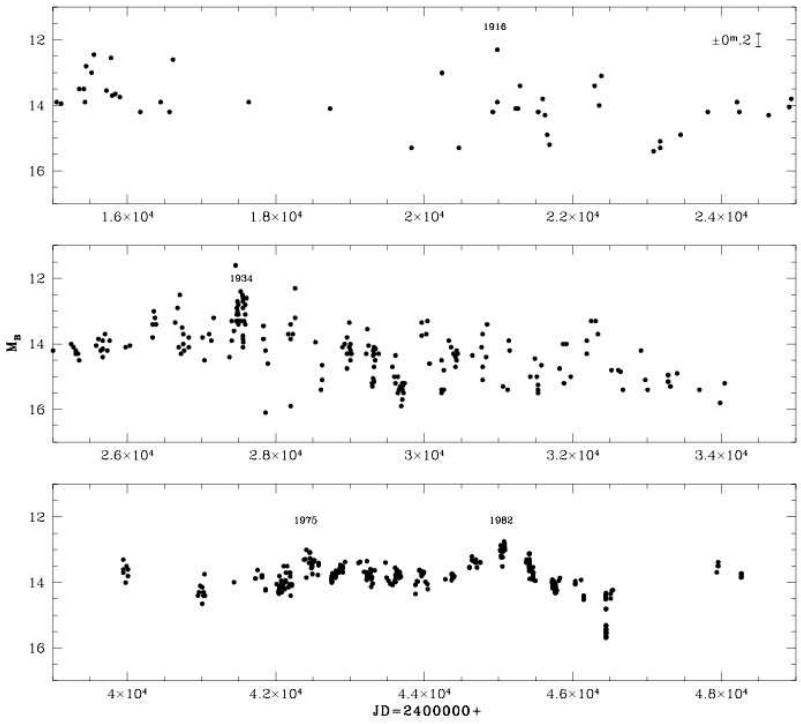


Figure 2.2: The long–term optical ($B$ band) light curve of Mrk 421 since 1900. From Liu et al. (1997).

that clearly demonstrated that the source was actually extra–galactic if interpreted following the Hubble's law (Hubble, 1929b).

This had enormous consequences, namely:

- The source was extremely powerful, being brighter than a standard galaxy in spite of the distance
- The emitting region had to be very compact (size of the order of the Solar System) in agreement with the fast variability shown in optical
- An extremely efficient process was at work, converting energy into radiation
- Some unknown reason allowed the source to apparently violate the Eddington limit, as a high power from a small source implied high flux energy density and high radiation pressure.

Other radio sources were identified with galaxies, sometimes showing also jets of material protruding from the galaxy core.

All these observation hinted towards a new class of sources, sometimes clearly associated with the nuclei of visible host galaxies,, sometimes extremely distant (high redshift, no host galaxy associated such as, for instance, PG 1553+113), and therefore intrinsically characterized by high and highly variable observed power, in all the bands from radio to optical, (to X-rays, as soon as these became accessible to observation). The rapid variations led to interpreting the sources as extremely compact, apparently violating the Eddington luminosity limit. Moreover, the spectral shape could not beconciled with standard stellar energy release mechanisms, where MeV photons are produced in the core by nuclear reactions, but they are thermalized along their path to the stellar surface. Moreover, photons below the Lyman limit at 912 nm would be absorbed when interacting with the neutral hydrogen of the stellar atmospheres, cutting off any emission at high energies: a feature generally observed in standard stars and in standard galaxies as well. For sure, some non stellar process has to be invoked to explain such spectra. 3C 273 became the first source of the "*quasar*" class, named after the locution "quasi–star", to account for both its star–like appearance and its peculiar extragalactic nature, that cast it in a totally different and new category.

As an example, in Figure 2.3 an optical (R filter) image of the bright *blazar* PG 1553+113 is shown, from Treves et al. (2007). The brightness of the point-like source and the absence of a space–resolved contribution from the host galaxy are clearly visible. In Figure 2.4 instead the optical, high resolution spectrum of the same source reveals a flat, broad band continuum with no hint of absorption ot emission lines. The prominent features redwards of 6000 Å are telluric absorptions due mainly to athmospheric oxygen.

## 2.2 Active Galactic Nuclei

Those galaxies showing peculiar spectral features, not compatible with simple stellar processes, and mainly a very bright nucleus, eventually dominating the total galaxy flux in the optical are now believed to host an *Active* Galactic Nucleus (AGN). The speculated structure of this kind of source will be described in section 2.7; hereafter I'll report on two of the main observational features that lay behind the phenomenological classification of AGN: the morphology of the optical spectrum and the intensity and geometry of the radio emission.

### 2.2.1 Emission lines in optical spectra of AGN

The spectra of active galactic nuclei (AGNs) display prominent emission lines arising from gas photoionized by a nonstellar continuum source, showing also a prominent UV excess. These features are clearly visible in Figure

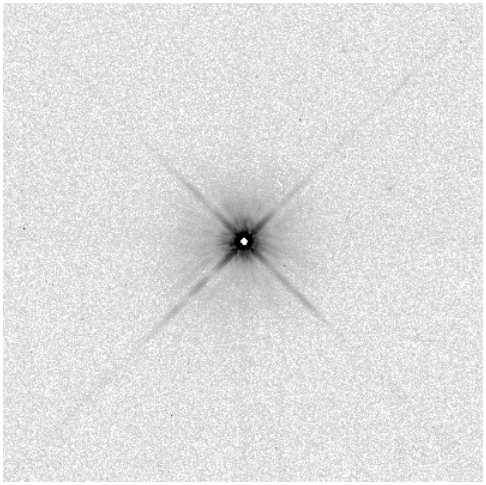

Figure 2.3: An optical (R band) image of PG1553+113. Image taken with the WFPC2 onboard of the Hubble Space Telescope. The field of view is 18.3 × 18.3 arcsec$^2$. From Treves et al. (2007).

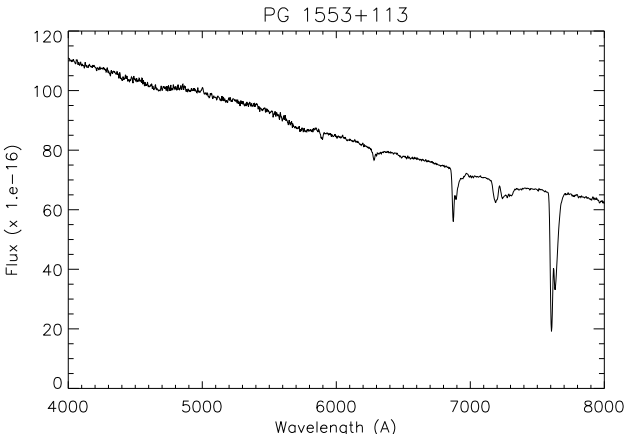


Figure 2.4: High resolution optical spectrum of PG 1553+113, obtained with the FORS spectrograph at VLT. The source shows a flat, featureless optical spectrum where only telluric absorption bands are evident, on a flat featureless continuum. From Treves et al. (2007).

2.5, where a composite optical spectrum of *quasar* is plotted, taken from Vanden Berk et al. (2001) and built with data from the Sloan Digital Sky Survey (SDSS, Fan et al. 1999; Adelman–McCarthy et al. 2008).

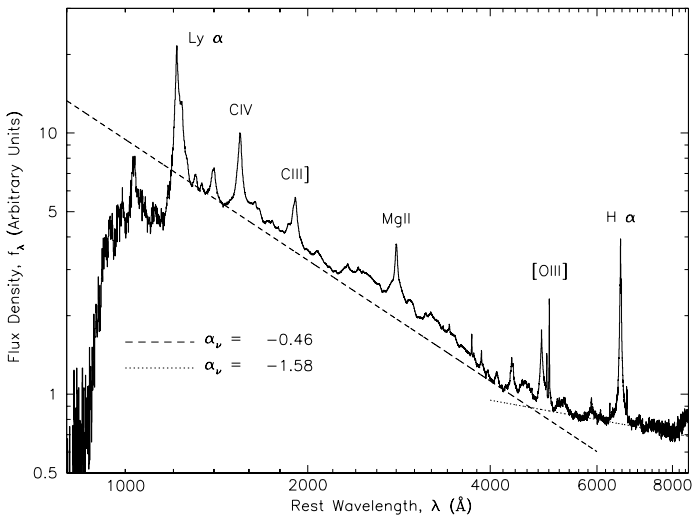


Figure 2.5: A composite optical–UV spectrum of *quasars*, built from SDSS (Vanden Berk et al., 2001). The UV excess and the bright, Doppler–broadened emission lines distinguish well this kind of source from standard stars and galaxies.

Forbidden lines are narrow (Doppler widths of hundreds of km/s) while semi–forbidden and permitted lines are broad (Doppler widths of thousands of km/s). Narrow lines vary over years or more, whereas broad lines vary over days and months, depending on luminosity (Vanden Berk et al., 2004). These considerations identified the narrow line region (NLR) as a low-density region up to hundreds of parsecs from the central engine with velocities characteristic of motion within a galactic potential, and the broad line region (BLR) as a higher density region within the innermost parsec with velocities characteristic of motion within the potential of a supermassive blackhole.

### 2.2.2 Radioloud vs. Radioquiet AGN

In the radio band, most of the AGNs do not show important emission (radioquiet AGNs), except for a $\sim 10\%$ fraction that is therefore indicated as radioloud. The dichotomy has been evidentiated by means of the *radioloudness* parameter, that is built as the ratio of fluxes in the B optical band ($F_B$) and at the radio frequency of 5 GHz ($F_{5\mathrm{GHz}}$)

$$R \equiv \frac{F_{5\mathrm{GHz}}}{F_B} \tag{2.1}$$

The threshold $\bar{R} = 10$ discriminates radioquiet and radioloud sources. Early studies Kellermann et al. (1989) evidentiated a bimodal distribution with peaks at $R \approx 1$ and $R \approx 100$; in spite of some later debate, this result can still be regarded as valid. Even if selection effects can be invoked, the fraction of radioloud AGNs must be a minority in the whole class, not exceeding $\approx 20\%$ of the total.

### 2.2.3 Radioloudness and jets

Intimately connected to the radioloudness there is another important property characterizing some AGNs: the presence of jets of matter expelled from the central engine and extending on scales as long as Megaparsecs (Begelman et al., 1984). The reasons lying behind the formation of jets (and, consequently, behind the radioloud/radioquiet dichotomy) are still under profound debate, even if the role of the black hole spin is commonly believed to be significant (Blandford, 2005).

#### Fanaroff–Riley classification of extended radio sources

When the radio sources are spatially resolved with single radiotelescopes we speak of *extended* radio sources. Amongst these, another division has been made based on a morphological basis, namely the dominance of the emission coming from the core ("core dominance") upon the one originated in the radio "lobes" associated to the jets (Fanaroff & Riley, 1974). It comes out that the different morphology robustly correlates with a separation in the low frequency (178 MHz) radio power, with sources where the lobes dominate the core (referred to as FRII) always surpassing the level of $10^{25}$ W/Hz/sr while the core dominated ones (FRI) lay systematically below this level. Eventually, this division could be related to differences in the radiative efficiency of the accretion flow, with the powerful, lobe dominated FRII accreting efficiently and the dimmer, core dominated FRI accreting inefficiently (Ghisellini & Celotti, 2001).

#### Compact radio sources

A small fraction of radioloud AGNs appears point–like in observations with single radiotelescopes, and are said to be *compact*. Except for subclasses of intrinsically compact sources, likely to be young (see e.g. Orienti et al. 2010) these can be interpreted as radiogalaxies (of any of the FR types) with the jet closely aligned with the line of sight.

### 2.2.4 Other categories: a bit of AGN taxonomy

Historically, many different AGN subclasses have been individuated, based on various observational discriminants. This has led to a plethora of names, where ambiguity and incoherences are all but rare. The most important are recalled for further reference.

**Seyfert galaxies:** AGNs hosted into a spiral galaxy. They show significantly lower bolometric luminosities with respect to the ones in ellipticals; can be further divided in type 1 and 2 based on the width (above or below $\sim 1000$ km/s respectively) of the optical lines. In the case of narrow lines, there is also evidence for forbidden lines such as [OII],[OIII].

**Type 1 / Type2 *Quasars*:** Radioquiet AGNs hosted showing broad (Type 1) or narrow (Type 2) optical emission lines. When the host galaxy can be observed, it is usually an elliptical (Bahcall et al., 1994; Falomo et al., 2005; Dunlop et al., 2003);

**Radio *Quasars*:** Radioloud AGN hosted into elliptical galaxies, and showing strong, broad lines in the optical spectra. Are further split in Flat Spectrum Radio *Quasars* (FSRQ) and Steep Spectrum Radio Quasar (SSRQ) , based on the spectral index of the radio spectrum

**BL Lacs:** Named after the source BL Lacertae, are radio compact sources with flat radio spectrum, showing higly variable and polarized optical flux and optical spectra with weak (equivalent width EW $< 5$ Å) lines.[2]

## 2.3 The AGN unified model

Dealing with so many different kinds of objects is of course a threat to the scientist, as his will to find properties that can be of the most general validity is obviously frustrated. So it's both reassuring and operatively helpful to search for an unified scheme that can explain simply the observational variety that AGN show. This has been tried, with remarkable success, with the AGN unified model. The first step was the unification in the radioquiet class (Antonucci & Miller, 1985; Antonucci, 1993), after extended to the radioloud family (Urry & Padovani , 1995): this model simply reduces all the different categories of sources previously introduced to a single class, characterized by great geometrical anisotropy. Most of the variety in the

[2]Unfortunately this classification, based on observational properties instead of physics, has some intrinsic weaknesses, as the EW ,and therefore the classification, can change in presence of a variable continuum; moreover, it leaves undistinguished the case of weak lines and the one where no lines are produced, that are much different in concept.

observational properties can therefore be explained in terms of the different viewing angles to the source, that is not spherically simmetrical, but shows relevant anisotropies that will be better addressed in the following. However, some dichotomies, such as the radioloud/radioquiet, FRI/FRII, FSRQ/BL Lac divisions cannot be explained in terms of the orientation. This points to intrinsic differences in the source, depending on some internal parameters to be further investigated.

### 2.3.1 Structure of the central engine

General consensus has nowadays been reached upon the structure of the central engine of AGN The prime mover is believed to be a Super–Massive Black Hole (SMBH) accreting matter from the surrounding regions of the host galaxy. In the current paradigm, in the center of every galaxy is hosted a SMBH (see Fig 2.6).

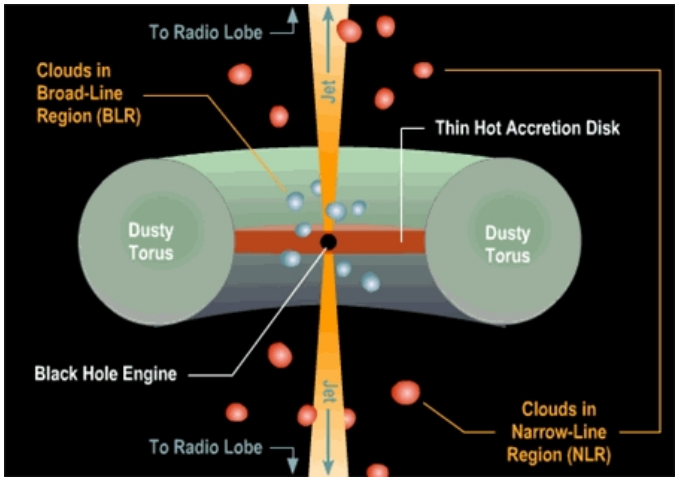


Figure 2.6: Cartoon representing the currently accepted model of the central engine of AGN. The central SMBH is surrounded by accreting material arranged in a thin disk, ∼0.1–1 pc wide. A wider and thicker dusty torus surrounds the region. If a jet of relativistic plasma is expelled orthogonally to the disk plane, it shines gas clouds that in the innermost regions show great velocity dispersion and originate Doppler–broadened optical lines (Broad Line Region), while the most distant ones are colder and less dense as indicated by the narrower line profiles (Narrow Line Region) and the presence of forbidden lines.

The mass of these black holes ranges in the interval $3\times10^6 M_\odot \lesssim M_{BH} \lesssim 3\times10^9 M_\odot$ (see e.g. Goulding et al., 2010, and references therein), where $M_\odot$ is the mass of the Sun ( $\approx 2\times10^{33}$ g ). These masses are obviously not compatible with the black holes believed to originate from the last phases

of the life of massive stars, that cannot be heavier than a few tens of solar masses; hence the Super–Massive attribute, and the awareness that they must have a completely different genesis. A rather solid correlation exists between the mass of the SMBH and observable properties of the host galaxy, such as the velocity dispersion around the core (Kormendy & Gebhardt, 2001); this points to a common evolution of the galaxy and the hosted SMBH (Ferrarese & Ford, 2005). The vast majority of galaxies shows no activity beyond the common stellar processes, therefore the SMBH is usually quiescent; the $\sim 1\%$ of the galaxies showing non–stellar activity forms the AGN class. Its intense gravity attracts matter from the innermost part of the galaxy, where an accretion disk of infalling matter is formed. At this point, some property of the system, which could be the black hole spin $\vec{S_{BH}}$ determines whether a part of the accreted matter is expelled outwards in jets of plasma orthogonal to the disk plane. If no jet is formed, the source emits only from the accretion disk. Otherwise the jet itself contributes dramatically to the emitting power and the spectrum of the produced emission. In AGNs, the accretion of gas onto the SMBH produces release of gravitational energy under form of kinetic energy and eventually radiation (Rees, 1984). The amount of energy that can be released in this way reaches the 10% of the rest mass of the incoming matter. The efficiency of such a process can hardly be achieved otherwise: for instance, nuclear fusion processes can free at most few MeV for each hadron involved, giving an efficiency $\approx 1\%$. Such a great efficiency is needed to account for the high power observed in these bright and distant sources, and this was indeed the main reason to propose such a model for AGN emission. Also the compactness of such a source allows to explain the observation of variability on time scales ($t_{var}$) as short as days, that constrain the size of the emission region within the light crossing time $R < ct_{var}$. The acceleration of matter during the infall onto the SMBH warms the gas up to $T \sim 10^5 K$ ; therefore the power is mainly emitted as UV/X–ray radiation, even if a fraction is radiated at longer wavelengths, due to absorption/re–emission processes involving dust and gas surrounding the central engine.

In this picture, the SMBH is surrounded by an accretion disk constituted by infalling gas. The disk inner radius can be of a few *Schwartzschild radii*[3] is within 0.1 pc ($10^{17}$–$10^{18}$ cm), while the disk thickness is lower (*thin* disk). The disk loses gravitational potential energy in the infall and angular momentum through viscous or turbulent torques (Shakura & Sunyaev, 1973). This energy is released thermally, through the production of the optical–UV "blue bump"; the X–ray portion is likely to be due to Inverse Compton scattering of UV photons due to a population of hot electrons surrounding the

[3]To any point or spherically simmetric mass can be associated its *Schwartzschild radius* $R_S$, the distance from the center where the escape speed equals the light speed. In the relativistic case it means $R_S \equiv \frac{GM}{c^2}$, while in the classical Newtonian approximation the value is doubled.

disk. At distances of 0.1–1 pc ($10^{17}$–$10^{18}$ cm) from the central black hole (BH), lie the hot, photoionized gas clouds responsible of the broad (FWHM $\sim 3 - 10 \times 10^3$ km/s) optical lines in *quasars*. The BH + disk structure is surrounded by a thicker, larger (1–10 pc) dusty torus, further reprocessing the continuum into IR photons. Depending on the orientation of the plane of the disk/torus w.r.t. the observer's line of sight the torus may completely absorb the broad lines coming from the inner BLR in Type 2 *quasars* and Seyfert galaxies[4].

At larger scales ($\approx$ 100 pc) the Narrow Line Region is found: again, constituted by gas clouds that emit either due to photoionization by a strong continuum (e.g.the disk) either due to shocks *in situ* (Binette et al., 1985).

These clouds emit the narrow optical lines, with smaller Doppler broadening (FWHM $<$ 1000–2000 km/s) with respect to the BLR, because being further away from the gravitational well they are slowers. Also, the larger size scale accounts for the longer variability time scale.

### AGN originating relativistic jets

The aforementioned ingredients are common to the whole AGN population. In a fraction, corresponding to the radioloud population, a further, structure is present exerting a fundamental role in the generation of the observational properties of the class: the relativistic jet.

The formation of the jet is one of the most fundamental open problems in astrophysics. It's currently assumed that jets are produced close to the central black hole. The key of the jet formation should reside in the rotation of a rapidly spinning BH, described in the formalism of general relativity by the Kerr metric (Misner et al., 1973). The power carried by the jet may be extracted from the BH spin (Blandford & Znajek, 1977) and/or from the accretion disk (Blandford & Payne, 1982). In both scenarios, a major role in channeling power into the jet must be played by the magnetic field. Another possibility is that the crucial parameter is the BH mass (Laor, 2000).

A schematic graphical representation of how the unified model accounts for the different phenomenological classes of AGN is given in Figure 2.7 taken from Torres (2003).

### Radioquiet unification

In the case of radioquiet AGNs, the wide range of subclasses observationally established can be explained well in terms of the anisotropy induced by the

[4]In the high $z$, earlier AGN population, the dusty torus can be thick and dense enough to obscure completely the AGN at wavelengths below the soft X–rays (Compton–thick AGN). This has strong implications on research dealing with AGN evolution and cosmology, but the whole subject regards structures far beyond the horizon (see Section 3.7) nowadays accessible to VHE telescopes, and therefore will not be touched here.

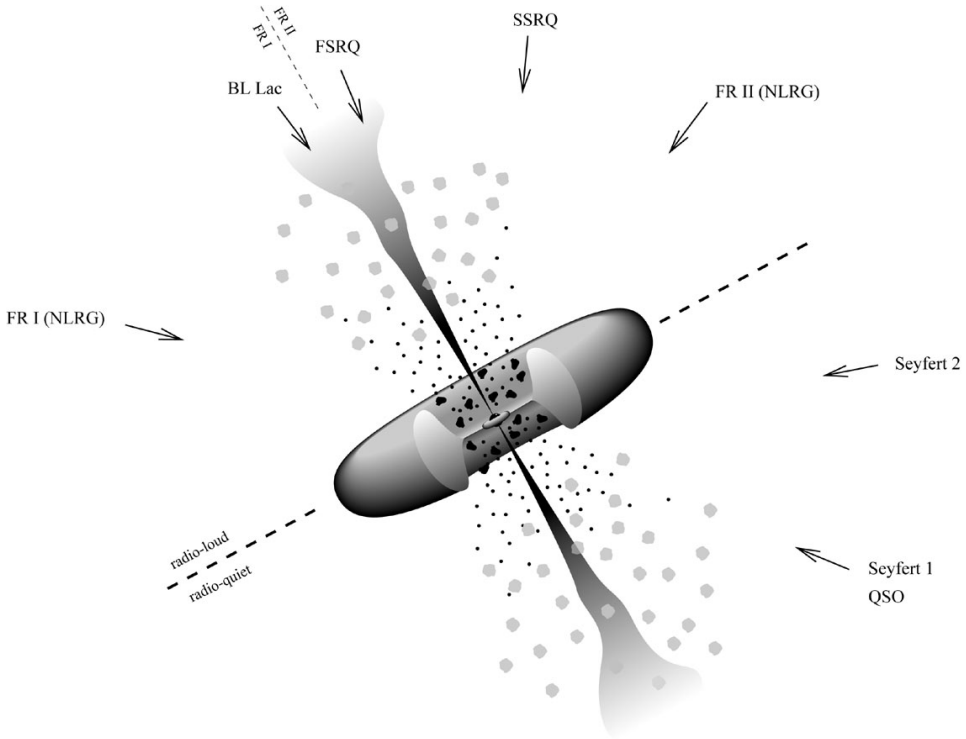


Figure 2.7: Schematic view of the AGN unified model, taken from Torres (2003) and references therein. Depending on the viewing angle, the dusty torus may hide or not the BLR. In the radioquiet domain, this gives rise to the Type 1/Type 2 dichotomy both in Seyfert Galaxies (dimmer and hosted in spirals) and in Quasi Stellar Objects (QSO), brighter and preferably hosted in giant ellipticals). In the radioloud domain, a jet is formed, that may (*blazars*) or may not (radiogalaxies) point at the observer. When the viewing angle is large, the BLR is hidden in radiogalaxies as well (NLRG). The parent population of BL Lacs and FSRQ are likely to be FRI and FRII radiogalaxies respectively, with SSRQ being at intermediate angles between FSRQ and FRII radiogalaxies.

existence of an optically thick dust torus surrounding the accretion disk (Antonucci, 1993). Depending on the orientation of the line of sight to the torus, the AGN can be totally obscured (when the torus is edge on). When the angle between the axis of the torus and the line of sight is large a type 2 *quasar*, with narrow lines, is observed. At lower angles, the innermost BLR comes into sight and the AGN becomes observationally a type 1 *quasar*.

**Radioloud unification**

In the case of radioloud AGN, characterized by relativistic jets, when the jet is seen at large angles we have radiogalaxies (lobe or core dominated). When the angle is of only few degrees, the *blazar* class is observed. Sources belonging to this class show relevant, or in most extreme case, contribution from the jet to the luminosity. Relativistic effects play a non negligible role and will be addressed later.

**Orientation, and that's all?**

In the end, the different orientations account for a great part of the observational differences among AGN. Only the presence or absence of the jet, the FRI/FRII separation, the presence or absence of optical emission lines still remain unexplained. So, there is an only kind of sources, but some of its physical properties tune the above mentioned features. The parameters that are speculated to be discriminant in these cases are the mass of the SMBH $M$, the accretion rate $\dot{M}$ , with a possible influence of the environment as well.

## 2.4 *Blazars*

Summarizing the elemnts already introduced in the previous section *blazars* are a (quite rare) subclass of active galactic nuclei characterized by:

- Radio–loudness (R $>$ 10)
- Compact radio core
- Flat or inverted radio spectrum ($\alpha_r \lesssim 0.5$ ; $f_\nu \propto \nu^{-\alpha}$)
- High ($> 3\%$) optical and radio polarization
- Intense, fast and basically irregular time variability at all frequencies

In the unified model these sources are interpreted as radio–loud AGN with the jet closely aligned to the line of sight. This accounts easily for the compact morphology of the radio flux, and also for the brightness that is enhanced by relativistic beaming effects that will be discussed in Section 3.2.

### 2.4.1 FSRQ and BL Lacs

Flat Spectrum Radio *Quasars* and BL Lacs present similar strong non–thermal continuum, but they differ in the optical spectrum: FSRQ show emission lines usually seen in *quasars* (hence the name). BL Lacs are characterized by the weakness or even absence of optical lines and the strong

polarization and the high flux and variability, which are enhanced for the observer by the "relativistic beaming" of the emission.

*Blazars* are quite peculiar sources, and should be rare indeed. Roughly, 10% of AGN's are radioloud, and only $\sim 1\%$ of these, assuming random isotropical distribution (which sounds extremely reasonable in the light of the observationally sound and theoretically convincing *cosmological principle*, see e.g. Peebles 1993), should have its axis aligned with our line of sight within 15°. If we consider the CGRO/EGRET catalogue of sources, it's relevant that these rare source make up for the vast majority of the identified sources, and a significant ($\sim 25\%$) fraction of the whole catalog. This evidentiates how determinant is the observative bias due to the orientation of this highly anisotropic source.

## 2.5 Spectral Energy Distribution of *blazars*

*Blazars* emit in the electromagnetic spectrum at all wavebands, which is a clear signature of the non–thermal processes at work in the jet. All the sources in the class share the general shape of the Spectral Energy Distribution (SED), that when plotted as $\nu$ vs. $\nu F_\nu$ shows two broad bumps, as shown as an example in Figure 2.8. Another important feature of the SED is also its variability, that tends to be more intense and rapid at higher energies, a feature that can be exploited in order to understand the mechanisms at work.

### 2.5.1 The *blazar* sequence

A very important result has been achieved by Fossati et al. (1998) by means of a statistical study on a sample of 126 *blazars*. Average SED have been built, on subsamples selected according to the mean radio flux. Some relevant facts were evidentiated:

- the low energy bump peaks in different bands for different radio flux, and the peak frequency decreases as the radio power increases;
- the peak frequencies of the two bumps correlate;
- the luminosity ratio[5] of the two peaks increases along with the bolometric luminosity.

This description was very powerful because linked all the *blazars* into a sequence built with only one parameter, related to the luminosity. Figure 2.9, taken from Donato et al. (2001), illustrates this result.

[5]This ratio is also also called "*Compton dominance*".

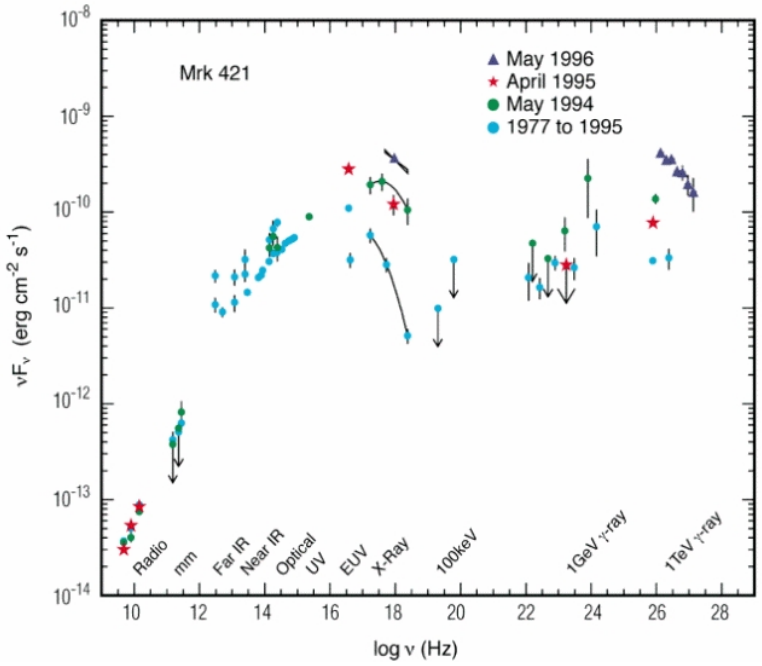


Figure 2.8: As an example of the characteristic SED of *blazars*, a $\nu$ vs. $\nu F_\nu$ plot built with archival Mrk 421 data is presented. The main features are two broad bumps, arguably due to non–thermal processes in the relativistic jet. Taken from Buckley (1999).

Within the sequence, one extreme is occupied by the FSRQ, that show: high radio power, low energy peak in the IR, high energy peak at keV–MeV energies and the bolometric luminosity is dominated by the high energy bump. At the other extreme the BL Lac sources, with lower radio power, higher peak frequencies and less dominated by the high energy bump. Within these sources, two subclasses can be distinguished, based on the position of the peak energies (Giommi & Padovani, 1994): Low–peaked and High–peaked BL Lac objects (LBL and HBL, respectively).

LBL are more luminous, and have the low energy peak in the infrared–optical band, while the second one is found at MeV–GeV energies. HBL instead present the first peak in UV–X rays,while the second culminates in the GeV–TeV energy band; the two bumps have on average nearly equal bolometric luminosities. It must be mentioned that the *blazar* sequence is still a debated item: some authors (see e.g. Padovani, 2007) tend to rule it out as a product of an observational bias rather than a real effect. An important success of the *blazar* sequence was the discovery at TeV energies of many of the BL Lacs proposed as favorable candidates by Costamante et al. (2001), based on its predictions. Although born on an observational basis,

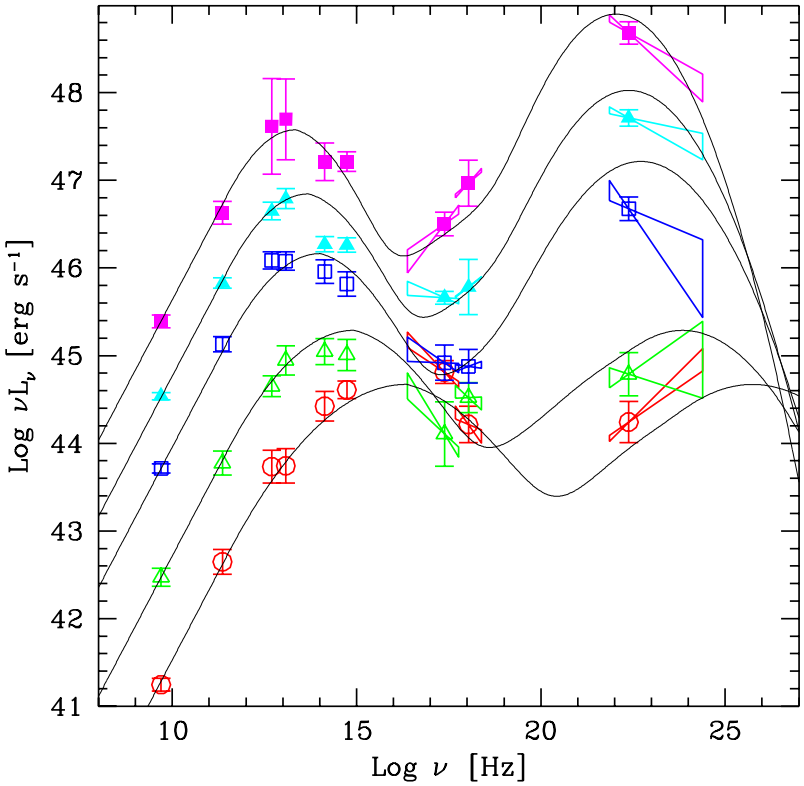


Figure 2.9: Average SED, built from the *blazar* sample of Fossati et al. (1998) split in bins of radio power. Average values of radio, optical, hard X–ray and $\gamma$–ray (from CGRO/EGRET) fluxes and spectral indexes are plotted. The continuous black lines lines report the SED as modeled within Donato et al. (2001). The plot is taken from this latter paper. The most powerful radio sources show the lowest peak energies and the highest Compton dominance and bolometric power, and belong to the FSRQ *blazar* subclass. The opposite end of the sequence, either in terms of radio power or of peak energy or of Compton dominance, is populated by the BL Lac subclass, with High–peaked BL Lacs (HBL) showing the smallest radio and bolometric power, the highest peak energies and the hardest spectral index in the $\gamma$–ray domain, while Low–peaked BL Lacs (LBL) show less extreme properties.

the sequence can be fruitfully interpreted in terms of the source physics, as recalled in Section 3.3.4.

# Chapter 3

# Physics in *blazars*

In this chapter a brief overview of the most important physical topics involved in the *blazar* phenomenology is given.

## 3.1 Particle acceleration in the jet

In order to produce non–thermal spectra that extend up to TeV $\gamma$–rays, particles need to be accelerated up to very high energies. In literature (see e.g. Vietri, 2006) the best rated mechanisms is the *first order* Fermi mechanism that can be active at the strong shocks in the jet. Another mechanism for accelerating particles by means of random scattering could be the *second order* Fermi mechanism (Fermi, 1954), but it has two important limitations:

- the mean relative energy gain $\langle \frac{\Delta E}{E} \rangle$ is of second order in $V/c \ll 1$, where $V$ is the velocity of the scatter targets (Vietri, 2006); therefore it is a slower process (Rieger et al., 2007);
- it can produce particle populations that are distributed in energy as power laws with any spectral index, against the observational universality of indexes $p \approx 2$–$3$;

Instead, the first order process that can be active around the shocks (Bell, 1978; Blandford & Ostriker, 1978) is faster ($\langle \frac{\Delta E}{E} \rangle \propto V/c$) and produces spectra with slopes that are well determined, such as $p \sim 2$ (Vietri, 2006) for strong shocks. Anyway, the situation is more complex and both processes perhaps contribute to acceleration in AGN jets (Rieger et al., 2007).

## 3.2 Relativistic effects in *blazars*

There is evidence that the jets carry highly energized matter at relativistic speeds; therefore relativistic effects must be taken into account when in-

terpreting the observations. One of the most compelling evidences is the observation of superluminal motions in radio jets.

### 3.2.1 "Superluminal" motion in jets and its consequences

Since the '70 astronomers began puzzling around some unexpected behavior of jets, when spatially resolved by means of VLBI radio interferometry. Some bright jets showed *knots*, regions along the jet significantly brighter than the others, probably connected to shock fronts in the plasma. Long term monitoring of the jets indicated apparent superluminal motion of these knots, with apparent velocities up to 10–15 c. The phenomenon had actually been predicted by Martin Rees (Rees, 1966) and is related to a tricky effect of the finiteness of the speed of light. When the angle between the line of sight to the jet and its direction (*viewing angle*) is small, the source "follows" its own emitted photons, so that the travel time to the observer is progressively reduced; this result in a contraction of observed time intervals $\Delta t_{obs}$ with respect to the proper time intervals and therefore in an enhancement of the transverse velocity.

Even if jets reassuringly do not violate the special relativity prescriptions, nevertheless they move at a substantial fraction of $c$: the threshold for obtaining apparent superluminal motions with $\beta_{app} \equiv v_{app}/c > 1$ is $\beta \simeq 0.7$ (Rybicki & Lightman, 1986).

### 3.2.2 Doppler factor

If an emitting source moves with bulk speed $\beta \equiv v/c$, and *Lorentz factor* $\Gamma \equiv (1-\beta^2)^{-\frac{1}{2}}$, a Doppler factor

$$\delta \equiv \frac{1}{\Gamma(1-\beta\cos\theta)} \tag{3.1}$$

The observed $\delta$ as a function of the viewing angle $\theta$ and for different values of the Lorentz factor is plotted in Figure 3.1. It can be shown that at $\theta = 0$, $\delta = 2\Gamma$; while at $\theta \simeq 1/\Gamma$ $\delta \simeq \Gamma$.

This has some important consequences on the observations, namely:

- Every time interval measured in the observer's reference frame is correspondingly shortened with respect to the source frame: $\Delta t_{obs} = \Delta t_{em} \cdot \delta^{-1}$
- The observed frequencies are Doppler boosted with respect to the ones emitted: $\nu_{obs} = \delta \nu_{em}$
- If radiation is isotropically distributed in the source frame, it is beamed along the motion direction (*relativistic beaming*), within a cone of half–aperture $1/\Gamma$. This effect enhances the observed flux of a factor $\propto$

$\Gamma^2$ for an on–axis observer, while at larger viewing angles the flux is strongly suppressed.

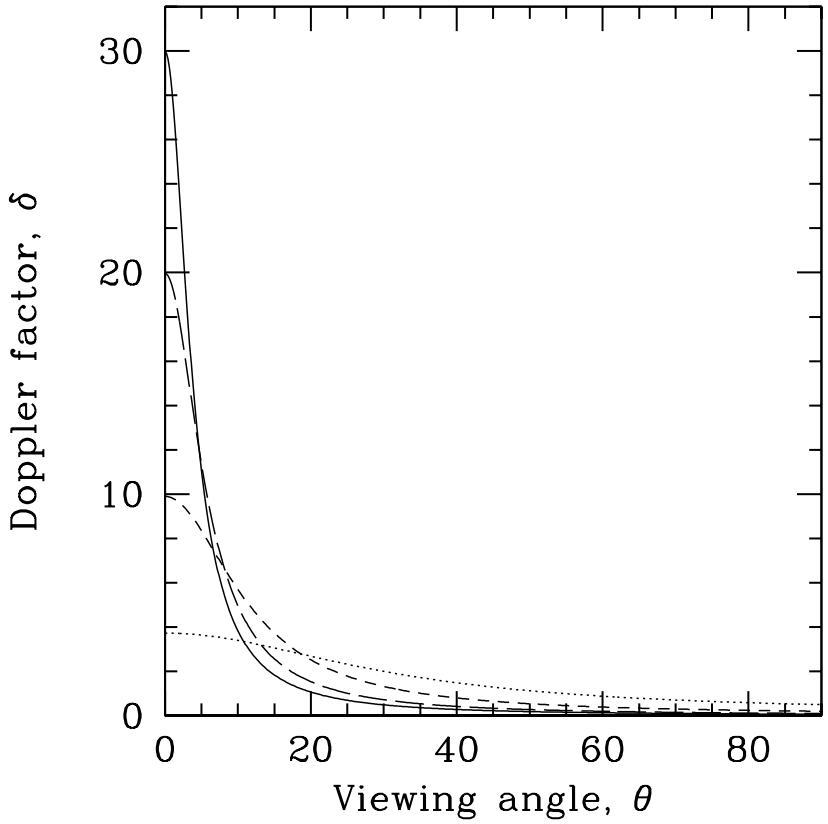


Figure 3.1: Plot of the Doppler factor $\delta$ as a function of the viewing angle $\theta$, for different values of Lorentz factor: $\Gamma = 2$ (dotted line), $\Gamma = 5$ (short dashed line), $\Gamma = 10$ (long dashed line), $\Gamma = 15$ (solid line). At $\theta = 0$ $\delta = 2\Gamma$, while at $\theta = 1/\Gamma$ $\delta = \Gamma$.

All these effects have important observational consequences, the most immediate one being the introduction in $\gamma$–ray observations of a powerful selection effect in favor of the closely aligned *blazar* jets, that due to their large Doppler factors, can be detected at higher energies and with enhanced flux density.

## 3.3 Emission Models

In the current picture, the two bumps visible in *blazar* SEDs are explained by different emission processes. The high degree of polarization observed in

the optical and radio emission of *blazars* strongly supports the interpretation of the low energy bump as being produced by a population of relativistic electrons in the jet, spiraling along the magnetic field lines and therefore radiating due of the synchrotron process.

Instead, the origin of the high energy bump is more debated, and is the main ground where emission models differentiate, and consequently, where could in principle be validated or ruled out by observations. The main dichotomy regards which kind of relativistic particles is supposed to produce the high energy bump of the SED. Some models, where the key role is played by relativistic protons in the jet, are called *hadronic*; instead *leptonic* models attribute the origin of second bump to the electrons as well, by means of the Inverse Compton (IC) scattering processes. Currently no compulsory evidence is available to rule out one of these groups of models even if leptonic ones are somehow more popular at the present; nevertheless, as the modeling present in this work has been made in the framework of a specific leptonic model, only a summmary recall will be given of the hadronic ones, while a more detailed description of the adopted model will be given.

### 3.3.1 Hadronic models

In this family of models, the key role in the production of the high energy emission is played by protons accelerated in the jet. When these models were first proposed, one of their appealing features was that relativistic jets in AGNs were regarded as a favored candidate for the production of the cosmic rays; therefore it was natural to assume an important role of the protons also in the observed radiation. Now this argument is no more that crucial, as other alternative sites of production of cosmic rays are considered.

Earlier models attributed the non–thermal polarized emission to electrons generated as secondaries in $p$–$p$ collisions of high energy protons in the jet interacting with ambient gas (Perola, 1969) , but soon appeared that gas densities in extra–galactic sources were not sufficient for producing the observed radiation by means of such processes.

Instead, in the later *proton blazar* model (see e.g. Mannheim 1993) TeV protons interact with ambient photons at UV/X–ray energies, starting a pair cascade (Proton Initiated Cascade, or PIC), of the form

$$p + \gamma \rightarrow \pi + H \tag{3.2}$$

where $H$ stands for an hadron (Mannheim et al., 1991). The $\gamma$–ray flux observed is then produced by the successive generations of particles, created at progressively lower energies (MeV–GeV). In this model the peak of the SED is directly connected at the energy at which the source becomes optically thin to the $\gamma\gamma$ interaction.

Successive refinements of this scheme have been proposed to model the TeV emission observed from BL Lacs (Mücke et al., 2003).

It's worth mentioning also the model from Aharonian (2000) where the possibility that in *blazars* protons with energies $E \approx 10^{19}$–$10^{20}$ eV could radiate due to synchrotron process rather than by PIC is considered, provided that sufficiently large magnetic fields ($\sim 50$ G) permeate the jet.

Generally, all hadronic models share some common features:

- they require large magnetic fields (of the order of tens of Gauss;)
- the acceleration efficiency is lower for proton than for electrons due to their higher mass;
- for the same reason, acceleration and cooling times are also longer than for leptons.

As far as the agreement with observations is concerned, these models need to introduce *ad hoc* assumptions in order to allocate the observed correlations between the variations of the two peaks, that is more naturally accounted for by leptonic models, where both peaks are produced by the same particles. Also the fast variability is hardly reproduced due to the longer time scales and lower acceleration efficiency for protons than for electrons. On the contrary, evidence for "orphan" flares such as the one observed by Whipple in 1ES 1959+650 (Krawczynski et al., 2004) when quiescent in X–rays, has been claimed as more easily explained here (Böttcher, 2005). Evidence that hadrons at least contribute a fraction of the VHE $\gamma$–ray flux would emerge in case associated neutrino emission should be observed, ruling out a purely electromagnetic process, and calling for the decay of charged pions.

### 3.3.2 Leptonic models

Leptonic models explain the $\gamma$–ray emission in *blazars* with Inverse Compton scattering of soft photons by the same electron population that produces the low energy bump by the synchrotron process. A common feature of all this models is the basic picture of the emitting region, as a "blob", a spherical, region filled of hot plasma and magnetic field, coherently moving away from the central engine at relativistic speed. The models of this class basically differentiate on the origin of the population of soft target photon involved in the scattering. A mixture of different populations is also possible, leading to a sum of contributions, dominated by the population that happens to be denser *in the jet frame*. The most appealing features ot leptonic models are:

- simple models reproduce well multiwavelength data;
- leptons can be easily accelerated to TeV energies by means of the shock mechanism;

- they can radiate efficiently by means of synchrotron and inverse Compton scattering.

Especially the last two features favor leptonic models against hadronic ones.

### Synchrotron Self–Compton

In the Synchrotron Self–Compton (SSC) scheme (see e.g. Maraschi et al., 1992) the target photons are produced in the same jet, and belong to the soft tail of the synchrotron spectrum. This model is one of the most predictive, as it involves the lowest number of parameters, and foresees an intimate connection between the emission in the low and high energy bumps. The success in reproducing the observed SED in spite of the very few parameters involved and, even more, the diffuse evidence for correlated variability between $\gamma$ rays and lower energy bands (optical, X rays) in *blazars* have stimulated a widespread interest in these models, that are nowadays amongst the most popular ones. Actually, the modeling in this work has been made within the framework of SSC models. In particular, the modeling of Mrk 421 SED within this research (see Section 8.13.1) has been made assuming the SSC version discussed in Tavecchio et al. (1998), that is summarily recalled in Section 3.5.

### External Compton

In the External Compton (EC) model the target soft photons for the IC scattering are not found in the jet, but preferentially provided by the central region of the AGN: directly from the accretion disk or reprocessed by the BLR. The photons emitted from the disk may interact with the gas clouds in two ways: they can be simply reflected by electrons (Thomson scattering) or absorbed and reemitted, mainly in the broad optical lines.

The original idea of Dermer & Schlickeiser (1993) involves the UV radiation from the accretion disk, but its role must be weak as in the change of reference between rest and jet frame it suffers a relativistic de–beaming that significantly decreases its density. Instead, radiation reprocessed in the BLR and back re–emitted towards the outgoing jet, for the same reason is strongly amplified. Eventually, thermal near–IR photons reprocessed in the dusty torus can be another target for the IC scattering; process that could provide the dominant contribution to the luminosity in the 10 keV – 100 MeV band (Błażejowski et al., 2000).

### Mirror model

Another mechanism that has been speculated (Ghisellini & Madau, 1996) is the so called *Mirror Model*, where the beamed synchrotron emission from the

jet can be reflected by the BLR and shine the jet itself. The double change of reference frame (from the moving source, to the standing BLR, back to the source frame again) leads to a great enhancement of the surface density of the soft radiation available for the Inverse Compton scattering. On the contrary, constraints on the travel time of the radiation must be taken into account, leading to a severe suppression of the total emission (Boettcher & Dermer, 1998; Bednarek, 1998). This model is somehow a refinement of the SSC, in the sense that the target photons for the IC are provided by the jet itself; the difference is that in the SSC the source sees the radiation at rest, while in the mirror model a double Lorenz–boost is considered.

It is generally accepted that, amongst leptonic models, the ones adopting as dominant the EC process are more likely a good description of the source in the case of powerful FSRQ, where prominent thermal features such as the blue bump and the bright broad optical lines provide plenty of soft target photons while SSC should dominate in the less luminous BL Lac class.

### 3.3.3 Inhomogeneous models

The aforementioned models share the assumption that the emission region is *one*, homogeneous and emitting as a whole: the relevant physical parameters assume unique values all across the region itself. Relaxing this assumption allows to consider contributions from different regions where the physical parameters can assume different sets of values, and their interplay as well.

In this way the agreement with the observation is more easily reached, on one side because the source can be modeled in further detail and more complex physical processes can be accounted for; on the other for the simple, brute reason that the model spans a wider parameter space, provided with bigger dimensionality. But also some drawbacks are obvious and worth of being mentioned: namely, additional complexity, both conceptual and computational, and wider unresolved degeneracies in the parameter space, leading to less predictive, weaker conclusion.

On top of that homogeneous models naturally explain the correlated variability in various energy bands making the adoption of a more elaborate scheme avoidable, at least under this specific respect.

#### Spine–layer model

As an example of inhomogeneous model, the *spine–layer* model (Ghisellini et al., 2005) assumes that the jet is structured in a inner, faster and narrower *spine* and a surrounding, slower and less collimated *layer*, reproducing within the jet the structure observed in VLBI radio maps. In this framework, one component sees the (beamed) radiation produced by the other, and this enhances the Inverse Compton emission of both components. The Inverse Compton emission of the spine is anisotropic in its frame, possibly produc-

ing a deceleration of the spine by the "Compton drag" effect. This scenario has been invoked to account for the high luminosity of the TeV emitting BL Lacs. In homogeneous model, this can be accomplished by very high bulk motion of the source so that the Doppler boost (see Section 3.2.2) of the radiation is maximized. The first solution strikes with the observation that the motion of the radio knots in the same sources is indeed much slower than model predictions; moreover, such high values of the gamma motion are in contrast with the count statistic of the parent population of BL Lacs, believed to be the FRI class of radiogalaxies. In this scenario, the slow layer may also be a relatively strong high–energy emitter, eventually pointing to radiogalaxies as potential VHE emitters in spite of the still scarce number of discoveries.

### 3.3.4 The *blazar* sequence interpreted through emission models

Although built on a phenomenological basis, dealing with the connection between the radio power and other observational parameters such as the inverse correlation with the peak frequencies of the SED bumps, the concept of the *blazar* sequence (see Section 2.5.1) can be understood in terms of the source physics following the so called *cooling paradigm* (Ghisellini et al., 1998). In the framework of one–zone leptonic models the peak frequencies are related to the maximum energy achieved by the hot electrons within the source. This is set by the balance of the acceleration and of the cooling. In FSRQs the prominent BLR provides plenty of target soft photons to be scattered, and therefore the cooling is severe; instead in featureless BL Lacs this contribution from external radiation is missing and the cooling consequently lower. The electrons can be freely accelerated to higher energies, hence the shift at higher energy of the peaks.

## 3.4 Some general constraints to models and parameters.

There are general arguments that reduce the freedom in setting the parameter models.

#### Size and location of the emission region

As far as the size of the emitting region $R$ is concerned, the short variability timescale observed (e.g. in X rays, $t_{var} < 1$ day ) implies that the region is not larger than $2 - 3 \times 10^{16}$ cm.

Typical variability timescales of BL Lacs and FSRQs fix the source size at $\sim 10^{15}$ cm and $\sim 10^{16}$ cm respectively.

This condition in turn has consequences on the location of the emitting region, in terms of its distance $d$ from the central engine: if we assume a jet opening angle $\theta_{jet} \sim 5^\circ$ (0.1 rad), this implies that $d < 2 - 3 \times 10^{17}$ cm (Ghisellini & Madau, 1996).

However other models locate the emitting region at a much farther distance from the central engine ($\sim$ 10 pc, see e.g. Marscher et al., 2008; Sikora et al., 2008), but in this framework day–scale variability in flaring FSRQs like 3C 454.3 or PKS 1510-089 (Tavecchio et al., 2010a; Bonnoli et al., 2010; Foschini et al., 2010) can be hardly explained. Anyway sub–hour scale variability in extreme BL Lac flares, such as PKS 2155-304 (Aharonian et al., 2007), Mrk 501 (Albert et al., 2007f) and the same Mrk 421 (Gaidos et al., 1996) is hardly reproduced also at these distances; a proposed way to solve this problem is emission in"needles" (Ghisellini & Tavecchio, 2008)). Another constraint (this time, a lower limit) to the location of the emitting region is set by the optical opacity of the innermost regions of the engine: $\gamma$ rays emitted too close to the emission disk, are absorbed through pair production. The pairs would then energize through the Inverse Compton scattering the UV photons of the blue bump, producing new $\gamma$–rays, again absorbed in a long chain of processes, eventually redistributing the energy of the initial $\gamma$ rays into X–rays. This should produce an observable X–ray excess that is not revealed. Therefore, the emission region is located at distance $d > 10^{17}$ cm from the SMBH, where this process is suppressed.

Matching the two criteria, the position of the source can be constrained at $d \sim 10^{17}$ cm from the central SMBH.

## 3.5 The simplest SSC

Within this research project, best fits to the multiwavelength data of Mrk 421 have been performed in the framework of a simple homogeneous SSC model: the one elaborated and fully described in Tavecchio et al. (1998), that will be summarized hereafter.

The most noticeable feature of the model is that it allows a non–degenerate description of the source in terms of the model parameters (reported in Section 3.5.1) once the requested observational parameters (reported in Section 3.5.2) are provided.

### 3.5.1 Basic picture of the model and relevant parameters

In this model the source is assumed as a sphere of radius $R$, filled of relativistic electrons and of a *tangled* magnetic field of intensity $B$. Tangled means that the direction of the magnetic field $\vec{B}$ within the source is random and isotropic, with no symmetries or privileged directions.

The energy distribution of the electrons is assumed following a broken power law. If for simplicity the total energy of the electrons is expressed by the (adimensional) Lorentz factor $\gamma = E/m_e c^2$, with $m_e$ the rest electron mass, this distribution can be expressed as:

$$N(\gamma) = \begin{cases} K\gamma^{-n_1} & \text{if } \gamma_{min} < \gamma < \gamma_b \\ K\gamma_b^{n_2-n_1}\gamma^{-n_2} & \text{if } \gamma_b < \gamma < \gamma_{max} \end{cases} \tag{3.3}$$

The distribution is thus determined by 6 parameters, namely:

- the *power indexes* $n_1$ and $n_2$, associated to the slope[1] of the electron distribution in the low energy and high energy branch respectively;
- the *break energy* $\gamma_b$ where the slope changes from $n_1$ to $n_2$ and the two branches of the distribution are connected;
- the minimum and maximum energy of the electron population $\gamma_{min}$ and $\gamma_{max}$;
- the normalization factor $K$, associated to the number density of the electrons in the blob, assumed uniform in the region.

A graphical representation of the broken power law distribution is given in Figure 3.2.

The main, basic results of the model, such as the position of the peaks and the peak luminosity are rather independent from the values of $\gamma_{min}$ and $\gamma_{max}$, until the inequality

$$\gamma_{min} \ll \gamma_b \ll \gamma_{max} \tag{3.4}$$

On the contrary these two parameters also play a role when broad band multiwavelength data are available and the model wants to account for the complete SED.

The source moves rigidly and relativistically, along the jet in the outwards direction, with *bulk Lorentz factor* $\Gamma$. This implies a Doppler factor $\delta$, that depends on the viewing angle according to the derivation reported in Section 3.2.2. Therefore, on top of the 6 parameters describing the electron distribution, 3 more play a role in the model, for a total of 9:

- the size of the emitting region $R$;
- the intensity of the magnetic field $B$;
- the Doppler factor $\delta$.

[1] When plotted in a logarithmic diagram.

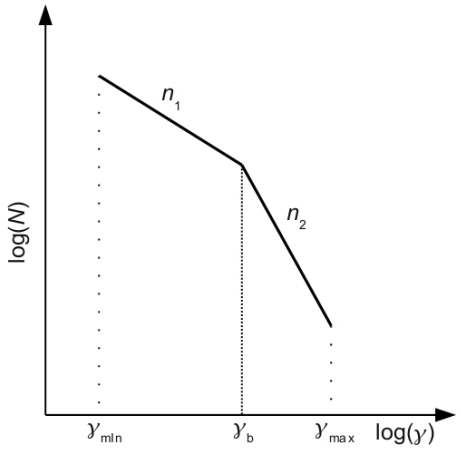


Figure 3.2: A schematic plot of the energy distribution of the relativistic electrons in the source, as assumed in the SSC model from Tavecchio et al. (1998). The distribution follows a broken power law profile, characterized by the 6 parameters $n_1$, $n_2$, $\gamma_{min}$, $\gamma_b$, $\gamma_{max}$, $K$ described in the text.

In the general case, with non negligible contribution from EC processes, also other parameters describing the ambient photons would be necessary to complete the model. They will not be mentioned in the following, as the source of interest is an HBL where the SSC is widely believed to dominate over any other contribution.

### 3.5.2 Observational parameters

On the side of observations, portions of the full SED profile are available, depending on the available instruments and their accessible bandpass. Obviously, the richer the multiwavelength coverage, the tighter the constraint on the model parameters. In first approximation, the SED can be described in terms of a few observational quantities, namely:

- the frequencies of the synchrotron peak $\nu_S$ and of the Inverse Compton peak $\nu_C$ ;
- the spectral energy density at the peaks, $\nu_S F(\nu_S)$ and $\nu_C F(\nu_C)$, or equivalently the luminosity densities $\nu_S L(\nu_S)$ and $\nu_C L(\nu_C)$ ;
- the photon indexes redwards and bluewards of both peaks $\alpha_{1S}$, $\alpha_{2S}$, $\alpha_{1C}$, $\alpha_{2C}$.

This schematic representation of the SED profile is depicted in Figure 3.3.

Another important observable is the variability timescale $t_{var}$, that can be derived from features in the light curve.

In this scheme, it's clear that the most informative observations are those performed in the bands around the two peaks; this has also the practical benefit of minimizing the experimental uncertainties, as the brightest portions of the source spectrum are observed.

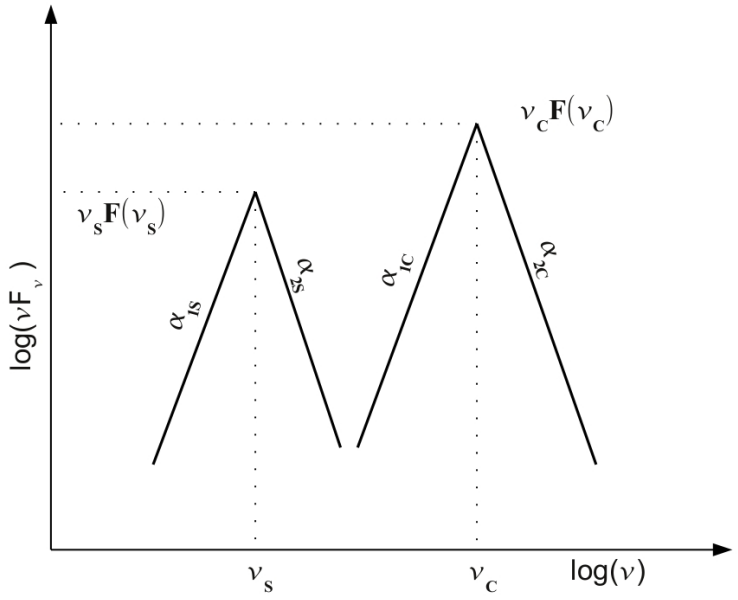


Figure 3.3: A schematic graphical representation of the main observable features characterizing the SED of *blazars*. Peak frequencies ($\nu_S$, $\nu_C$), energy densities ($\nu_S F(\nu_S)$, $\nu_C F(\nu_C)$) and the slopes redwards and bluewards of both peaks ($\alpha_{1S}$, $\alpha_{2S}$, $\alpha_{1C}$, $\alpha_{2C}$) are illustrated. Another crucial observable is the variability timescale $t_{var}$, that can be derived from features in the light curve.

The aim of any model is to reproduce the observations when some, better if unique, set of the model parameters is chosen.

Whereas the full numeric computation will be used to perform the fitting of the data, in the case of the simple SSC model considered here full analytical formulae have been developed in Tavecchio et al. (1998) that are very useful to relate the observational to the model parameters and cast a deep insight in how the physics of the source justifies the observations.

### 3.5.3 Synchrotron emission

Synchrotron radiation is generated when charged particles, moving in a region filled with magnetic field, spiral around $\vec{B}$ due to the Lorentz force. At any given energy, the most efficient radiators are the particles with greater specific charge $q/m$, that are the most accelerated ones. Recalling the standard theory (e.g. Rybicki & Lightman 1986), in the $\delta$–function approximation, some noticeable formulae can be derived (Tavecchio et al., 1998).

The frequency of the synchrotron peak $\nu_S$ can be expressed in terms of $\gamma_b$, $\delta$ and $B$ as:

$$\nu_S = 3.7 \cdot 10^6 \, \gamma_b^2 \, \frac{\delta}{(1+z)} \, \frac{B}{[1\mathrm{G}]} \, [\mathrm{Hz}] \tag{3.5}$$

where the factor $1/(1+z)$ accounts for the cosmological redshift of the source.

The peak luminosity can be written as

$$\nu_S L_S \simeq \frac{8}{9} \sigma_T c B^2 R^3 K \gamma_b^{3-n_1} \delta^4 \tag{3.6}$$

where $\sigma_T$ is the Thomson cross section, that in turn can be written in terms of the classical electron radius $r_e$:

$$r_e = e^2/m_e c^2 = 2.82 \times 10^{-13} \text{ cm} \tag{3.7}$$

$$\sigma_T = \frac{8}{3} \pi r_e^2 = 6.65 \times 10^{-25} \text{ cm} \tag{3.8}$$

As far as the spectral indexes are concerned, power law distributions of radiating electrons produce power law synchrotron spectra (Vietri, 2006), with the photon spectral index $\alpha$ and the electron index linked $n$ by the relation

$$\alpha = (n-1)/2 \tag{3.9}$$

### 3.5.4 Inverse Compton emission

The Inverse Compton process is a simple electron–photon scattering

$$e_0^{\pm} + \gamma_0 \rightarrow e^{\pm} + \gamma \tag{3.10}$$

where, differently from the direct process, the energy is transferred from the electron to the photon.

Two different regimes can be identified, depending if the energy of the target photons $h\nu_0$ is (Thomson limit) or not (Klein–Nishina regime) negligible with respect to the electron rest energy $m_e c^2$.

The Klein–Nishina cross section can be written

$$\frac{d\sigma}{d\Omega} = \frac{r_e^2}{2}\frac{\epsilon_0^2}{\epsilon^2}(\frac{\epsilon_0}{\epsilon} + \frac{\epsilon}{\epsilon_0} - \sin^2\theta) \tag{3.11}$$

where $\epsilon = h\nu$ and $\epsilon_0 = h\nu_0$ are the energies of the target and scattered photons respectively, and $\theta$ is the scattering angle

In the Thomson limit the scattering is elastic ($\epsilon = \epsilon_0$, *Thomson scattering*) and the cross section reduces to

$$\frac{d\sigma_T}{d\Omega} = \frac{r_e^2}{2}(1 + \cos^2\theta) \tag{3.12}$$

The IC peak is determined by electrons of energy $\gamma_b$ scattering the soft photons at frequency $\nu_S$ (see e.g. Ghisellini et al., 1996).

In the Thomson limit therefore the frequency of the IC peak can be written as

$$\nu_{IC} \propto \nu_s \gamma_b^2 \delta \tag{3.13}$$

and the luminosity

$$\nu_{IC} L_{IC} \propto K^2 B^2 R^4 \delta^4 \gamma_b^{2(3-n_1)} \tag{3.14}$$

The quantitative treatment of the Klein–Nishina regime is far more complex and not reported, but the SSC code described in Tavecchio et al. (1998) keeps it into full account. Qualitatively, the main outcome is that the interaction cross section drops in this regime, and consequently the emission at the highest energies is depressed.

For instance, the position of the IC peak is determined as

$$\nu_{IC} \propto \gamma_b m_e c^2 \delta \tag{3.15}$$

following an approximate analytical Klein–Nishina treatment of the Compton process in the "step function" approximation, where the transition between the Thomson and Klein–Nishina regime is approximated as a sharp drop of the cross section from $\sigma_T$ to 0 when the threshold of the Klein–Nishina regime

$$\gamma\nu = \frac{3}{4}\frac{m_e c^2}{h} \tag{3.16}$$

is reached.

As far as the observed spectral slopes are concerned, it can be shown (see again Tavecchio et al., 1998) that in the Thomson limit a power law electron population produces a power law photon spectrum where the indexes are again connected by

$$\alpha = (n-1)/2 \tag{3.17}$$

such as in the synchrotron process (see Eq. 3.9). In the Klein–Nishina regime the slope of the photon spectrum is steepened again due to the decay of the cross–section.

## 3.6 Model parameters and observations

To understand qualitatively the importance of the various model parameters, it can be enlightening to review how the observed quantities scale with variation of each single physical parameter describing the source.

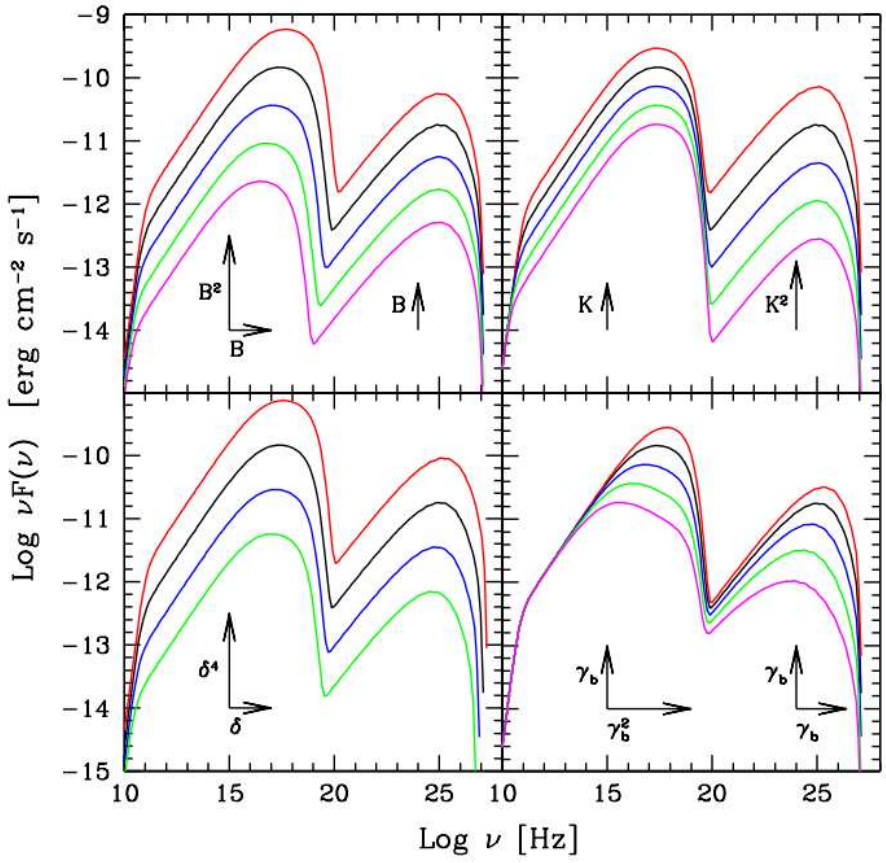


Figure 3.4: A plot illustrating how the observed peak frequencies and luminosities scale with variations of the parameters $B$, $K$, $\delta$, $\gamma_b$. Courtesy of F. Tavecchio.

This is illustrated in Figure 3.4. It must be noted that he shown dependences are directly deriving from the formulae in the case of the synchrotron peak. Instead, the scaling of the position of the Inverse Compton peak takes into account both regimes, and should be intended as a rule of thumb, not deriving exactly from any of the reported approximated equations.

From Eq. 3.5 and 3.6 we have that the synchrotron frequency $\nu_s$and luminosity $\nu_s L_S$ scale with $B$ and $B^2$ respectively, while the IC peak frequency does not depend on $B$ and the IC luminosity is linear in $B$.

The normalization of the electron density $K$ determines the number of radiating particles in synchrotron ($v_S L_S \propto K$) , while both the number of scattering electrons and of target soft photons as far as the Inverse Compton process is considered ($v_{IC} L_{IC} \propto K^2$).

As far as the role of the Doppler factor is concerned, the peak positions depend linearly on it ("blue shift" of the frequencies), while the luminosity depends on $\delta^4$, due to the coherent sum of contributions of the frequency shift, the contraption of the time interval and the relativistic beaming of the flux density. These scaling relations interest the whole SED, as they depend on the change of reference frame between the source and the observer. Finally, the break energy $\gamma_b$: $\nu_S$ scales quadratically with it (Eq. 3.5) and $\nu_S L_S$ linearly (Eq. 3.6). the dependence of the position of the IC peak instead is linear both infrequency and in luminosity.

## 3.7 Opacity of universe at GeV-TeV energies

The Universe is not fully transparent to VHE $\gamma$ rays, due to the effectiveness of the pair production process in scattering of high energy photons against ambient soft (IR, optical,UV) photons of the Extragalactic Background Light (EBL Stecker et al., 1992):

$$\gamma_{VHE} + \gamma_{EBL} \rightarrow e^+ + e^- \tag{3.18}$$

The pair production is a threshold process; the minimum energy in the center of mass frame for the process to occur is $2m_e c^2$, the rest mass of the two electrons that are produced. Performing the correct relativistic calculation in the observer's reference frame, this translates into the condition

$$h\nu_{VHE} \cdot h\nu_{EBL} > m_e^2 c^4 \tag{3.19}$$

The cross section of the process peaks around two times the threshold, so that the problem can be in first approximation idealized as having one preferred target frequency for each VHE $\gamma$–ray energy,

$$h\nu_{EBL} \simeq 5 \cdot (\frac{E}{100\text{GeV}})^{-1}\text{eV} \tag{3.20}$$

A 100 GeV $\gamma$ ray is therefore more effectively absorbed by near UV photons.

It must be noted that the photons that we measure as of energy $E$, were generated at redshift $z$ with energy $E(1+z)$, and observers at rest along the path would observe it at intermediate energies. Therefore the density of absorbers that VHE photons find along their path changes both due to the shift in the rest frequency of the preferential targets, and to the cosmic evolution of the background light at the various epochs.

The background is poorly known, as its measurement is difficult due to prominent foreground contributions. Figure 3.5 reports a recent compilation of the different measurements. lower and upper limits that can be found in Mazin & Raue (2007). Rather important are the lower limits set by means of galaxy counts, as in the works of Madau & Pozzetti (2000) and other similar in the following years.

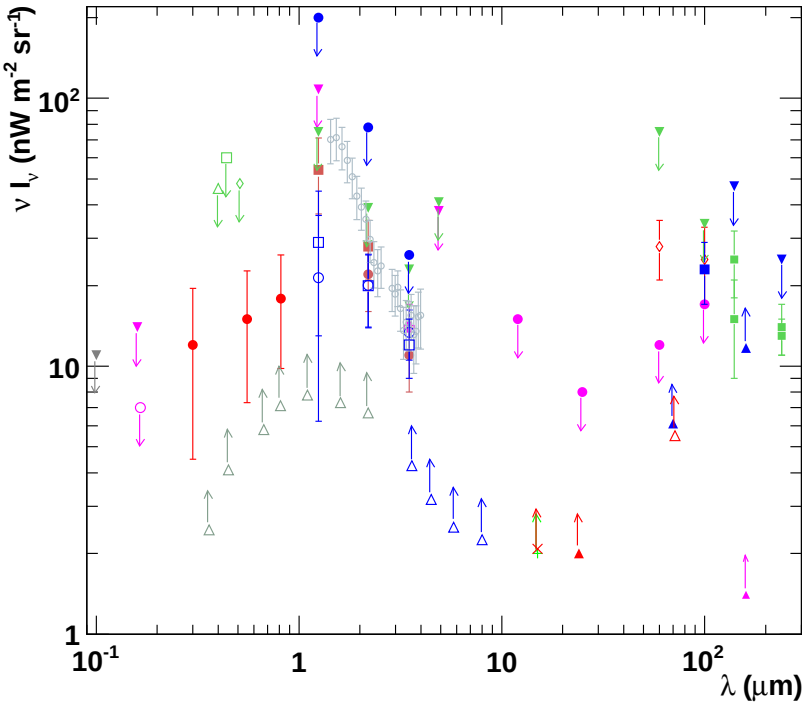


Figure 3.5: A compilation of different measurements of the Extragalactic Background Light, from Mazin & Raue (2007). Two broad bumps can be seen, around $\sim$ 1 and $\sim$ 100 $\mu$m, due to redshifted starlight and absorbed/emitted starlight reprocessed by dust respectively.

Many different models (e.g. Stecker et al., 2006; Franceschini et al., 2008; Gilmore et al., 2009; Domínguez et al., 2010; Kneiske & Dole, 2010) have been therefore proposed for the computation of the optical depth $\tau(E, z)$, that links the observed flux $\Phi_{obs}$ to the one emitted from a source at redshift $z$, $\Phi_{em}$ :

$$\Phi_{obs}(E) = \Phi_{em}(E) \cdot e^{-\tau(E,z)} \tag{3.21}$$

It has been shown that this absorption effect introduces an energy–dependent *EBL horizon*, defined by the $\tau(E, z) = 1$ condition (see Figure

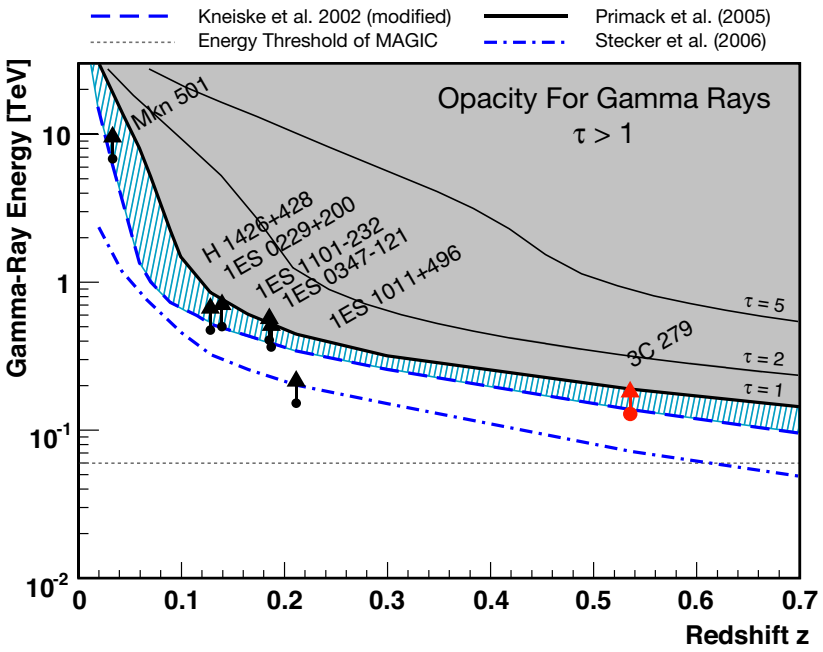


Figure 3.6: The $\gamma$–ray horizon (defined buty the $\tau(E, z) = 1$ condition) as predicted by different EBL models (Kneiske, Primack, Stecker) is reported in the picture, together with the constraints set to the $\gamma$–ray horizon from the observation of *blazars* at VHE energy. The thick black line is the horizon corresponding to the minimum EBL compatible with the lower limits set by galaxy counts (Primack et al., 2005). The blue shaded area is the range allowed between the constraint set by the VHE detected *blazars* and the aforementioned "minimum EBL" horizon. From MAGIC Collaboration (2008).

3.6). Given an observed energy $E$, the flux from sources located beyond the horizon is suppressed by a factor greater than $e$. Lowering the observed energy widens the observable portion of Universe, and this is a major reason to aim to VHE instruments characterized by a low energy threshold (just as MAGIC was designed). It's worth noticing that in 2008 MAGIC detected the distant FSRQ 3C 279 at $z = 0.536$ (MAGIC Collaboration, 2008); the discovery of this faraway source as a VHE emitter constrains the EBL next to the very low lower limit derived from galaxy counts, and could point to an universe more transparent than expected at VHE energies. Other, more exotic explainations of this extra–transparency of the Universe have been claimed: such as the one involving photon oscillation to other light bosons that can travel long distance without being absorbed (Roncadelli et al., 2009).

Powerful extragalactic sources of $\gamma$ rays can be in principle used as probes of the EBL along the path to the observer. As the EBL, at each epoch, is related to stellar formation rates and galaxy evolution, the availability of many such probes, distributed in redshift, allows measurement of its evolution at various epochs, leading to information on relevant comological issues on the evolution of galaxies.

An alternative, interesting application of EBL is the derivation of constraints to the distance of sources of undetermined redshift can be set, once the EBL is assumed (Aliu et al., 2009b; Prandini et al., 2010).

A last issue that has arisen great interest in the last months (Neronov & Semikoz, 2009; Neronov & Vovk, 2010; Tavecchio et al., 2010c; MAGIC Collaboration et al., 2010) related to EBL absorption is production of $\gamma$–ray halos, due to the interplay of EBL absorption of UHE and VHE photons from *blazars*, that produces $e^{\pm}$ pairs, and the Inter Galactic Magnetic Field (IGMF) diffusing them. These energetic electrons and positrons in turn eventually produce new $\gamma$ rays of lower (MeV – GeV) energy by means of further Inverse Compton scattering on the photons of the Cosmic Microwave Background (CMB) at 3 K, by far the most diffuse in the Universe ($n \sim 400$ cm$^{-3}$). *Lower* limits on the IGMF have been recently set in this way ($B_{\rm IGMF} \gtrsim 10^{-15}$ G, Tavecchio et al., 2010b).

# Chapter 4

# Imaging Air Cherenkov Telescopes

In Section 1.2.2 satellites for $\gamma$–ray astronomy were briefly recalled, and amongst them the LAT detector on board of *Fermi*. Although extending the observable energy band at higher energies than its precursor CGRO/EGRET some intrinsic limitations of satellite–borne telescopes are patent even in this state of the art detector:

- higher energy photons are hardly detectable, due to the radiation length exceeding detector dimensions. This spoils the energy resolution of the detector, as showers are not fully contained in its volume and calorimetry is systematically inaccurate. Moreover, at energies above 100 GeV the performance of the anticoincidence shield worsens, thus rejection of spurious tracks due to charged particles crossing the telescope becomes harder;

- collection area is intrinsically and unavoidably small, while high energy photon flux is vanishing with power law.

These limitations are overridden by alternative and fruitful ground based telescopes, as already anticipated in section 1.2.3. In this chapter a summary of the Imaging Air Cherenkov technique is given.

## 4.1 Imaging Air Cherenkov technique

Earth atmosphere is not transparent for high energy cosmic rays, that are absorbed in interactions with the atoms of the atmosphere. Of course this prevents direct detection of VHE photons from the ground; satellites are mandatory to achieve this task. But on the other hand, indirect detection is possible. The interaction of VHE particles (not only photons, but leptons and hadrons too) with the atmosphere gives rise to a cascade of secondary

products. As long as these products are charged and superluminal in atmosphere, they radiate near–UV and optical photons in a narrow cone around their flight direction, due to the Cherenkov effect, originating a rapid (time scales of $10^{-9}$ s) flash of light. This signal is faint on average with respect to Night Sky Background (NSB), but that can dominate it if time sampling frequency is appropriate. The detection is therefore two times indirect, but anyway the energy and direction of the primary photon can be reconstructed, allowing VHE spectra and VHE sky imaging. Under some respect, in the IACT technique the atmosphere plays the role of the absorbing material of a giant calorimeter, where the actual telescope is the sensitive device. Therefore IACTs benefit of the advantage of a huge effective collection area, of the order of $10^9$ cm$^2$: much bigger than the actual size of the instrument.

## 4.2 Extended Air Showers

The interaction of High Energy particles with the atoms of the atmosphere produces large cascades of secondary particles, called also *Extender Air Showers* (EAS). More precisely, $\gamma$–rays interact electromagnetically, giving rise to cascades of $e^{\pm}$ pairs and again, photons. Hadrons produce a wider spectrum of particles, including $\pi$, by means of the strong nuclear interaction. Therefore hadronic cascades have a different developement, but again the products produce Cherenkov flashes. Electromagnetic and hadronic cascades are anyway morphologically different, and this can be exploited in order to distinguish events of the two kinds. This discrimination is crucial, as charged particles arrive on the Earth after a curved path due to the magnetic fields that fill up the Universe, including our Galaxy and the intergalactic space (see e.g. Zeldovich et al., 1983, for an exhaustive review); IACTs instead perform VHE imaging of the sky relying on the straightness of the path that the photons follow from the source to the observer, so that the incoming direction observed on the Earth allows to trace back the original emitter. Therefore hadronic events in this context constitute an undesired background, that the observer needs to separate and reject from the photon induced events.

### 4.2.1 Electromagnetic cascades

The cascades initiated by photons or by $e^{\pm}$ are driven by electromagnetic interactions, and involve mainly Bremsstrahlung[1] radiation and pair production.

[1] A term of common use in Particle Physics, mutuated from German and mantained for historical reasons. The meaning is "braking radiation".

### Bremsstrahlung

This is the radiation produced by accelerated motion of charged particles in electrical fields. It's clearly relevant for light charge carriers (i.e. $e^{\pm}$) and vanishes for interaction of charge–anticharge pairs of the same weight (due to compensation of electrical dipole momenta). In atmosphere, electrons and positron deviate in the electrical field of ions and atomic nuclei.

It can be formally expressed as

$$e^{\pm} + \gamma' \rightarrow e^{\pm} + \gamma \tag{4.1}$$

where $\gamma'$ is the virtual photon of the electric field that takes part in the interaction.

In relativistic regime, the energy loss per length $X$ can be expressed as

$$-\frac{dE}{dX} = 4\alpha N_A \frac{Z^2}{A} z^2 r_e^2 (\frac{m_e}{m})^2 E \ln \frac{183}{Z^{1/3}} \tag{4.2}$$

with $\alpha$ the fine structure constant, $N_A$ the Number of Avogadro, $A$ the atomic number, $A$ the mass number, $r_e$ and $m_e$ electron's classical radius and mass respectively, $m$ the mass of the involved ion. $z$ its charge and $E$ its energy (Longair, 1992).

### Pair production

This phenomenon derives from interaction of high energy light with matter. In the electrical field of ions or nuclei, a virtual photon $\gamma*$ can interact with the incoming VHE photon in the process

$$\gamma + \gamma^* \rightarrow e^+ + e^- \tag{4.3}$$

As in the case of interest $E_\gamma \gg E_{\gamma^*}$ and $E_\gamma \gg m_e c^2$, it can be assumed that each of the emerging leptons carries half of the energy of the primary $\gamma$–ray: $E_{e^\pm} = E_\gamma/2$.

### Developement of the electromagnetic cascade

An important element is that the radiation length for the pair production in the ultrarelativistic limit $\xi_{pp}$ and for the bremsstrahlung $\xi_{brems}$ process are nearly the same (Longair, 1992). This is not surprising as both processes involve a photon and an electron, therefore are basically the same in quantum electrodynamics and share the same Feynman diagrams.

Therefore, the idealization illustrated in Figure 4.1 can be made. A common typical distance in air $X_0$ is considered for both: after traveling a distance $X_0$ in atmosphere, a photon produces a pair, and a lepton radiates half of its energy by means of bremsstrahlung.

When a primary $\gamma$–ray with energy $E_0$ enters the atmosphere, and produces a pair. The pair radiates via the bremsstrahlung process and in turn the new photons produce pairs. On average, after any typical length the number of particles in the shower is doubled, and their energy is halved, therefore after a distance $nX_0$, the cascade contains $2^n$ particles of average energy $E_0/2^n$.

The shower extinguishes when the energy of the final products approximates the *critical energy* $E_C$, that in air is $\sim$ 83 MeV (Longair, 1992). Below this energy, ionization losses dominate over the bremsstrahlung for electrons, while the photoelectric absorption and Compton scattering start competing with the pair production for photons.

Therefore the electromagnetic cascades show these peculiar properties:

- only photons and $e^{\pm}$ are produced;
- the initial growth of the cascades is exponential;
- the maximum number of particles is proportional to $E_0$: $N_{max} \sim E_0/E_C$;
- beyond the maximum, the electron flux drops due to ionization losses and the shower is rapidly extinguished.

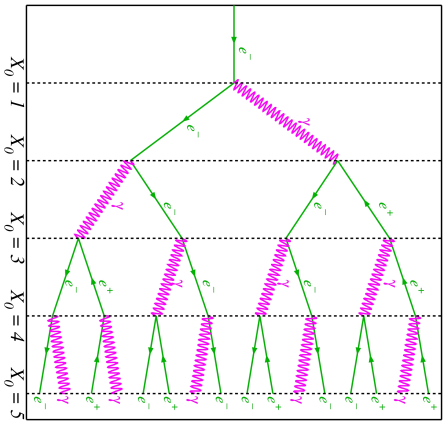


Figure 4.1: Scheme of the developement of an electromagnetic cascade in atmosphere. As the shower digs in atmosphere, after each distance $X_0$ the number of particles doubles, while the average energy is halved.

### 4.2.2 Hadronic cascades

The vast majority of the particles in cosmic rays is constituted by high energy nuclei, and especially protons. Being charged particles, on the cosmic paths even the weak interstellar, galactic and intergalactic magnetic field can bend their traiectories, destroying the connection between their arrival direction on the earth and the position in the sky of the emitter. Anyway they constitute a strong, rather isotropic background for VHE photon detection in IACT astronomy. In Figure 4.2 the various processes involved in the developement of hadronic cascades are represented: these include secondary heavy nucleons and pions. The charged pions in turn decay in muons and these may under certain conditions in electrons, starting secondary electromagnetic showers. The neutral $\pi_0$ decays in energetic photons, originating $e^{\pm}$ couples and subsequent electromagnetic showers.

The salient features of the nucleonic cascades can be summarized as:

- The secondary pions and nucleons continue to multiply in successive generations of nuclear collision, down to the threshold energy for multiple pion production ($\sim 1$ GeV). At the end the energy of the primary nucleus is split in pions, charged particles and antinucleons (*pionization*).
- Secondary protons release energy by ionization and those below 1 GeV are stopped.
- $\pi_0$ decays with short lifetimes ($1.78 \times 10^{-16}$ s) with the process $\pi_0 \rightarrow 2\gamma$. The photons initiate electromagnetic showers.
- Charged pions decay in flight into muons ($\pi^+ \rightarrow \mu^+ + \nu_\mu$; $\pi^- \rightarrow \mu^- + \bar{\nu_\mu}$), with mean lifetime $\tau = 2.55 \times 10^{-8}$ s.
- These muons radiate by ionization, but do no take part into nuclear interactions anymore. The low energy ones ($\gamma \lesssim 20$) decay weakly into positrons, electrons and muon neutrinos, with $\tau = 2.2 \times 10^{-6}$. The muons produced by very high energy pions, in the uppermost atmosphere, are very penetrating, and reach ground.

## 4.3 Cherenkov radiation

Charged particles traveling through a medium of dielectric constant $\epsilon$ (and refractive index $n = \sqrt{\epsilon}$) with speed $v > c/n$, the speed of light in the medium, emit radiation via the *Cherenkov effect*. From a microscopical point of view, the effect arises from the Coulomb interaction. When a charged particle travels through air, it polarizes the molecules in the neighborhoods of its trajectory; these behave in first approximation as electrical dipoles,

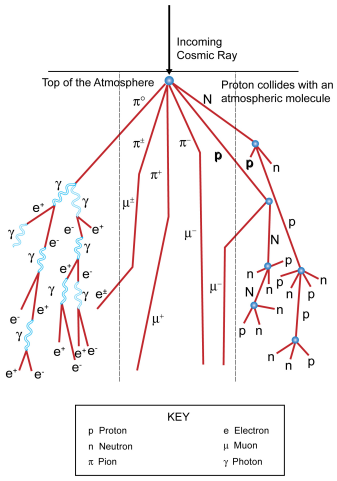


Figure 4.2: Sketch of the possible interactions of cosmic rays with atmosphere.

that change their orientation following the charged particle. If the speed of the free charge exceeds $c/n$, the reaction of the dipoles is instead delayed by the light travel time, and this leads to the production of a shock wavefront in the electromagnetic field, detectable as a light flash. The effect is illustrated by means of the Huygens Principle in Figure 4.3.

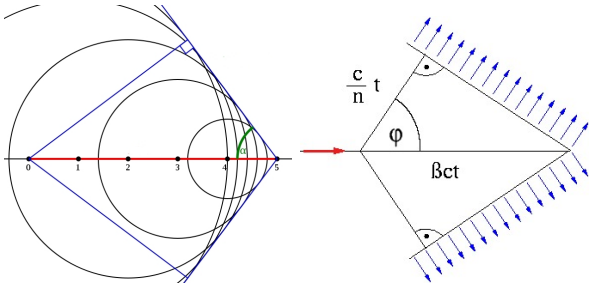


Figure 4.3: Left panel: Huygens construction of the Cherenkov effect. Spherical wavefronts, originated all along the trajectory of the superluminal charged particle, sum constructively on an expanding conical surface. Right panel: the aperture angle of the cone can be calculated by simple plane geometry.

A charged particle (for simplicity, an electron) travels through air with speed $v$. At each point along its trajectory a spherical wave expanding with speed $c/n$ is produced. As long as $v < c/n$, wavefronts generated at different points and times do not intersect. As soon as $v \geq c/n$, wavefronts

sum constructively along a conical surface.

The aperture angle $\phi$ of the cone can be written (see Figure 4.3, right panel) in terms of the refraction index $n$ of the dielectric and of the speed of the charged particle $\beta \equiv v/c$ as:

$$\cos(\phi) = \frac{c/n \cdot t}{\beta c \cdot t} = \frac{1}{\beta n} \tag{4.4}$$

This wavefront travels outwards and represents the Cherenkov flash. Given a refraction index $n$ the angle is constrained in the range $[0, \arccos \frac{1}{n})$, and increases with the increasing speed of the particle.

In air, the refraction index is near to unity ($\Delta n = n - 1 = 2.76 \times 10^{-4}$ at sea level Longair 1992). This implies that the speed of particles must differ from $c$ by a very small fraction, and that the aperture of the cone is narrow ($\sim 1^\circ$).

The threshold speed for the Cherenkov effect $v_t$ can be easily converted into a minimum Lorentz factor:

$$\frac{v_t}{c} = \frac{1}{n} \Rightarrow \gamma_t = (1 - \frac{v_t^2}{c^2})^{-\frac{1}{2}} = (1 - \frac{1}{n^2})^{-\frac{1}{2}} \approx (2\Delta n)^{-\frac{1}{2}} \tag{4.5}$$

Thus, in atmosphere at ground level $\gamma_t \approx 40$. Therefore the energy threshold for the production of Cherenkov radiation is 20 MeV in the case of electrons.

It is interesting to recall that already Blackett (1948) proposed that Cherenkov light emitted by cosmic rays and secondary charged particles contributed the 0.01 % of the Light Of Night Sky (LONS).

## 4.4 Principle of imaging detection of EAS

In Figure 4.4 is illustrated how the imaging of showers can be performed. The radiation length for a $\sim 1$ TeV $\gamma$ ray is $\sim 33$ g/cm$^{-2}$, and its interaction in atmosphere ($\sim 1000$ g/cm$^{-2}$ thick, Longair 1992) initiates at height $\sim 20$ km.

As the shower digs in the atmosphere, the primary energy is released completely in the shower products, while the superluminal charged products shine their Cherenkov light flash. In the meanwhile, the shower grows in the transverse direction, and the Cherenkov angle opens due to the barometric increase of air density. A telescope focused at $\sim 10$ km can image the core of the shower, as an elongated, roughly elliptical image. The major axis of the image is the projection on the camera plane of the shower axis, therefore pointing to the position of the apparent source direction on the camera plane. Due to the opening angle of the shower (1–2°) and the height of the shower development ($\sim 10$ km) the Cherenkov flash shines an area of approximate radius $\sim 120$ m at ground level. This is the reason for the

huge collection area of such telescopes, in great excess of the mere mirror surface.

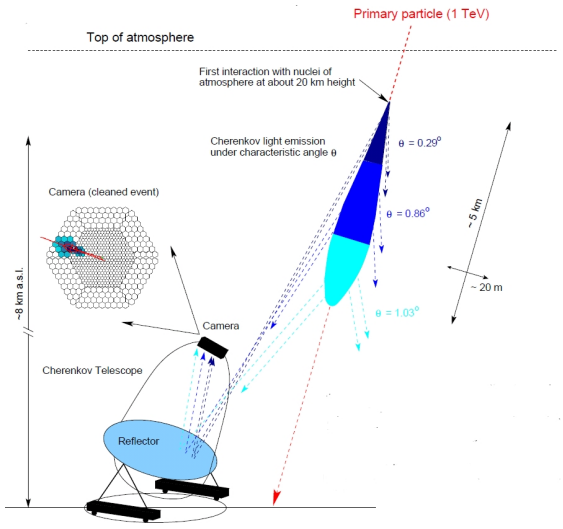


Figure 4.4: A sketch illustrating how the imaging of extended air showers is performed by Imaging Air Cherenkov telescopes.

### 4.4.1 Cascade progenitors and shower images

The main goal of the Imaging Cherenkov Technique is the discrimination between cascades initiated by different progenitors. Figure 4.5 can qualitatively illustrate how in principle the rejection of background can be performed.

Showers initiated by $\gamma$ rays tend to be compact and narrow, and with high charge surface density (upper left panel). The shape tends to be roughly elliptical and with rather clean edges.

Hadronic showers tend to produce wider images, more fragmented and irregular (upper right and lower left panel).

Muons traveling towards the telescope produce characteristic ring–shaped images (lower right panel), or arcs if the impact parameter is large. The rejection of the background due to showers initiated by charged particles can therefore be performed by means of a refinement of this basic concepts, aiming to be able to discriminate the different progenitors from the topology of the showers and a few parameters that describe them efficiently (see Section 6.6).

The rejection method was initially proposed in a fundamental paper by Hillas (1985).

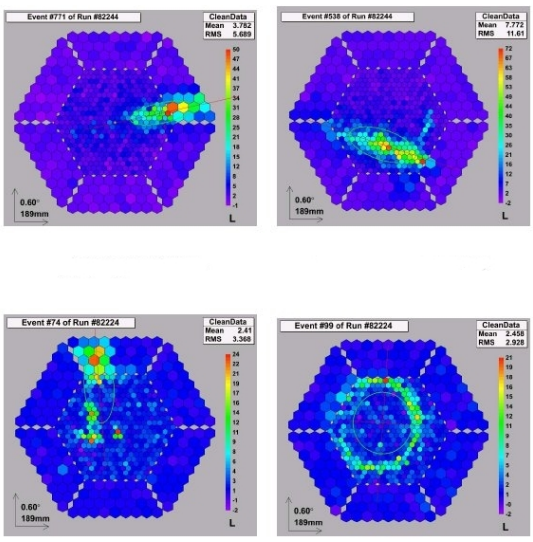


Figure 4.5: Some examples of shower images collected on the MAGIC camera and produced by showers initiated by different progenitors: a probable $\gamma$ ray (upper left panel), two likely hadrons (upper right and lower left panel) and a muon (lower right panel). Parameters describing efficiently the different morphology can be used to perform the discrimination of the $\gamma$–rays from the background due to charged progenitors.

## 4.5 Key Features of an Imaging Air Cherenkov Telescope

Some of the most important features that characterize the performance of IACTs are reviewed here.

### 4.5.1 Energy Threshold

As in the VHE range even the most hard emitters show decaying spectra with photon indexes $\alpha > 2$, it's obviously important to extend the lower end of the observed energy band. A low threshold widens the sample of accessible sources, increases the observable fluxes, extends the observable portion of the Universe as the $\gamma$–ray horizon (see Section 3.7) slides farther away with decreasing observed energies.

A simple formula connects the energy threshold $E_t$ to the telescope characteristics (Fegan, 1997):

$$E_t \propto \sqrt{\frac{\Omega\tau\phi}{A\eta}} \tag{4.6}$$

where $\Omega$ is the solid angle subtended by the detector, $\tau$ is the electronic integration time of the system, $\phi$ is the photon flux from the NSB, $A$ is the area of the mirror, $\eta$ is the quantum efficiency of the photon detector. It emerges that, for a given FOV and level of night sky brigntness, the best performance is achieved by means of a small integration time, a wide mirror surface and a high quantum efficiency.

### 4.5.2 Evolution of the performance with the zenith angle

The performance of the IACT technique is heavily dependent from the elevation of the observed source.

As a rule of thumb, the energy threshold $E_t$ increases with some power of the $\cos(\theta)$:

$$E_t \propto \cos(\theta)^{-\alpha} \quad \alpha \simeq 2.5$$

Rather qualitatively, it can be stated that an exponent 2 comes from the geometrical dispersion of photons over a larger area, so that the surface density is lowered; another 0.5 comes from the increased extinction due to the longer path in atmosphere.

Instead, again because of the increased travel in atmosphere, the collection area of the telescope is increased, thus improving the point source sensitivity.

Therefore the sensitivity curves evolves with increasing zenith angle as such: the energy threshold increases, and the sensitivity curve slides at lower fluxes and extends to higher energies.

In Figure 4.6 this peculiar feature is illustrated, by means of the sensitivity curves of the MAGIC telescope for different ranges of zenith angles. Both Monte Carlo simulations (lines) and real measurements (points) are plotted.

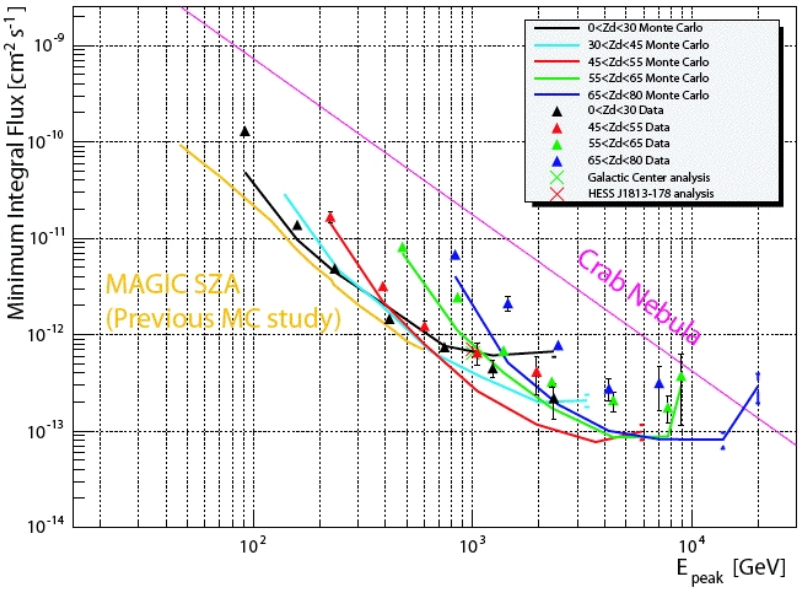


Figure 4.6: A plot based on MAGIC sensitivity, illustrating the evolution of the energy threshold and of the sensitivity curve with the zenith range of the observations. The minimum energy threshold is reached next to the zenith, thereafter increases with increasing airmass. The sensitivity curve instead extends to lower fluxes and to higher energies, due to the increase of the collection area at each observed energy.

# Chapter 5

# The MAGIC–I Telescope

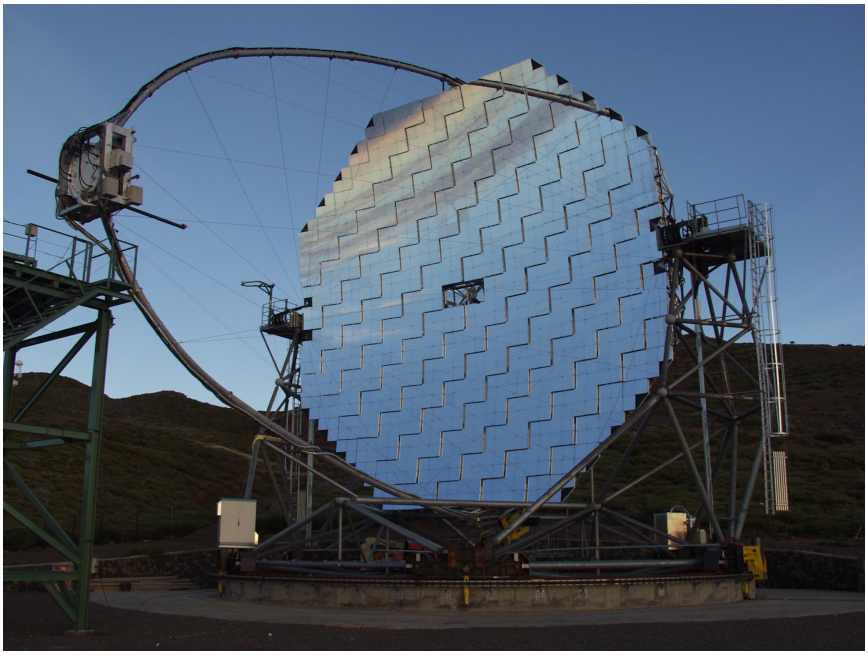

Figure 5.1: A photograph of the MAGIC–I Telescope. The lightweight frame with altazimutal mount, the 17 m diameter tessellated aluminium mirror, the photomultiplier tube camera at the prime focus are visible; description in the text.

### 5.0.3 The MAGIC collaboration

The MAGIC–I telescope was projected and built by a consortium of european Universities and research institutes. The project dates back to the 90's, based on the experience gathered running the previous HEGRA array

Daum et al. (1997). The telescope construction spanned the years 2001–2003 and the commissioning ended in late 2004. The Collaboration, which was founded by a few leading institutes, (namely the German BMFB and MPG, the Italian INFN, and the Spanish CICYT) has now increased to $\sim$ 150 physicists, coming from $\sim$ 20 Institutes and Universities all cross Europe.

### 5.0.4 Telescope site

The telescope is located in the western Canary Island of La Palma, on the top of the extinguished Taburiente volcano, at an altitude of $\sim$ 2200 m above sea level (a.s.l.). Geographic coordinates of the telescope site are: 28.75° N, 17.89° E.

The top of the mountain, that is called Roque de Los Muchachos[1] is particularly suitable for astronomy, so that the vast majority ($\sim$ 10) of the research telescopes currently in operation in Europe is located there; the area is, together with the Pico Teide in Tenerife, part of the North European Observatory.

The main reasons of this widespread favor are:

1. the site is quite high, reducing photon's path in atmosphere and thus signal dispersion and absorption;

2. the island faces the Atlantic Ocean, that, being an extremely flat surface, favors laminar instead of turbulent motion of air masses, that is a major threat at optical wavelengths as the latter worsens the athmospheric *seeing*;

3. El Roque usually stands above the "thermal inversion point"[2] so that clouds usually lie below the observatory height, and do not prevent observations;

4. the island is quite uncrowded, and being $\sim$ 100 km faraway from the more populated Tenerife, has low light pollution levels; moreover, a tight specific law of the Spanish Government keeps it under strict control; finally, the cloud carpet that usually lies below the observatory level to the east acts as a shield against direct light pollution from the coastal towns.

[1] Due to some strange rock formations on the very top, that might resemble a group of boys.

[2] Air temperature decreases up to a certain altitude, then increases again. The position of the temperature minimum is the preferential site for condensation of water vapor into clouds.

## 5.1 The telescope structure

In the following, I describe summarily the subsystems that constitute the telescope, starting with the frame and then trying to follow the ideal path that the physical information follows from the EAS to the storage system.

### 5.1.1 The frame

The telescope frame is made of a grid of lightweight carbon fiber tubes, connected by aluminium elements ("tube and knot" system); both the used materials and the adopted design managed to limit the total weight of the moving part to less than 20 tons[3]. The mount scheme is altazimuthal, as needed for all the biggest telescopes. The frame can move in the azimuth direction by sliding on a circular horizontal rail, and in elevation, where motors can rotate it around an horizontal axis. As usual for this kind of mounts, the tracking of sources requires combined movements in both degrees of freedom; moreover, there is a forbidden region around the zenith, ($\alpha < 1.5^\circ$) where the tracking would require excessively high speeds in azimuth (asymptotically infinite when $\alpha \to 0$). The last specific feature of altazimuthal mounts is that the field of view rotates around the camera center during the tracking. In standard optical telescopes this is usually neutralized by some derotation hardware bearing the camera; instead in MAGIC the dimensions and weight of the camera, and the need for a light structure capable of fast movement discouraged such an approach; derotation is implemented instead in the analysis software, where the correspondence between sky directions and camera positions at any time are recalculated from camera pointing coordinates, camera orientation and the UT time.

#### Drive

The movement around the azimuth axis is ensured by two 11 kW motors, while one of the same power is enough to drive the elevation movement. The control of the telescope position is performed by means of 14–bit shaft encoders, one for the azimuth and 2 for the elevation, in order to check for deformations of the mirror dish geometry due to the varying effect of gravity at different elevations. The accuracy of the control is $\sim 0.02^\circ$, so well below the angular resolution of the instrument, which is esteemed $\sim 0.1^\circ$.

Due to the relatively light–weight moving structure (frame, mirror, PMT camera) MAGIC can be repositioned on a timescale of tens of seconds, far less than any concurrent IACT. In the worst cases, the repositioning takes less than 100 s, while the average repositioning time is $\sim 40$ s. The fast repositioning of MAGIC is one of its peculiar features (rare non only amongst IACTs, but even with respect to smaller astronomical imaging instruments),

[3]The total weight, undercarriage included, amounts to $\sim 65$ tons.

that allows for observation of the prompt emission of Gamma Ray Bursts (Albert et al., 2007e); moreover, on a more general basis, the small repositioning overheads favor the adoption of quite elastic observation schedules, where alerts on other interesting transient phenomena, like AGN flares, can be swiftly and efficiently followed. This puts MAGIC on the forefront for coordinated multi–wavelength campaigns on variable sources.
The information on the telescope pointing from the shaft encoders is not enough to determine the direction of the optical axis of the instrument, due to the bending of the structure. Therefore a calibration has to be performed. This is accomplished by means of a dedicated CCD camera, (the "T–Point" camera) located at the center of the telescope dish; bright stars are imaged, allowing for the calibration of the pointing. To produce an accurate bending model for the telescope, $\sim 150$ star have to be imaged, spanning the whole relevant range of azimuth and elevation angles. This is performed regularly, usually when the Moon is bright and no observation is possible. This calibration, together with the accuracy of shaft encoders, leads to a tracking accuracy of $0.01^\circ$. However this is correct until the bending is constant in time and there is no exceptional/irregular bending. The actual pointing is therefore constantly checked all along the data acquisition by means of another camera (the "Starguider" camera).

**Starguider**

To check the effectiveness of the tracking system MAGIC relies on a starguider system. This subsystem checks if there is any *mispointing*: an angular offset between the nominal coordinates that are tracked and the direction actually imaged on the center of the camera. A dedicated CCD Camera (Starguider Camera) is installed at the center of the dish. The camera has a wide FOV ($4.6^\circ \times 4.6^\circ$), and images the sky surrounding a part of the PMT camera. The position of the camera itself is determined by 6 LEDs installed on its edge. The starguider detects the stars in its FOV and tries to recognise the ones expected from catalogues around the telescope pointing. This allows to reconstruct which position is actually tracked, except for residuals of the order of $0.02^\circ$.

An interesting additional benefit of the starguider system is that, from the ratio of the number of recognised star to the number of visible stars expetcted in the FOV, an indicative evaluation of the simultaneous atmospheric conditions (cloud coverage in the FoV, haze) can be done both during datataking and when analyzing data offline.

### 5.1.2 The mirror

The wide (17 m $\varnothing$) aperture of the MAGIC–I mirror by itself led to the construction of a tessellated primary mirror. The whole surface amounts to

236 $m^2$, and is made of groups of four $49.5 \times 49.5$ $cm^2$ mirrors, mounted on a single frame in a $2 \times 2$ arrangement[4]. The mirror is thus built out of 956 0.25 $m^2$ elements. The tessellated surface follows a paraboloidal shape, with a very short focal ratio: being f the focal length, and D the aperture of the mirror, $f/D = 1$. The reason for the parabolic surface is is that it is an *isochronous* surface; that is, it preserves the phase of wavefronts. This follows naturally from the geometrical property of the parabola, which, given a line (the *directrix*) and an external point (the *focus*), is the locus of points equidistant from both; so light rays form a distant source travel the same path to the focus, no matter where they encounter the surface.

The importance of isochronism is twofold:

- The mirror is wide, and with a short focal ratio. Therefore, e.g. an easier to build spherical mirror would introduce a time "smearing" of signals of some ns, comparable to the expected time span of the Cherenkov flashes produced by the $\gamma$–ray induced EAS; this would set a lower limit on the time resolution, worsening the signal–to–noise (S/N) ratio with respect to the NSB;

- as will be shown in Section 6.5 a time resolution well below the Cherenkov flash duration is higly desirable, as relevant physical information can be gathered from the time development of the shower image; this possibility is anyhow tightly bound to the time coherence of the collected photons.

The individual mirror panels are made of 5 mm thick AlMgSi alloy plates, that are glued upon an aluminium honeycomb. The surface is diamomd milled to spherical surfaces (for the sake of simplicity) of increasing curvature radius (from the center to the edges) in order to approximate the desired paraboloidal profile. The average reflectivity of the mirrors is $\sim 85\%$, while individual panels range from 80% to 90%; consideration must also be taken that it can evolve with time, due to cleaniness of the surface and the aging.

Both these issues are rather relevant in MAGIC as it is an unshielded instrument so it's prone to the settling of layers of Saharan dust (*calima*, especially abundant in summer) and to its polishing action, favored by the strong winds blowing at El Roque. Along with the observations a quantity called Overall Light Collection Factor (OLCF, see Appendix C) is constantly monitored; it depends (not uniquely) from reflectivity of the surface that is thus kept under control as well.

The support panels originally matched each other side by side in the dish, but this led to mutual obstacle to the adjustment movements necessary for the Active Mirror Control (see 5.1.2), as the arrangement revealed too tight. Therefore in 2005 the mirror panels have been rearranged in a chessboard

[4]Actually the frames at the edge of the surface may carry only three mirrors each.

structure, where 50% of the panels are shifted backwards of $\sim 6$ cm to allow for unimpeded movement. This introduces a time delay of the light travel paths which is anyway within 0.5 ns, therefore negligible.

The parabolic shape has a drawback in the coma aberration, that elongates off-axis images ($\sim 7\%$); this effect is enhanced by the rather short focal ratio , that was nevertheless unavoidable to contain the dimensions and the weight of the PMT camera and of its support.

#### Active Mirror Control

Due to the varying effects of gravity at different position, the dish undergoes deformations that would distort the image on the focal plane. This is corrected by means of actuators, two for each 1 $m^2$ panel.

The control system is based on a set of red ($\lambda = 6350$ Å) laser pointers, installed in the center of each panel. Upon activation from the control software, eache laser is switched on projecting a spot on the cover of the PMT camera (kept closed in this operation). The cover is imaged by a dedicate camera (AMC camera), and the deviation of laser spots with respect to their nominal positions is determined, using as reference some LEDs installed on the camera cover. This ensures that the symmetry axis of the reflecting surface is correctly aimed to the center of the camera, and that each panel is correctly oriented. The adjustment can be even done with stars, as the AMC camera can detect the spots produced on the camera cover by individual mirrors, move them to the nominal position and store the absolute positions of the actuators for each elevation and azimut of observation. These values are stored in dedicated tables (Look Up Tables, or LUT) and recovered by the control software when adjustment is needed (even while tracking).

This adjustment allows MAGIC to work always with its best optical PSF, instead of suffering image degradation depending on the observed direction in the sky.

## 5.2 The camera

The camera of the MAGIC–I telescope is mounted at the primary focus of the reflector. It receives the light collected by the mirror, producing in each pixel (that happens to be a photomultiplier tube, or PMT ) an electric current, that is then converted to an optical flash and transmitted to the counting house by means of optical fibers. The camera has an hexagonal shape, and is made of two different kinds of PMTs.

The innermost part of the camera is made of 397 0.1° FOV tubes; the total FOV of this region amounts to $\sim 2°$. This inner camera is surrounded by four rings of bigger, 0.2° FOV tubes, for a total of 576 pixels. This solution was intended to reduce camera and electronics costs, but introduces no additional image degradation, as matches the off–axis increase of the PSF due

to optic aberrations. The bulb heads are hemispherical, therefore hexagonal Winston cones are installed on each PMT to enhance the "filling factor" of the camera[5]. In order to be sensitive to the UV portion of Cherenkov flashes as well, a wavelength shifter coating is deposited on the entrance window of each tube. The camera is protected from athmosferic events by a water–tight window made of UV transparent plexiglass. Moreover two opaque lids protect the PMTs from the potentially harmful light of the Sun and of the full Moon.

The PMTs are operated with negative high voltage, at a rather low gain, different for inner ($3\times10^4$) and outer ($2\times10^4$) pixels. This low gain is the key element of the peculiar capability of MAGIC of observing under moderate moonlight, without damaging the detector hardware.

In Figure 5.2 the quantum efficiency of the PMTs constituting the inner camera is plotted. The maximum QE is $\sim$ 30 % at $\sim$ 4000 Å . The diagram also shows the improvement in the sensitivity to the UV portion of the Cherenkov spectrum introduced by the wavelengh shifter coating.

The PMTs are fast photodetectors, that provide analog signals with small time duration ($\approx$ 1 ns FWHM). Also, the intrinsic noise is very low. Therefore, they are very suitable for the purpose of catching the weak, ns time-scale signal generated by EAS–induced Cherenkov flashes.

At the base of the PMT the signal is AC coupled, and enhanced by an ultra–fast preamplifier, with a gain of $\sim$ 6. The signals are converted back into light by means of vertical cavity surface emitting laser diodes (VCSELs). The analog optical signal is then sent to the counting house, through 162 m long optical fibers. This optical trasmission of signals is intended to minimize the dispersion of signal along the long path to the counting house; other advantages are the absence of electromagnetic pickup and the lack of signal attenuation. The electric to optical conversion is needed in order do decouple the photomultiplier camera from the readout system. This way, the camera is lighter; the lower momentum of inertia makes the fast repositioning viable.

After reaching the counting house, the analog signal is then converted back to electrical, by means of fast GaAs PIN diodes, in the receiver boards. Another amplification is performed, then the signal is split: one part is routed into the trigger system, the other into a Fast Analog to Digital Converter (FADC) that performs the digitization.

[5]The term filling factor is of more widespread use when dealing with CCDs, where it defines the ratio of the actual sensitive area of pixels to the area they occupy on the chip surface.

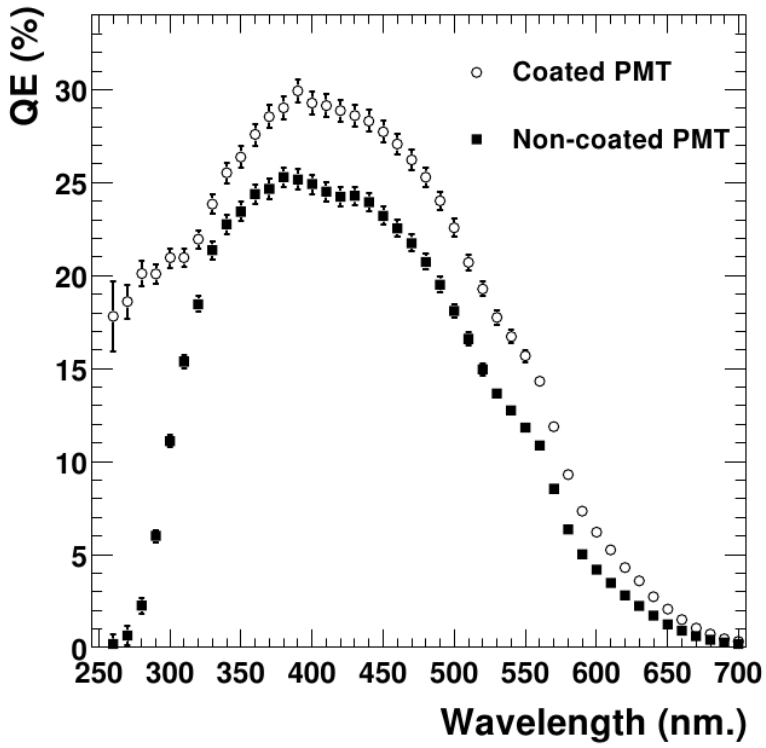


Figure 5.2: Plot of the quantum efficiency of the photomultiplier tubes in the MAGIC–I camera, as a function of wavelength (expressed in nm). The maximum efficiency is $\sim$ 30% in the blue; in the near–UV a remarkable improvement is introduced by the wavelength shifter coating.

## 5.3 The trigger system

The full, unfiltered data flow in a 576 channel camera with high time sampling would be overwhelmingly huge, and dominated by noise and undesired signals from the NSB. To give some numbers, above 200 GeV MAGIC–I detects $\sim$ 5 $\gamma$ rays every minute from a bright source such as Crab Nebula (see Appendix A); therefore only a small fraction of the observing time is actually of interest. Moreover, the DAQ saturation limit around 1 kHz cannot be surpassed. As the full acquisition of an event needs $\sim$ 30 ns, this means that the DAQ can be active for less than $10^{-4}$ of the elapsed time. To reduce significantly the data flow, without losing valuable information, a trigger system is needed, performing a real time filtering of the data, that are stored on disk only if trigger conditions are fullfilled. The trigger system of MAGIC–I is based on three levels (called L0, L1 and L2) of trigger, even if currently the L2 trigger is disabled.

### 5.3.1 Level 0

The first check is performed on individual pixels, and involves the discrimination of the signal level in the pixel. Only 325 pixels the inner part of the camera are involved in this operation; the FOV of the L0 trigger region is therefore $\sim 1^\circ$. Anyway, less than 10% of the $\gamma$–ray induced showers will be imaged outside of the trigger region; on the other hand, a lot of flashes that are very likely to have different origin (e.g. hadronic) would trigger a more extended trigger system[6]. The discriminator hardware receives the pixel signal, and produces a digital signal ($\sim 6$ ns long) if a certain threshold is reached. The *discriminator threshold* (DT) is set by software, and is chosen individually for each pixel, depending on the NSB level (that affects the whole camera) and pixel peculiar issues (e.g. a bright star in the FOV of the PMT). The optimal individual rate is $\approx 2 \times 10^5$ Hz. An automated routine called Individual Pixel Rate Control (IPRC) continuously adjusts the pixel thresholds, in order to keep the individual rates within a predefined working range. This way, for instance, DTs are raised in pixels shined by bright stars and lowered when pixel trigger rates are too low.

### 5.3.2 Level 1

After positive response from the Level 0 trigger, a more complex, topology check is performed, which is a next–neighbor coincidence test. This exploits the geometric compactness of shower images, something that random coincidence of signals from NSB is unlikely to reproduce. The signals from Level 0 pixels are grouped into 19 hexagonal cells, each containing 36 pixels. The cells overlap partially. Level 1 trigger criterion can be chosen amongst different options, differing for the number of next–neighbors (NN) that is requested for triggering the acquisition of the signal. The implemented schemes include 2NN, 3NN, 4NN and 5NN. The standard one during normal datataking is 4NN, that in dark night leads to a trigger rate of $\approx 300$ Hz at low zenith angles. Following the evolution of the IACT performance with zenith angle (see Section 4.5), also the Level 1 trigger rates show a dependency with zenih angle: the rate $R$ at zenith angle $\theta$ can be expected as:

$$R(\theta) \simeq R(0) \cdot \cos(\theta)^\alpha \quad \alpha \simeq 0.5$$

where $R(0)$ is the rate when the telescope points at the zenith.

[6]This reasoning holds for sources imaged on–axis; when sources are imaged off–axis a wider fraction of potential $\gamma$–ray induced showers from the source is lost at trigger level; this induced to project the MAGIC–II camera with a wider trigger area.

### 5.3.3 Level 2

The last trigger level implements by means of programmable logic some more complex, physical checks on the events accepted by the L1 trigger. As an example, Hillas ellipses with major axis pointing to the source position could be discriminated from the ones pointing in a perpendicular direction. This level is anyway disabled at present time, and definite plans for its usage in the future are missing either.

## 5.4 Digitalization and data storage

Before February 2007 the digitalization of signals was performed by means of 8–bit 300 Msamples/s FADC electronics, with dual gain to enhance the dynamic range. The sampling rate required that signal pulses from PMTs were stretched in time to $\sim 6 - 7$ ns to ensure a sufficient sampling of the signal.

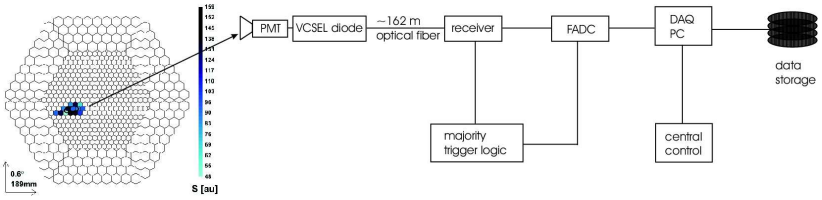


Figure 5.3: A schematic view of the MAGIC–I readout chain. The charge signals generated by the PMTs are back converted to optical by the VCSELs and then routed via 162 m long optical fibers. Signals are then splitted between trigger and receiver boards. Triggered signals are digitized and stored by the DAQ.

Fast FADCs are commercially available, but would be very expensive and power consuming for the readout of the whole MAGIC–I camera. To reduce the costs a 2 GSamples/s alternative system has been developed at MPI in Munich. This is based on a novel fiber–optic multiplexing technique, relying on the fact that the signal duration (few ns) and the trigger frequency ($< 1$ kHz) lead to a very low duty cycle for the digitizers. It consist of 10–bit 2 Gsamples/s FADCs, that digitize consecutively 16 channels one at the time. The delays of the analog input signals are obtained by means of different length of optical fibers. The total cost of this solution is 15% of a system based on one FADC per channel.

A distributed data acquisition system based on GBit Ethernet and Fiber-Channel technology allows the readout of 100 kB events with a continuous rate up to 1 kHz.

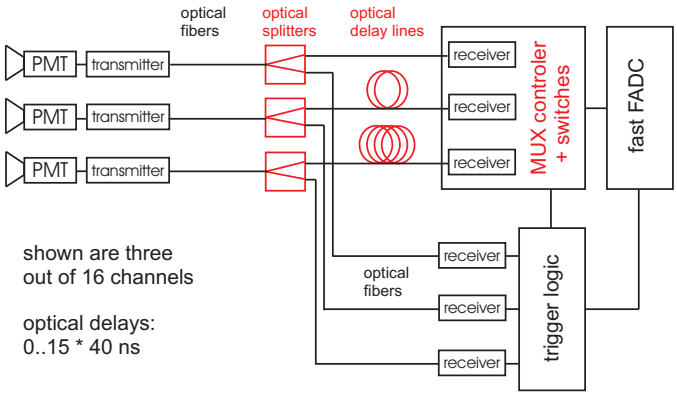


Figure 5.4: A sketch illustrating the multiplexing technique used in the MUX FADCs. Each fast FADCs reads serially 16 channels (only 3 are displayed), each one lagging the previous one by 40 ns. The delays are introduced by means of optical delay lines.

This fast sampling has a twofold positive impact on the performance of the telescope:

1. Cherenkov flashes are very narrow in time (2–3 ns). A small integration time reduces the contamination from background due to the NSB;

2. A detailed sampling of the time structure of the gamma ray signal allows a better image cleaning, and the measurement of time image parameters that can be used in the data analysis.

   In the end this translates into improved telescope sensitivity.

## 5.5 Telescope operation

In the following, I'll describe how the actual data–taking is performed, and some issues regarding the schedule and the practice of observations with MAGIC.

### 5.5.1 Shifts

The MAGIC telescope is a refined instrument, and a vast part of the tasks directly (data acquisition) or indirectly (telescope check–up and performance evaluation) involved in the astronomical observation are implemented into highly automated routines. Nevertheless, as is standard for such complex (and expensive) instruments, the variety of the problems that may be encountered along data–taking (hardware failures, sofware bugs, electrical

power–cuts, atmospheric adverse events) and that might potentially ruin not only the data quality, but the telescope itself, imposes that every operation is performed and supervised locally by a crew of telescope operators.

In the current operation routine, the crew is composed by four collaborators, that operate the telescope starting from 2 hours before astronomical sunset until $\sim$ 1 hour after sunrise. This is done every night, except for the 3–4 days surrounding the full moon, when no observation can be performed due to the high brightness of the night sky, potentially harmful for the PMT camera.

The crew is formed by a Shift Leader, a Deputy Shift Leader and two telescope operators and is responsible of the data–taking.
This includes preparing the telescope for the observation and guiding it according to the schedule, checking the performance of all the subsystem, and eventually reacting to the problems that may affect datataking or event harm the telescope hardware.

It must be remarked that due to the potential injury[7] that may derive from night–time intervention on the telescope, especially in certain areas, every action different from the standard data–taking must be performed **if and only if the safety rules are tightly fulfilled**.
Telescope access and hardware manipulation are restricted to acknowledged experts and under the supervision and responsibility of the Shift Leader, who comes to be the GLIMOS[8] in night time, while in daytime the role is taken by the Telescope Site Manager.

### 5.5.2 Schedule

The shift crew, compatibly with telescope performance and weather conditions, has to stick as much as possible to an observation schedule that is planned in advance, but that can be modified on short notice as reaction to Target of Opportunity (ToO) alerts, usually sent from different instruments (e.g. X–ray satellites or optical telescopes).

The schedule is prepared taking into account the decisions of the Time Allocation Committee (TAC), an internal board that evaluates the scientific proposals for observation and assigns the requested observing time to the most promising ones. This is done at the beginning of each observation Cycle, a period of 13 lunar months starting in June. This means that in every cycle $\approx$ 1100 h of dark time and $\sim$ 500 h of partial moon time can be disposed of. The accepted proposals then receive definite time slots according

[7] Unfortunately, we had a cruel demostration of how danger can materialize unexpectedly at any time in September 2008, when we suffered the sudden and tragic loss of our colleague Dr. Florian Goebel; loss that is unvaluable from the human side of view no less than from the scientific one.

[8] Group Leader In Matter of Safety

to the observability of sources, and, hopefully, the fulfillment of the requests from the observers (zenith angle range, light conditions, time constraints in MWL observations coordinated with other observatories, and so on). GRB and ToO proposals, dealing with unpredictable transient phenomena, receive a pool of hours but obviously no fixed time window. In the case of ToO, the observation is started if the conditions for triggering ToO observation included in the proposal are fullfilled and the Principal Investigator (PI) of the research explicitly asks for activation of the ToO observation. Being extremely reaction-time critical, observations of GRB alerts are always started, perhaps to be aborted as soon as robust arguments pushing against the observation arise.

In order to resolve conflicts amongst observations requested in different proposals that compete for the same time windows, a priority hierarchy of observation types has been established, as follows:

1. GRB
2. Fast ToO observations
3. Physics–driven fixed time observations
4. Multi–wavelength fixed time observationse
5. Slow ToO observations
6. Regular observations

### 5.5.3 Good observing conditions

To ensure hardware safety of the telescope the following conditions must be fulfilled:

- Elevation $< 88.5°$
- Humidity $< 90\%$
- Wind speed $< 35$ km/h
- Average current in PMT $< 7\,\mu$A
- Maximum current in individual PMT $< 20\,\mu$A

The conditions on PMT current become effective during moon time and twilight. Generally speaking, Moon phase must be that illuminated fraction is below 80% of full moon, and angular distance between tracked position and Moon disk must exceed[9] 30°. In practice, atmospheric conditions may

[9]Even observations with very high angular distance to the moon must be avoided, as camera might be directly shined by moonlight.

alter the diffusion of moonlight and PMT currents must be carefully checked. This allows for $\sim$ 300 h/year (ideally, 600 h/year) of extra data. The quality is lower than in proper dark observations, as the brighter optical background forces more selective L0 trigger thresholds, that lead to lower sensitivity and a higher energy threshold. Regarding Twilight observations, the astronomical sunset is defined as the moment when Sun elevation reaches $-18°$; the low gain of magic camera allows for 20 minutes of twilight observation each day, summing to roughly 100 h per year. The data quality resembles the one of moon data, with the additional difficulty that light conditions are rapidly changing.

In addition to the safety concerns, care must be taken that data is not affected by a low sky transparency: so during observation regular checks are made that no clouds, haze or dust interfere with the observation.

The dust is a threat rather often in Canary Islands, especially in summer, due to an atmospheric phenomenon called Saharan Air Layer (SAL) or, commonly *calima*: the transit, at typical altitudes of 4–5 km, of a layer of Saharan dust carried by the wind.

This can be done in various ways:

- the weather station integrates a bolometer, that measures a parameter *cloudiness* that describes atmospheric transparency;
- a low atmospheric quality affects the trigger rate: unusually low rates may depend on poor sky;
- the ratio of recognised stars to the expectation from catalogues in the starguider field of view may also depend on low atmospheric transparency;
- the atmospheric transparency is also measured every night by the Carlsberg Meridian Telescope, that is a few hundreds meters away from MAGIC.

Data taken with moderate cloudiness or calima extinction can still be analyzed, but with greater care and more uncertain systematics.

### 5.5.4 Standard datataking queue

The standard data acquisition involves three kinds of run: pedestal, calibration and data runs.

- Pedestal runs: these runs contain usually 1000 events, taken with random trigger and are used to calculate the pedestal offsets for the calibration runs.

- Calibration runs: these runs contain usually 4096 events, taken with the standard calibration light pulses from 10 UV LEDs and the calibration trigger. Thes runs are used to calculate the conversion factors from FADC counts to the number of photoelectrons, and the offset in the arrival time.

- Data runs: these runs contain usually $\sim 6 \times 10^4$ events, taken with the L1 trigger. This number of events corresponds to $\sim 1$ GB of disk space. Whenever this threshold is reached a new run is started automatically, with no dead time. Interleaved to the sky-generated events, calibration pulses identical to the ones fired during the calibration run are produced, with a rate $\approx 30$ Hz. These events allow for keeping track of the evolution of conversion factors ad arrival time offsets along the datataking.

The standard datataking on a source starts with acquisition of a pedestal-calibration couple; thereafter, data runs are taken until the tracking is stopped or one hour of data acquisition has passed. Exception to this order is made whenenever reacting to GRB alerts: in this case the importance of observing with the least possible delay with respect to the *burst onset time* $T_0$ suggests to postpone these ancillary runs to the end of the observation.

### 5.5.5 Tracking modes

The telescope can perform observations in two fundamental modes, that differ basically for the position of the source on the camera, and therefore for the way the background is estimated. The choice between the two is at will of the researchers that proposed the observations, so the schedule attains to the requests of the proposal.

#### On–Off mode

In this operation mode the VHE source (known or potential) is imaged on axis. This has the advantage that the trigger region is optimally shined by the EAS produced by high energy photons originated in the observed source. The drawback is that some additional measurement is needed in order to have an estimation of background. This comes from so–called Off data: observations of a region where no sources are expected, so that only background from hadronic showers and eventually from high energy leptons and background diffuse gamma rays is observed. Therefore Off data must be closely comparable to On data concerning:

- atmospheric conditions and L1 trigger rates;

- NSB brightness level of the imaged field;

- distribution in zenith angle;
- telescope configuration and performance.

Usually, when a proposal is made requiring On–Off mode, some observing time is dedicated to Off data; nevertheless, this diminishes the time dedicated to the source. Moreover, the optimal choice for reducing sistematic incoherences between background and source observation would be to observe alternatively both in the same nights; something that is acceptable when performing deep exposures on some source that is thought to emit a steady photon flux, but conflicts with the need for full time coverage of the source when performing more time critical observations, for instance observing known or suspect transient states. Potentially, background estimation could be done even exploiting archival data on different sources where no signal has been detected; this is actually a delicate issue, as MAGIC is still a rapidly evolving instrument, so that deep care must be taken that On and Off data are actually well matched. A benefit of the On–Off mode is that systematics introduced by camera inhomogeneities are better neutralized, as the same camera observes the background and the source, with the same inhomogeneity pattern.

**Wobble mode**

Another tracking mode originally proposed by Fomin et al. (1994) and adopted in many IACTs is the so called Wobble mode. It consists of imaging the source with some offset from the camera center. This asymmetry allows to observe simultaneously source and background in different regions of the camera. As the acceptance of different camera regions is obviously different, and this introduces systematics that are especially strong for low energy events, the offset in the tracking must be changed, e.g moving the source between two positions, W1 and W2, that are symmetrical w.r.t. the camera center. This swaps the roles of the background and on-source camera regions, averagin the discrepancies and therefore reducing systematics; this oscillation around the source position in the sky giver rise to the "Wobble" denomination. The standard solution adopted in MAGIC observations is an offset of $0.4^\circ$ and 20 minutes of observations on each position before changing the pointing. The offset amounts to a few times the telescope PSF, so grants a good separation of the background from the source, but at the same time is small enough than the source is still inside the trigger region, limiting the drop in trigger acceptance by $\sim 20\%$.
Except for the first observation cycles, and a late revival in the last months due to the possibility of performing On–Off observations with the newly designed sumtrigger (Aliu et al., 2008), enhancing the sensitivity below 100 GeV, Wobble mode is the most common observation mode of the MAGIC telescope. The main advantages are:

- background estimation relies on the same runs whence source events are obsserved: therefore ZA distribution, night sky brightness, atmospheric conditions, trigger rates and telescope behaviour are *intrinsically* the same;
- there is no need to waste observation time for background observation;
- time coverage of variable sources is optimal.

On the other hand, disadvantages of wobble mode are: the $\sim 20\%$ lower trigger acceptance; flux uncertainty in light curves due to change of source position on the camera; additional systematic in background determination if, for any reason, observations in W1 and W2 positions are unbalanced. For instance, in case of short exposures sometimes one wobble position is missing; therefore averaging on camera inhomogeneities cannot be invoked in such case.

# Chapter 6

# Analysis of MAGIC data

In this chapter, a description of the standard analysis chain of MAGIC data is given. The standard software is the MARS[1] package, a suite of tools specifically developed for the analysis of MAGIC data, written in C++ language and based on the ROOT framework.

## 6.1 Fundamental steps

The target of observations with the MAGIC telescope is to perform imaging and spectroscopy of VHE photon sources.
Therefore the key steps of the analysis process are:

1. Rejection of NSB. This step selects background–subtracted camera images of Cherenkov flashes, either produced by a nucleonic or $\gamma$-ray VHE primary.

2. Discrimination of the $\gamma$–like events from the hadron–like ones. This step allows discrimination of VHE photons against the intense hadronic background.

3. Estimation of the energy of the primary photon for each $\gamma$–like event. This step naturally leads to the VHE energy spectrum of detected sources.

4. Determination of the incoming direction of the $\gamma$–like events. This allows the production of VHE skymaps

## 6.2 Analysis chain

The analysis chain is composed of a few main steps:

[1] MAGIC Analysis and Reconstruction Software

- Calibration: the digitized information for each pixel must be translated into the number of photoelectrons generated in the PMT and into the information on the arrival time of signals. This step relies on dedicated ancillary data (pedestal and calibration runs) and on calibration events that are interleaved during the datataking.

- Image Cleaning: pixels containing noise (mainly, from NSB) are excluded from the images, and the surviving pixels are used for the calculation of the image parameters.

- Image reconstruction and Hillas parametrization (Hillas, 1985), performed by means of the `star` program.

- Calculation, by means of trained Random Forests (RF) , of optimal multi-dimensional matrices for $\gamma$/hadron separation and energy estimation. In the first case, the separation power of the matrices is optimized on the discrimination of a sample of simulated $\gamma$-like events (*train* sample) against a background sample. In the second, only simulated gamma events are needed.

- The trained matrices are applied to signal data and to background data. For each event, a probability of hadron origin (HADRONNESS) and an estimation of the energy of the primary are calculated. The same procedure is applied to a sample of simulated $\gamma$-ray events, independent from the one used in the previous step (*test* sample).

- Cuts are applied to signal and background, eventually evidencing some positive excess in the signal data in case of detection.

- The effective collection area of the telescope is calculated from the *test* sample of MC simulated events.

- The effective duration of the observation (*effective time*) is calculated from the data sample.

- The flux, spectrum and ligh tcurve of the source are determined, in bins of estimated energy.

- The energy spectrum is unfolded taking into account the energy resolution of MAGIC and other analysis effects. A physical spectrum, in bins of true gamma energy, is obtained.

## 6.3 Simulated $\gamma$-events

In various steps of the analysis chain Monte Carlo simulated $\gamma$-ray events are involved; namely, we need these events for:

- optimization of the gamma–hadron discrimination;
- optimization of the energy estimation for primary $\gamma$–ray events;
- calculation of the effective collection area of the telescope, mandatory for deriving the spectrum, the flux and the light curves;

and a few other ancillary tasks. This is unavoidable at present, as no artificial test beam of real VHE $\gamma$–ray EAS can be used to calibrate the response of the telescope to real $\gamma$–ray initiated showers.

Obviously a tight adherence of simulated events to real data is a key issue for the reliability of the whole analysis; this issue has been deeply investigated (Majumdar et al., 2005) and a good agreement in parameter distributions between MC simulated $\gamma$-ray events and the excess events from a real $\gamma$-ray source has been found.

Even if hadron showers also have been simulated for MAGIC, these are not used as a part of the standard analysis.

One reason is that, differently from MC $\gamma$ events, the agreement with real hadronic events is poor. The reason is commonly believed to be twofold:

- lack of sufficient statistics: this depend from the fact that hadron simulation is a computationally cumbersome task, due to the variety of reactions involved, that have to be modeled in the simulation;
- again due to the complexity of the reactions involved, probably present simulation codes hardly represent the real evolution of hadronic showers.

On the other hand, the need for simulated hadron events is by far less urgent, as there is plenty of real datasets that are actually rather pure hadron samples. Even from a rather bright source, like Crab Nebula, MAGIC detects $\sim$ 5 $\gamma$–ray events each minute, while hadron-induced events are at least 2 order of magnitude more frequent. Therefore, not only OFF data, but even samples taken on tentative sources that showed no signal, or even weak sources up to a flux level $\sim$ 10% of Crab Flux can be used as samples containing hadron events, for instance, for the training of $\gamma$/hadron separation matrices.

### 6.3.1 Air shower simulation

The developement of both $\gamma$-ray and hadron initiated EAS has been simulated with CORSIKA[2], (Heck et al., 1998), with some specialization for the MAGIC telescope. This software simulates air showers, including iteractions and decay processes of photons, electrons, muons and hadrons. For each particle, information on its position, direction, energy and arrival time

[2]COsmic Ray SImulation for KAscade

| Parameter | Standard $\gamma$-rays | High Energy $\gamma$-rays | protons |
|---|---|---|---|
| Energy range | 10 GeV - 30 TeV | 10 GeV - 30 TeV | 30 GeV - 30 TeV |
| Spectral slope | $-2.6$ | -1 | -2.75 |
| Impact parameter range | 0-300m | 0-300m | 0-400m |
| ZA range | $0^\circ - 45^\circ$ | $0^\circ - 45^\circ$ | $0^\circ - 30^\circ$ |
| Azimuth range | $0^\circ$ and $90^\circ$ | $0^\circ$ and $90^\circ$ | $0^\circ$ and $90^\circ$ |

Table 6.1: Synopsis of the parameters used for the production of the Monte Carlo samples.

is accounted. The tracking of each individual particle consider ionization losses, multiple scattering, decay processes and the geomagnetic effect. The hadronic interactions are simulated in two different ways, depending on the energy of the particles: the "GHEISHA" code below 80 GeV, the VENUS code above. The simulation of the electromagnetic interactions is made by means of the EGS4 code.

Additional routines, supplied by the HEGRA collaboration are used for simulation of the Cherenkov radiation. Some custom options implemented specifically for MAGIC are:

- information on the wavelength of the Cherenkov photons, that is important as the detector response is wavelength–dependent;
- information on the kind of the parent particle of Cherenkov photons.

In Table 6.1 the parameters used for generation of the showers are reported. It can be noted that two population of simulated $\gamma$-ray events are produced: "standard" and "High Energy" (HE) with different spectral slopes. This is useful to make available a sufficient number of hiigh energy $\gamma$-ray events, very important for a good estimation of the collection area of the telescope at high energies, at a reduced computational cost.

The attenuation of the Cherenkov photons in atmosphere is accounted in a later separate step in CORSIKA. The standard U.S. atmosphere is adopted, and Rayleigh scattering, Mie scattering and $O^3$ absorption are taken into account.

### 6.3.2 Reflector simulation

The rays of Cherenkov photons are traced throughout the atmosphere until they reach the camera. Their location on the camera and arrival times are obtained simulating the reflection on the real mirror dish structure. Each of the 956 mirrors is simulated, using its curvature radius and center position. The optical PSF of the telescope is taken into account by convolving the calculated arrival position with a 2–D Gaussian, with $\sigma$ determined from real observations, by means of the muon ring analysis (Appendix C).

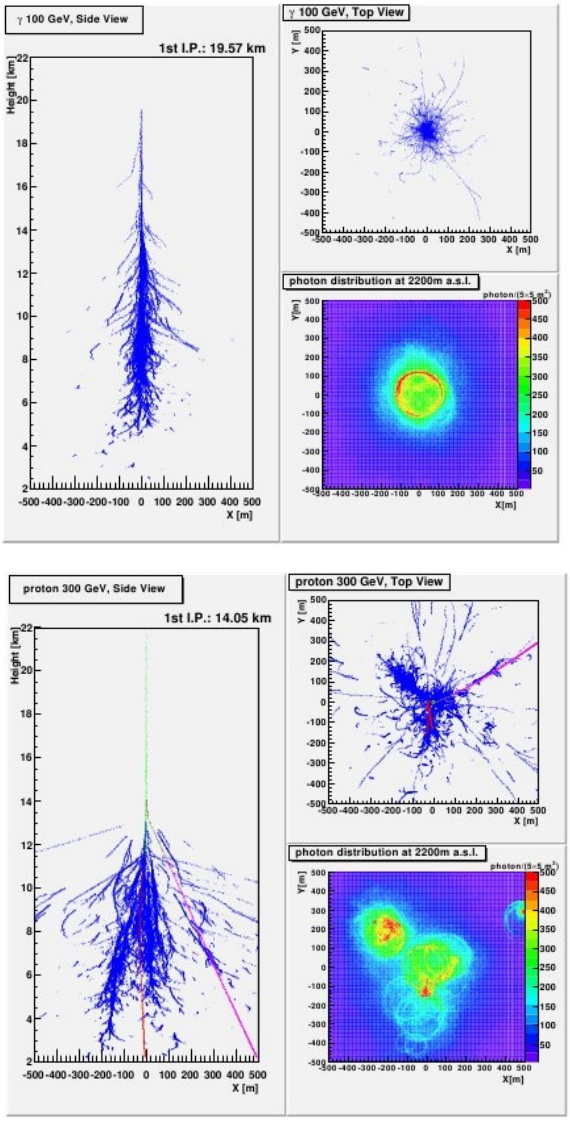


Figure 6.1: Results of the simulation of an electromagnetic ( 100 GeV photon, upper panel) and an hadronic (300 GeV proton, lower panel) shower. A projection on the vertical and on the horizontal planes of the shower is displayed in both cases, plus a two–dimensional map of the Cherenkov light distribution at ground level (bottom–right corner of each panel). The purely electromagnetic shower is more compact under all considered respects.

### 6.3.3 Camera simulation

At last, the behaviour o the MAGIC camera is simulated. The single features that are taken into account are:

- the camera geometry, and the pixelization of reflector images that it introduces;
- the addition of the light of the night sky, modeled as Poisson–distributed with mean value of $\mu = 0.13$ phe$^-$/pixel/ns;
- the efficiences for photon trasmission at the camera entrance: 92% transmittance of the cover plexiglass window, collection efficiency of the Winston cones (94% max and varying with the incident angle of the photons;
- the Quantum Efficiency of the photomultiplier: max. 30 % and depending from wavelength (see Figure 5.2);
- the electron collection efficiency at the first dynode of the PMTs: 90%;
- generation of the analog pulse;
- the trigger logic (see Section 5.3): both Level 0 (discriminators) and Level 1 (next–neighbor coincidence);
- electronic noise, that is generated in the trigger logic and in the FADCs is simulated with Gaussian shape, and parameters based on the measurements made on the readout circuit:
- finally the MUX digitization process is simulated.

The tuning of the simulation based on the PSF and the overall light collection efficiency of the telescope (see Appendix C), as measured by the analysis of the ring images of single muons with low impact parameters, has been implemented in the camera software as well.

## 6.4 Calibration

### 6.4.1 Signal extraction

The data acquired by the telescope are recorded on disks, in the form of one so called "raw" file. These files store, for each event that triggered Level 1 logic, the digitized charge in PMTs and arrival time; for each channel, and for each of the 60 time slices around the event. This means $\sim 1$ GB of data for every 200 secs of observation.

Now the signal due to Cherenkov flashes has to be separated from the noise coming from NSB; this is particularly crucial for weak signals.

A cubic spline is applied to find the maximum pulse within the useful time range of the FADCs ($\sim 30$ ns). The position of the maximum of the spline is taken as arrival time of the signal at that pixel. The total intensity of the signal is obtained by integrating the spline in a range of 7.5 ns. The

time resolution of each pixel has been estimated $\sim$ 0.4 ns RMS for a 40 phe$^-$ signal, through the study of the pixel time spread in calibration events. This value could be improved by a more sophisticated pulse reconstruction method.

### 6.4.2 Conversion to photo–electrons

The extracted signal amplitude is converted into the number of phe$^-$ in a pixel, by using a proportional relation. This conversion factor can be measured in various ways, relying on the special calibration runs. The *F–Factor* method (Gaug et al., 2005) is the one applied in the standard magic analysis performed here. The concept of the method is the following: the number of photoelectrons generated by calibration events has Poissonian distribution, with mean N and standard deviation $\sqrt{N}$. The number of FADC counts, after pedestal subtraction, has some mean $\bar{Q}$, and RMS $\sigma$, which is wider than $(\bar{Q})^{\frac{1}{2}}$, due to the multiplication process in PMTs (that can be measured in laboratory) and minor effects induced by the following processes in the acquisition chain, that are here neglected. This can be written as

$$\frac{\sigma}{\bar{Q}} = F\frac{1}{\sqrt{N}} \tag{6.1}$$

In MAGIC, an averaged $F$–factor of 1.15 is used for all PMTs.

The conversion factor $C = N/\bar{Q}$ can be calculated squaring 6.1 and rearranging the terms.

$$C = \frac{N}{\bar{Q}} = F^2\frac{\bar{Q}}{\sigma^2} \tag{6.2}$$

The calibration runs contain 4096 calibration events. This is enough to bound statistical errors in the calculation of $\bar{Q}$ and $\sigma$ within 2%. The conversion factors are then applied to data events, so that from $Q$, the number of FADC counts, the number of photoelectrons in each channel $N$ can be derived for each pixel of the image.

#### Bad pixels

A few pixels (usually $\sim$ 10) cannot be calibrated; this is due to hardware misfunction, be it the PMT itself, or some other component in the acquisition chain, like the optical fiber of the receiver board. These pixels are useless for the analysis, and are labeled as *bad*. To overcome partially the camera incompleteness that would derive from leaving holes in the image, a linear interpolation of the neighboring pixels is calculated and the result is taken as signal of the bad pixel. This is done only if there are at least three properly working pixels amongst the six surrounding the bad one.

## 6.5 Image Cleaning

The image cleaning is operated on the recorded events, to determine which pixels were shined from the shower image, as those are the only ones that have to be used for the determination of Hillas parameters.

Various different algorithms can be used to perform this task. Extensive studies have been carried on to establish the most suitable, for the MAGIC telescope and the various observing conditions. As a rule of thumb, compromise has to be found between the conflicting needs of a low energy threshold, that points to loose cleaning criteria, and of high robustness of the analysis and moderate pollution from noise–generated fake shower events. Two optimal "standard" procedures have been implemented: one involving only pixel charge, the other taking into account even time information. The second one has been proved more efficient, especially after the upgrade of the DAQ to the MUX, and is currently the one that is adopted routinely for production of the standard cleaned data available from PIC database.

### 6.5.1 Absolute Cleaning

The standard absolute cleaning, called $10-5$ identifies *core* pixels, that must contain $Q_{core} \geq 10$ phe$^-$; and neighboring *boundary* pixels, that must fulfill the $Q_{boundary} \geq 5$ phe$^-$ condition.

The algorithm initially selects the *core* pixels, as the ones containing more than 10 phe$^-$ *and* with another *core* pixel amongst its neighbors. Once one or more *islands* (separate groups) of core pixels have been identified, boundary pixels are searched for: these must pass the $Q_{boundary} \geq 5$ phe$^-$ and be neighbors of at least one *core* pixel. The standard algorithm does include only one boundary ring: pixel with more than 5 phe$^-$ that are neighbors of boundary pixels but not of core pixels are excluded from the image.

The choice of the minimum charge values for core and boundary pixels represents a compromise between lowering the analysis threshold and avoiding pollution from NSB that could ruin the reconstruction of the image parameters.

### 6.5.2 Time Cleaning

In the so called "time cleaning" a somehow analogous procedure is followed, where the thresholds for the charge in the pixels are loosened, so that images with higher pixel number are obtained. The additional constraints on the time structure of the events prevent contamination from NSB simulated signals. A first constrain regards core pixels, that must show arrival times within a time interval $\Delta t_1$ from the mean arrival time of all the core pixels. Moreover a pixel is considered boundary if: its charge passes the charge

threshold for boundary pixels, at least one neighbor is a core pixel *and* and the difference in arrival time between it and the core pixel is within $\pm\Delta t_2$. This allows to keep more information from boundary pixels, but still discriminating between real tails of the Cherenkov images and NSB fluctuations: as the time windows are quite narrow, the probability of including a time coincident fluctuation is small.

This procedure has been proved as more efficient, as allows a better statistics for low size events, without compromising the background rejection, and more accurate image reconstruction (as shown in 6.5.3. Therefore it's currently the standard cleaning performed routinely for the production of the cleaned data stored in PIC database. The standard setting has been optimized with the following setting: 6 phe$^-$ for core pixels, 3 phe$^-$ for boundary pixels, $\Delta t_1 = 4.5$ and $\Delta t_2 = 1.5$ ns. These values have been optimized with Monte Carlo studies (Tescaro et al., 2008).

Even different algorithms for image cleaning with time information have been used, for instance for the analysis of MAGIC observations of Crab Nebula (Albert et al., 2008a).

### 6.5.3 Moon time cleaning

MAGIC has the peculiar feature of allowing observations under moderate moonlight. In these conditions NSB is brighter and the noise level is enhanced. Some dedicated studies suggested that in these conditions, the compromise between low energy threshold and robust rejection of noise is optimally performed with a 10–5 cleaning *with* time constraints.

## 6.6 Image parameters

The software that performs image cleaning (`star`) not only selects the pixels belonging to the shower image, but even calculates from them a total of $\sim 25$ parameters that are the information used in the subsequent parts of the analysis chain[3] The parameters are an extension of the classical image parameters originally proposed by Hillas (1985).

### 6.6.1 Source independent parameters

Hereafter I report a list of the most relevant parameters for the $\gamma$/hadron separation and for the energy estimation of the primary VHE photons. A fundamental feature of the parameters is whether they depend or not from the knowledge of the source position in the sky, so for better clarity I list first the "source independent" parameters:

[3]This step reduces of a factor $\sim 20$ the space needed for data storage: from the $\sim 100$ MB of a standard calibrated run to the $\sim 5$ MB of the corresponding cleaned run.

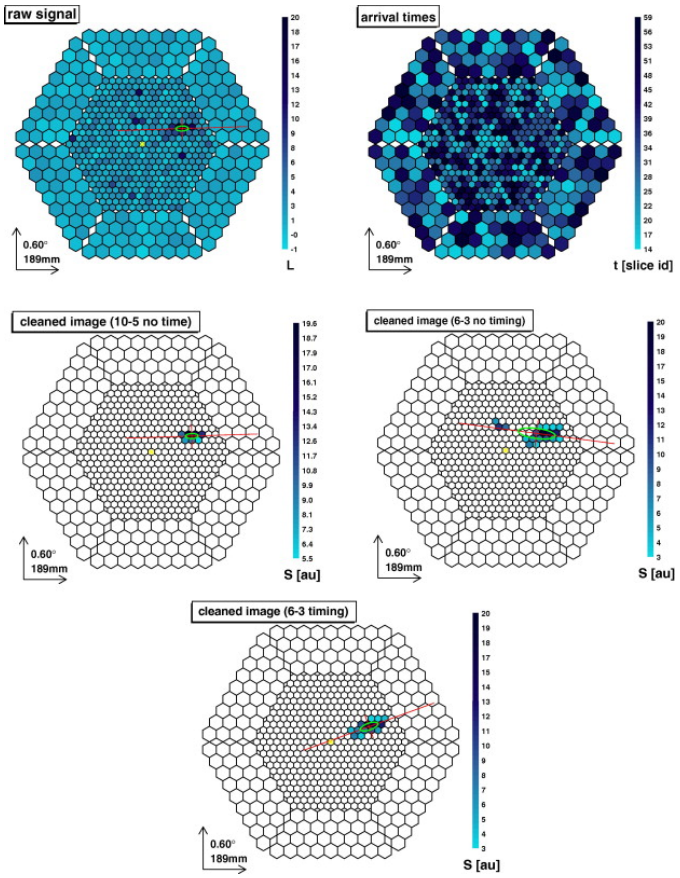


Figure 6.2: Example of comparison of various cleaning levels on the same event. The two upper panels report the data available after calibration: pixels charge (upper left panel) and arrival time (upper right) distributions. Below, the standard 10–5 absolute cleaning (middle–left), a looser 6–3 absolute cleaning (middle-right) and standard 6–3 *time* cleaning (bottom panel) are applied. With respect to standard 10–5 cleaning, the lowered threshold of the absolute 6–3 include more pixels in the image, but some can be due to strong NSB fluctuations. Consideration of the arrival time distribution reduces this contamination, and the major axis of the charge distribution is better reconstructed.

- SIZE: The total charge contained in the cleaned image. This parameter is roughly proportional to the energy of the primary $\gamma$–ray, behold that the impact parameter of its path is $< 120$ m;
- LENGTH: the RMS of the charge distribution along its major axis. This is an efficient parameter for $\gamma$/hadron separation, as at fixed SIZE $\gamma$–ray induced showers are spatially more compact (i.e. their LENGTH

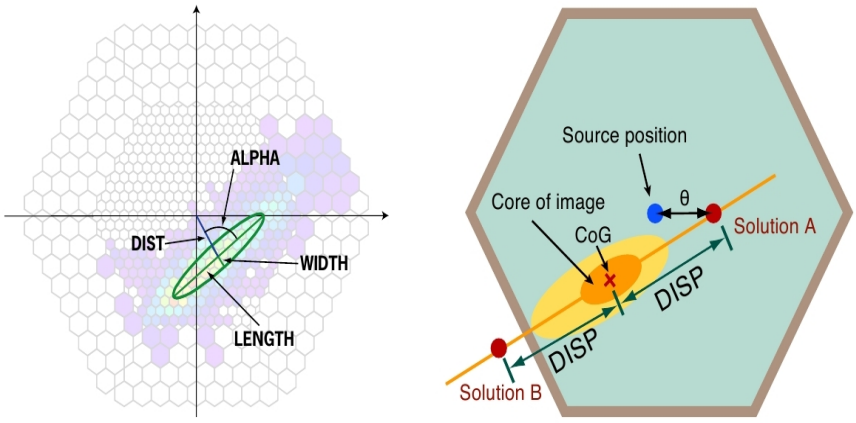


Figure 6.3: Graphical representation of some image parameters, including the original ones proposed in Hillas (1985).

is lower) than hadronic ones;

- WIDTH: the RMS of the charge distribution along the minor axis of the image. This also is a powerful parameter for separation, as the transverse momentum of purely electromagnetic EAS is lower than in hadronic cascades, leading to lower WIDTH at fixed SIZE;
- CENTER OF GRAVITY, or COG: the baricentre of the charge distribution of the image;
- CONC(N): a set of parameter that describe the concentration of the image. CONC(N) is defined as the ratio between the light contained in the N pixels with strongest signal, to the SIZE of the image. Showers initiated by $\gamma$ rays tend to be more concentrated than hadronic ones, therefore CONC(N) also contributes good rejection power.
- M3LONG: the 3rd moment of the light distribution along the major axis, that measures the asymmetry if the signal distribution along it. As the head of the shower is expected to be more concentrated than the tail, this parameter helps to detect the part of the image closer to the incident particle direction. This is of great utility in order to discriminate between the two solutions for the incoming direction of primary $\gamma$ rays that are found with the DISP method. Unfortunately, for low SIZE this parameter is poorly defined and of little utility.
- LEAKAGE: the fraction of light contained in the image pixels in the outermost ring of the camera. When this parameter exceeds $10--20\%$ there is a high probability that a relevant part of the image is missing. This means that the images are probably truncated, something

quite likely for events above 2 TeV. This leads to unreliable energy estimation and this parameter is used to reject these events from the analysis.

### 6.6.2 Source dependent parameters

Hereafter a few other parameters, that instead depend on the known (or postulated) position of the source.

- DIST: the distance between the CoG of the image and the expected source position in the camera. It's correlated to the impact parameter of the EAS and therefore useful to improve the energy estimation. It's also worth noticing that this is a parameter that is usually well determined in low SIZE images too, while others become more and more uncertain.

- ALPHA: the angle between the major axis of the image and the line connecting the CoG with the source position in the camera. As the symmetry axis of the image is the projection of the axis of the EAS, and this in turn points to the source position in the sky, the major axis of the Hillas ellipse should point to the source position in the camera plane. Hence, in the case of events originated from $\gamma$ rays arriving from the source, the ALPHA parameter of $\gamma$ events is expected to be preferentially small. Instead, showers of hadronic origin or initiated by leptons or diffuse background $\gamma$ rays produce an isotropical background, incoming from every direction in the sky, without any preferred orientation. Therefore their ALPHA distribution is rather flat, except for distortion introduced by the geometry of the trigger region. This makes ALPHA one of the most powerful parameters for background rejection.

- $\theta^2$: $\theta$ is the angular distance between the real source position and the reconstructed incoming direction of the event. The reconstructed direction is obtained with the DISP method. The direction distribution for gamma rays should peak next to the source position, while should be homogeneous for background events. For graphical convenience, $\theta^2$ instead of $\theta$ is calculated, as an homogeneous distribution on the sky leads to a constant distribution in $\theta^2$ but to a linearly increasing distribution in $\theta$. This is due to the fact that equally spaced, $\Delta\theta$ thick bins in $\theta$, cover on the camera plane an area $2\pi\theta\Delta\theta$. The distribution for a $\gamma$-ray signal instead peaks at $\theta^2 = 0$ deg$^2$.

- DISP: it is defined as the distance between the center of gravity of the shower image and the source position on the camera plane.

### The Disp method

The reconstruction of the origin of a $\gamma$–ray event with a single telescope is possible with the DISP method (Fomin et al., 1994; Lessard et al., 2001).

In the DISP method the source position is assumed to lie along the direction of the major image axis. This is reasonable, as the major axis is the projection on the camera plane of the shower axis. The DISP is parametrized as a function of all the previously cited parameters, except for CONC and DIST. A standard parameterization for DISP is:

$$\mathrm{DISP} = a\,(\mathrm{SIZE}) + b\,(\mathrm{SIZE}) \cdot \frac{\mathrm{WIDTH}}{\mathrm{LENGTH}} \tag{6.3}$$

where $a$ and $b$ are second-order polynomials found by fitting MC simulated $\gamma$–ray showers (Domingo-Santamaria et al., 2005).

The reconstructed event origins have then to be corrected for possible mispointing by using the information available from the starguider camera.

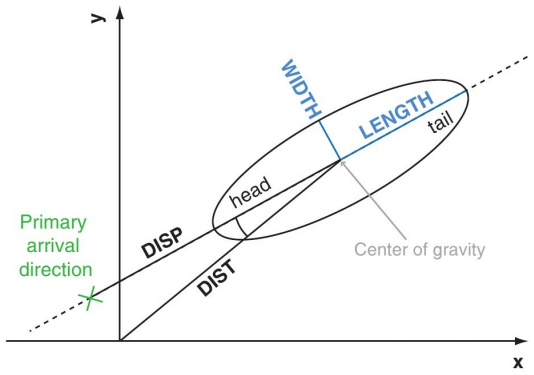


Figure 6.4: Illustration of the DISP parameter used for the reconstruction of the arrival direction. It is defined as the distance between the center of gravity of the shower image and the estimated source position.

The DISP method suffers of an important degeneracy, as for each event two candidate arrival directions are determined (called *ghosts*). The M3LONG parameter can be used to judge which one is the correct one, placing the source closer to the head of the image. Also the time structure information can be used to resolve the degeneracy, as the head of the image should be imaged *after* the tail.

### 6.6.3 Time parameters

Some powerful parameters related to the time structure of Cherenkov flashes can efficiently improve the rejection of background. The most important two, and the ones that are used in standard *time* analysis are:

- RMS TIME: the root mean square of the arrival times of all pixels belonging to the image after cleaning. This measures the dispersion in arrival times of all the pixels, irrespective of their geometrical position. It has been suggested as a possible background discriminator in (Mirzoyan et al., 2006).

- P1GRADIENT: measures the time evolution of the arrival times of signal along the major axis of the image. Pixel coordinates are projected along the major axis, so that the description is reduced to only one dimension. It can be used to resolve the degeneracy arising from the DISP method (see Section 6.6.2.

### 6.6.4 Filter cuts

The most immediate use of the image parameters calculated in this step is the application of the so called *filter cuts*, that are basically quality cuts that expunge from the analysis images that are unlikely to be generated by air showers. The fundamental ones are:

- *Spark* events: spark events are believed to be images originating from a discharge in the PMT surface. The light reflected from the plexiglass camera cover can trigger the DAQ, if a group of pixels is involved. The images have high SIZE in just a few (completely saturated) pixels; a cut in the plane Log(SIZE)–Log(CONC) can easily remove them. The rate of spark events is $\sim 1 - 2$ Hz, with uniform distribution on the camera. A standard parametrization is

$$1.5 - 4 \cdot \log(\text{CONC}) < \log(\text{SIZE})$$

- LEAKAGE cut: it excludes those images (mostly produced by high energy primary photons) having a significant signal on the rim of the camera, thus leading to misreconstructed image parameters, in particular to wrong energy estimation.

- $N_{core}$ cut: a cut on the minimum number of core pixels, usually set to 4. This cut allows to remove those images made of few pixels, and hence poorly reconstructed, especially as far as geometrical parameters, such as ALPHA, are concerned.

- $N_{island}$: this cut removes the images reconstructed using pixels separated in more than $n$ disjunct groups.

## 6.7 $\gamma$/hadron separation

The previous steps lead to selection of images likely to be due to Cherenckov flashes produced in the superluminal motion of the cascade products of a

high energy primary particle entering the earth's atmosphere. At this point, however, the signal is still contaminated by unwanted noise, as the cosmic rays are by far dominated by the undesired hadronic component. As an example, a fairly strong $\gamma$-ray emitter like the Crab Nebula, is dominated by background events in the ratio $\approx 1:1000$. For the detection of signal is therefore necessary an effective suppression of hadron images, without losing a remarkable amount of $\gamma$–ray events. This rather crucial task is called $\gamma$/hadron separation, and is performed by calculating for each image, an additional parameter, called HADRONNESS, that represents the probability that the image derives from an hadron.-initiated EAS. Like a probability, HADRONNESS ranges in the $[0, 1]$ interval. A value $\sim 1$ means that the image has a high probability of deriving from a hadronic primary; on the contrary, low HADRONNESS points to an electromagnetic cascade, therefore high probability of a $\gamma$–ray primary. The background suppression is thereafter obtained tuning a HADRONNESS cut, that rejects all the events with Hadronness above the selected threshold.

### 6.7.1 Classification methods

The calculation of HADRONNESS for each event is done by means of a multidimensional classification technique, the Random Forest method, originally developed by Breiman (Breiman, 2001). This algorithm was preferred amongst different other approaches, such as evolutions of the method proposed by Hillas (1985), involving cuts on the image parameters, with cut values depending on the zenith angle of observation. Anyway, these have been also tested as tools for the analysis of MAGIC data (see Albert et al., 2008b, and references therein).

### 6.7.2 Random Forest method

The Random Forest consists of a forest of *decisional trees*. A decisional tree is a cascade of tests in the multidimensional space of the discriminating parameters used for the classification. The object of the test are the elements to be classified, that can be identified with the $n$–dimensional vector of their values for the $n$ considered parameters. Each test is performed by applying a simple cut on one of the parameters. Each time a test is performed, the tree is branched, or equivalently, a partition in the parameter space is determined. To this partition of the parameters corresponds a partition of the element population: initially all the elements occupy the root node; at each node, they are separated according to the test result, sliding along the branches of the tree (see Figure 6.6) into one of the two *successor nodes*. The branching process ends when the nodes are occupied by a number of events lower than a predefined threshold, or when all the elements that occupy the node belong to the same class. In the original algorithm of Breiman (2001)

these final nodes flag the elements as belonging to one of the two classes, according to the majority of the elements in the node. In the MAGIC implementation, an average value is calculated, so that if the node contains $N_a$ and $N_b$ elements of the $a$ and $b$ class, and a vote $l_a = 0$ and $l_b = 1$ correspond to each of the two classes, the vote in the node is

$$v = \frac{N_b}{N_a + N_b} \tag{6.4}$$

If a forest counting $M$ trees is applied to the data, each element will receive $M$ votes, and the final vote will be an average over the forest:

$$v = \sum_{1}^{M} \frac{v_i}{M} \tag{6.5}$$

In order to measure the classification power (separation ability) of an image parameter, the *Gini index* is used, as frequently in classification methods. The Gini index for each node is a function of the population of $a$ and $b$ events in the node and of the total population, and is 0 for nodes containing pure populations. For each split, the Gini index is a normalized function of the two successor nodes. Minimization of the Gini index sets the best parameters and also the best cut value of the parameter. Therefore, optimization of the set of cuts in the parameter space can be done on a sample of elements whose classification is a priori known. After the RF optimization, a partition of the parameter hyperspace is available. To each hypercube corresponds a vote ranging from 0 (belong to the $a$ class) to 1 (belong to the $b$ class), that classifies all the data whose parameter vector lies in the hypercube.

### Random forest method for the Hadronness

A simple implementation of the principles exposed in the previous Section, allows to split MAGIC events in the "gammas" and "hadrons" classes, based on the parameters calculated on the cleaned shower images. The result of the discrimination on test samples of simulated $\gamma$ ray events and real hadron events is shown in Figure 6.5

### Random forest method for the energy estimation

Even if created for discrete classification, the method can be extended to the estimaton of a continuous quantity (see Albert et al., 2008b). The estimation of energy of primary $\gamma$ rays in MAGIC is also performed by means of the Random Forest method.

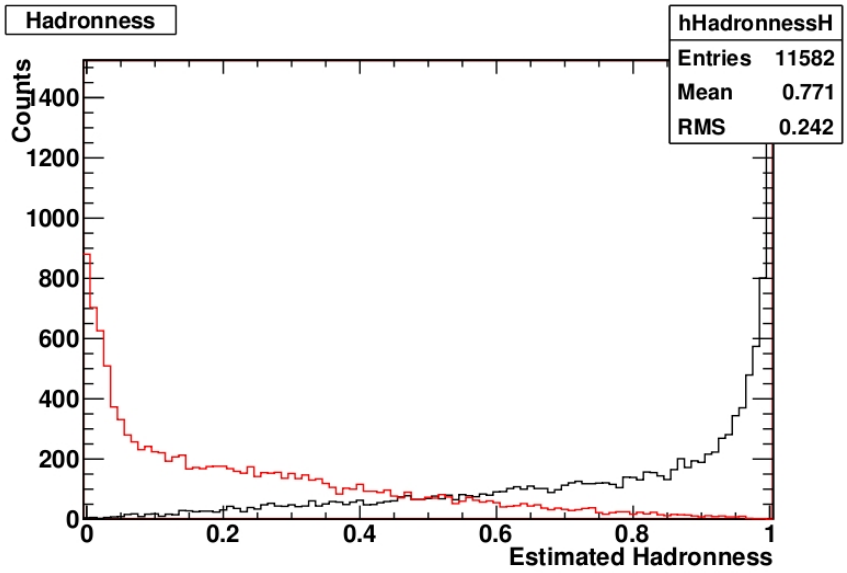


Figure 6.5: Histograms of HADRONNESS, measured by means of the RF method, for two test samples of Monte Carlo simulated $\gamma$–ray events (red line) and real data (black line), arguably hadronic events to a high degree of purity. A cut in HADRONNESS allows to reject most of the background (concentrated around HADRONNESS $\simeq 1$), keeping the vast majority of $\gamma$ rays (concentrated around HADRONNESS $\simeq 0$).

### Choice of the training samples

As all the supervised classification methods, Random forest relies on training samples, where the correct classification is correctly known *a priori*, to select the set of classification trees that grants optimal separation of data. Due to the lack of pure sets of real $\gamma$-ray images, a set of MC simulated images is used as training sample. The requests here are that:

- The MC have been generated for the actual telescope configuration at the time of observations
- The simulated events have been generated assuming the correct optical PSF of the observation.
- The MC events are simulated with the same observation mode (wobble or onoff) of the data to be analyzed
- The MC events have been calibrated and cleaned homogeneously to the data to be analyzed

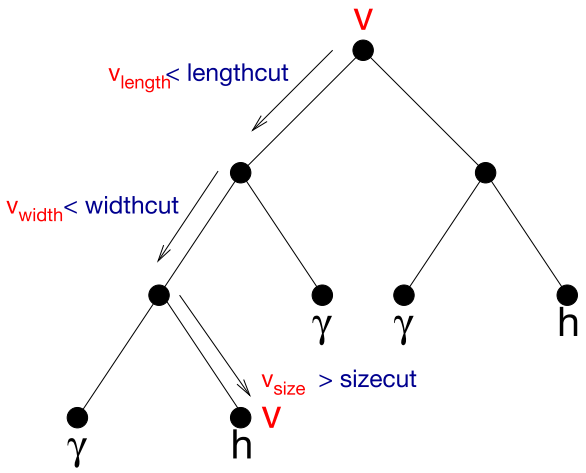


Figure 6.6: Sketch illustrating how the decision tree selects data based on the discriminant parameter used. Data are subject to checks on the value of the parameters, namely: LENGTH, WIDTH, SIZE. Each check splits the dataset. At the end of the branching, data are labeled as $\gamma$–like or hadron–like.

Finally, the analyzer can dispose whether enrich the high energy part of the energy spectrum of MC simulated events; this increases the statistical robustness of the classification in the high energy region, but at the cost of needing a rather big hadron sample, (the reason is explained below).

The hadron sample for the training is instead selected from real datasets, provided that:

1. The observing conditions are similar to the ones of the dataset that has to be analyzed: ZA range, weather conditions, trigger rates, telescope performance[4]

2. Contamination from real $\gamma$-ray events is small.

The second condition is quite easily fulfilled, as even for a strong emitter like CrabNebula, $\gamma$-ray fraction is of the order $10^{-3}$. Therefore, not only background data, but even data from weak sources (F $\lesssim$ 10% of the Crab) can be safely used. Thus when performing blind searches, or observing potential sources that are believed to be weak, or known but weak sources, the dataset itself can be safely integrated in the hadron sample; for this part of the sample the first condition is therefore intrinsically matched. Obviously, this must be reconsidered if the source reveals instead a strong (may be inexpected) signal, and the analysis must be redone with another hadron

[4]The rapid technical evolution of MAGIC usually constrains the time span where compatible archival data can be looked for

sample of comproved purity.

As a rule of thumb, for analysis of data taken in On–Off telescope mode, the dedicated Off data is always a good hadron sample, and even On data in case of weak sources. For analysis of data taken in Wobble mode, the data itself can be used as hadron sample for the training, if the source is weak. Otherwise, samples fullfilling both conditions from independent data set must be selected.

Another consideration must be done regarding short datasets. Before training the RF, a subsample of the hadron data is extracted from the initial sample, in order to adequate the size and Zenith angle distributions of the hadrons to those of the simulated $\gamma$-ray events. This is because, even if Size and ZA cannot be used as classification parameters (no total charge and no incoming direction can be thought as more gamma-like than hadron-like, or vice versa) these quantities parametrize other discriminating values; therefore, if hadrons and MC events had significantly different size and Zenith angle distributions this would bias the classification. This forces to expunge hadron data to match the distributions of simulated photons, and therefore the initial pool of hadrons must be relatively big; this is even more true if High Energy MC events are used: the size distribution of simulated $\gamma$-ray events becomes quite hard, while the size distribution for hadrons is steeper, reflecting the known energy spectrum of cosmic rays. This means that many more hadron events of low size must be rejected to match the distributions. As a consequence, selection of samples amongst archival independent datasetes is actually unavoidable in case of short datasets.

It must be noted that for this step data taken in On–Off mode can be used as hadron sample for the analysis of Wobble data, and vice versa, thus enhancing the possibility that proper hadron sample is available. The only mandatory additional task is that if source dependent parameters are needed, these have to be recalculated for the new source position on the camera, otherwise their distributions won't match the ones of the hadronic background.

This rather good availability of real hadron samples, and on the other side the poor adherence of simulated hadron showers to real ones, in spite of their computational complexity, point for sure towards the use of real hadron data as training sample for the $\gamma$/hadron separation.

### 6.7.3 Resizing and Rezenithing of the hadron sample

It's rather easy to realize that the Size and ZA parameters are not discriminant, as it can be argued that no direction in the sky and no total charge

measured in PMTs can be intrinsically more hadron–like or $\gamma$–like.

Nevertheless, many of the other image parameters, such as DIST for instance, have a functional dependency from these two. It is therefore useful to add these parameters to the others, but ensuring that they will not influence directly the classification. To obtain this, is necessary that the hadron and the MC samples are similarly distributed in each parameter. As, generally speaking, simulated events are always scarce and computationally expensive, the most convenient way is to discard a part of the hadron events. A selection of events is then made within the hadron sample, reshaping its SIZE distribution in order to match the one of the MC sample.

This operation is called RESIZING when performed on the SIZE distribution, and REZENITHING when performed on the ZA distribution.

After this the optimization of the classification matrices can be performed safely: the classification will have the proper dependency on the two parameters, but they will not influence directly the discrimination.

The REZENITHING has an intrinsic risk: if there is a hole in the hadron distribution, classification for that range of ZA will be biased towards photons. So, care must be taken that the hadron sample spans the whole range of the MC sample.As the data are rebinned in this procedure, in large bins of ZA 5° wide, this can be fulfilled quite easily, if the choice of the hadrons is careful.

### 6.7.4 Choice of parameters relevant for the classification

The set of input image parameters for the RF depends on whether the source dependent or independent approach is used to extract the signal.

#### Source dependent approach

In the source dependent approach, the source position is assumed known, and this additional information is exploited for the separation. Source dependent parameters are therefore given as input for the Random Forest method.

A typical choice of discriminating parameters contains WIDTH, LENGTH, DIST, CONC2, M3LONG, SIZE.

#### Source independent approach

In this approach, only source independent parameters are used for optimization of the classification method. Therefore, no bias is introduced by assuming an *a priori* source position. This approach is particularly well suited for a "blind" search in a region of te sky where no source is known, and, in case of known sources, it allows unbiased detection of the incident

arrival detection of the photons[5]. This approach is therefore the one needed for production of the VHE skymap.

In this case, the typical set of parameters is WIDTH, LENGTH,DIST, CONC2, M3LONG, SIZE.

### 6.7.5 Classification test

The multidimensional matrices that are produced by the optimization process are applied on an independent sample of MC simulated $\gamma$-ray events, to test the classification performance. It can be seen that the distribution are well separated above a certain size, while there is increasing overlap between hadron- and photon-induced EAS Cherenkov images.Even in the region where the Hadronness parameter is no more a faultless separator, good separation power can be expected from the orientation of the images, (i.e. the Alpha or $\theta^2$ parameters), that has not been taken into account yet. At even lower Size values, the images become rather small and contribution from residual unsubtracted noise progressively greater, compromising both the measurement of both Alpha and the M3long parameters, and the separation power related to image geometry is therefore definitively lost.

The $\gamma$/hadron separation is then done by selecting an hadron cut to be applyed to the events; as a general rule, care must be taken that the overall cut efficiency for MC $\gamma$-rays remains better than 50%; hadron suppression on the 99% level can be obtained. The accurate evaluation of the separation efficiency is anyway done at the level of the following step, the signal extraction.

## 6.8 Signal identification

After the background suppression, a signal can be searched in the surviving pool of events. The extraction can be performed in two ways: the so called ALPHA analysis and the so called $\theta^2$ analysis. Ideally, there are many common points between the two. First of all, a SIZE cut and an HADRONNESS cut are chosen, and applied. The choice is usually optimized on simulated $\gamma$–ray showers, requesting that a given fraction is not discarded.

Otherwise the cuts can be optimized as those that maximize the signal significance (or sensitivity) in the analysis some bright VHE source, like the Crab Nebula.

Then, a signal region is established, for instance, in the (ALPHA or $\theta^2$) distribution of the events. Events within the signal region are counted for both the on–source ($N_{on}$) and background ($N_{off}$) sample. The number $N_{excess}$ of excess events contained in the signal region is simply the difference

[5]Thus, for instance, telescope mispointing, or source intrinsic extension above the telescope PSF can be independently checked for.

$$N_{excess} = N_{on} - N_{off} \tag{6.6}$$

### Alpha analysis

In the case of Alpha– analysis, the signal region is determined by means of a cut in the Alpha parameter.

In the case of On–Off data, two different samples of events are available: one from the On observations, the other from the Off data. For each event the Alpha parameter has been calculated assuming the source at the camera center. From each sample, an histogram of Alpha is built, and then the events within the signal region are counted.

In the case of Wobble observation, only on source data are available, with two different source positions. For each event surviving the cuts, two values of Alpha are available, one with respect to the source ($\alpha_{\mathrm{ON}}$), and one with respect to the anti–source position ($\alpha_{\mathrm{OFF}}$) as shown in Figure 6.7. So each event is computed both in the On and in the Off histogram. As the two event are not completely uncorrelated as should be in this case, events in signal region in one of the two histograms are not computed into the other (so that the cut is completely symmetric between source and anti–source).

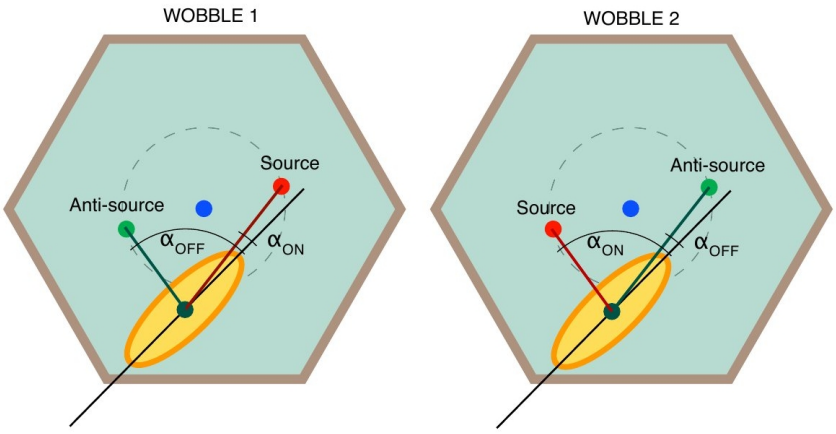


Figure 6.7: A graphical representation of the Alpha approach for signal extraction. From Mazin (2007)

In case that more Off positions are considered, the extension of the procedure is straightforward. For instance, in the case that 3 Off positions are used, for each event, 4 values of Alpha one with respect to each position are evaluated, with the same prescription to grant statistical independence of the samples. Then the 3 Off histograms are added and normalized. This allows to reduce of a factor $1/\sqrt{3}$ the fluctuations of background. As the

symmetrization of the wobbling does not fully cover all the positions, but only the source and its anti–source, this procedure can introduce systematic biases in case of consistent camera inhomogeneity, so that it's deprecated for analyses that extend to very low Size values, where camera inhomogeneity is rather severe (see Appendix B).

**$\theta^2$ analysis**

In this case the signal extraction is based on $\theta^2$ plots, where the signal region is defined by means of a threshold in the $\theta^2$ parameter, calculated with the DISP method. The $\theta^2$, being the distance between the reconstructed incoming direction of the primary $\gamma$ ray and the nominal source position, can be seen as a much more intuitive approach, based on the concept of "angular distance" on the sky.

The construction of the histograms is analogous to the case of ALPHA. The twofold degeneracy of the DISP method is solved by means of the information on the head–tail asymmetry carried by the M3LONG parameter (see Section 6.6.2).

### 6.8.1 Significance of the excess

The extraction of signal leads to two independent set of survived events, whether the signal extraction was performed with ALPHA or $\theta^2$ analysis:

- $N_{on}$ events in the signal region, from the on source observations;
- $N_{off}$ events within the signal region, from the background observations.

The determination of the statistical significance of an excess comes from the calculation of the probability that the positive excess, otherwise advisable as real photon contribution from the source, can be instead a simple fluctuation in the background measurement, and no source is present.

Some simple arguments can lead to a first simple formula. Assuming that $N_{on}$ and $N_{off}$ are measures of independent and Poisson distributed variables, and that no source is present,

- $N_{on}$ comes from a Poisson distribution with mean and variance $\langle N_B \rangle$
- $N_{off}$ comes from a Poisson distribution with mean and variance $\frac{\langle N_B \rangle}{\alpha}$, where$\alpha \equiv t_{on}/t_{off}$ takes into account the possibility of different effective time between on-source and background observation.

This leads to a significance $S$ of the excess $N_S$

$$S = \frac{N_S}{\sigma(S)} = \frac{N_{on} - \alpha N_{off}}{\sqrt{\alpha(N_{on} + N_{off})}} \tag{6.7}$$

The probability $P$ that a fluctuation in the measurement of a dark patch of the sky gives an excess count $N_S$ (significant at the $S\sigma$ level) or greater is

$$P(N \geq N_S) = \frac{1}{\sqrt{2\pi}} \int_S^\infty e^{-x^2} dx \tag{6.8}$$

Therefore the confidence level $CL$ of the detection is

$$CL = 1 - P \tag{6.9}$$

The expression 6.7 holds well if $N_{on} \sim 10$, $N_{on} \sim 10$ and $\alpha \simeq 1$. In the most general case, a more accurate alternative formula

$$S = \sqrt{2}\{N_{on} \ln [\frac{1+\alpha}{\alpha}(\frac{N_{on}}{N_{on}+N_{off}})] + N_{off} \ln [(1+\alpha)(\frac{N_{off}}{N_{on}+N_{off}})]\}^{1/2} \tag{6.10}$$

has been derived and tested by Li & Ma (1983). This last formula is the standard way of calculating significancies for detected signals within MAGIC standard software.

Some remarks:

- the value of $\alpha$ is usually taken as 1 in wobble observations, but only if only one background region is considered. This, also, ignoring that there can be differences in the trigger rate of the different Wobble pointings due to different brightness of the sky patches shining the trigger region;
- for data taken in On–Off mode, there is no intrinsic reason for which source and background observing times are equal; instead $\alpha$ happens to vary a lot.

The independence of source and background observations is obviously ensured for data taken in On–Off mode, as the samples of events are completely uncorrelated. For Wobble observations, where the pool of events is the same for on and off data, the cuts addressed in Section 6.8 grant that the two datasets are uncorrelated.

## 6.9 Sensitivity

In order to evaluate the capability of the telescope (and the effectiveness of the analysis) to detect weak fluxes, also the *sensitivity* can be used, defined as the minimum integral flux above a given threshold that can be detected at the 5 $\sigma$ level in 50 h of observation. The flux is usually expressed in units

of the Crab Nebula flux above the same threshold (Crab Units, or C.U.). The sensitivity of the telescope can be written as:

$$Sens(t) = \frac{N_{exc}}{\sqrt{N_{bkg}}} \cdot \sqrt{\frac{t}{T}} \tag{6.11}$$

where the simple formula 6.7 for the significance of an excess has been adopted, $t$ is the normalization time and $T$ is the observed time. As a rule of thumb, for On–Off observation in dark conditions and time analysis, the sensitivity of MAGIC–I to point sources has been evaluated $\sim 1.5\%$ of Crab Flux above 280 GeV (Aliu et al., 2009a).

An interesting parameter is, for a given spectrum and energy band, the sensitivity limit for a given observing time. This quantity is plotted in Figure 6.9 assuming a "Crab–like" power law spectrum with index $\Gamma = -2.6$ and a 200 GeV energy threshold.

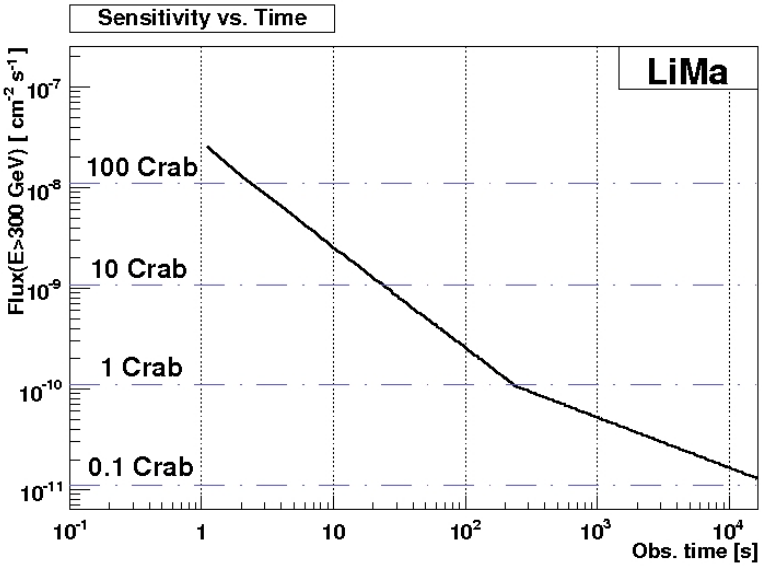


Figure 6.8: The magic integral sensitivity limit (expressed also in Crab Units) as a function of the integrated on–source time. The calculation is performed assuming a source with Crab–like spectrum, a 200 GeV energy threshold and the Li & Ma formula for calculation of significance (Li & Ma, 1983).

## 6.10 Energy Estimation

For the estimation of the energy of the events another Random Forest classification procedure is performed.

The main differences regard:

- no hadron sample is involved, as the training is based on the knowledge of the *true* energy of the primary simulated $\gamma$ rays;
- the single decision trees in this case do not have to answer a dicothomic question, but to determine a continuous quantity, the estimated energy of the events.

This problem is overcome dividing the MC training sample into many energy bins, and calculating the probability that any given event belongs to one of them. The estimated energy is then the mean of the possible energy values, weighted with the probabilities. This leads to a parametrization $E_{est} = E_{est}(E_{true})$ for the simulated events, that can be tested on an independent MC sample. This parametrization is called *migration matrix*.

The quality of the energy estimation is depicted by its resolution and the bias. The energy resolution can be defined as the standard deviation of a Gaussian fit to the quantity

$$\frac{\Delta E}{E} \equiv \frac{E_{est} - E_{true}}{E_{true}} \tag{6.12}$$

The energy resolution for MAGIC is $\sim 25\%$ above 100 GeV, but becomes worse below. The bias is the mean value of the same Gaussian fit. It can be shown that the parametrization is fairly linear and unbiased between 150 and $\sim 5$ TeV, but the energy is systematically overestimated at low energies and underestimated at high energy. This behaviour is common to all kind of energy estimators for different IACTs and must be taken into account when producing the final, physically significant spectrum.

**Classification parameters**

A standard choice of the parameters involved in the multidimensional classification in the source independent approach can be: Width, Length, Conc, Leakage, Size/(Length×Width).

In the source dependent approach, source dependent parameters such as Dist or P1Gradient can be added, improving the result.

Again, Size and ZA can be added, provided that the Resizing and Rezenithing (see Section 6.7.3) have been performed.

### 6.10.1 Energy threshold

A relevant parameter for evaluating the quality of the observations is the threshold energy of the Telescope $E_{thresh}$, the lower limit of the observable band of telescope, given the analysis and the cuts applied. This can be measured from the simulated events, after the Hadronness and Size cuts

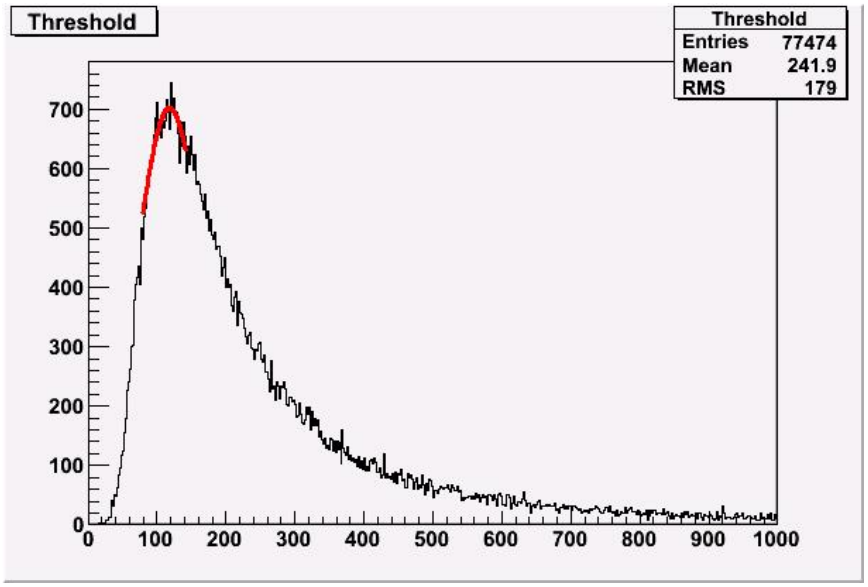


Figure 6.9: A plot illustrating how the energy threshold of the analysis can be estimated, from the peak energy of a Gaussian fit to the maximum of the histogram of true energy of simulated events, after that analysis cuts have been applied to the sample. This plot was produced during the analysis of OJ 287 discussed in Chapter 7.

have been applied. The distribution in $E_{true}$ peaks at a certain energy, where the detection efficiency of the telescope starts to drop. A Gaussian fit to the peak gives the value of $E_{thres}$. Figure 6.9 illustrates this procedure. The value obtained does not mean that the telescope cannot detect events below this threshold, but only that the effective area is considerably reduced.

## 6.11 Spectrum calculation

The differential spectrum is defined as

$$\frac{dF}{dE}(E) = \frac{dN_\gamma}{dE dA_{eff} dt_{eff}} \tag{6.13}$$

The quantities in the second member are: the number of excess events $N_\gamma$, the effective collection area $A_{eff}$ and the effective observation time $t_{eff}$.

It must be remarked that the number of excesses $N_\gamma$ is obtained with cuts that are looser than the ones used for detection of signal, as after the source signal is established, the total number of excess events and the energy threshold assume more relevance than the significance of the excess; therefore relaxed cuts allow a better acceptance for $\gamma$–ray induced showers.

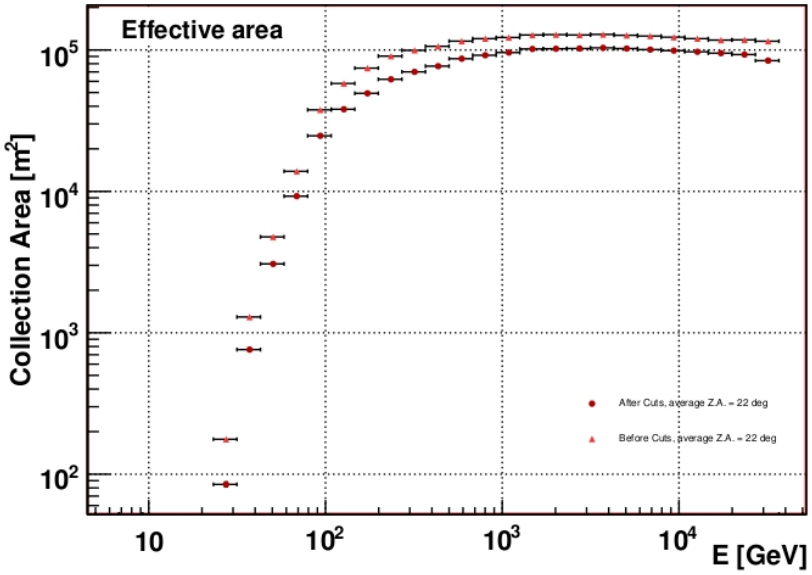


Figure 6.10: Plot of the collection area of the MAGIC–I telescope calculated from the MC simulated $\gamma$–ray events, before (orange markers) and after (red markers) cuts. The calculation is performed in bins of estimated energy.

The differential spectrum is calculated in bins of estimated energy, that may differ from the true energy the observed events. The calculation of the spectrum in bins of true energy is performed by means of the *unfolding* procedure, described in Section 6.11.1.

The statistical errors on the spectrum calculation are derived from the uncertainty in the number of excess events $N_\gamma$, in the effective collection area $A_{eff}$ and in the effective time $t_{eff}$. The latter is anyway negligibly small compared to the other sources of uncertainty.

**Calculation of effective area.**

The effective collection area of the instrument in each ZA and estimated energy bin is calculated from MC simulated events. For each $ZA$ bin the area where $\gamma$–ray events can be detected by the telescope is known, and it is multiplied for the ($E_{est}$ dependent) detection efficiency for MC events after all cuts, that is calculated, in every bin of estimated energy, as the ratio of the simulated $\gamma$ events that survived all the cuts to the initial number of simulated showers. The average on the ZA distribution of the data gives then $A_{eff}$, as a function of $E_{est}$.

**Calculation of effective time.**

The observation time $T$ is the sum of the time span of all the data runs taken; during this time a number $N_\gamma$ of events has been recorded.

The effective time $t_{eff}$ is instead a corrected quantity, related to $T$, that takes into account all the effects that alter the performance of the telescope with respect to an ideal detector. An example of this are "dead times": a time lapse during which the telescope remains uncapable of recording events because it's *busy* with processing the previous one. All these effects worsen the performance of the telescope, with respect to an ideal one, that would need $t_{eff} < T$ to observe the same number of events $N_\gamma$.

The calculation is based on the whole sample of observed events after cleaning, that are assumed Poisson distributed in time. The distribution of $\Delta t = t_i - t_{i-1}$, the differences in arrival time between each event and the previous recorded one, can be proved also Poissonian, with a characteristic time $\tau$.

This characteristic time $\tau$ can be measured from the experimental data: the histogram of arrival time differences of the data follows quite well a Poisson law, and the time characteristic can be measured from a best fit.

The effective time $t_{eff}$ can therefore be calculated as

$$t_{eff} = N_\gamma \cdot \tau \tag{6.14}$$

with $N_\gamma$ the number of recorded events.

This calculation holds well until $\tau$ is stable; but the acquisition rate depends on zenith angle, and on the observing conditions (e.g. weather); therefore the calculation is performed run by run.

### 6.11.1 Unfolding

This procedure corrects the spectrum for the finite energy resolution of the detector, and for the biases that affect energy reconstruction, mostly at the edges of the observable energy band.

These discrepancies from ideality distort the $\gamma$–ray spectrum. This effect can be written in formulas in the following form.

$$Y(y) = \int M(x, y) S(x) dx \tag{6.15}$$

where $x$ is the true energy, $y$ the estimated energy, $S$ the physical spectrum we want to reconstruct, $M(x, y)$ a function describing the response of the detector and $Y$ the observed energy spectrum. This can be discretized in a matrix formula

$$Y_I = \sum_j M_{ij} S_j \quad \equiv \quad Y = M \times S \tag{6.16}$$

where the indexes $i$ and $j$ run on the estimated and true energy bins, respectively, $Y$ and $S$ are the estimated and true energy distribution, respectively, and $M$ is the migration matrix.

The aim of the unfolding is to determine $S$, knowing $M$ and $Y$.

A first approach could be the deconvolution, consisting in the inversion of the migration matrix. But, the large correlation between neighboring bins lead to large fluctuations in their contents. Another, more convenient approach is the unfolding with regularization. This is based on the introduction of two additional terms: one, $\chi^2_0$ expressing the agreement between the observation $Y$ and the prediction $M \times S$, and the other, $Reg$, measuring the smoothness of $S$.

The solution for $S$ is obtained by minimization of

$$\chi^2 = \frac{w}{2} \cdot \chi^2_0 + Reg \tag{6.17}$$

after fixing the regularization parameter $w$. As a qualitative rule, if a a big value for $w$ is chosen, the regularization tends to lose importance: the unfolded distribution and the data fit each other very well, but the unfolded distribution is noisy. On the other hand, a small $w$ leads to a very smooth unfolded distribution, but significantly deviating from the measurement. The crucial issue in the procedure is therefore the proper choice of $w$, that is performed in various ways in different algorithms (Anykeyev et al., 1991), such as the methods proposed by Bertero (Bertero, 1988), Tikhonov (Tikhonov & Arsenin, 1979) or Schmelling (Schmelling, 1994), all available in the MARS standard software (Albert et al., 2007c).

A "dual" approach is performed in the so called *forward* unfolding, which assumes as starting point a parametrization of the true distribution $S$, and then compares $M \times S$ with the measured distribution $Y$. No regularization is performed here, and the procedure is the best fit, with corresponding errors, of this assumed distribution to data.

Operatively, unfolding results are accepted only if the results from different methods are consistent with each other and some additional criteria are fulfilled concerning the $\chi^2$ value and the regularization strength (Albert et al., 2007c).

### 6.11.2 Upper limits

In case that no significant excess is found in the signal extraction, an upper limit on the source flux (integral, above some energy threshold, or differential, in selected bins of reconstructed energy) can be calculated, based on the excess count observed (eventually negative), on the background counts

ad the related uncertainty, on an hypotesis regarding the spectral shape of the source and on the collection area of the telescope. Clearly, the tightness of upper limits relies on the accuracy of the observation the background, and this (amongst other factors) on the observation time.

The implementation of the upper limit calculation within the MAGIC standard analysis has been developed and discussed in detail in Albert et al. (2007e). The first step is, given an ALPHA or $\theta^2$ plot with no significant excess in the signal region, the calculation of an upper limit in the number of excesses. This means the highest number of excesses $N_{UL}$ that, at a certain *confidence level* CL (usually set at 95%) is compatible with a non detection, due to, e.g. negative background fluctuations neutralizing it. This task in the MARS software is accomplished by means of an implementation of the Rolke method (Rolke et al., 2005). The $N_{UL}$ is calculated given:

- the background event count in the signal region $N_{bgd}$;
- the uncertainty on $N_{bgd}$, $\Delta N_{bgd}$;
- the requested confidence level;
- the level of systematic uncertainty considered (usually within MAGIC a 30% value is considered).

Then, from $N_{UL}$ in excess counts an upper limit on the source flux can be derived.

The reconstructed number of events in a particular reconstructed energy bin $\Delta E_{rec}$ can be written as

$$N_{\Delta E_{rec}} = \int_0^\infty \phi(E) A_{eff}(E|\Delta E_{rec}) dE \Delta T \tag{6.18}$$

where $\phi(E)$ is the flux (in photons $\mathrm{cm}^{-2}\mathrm{s}^{-1}\mathrm{GeV}^{-1}$), $A_{eff}$ is the effective collection area after all cuts, included the cut in estimated energy $\Delta E_{rec}$ and $\Delta T$ is the total observed time interval. It must be carefully noted that the flux and the effective area depend on the *true* energy, while the cuts for the selection of the excess $N_{E_{rec}}$ and of the effective area $A_{eff}(E|\Delta E_{rec})$ in the *estimated* energy. The integral is computed in *true* energy $dE$.

As the effective area $A_{eff}(E|\Delta E_{rec})$ depends on the energy, a reasonable spectral shape must be assumed, e.g. a simple power law with Crab–like slope $\Gamma = -2.6$.

The expected spectrum is therefore

$$\phi(E) = k \times (\frac{E}{E_0})^\Gamma \tag{6.19}$$

where $k$ is a normalization factor, with the dimensione of the flux, and $E_0$ is the *pivot* energy chosen (e.g. 300 GeV).

Using equations 6.18 and 6.21 and resolving for the normalization factor $k$ we find

$$k\star = \frac{N_{\Delta E_{rec}}}{\int_0^\infty (\frac{E}{E_0})^\Gamma A_{eff}(E|\Delta E_{rec}) dE \Delta T} \tag{6.20}$$

where $N_{\Delta E_{rec}}$ is given, as the excess upper limit for the given energy bin calculated with Rolke statistics. The flux upper limit is then

$$\phi(E) = k_\star \times (\frac{E}{E_0})^\Gamma \tag{6.21}$$

## 6.12 Light curves

The term *light curve* is common to every branch of observational astronomy, whatever energy band is observed, and means simply the determination of flux in separate time interval, intended to perform a time sampling of the brightness of the source. This is particularly relevant in AGN observations in the VHE band, where variability time scales down to minutes can be observed (Gaidos et al., 1996; Albert et al., 2007f; Aharonian et al., 2007), and deep insight into the source properties is expected from them.

The light curve can be defined as a time–dependent generalization of equation 6.13:

$$\frac{dF}{dE}(E,t) = \frac{dN_\gamma(t)}{dE dA_{eff}(t) dt_{eff}(t)} \tag{6.22}$$

The time dependence of $A_{eff}$ comes naturally from the time dependence of source elevation, due to its apparent motion on the sky.

As in the VHE band the signal is seldom strong enough to perform this calculation in separate energy bins and in separate time bins, the integrated flux above a certain energy threshold $E_0$ is given.

$$F_{E>E_0}, t) = \int_{E>E_0}^\infty \frac{dN_\gamma(t)}{dE dA_{eff}(t) dt_{eff}(t)} dE \tag{6.23}$$

In the practice, calculation is performed inside time bins of width $\Delta t$ around the time $t$. The corresponding effective area is calculated form MC events, as a weighted mean on the ZA distribution of the source in the time interval.

The energy threshold is a sensitive parameter, as the number of excesses is dominated by the low energy part of the spectrum that follows, in first approximation, always a power law. A good choice is a value just above the steep drop in the collection area, otherwise strong systematics can arise from the strong dependence of the collection area (see Figure 6.10 on the estimated energy and from the uncertainty in energy reconstruction. This is even more important as no unfolding is performed for light curves, therefore

the low energy region where the linear correlation between estimated and true energy falls off has to be avoided.

## 6.13 Estimation of systematics

The measured spectrum and light curves are affected not only from statistical uncertainties, but also from systematic errors, difficult to evaluate. The sources of these systematic effects are various; their independent contributions must be added in quadrature to obtain the total estimation of systematics.

The most relevant contributions to systematic errors are (Albert et al., 2008a):

- The MC showers are simulated assuming the standard U.S. atmosphere and the Elterman model (Elterman, 1951) for the distribution of ozone and aerosols. Therefore:
  - Discrepancies between the assumed model of atmosphere and the actual atmosphere above the observatory may affect the results;
  - Variations in the athmospheric conditions, like pressure, temperature, humidity, haze, *calima*, are not taken into account and may induce underestimation of the primary energy.

  The systematic effect on the energy scale is assumed of the order of 15%, according to the average relative variation in the atmospheric transmission between summer and winter (Bernlohr, 2000);
- Limited knowledge of the telescope hardware:
  - The mirror reflectivity is assumed 0.85 (see also Appendix C), but depends on the dust present on the mirrors, and decreases with time due to surface aging. A 5% uncertainty on the energy estimation is assumed to derive from this effect.
  - The optical PSF of the telescope depends on the accuracy of the bending model of the telescope and of the active mirror control. Another 5% of uncertainty on the energy estimation is assumed to arise from the discrepancy between the real PSF and the one assumed in the simulation of the reflector.
  - The Winston cones and the plexiglass camera cover may provoke photon losses, especially if dust is present. Again, $3 - 5\%$ of uncertainty is considered.
  - The systematic error (again on energy estimation) on light–to–photoelectron conversion has been estimated $\sim 5-10\%$. Measurement of the conversion is difficult; the main source of uncertainty is the light collection efficiency of the first dynode in PMT tubes.

  - Trigger inefficiencies are probably the dominant effect. This has influence on both the flux measurement and the energy estimation. The assumed systematic is 20% at 150 GeV and decreases with energy, to a 5% at 1 TeV.

- Systematic effects introduced along the analysis procedure:
  - the F–Factor method (see Section 6.4.2) is responsible of a systematic error of 8% on energy estimation (Gaug et al., 2005);
  - a systematic error is introduced neglecting telescope dead times. This amounts to 2% and affects the flux measurement, independent of energy;
  - differences in details of the analysis (signal extraction, image cleaning, cuts, $\gamma$–hadron separation method, unfolding) have been estimated to carry a 3% contribution to systematic errors;
  - errors introduced by unnoticed software bugs. Obviosly hard to quantify, but estimated around 3%;
  - agreement between Monte–Carlo simulated $\gamma$–ray events and real data: this may affect the effective area calculation. A 10% effect is estimated, on both the absolute energy scale and the flux level.

All these contribution lead to systematic uncertainties onto the energy scale, the flux level and the spectral slope. The overall uncertainty on the energy scale is 16%. The error in the flux depends on the spectral slope of the source. The steeper the spectrum, the more relevant is the low energy flux, that is also more prone to systematic effects. An agreeable estimation is that for a rather Crab–like slope with $\alpha = -2.5$ the error on the flux is $\approx -30\% + 50\%$. For an $\alpha = -4.0$ slope, the error becomes $\approx -50\% + 100\%$. The asymmetry of the error band is justified from the observation that most systematic contribution lead to $\gamma$–ray flux reduction, or to underestimation of energy, that in turn again decreases the observed flux.

The systematic error on the spectrum slope is evaluated in 0.2.

The large errors in the flux are a common feature for IACTs, and may be largely attributed to the lack of a test beam of real $\gamma$–ray events useful to calibrate their response. Ideally some improvement could be found by cross correlation with the *Fermi* satellite (see Section 1.2.2), as the energy band of the two instruments partly overlap. An improved flux calibration can therefore derive from common observation of a standard, steady bright source, like the Crab Nebula (see Appendix A).

This is however not trivial, as the energy band accessible to *Fermi*/LAT extends up to 300 GeV, but with dramatically decreasing sensitivity due to its smallish collection area and the flux extinction due to the spectral slope of the source. Therefore a long integration time is needed, and this

somehow excludes applicability of this procedure to brighter, but strongly variable sources.

## 6.14 Online Analysis

Since fall 2007 an important analysis tool, that performs a fast data analysis, has been added to the MARS package. This software is obviously available in the computing center located at the telescope control house; actually, it was created specifically for running at the telescope site for the convenience of the observers.

The tools is based on a simplified version of the standard MAGIC analysis procedure, and provides a preliminary flux estimation immediately after the observation, as soon as the data files are available on the storage system. All along the data acquisition, the result is updated including the new runs.

The procedure is extremely swift as data undergo standard calibration and cleaning, thereafter some standard predefined matrices are applied to the data for hadronness calculation and subsequent background suppression.

Finally, the signal is extracted applying standard SIZE, HADRONNESS, ALPHA and ZA cuts. This fast analysis allows calculation of the $\gamma$–ray event rate from the observed sources, almost simultaneously to datataking; the delay is usually within a few minutes. From the $\gamma$–ray event rate an estimation of the flux level based on the rate received from the Crab Nebula when observed in similar conditions.

This tool has proven to be very useful in various ways:

- extension of observations in case of unusual flux from known sources, possibly pointing to some interesting activity e.g. am AGN flare;
- provision of real time alerts to other observatories in the context of coordinated campaigns, based directly on this early result, even if openly given as *very* preliminary;
- stimulation of immediate, deep, human–handled analysis of the selected datasets hinted as interesting, in order to confirm or disprove the early result and react promptly in case of confirmation; e.g. scheduling more observations, alerting other observatories or activating ToO proposals

# Chapter 7

# The LBL *blazar* OJ 287

## 7.1 The source

The *blazar* OJ 287 has been observed since 19th century, as can be easily checked from the optical ($V$ band) ligth curve shown in Figure 7.1, taken from Valtonen et al. (2008).

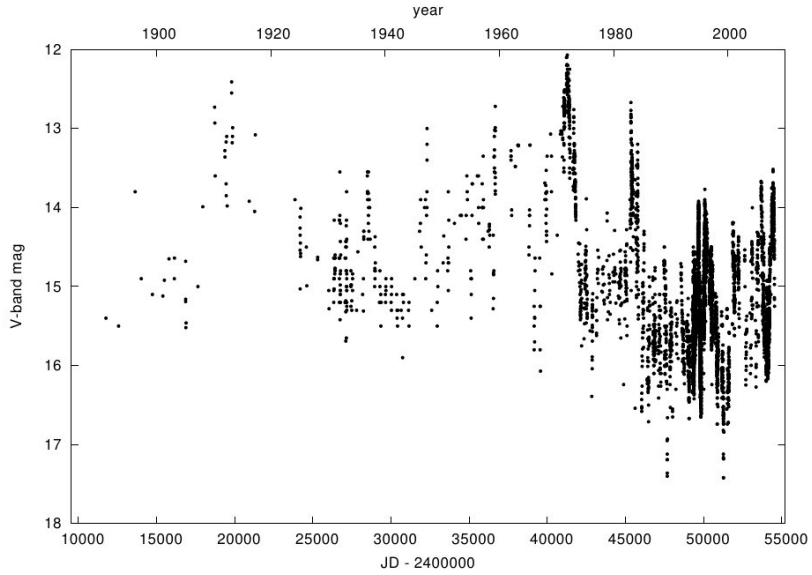


Figure 7.1: The historical light curve of OJ 287 in the $V$ band. Taken from Valtonen et al. (2008). The periodic ($T = 11.65$ years) double flare is visible.

At first, it was misinterpreted as an irregular variable star, of magnitude $m_V \sim 15$ when observed in quiescent state, as usual for this kind of sources before the concept of AGN was born: the more correct identification as a

*quasar* dates to 1968. Currently it is considered a High Optical Polarization BL Lacertae–like (briefly, HP BL Lac) AGN, according to the 12th edition of the Véron–Cetty & Véron AGN catalog (Véron-Cetty & Véron, 2006). Due to the position of the SED peaks, it belongs to the LBL subclass of BL Lacs.

The source is located in the Northern Sky, in the constellation of Cancer; the equatorial [J2000] coordinates are $(\alpha, \delta) = (08^h54^m49.87^s, 20°06'30.6")$, as measured with VLBI radio observations (Johnston et al., 1995). The redshift of the source, is $z = 0.306$ (Hewitt & Burbidge, 1989a,b; Stickel et al., 1989), that adopting a standard "concordance" cosmological $\Lambda$–CDM model (with $\Omega = 1$, $\Omega_m = 0.27$ and $\Omega_\Lambda = 0.73$ and $H_0 = 73$ km/s Mpc$^{-1}$) implies a luminosity distance of 1.54 Gpc, and a light travel-time of 3.360 Gyr (Hogg, 1999).

Great scientific interest arises from the peculiar optical light curve of the source (see picture 7.1), that shows quasi–periodic optical outbursts at $\approx 12$ years intervals, with two outbursts per cycle, split by a $\sim 1$ year long quiescent phase (Lehto & Valtonen, 1996). Due to this pronounced optical variability OJ 287 has been historically classified as an Optically Violent Variable (OVV).

Various hypotheses have been formulated to account for this regular behaviour:

- oscillations in the accretion disk (Igumenshchev & Abramowicz, 1999) or in the jet (Hughes et al., 1998) of a single black hole;
- variations in the accretion rate of a disk (Sillanpaa et al., 1988) of a binary black hole;
- wobbling of a jet in a binary black hole system, due to the precession of the accretion disk induced by the torque exerted by the companion black hole (Katz, 1997).

Howewer, the outburst sharpness (Valtonen et al., 2006) is poorly reproduced in these models. Another model, proposed by Valtonen et al. (2008) accounts better for this rapid optical variability (Sundelius et al., 1997). In this model the optical outbursts are associated with a binary black hole model, where the secondary black hole pierces the accretion disk of the primary during its orbits, at a costant phase $\phi$ and at $\phi + \pi$ (Lehto & Valtonen, 1996). A highly eccentric orbit is postulated, in order to account for the closeness of the two outbursts with respect to the orbital period. Within this model, the precession rate of the major axis is 39.0° per orbit, the eccentricity $\epsilon = 0.0663$, the mass of the primary black hole $18.0 \times 10^9 M_\odot$. These values are reasonable for merging binaries (Aarseth, 2008) and the BH mass at the upper edge of the mass range for *quasars* (Vestergaard et al., 2008) is compatible with the high luminosity of OJ 287 (intrinsic magnitude $M_V \sim -26$, as the distance module is 40.74).

The outburst onset time is also regarded as an indirect proof of the existence of gravitational waves (Valtonen, 2007) as the predicted flare time without gravitational waves would have been $\sim 20$ days later.

## 7.2 The 2007 multiwavelength campaign on OJ 287

In 1994 November OJ 287 had already been intensively observed in various bands ("The OJ 94 Project" Sillanpaa et al. 1996a). The optical outburst respected the foreseen periodicity and also the double–peaked structure with $\sim 1$ year interval was confirmed by the secondary outburst in 1995 December (Sillanpaa et al., 1996b).

In agreement with the confirmed 11.65 year optical periodicity (Sillanpaa et al., 1988; Valtonen et al., 2006b) in November 2005 the source underwent an optical flare, that could be interpreted as the first of the two optical peaks characteristic of its active phase.

In the radio band no enhancement of the flux was observed in association to the optical peak. This was in agreement with the interpretation (Valtonen et al., 2008) that predicts for the first peak a thermal origin in the vicinity of the black hole and the accretion disk (tentatively, the secondary BH piercing the accretion disk), while links the second peak to synchrotron radiation from the jet (Valtaoja et al., 2000). Actually, the second peak in the 1994–1995 outburst had shown a radio outburst with increased polarization (Pursimo et al., 2000) again supporting this scheme, but the evidence was not considered final. An interesting clue came instead from CGRO/EGRET, that reported a detection of OJ 287, that, although statistically marginal, was interestingly coincident with the 1994 optical flare (Shrader et al., 1996). This strongly suggested deeper investigation of the active state in the VHE $\gamma$–ray domain, with a sensitive detector such as MAGIC.

Consequently, expectation for the second, perhaps jet–related optical peak in November 2007 led to the planning of a multiwavelength campaign including the MAGIC–I telescope and a few other instruments covering the Radio (NMA[1]), Near–IR (KANATA telescope), optical (KANATA, KVA), and X–ray (*Suzaku*, *Swift*) energy bands. This broad coverage of the electromagnetic spectrum was intended to obtain detailed description of the SED of this intriguing source, in order to be able to validate or rule out the proposed models.

### 7.2.1 Observation strategy

The main scientific goal of the campaign was to deepen the insight of the source emission mechanism. Therefore, broadband multiwavelength simul-

[1]Nobeyama Millimeter Array

taneous observations both in the quiescent and in the flaring state were required, so that both the fundamental emission mechanism present in the low state and the source evolution related to the flaring state could be studied. Observations of the quiescent state (conventionally labeled as MWL I) were performed in April 2007, in coordination amongst the instruments joining the campaign. As this part of the campaign was focused on a low state, that could be safely assumed as a steady baseline in first approximation, the observations were not time critical, and could be scheduled in advance as "fixed time" MWL observations. Instead the time-critical observation of the flare state was started in November, as a ToO MWL observation (MWL II). The trigger of the MWL II campaign was given following an alert cast from the KVA telescope in La Palma, that monitored regularly the source. The Tuorla Observatory reported a week long, one magnitude ($m_V \approx 14$ instead of $\approx 15$ that is the quiescent baseline) increase of the optical (Johnson $R$ band) flux of the AGN; this fulfilled the conditions, agreed in advance amongst the observers, for the startup of this ToO observation.

In the following, MAGIC observations and the analysis results will be reported first. The analysis of MAGIC data collected during the MWL II campaign is one of the main tasks undertaken for this thesis. An independent one was performed by the PI of the MAGIC OJ 287 proposal, Dr. Masaaki Hayashida, and the two analyses agreed in the final results within uncertainties. Then, observations and results from the other instruments will be reported, and finally the published results (Seta et al., 2009; Hayashida et al., 2009) regarding emission modeling and interpretation of the observations will be shown.

## 7.3 MAGIC observations and results

MAGIC observations of OJ 287 were performed at low zenith angles (ZA $\lesssim 30°$) in order to reach the lowest possible energy threshold, and during dark time, in order to reduce NSB pollution.

This extremely careful scheduling was mandatory for at least three concurrent reasons:

- OJ 287 is classified as LBL: a kind of BL Lac source that is observationally depressed in VHE astronomy performed with IACTs. This is due to the poor match between the soft spectrum of these sources and the rather high threshold of the energy band accessible to IACTs: only a handful out of the 25 currently established extragalactic VHE sources are LBLs (namely, BL Lacertae Albert et al. 2007d and S5 0716+714 Anderhub et al. 2009a, both discovered by MAGIC), while the vast majority belongs to the HBL *blazar* subclass. Even when

observations of LBLs were successful, the signal was concentrated at low energy and with rather steep spectrum in spite of the quite active states that were exploited in order to enhance the chances of detection.

- OJ 287 is a mid–large redshift ($z = 0.306$) VHE candidate source, therefore prone to consistent EBL extinction of the TeV flux.

- Again due to the redshift, the whole spectrum is shifted at 30% lower energies w.r.t. the intrinsic, comoving spectrum due to the cosmological recession effect. This contribution is minor, but nevertheless concurs against detection.

For all these reasons, OJ 287 observations of MAGIC were a challenge to the performance and the sensitivity of the telescope; only signal at low energies could be reasonably expected, if any.

The later discovery of VHE signal up to 600 GeV from the even farther bright FSRQ 3C 279 (MAGIC Collaboration, 2008) at $z = 0.56$ (Marziani et al., 1996) achieved during its active phase in January 2008, showed that MAGIC–I, nearly alone amongst currently operating IACTs, could successfully observe VHE sources at such distances. Moreover, other LBLs have been discovered as VHE sources by MAGIC, so that in principle, the observation could be successful, despite the intrinsically soft spectrum and severe EBL absorption.

### 7.3.1 MAGIC observation in April 2007 (MWL I)

In April 2007 On–Off mode observations of OJ 287 were scheduled by MAGIC in the days 9, 10, 11 and 12, to be simultaneous with the X–ray satellite Suzaku joining the campaign (Suzaku observations are reported in section 7.4.3). Unfortunately, only 4.5 out of the 8 planned hours of on source data could be collected, due to bad weather on day 9 and to a GRB observation on day 11, that overrode the scheduled OJ 287 observation due to the higher priority (actually, GRB have the highest priority in MAGIC scheduling, see Section 5.5.2). The observations were performed during proper dark time (no NSB contribution from moonlight) and with zenith angles in the range $8° < ZA < 29°$. As far as the off–source sample is concerned, this amounted to 6.5 hours, including the dedicated Off observations and data from the GRB follow up observations that revealed compatible with the on–source data.

A source dependent, Alpha–analysis performed with the newly introduced time parameters in the cleaning and in $\gamma$/hadron separation did not reveal any signal from the source. Only upper limits on the VHE signal from the source could therefore be derived. The calculation was performed following Rolke et al. (2005), calculating integral upper limits at 95% confidence level (CL), and accounting for 30% of systematic uncertainty. The

upper limit on integral flux, above 200 GeV, was calculated as $1.06 \times 10^{-11}$ photons/cm$^{-2}$s$^{-1}$, corresponding to $\sim 5\%$ of the Crab integral flux above the same threshold. The upper limits calculated in bins of energy are reported in table 7.3.

### 7.3.2 MAGIC observation in November and December 2007 (MWL II)

In MWL II campaign, MAGIC observed OJ 287 in a total of 22 nights, in November and December. The observations were extended following a hint of signal shown in the Online Analysis (see Section 6.14), not confirmed by the offline analysis. Out of these nights, 3 were affected by bad weather and low trigger rates, incompatible with the remaining data set and were consequently rejected. Even in the good nights all the data runs were checked and discarded in case of low trigger rates, bad data quality or acquisition problems (such as, for instance, car flashes or hardware failures). A total sample of 41.2 hours of good quality data was selected for further analysis. The ZA distribution of the data ranged from 8° at culmination to 31°.

The dataset was retrieved from the PIC[2] database in the form of lists of events already calibrated and cleaned with the standard time (6–3,4.5–1.5) levels (see Section 6.5).

#### Sample of MC simulated events

As a preliminary step a sample of Monte Carlo simulated $\gamma$–ray events was recovered from the PIC database.

The MC samples were chosen such as they:

- were simulated for the wobble observation mode;
- were generated with a PSF of 10.6 mm, to be compatible with the optical PSF of the telescope at the time of observations, as measured from the muon ring analysis (see Appendix C);
- covered the whole ZA range spanned by the real dataset ($8° < ZA < 31°$);
- were cleaned with the same algorithm and threshold levels applied to the real data (time cleaning, 6–3, 4.5–1.5).

Only the "standard" (see Section 6.3) MC samples were considered here, because the source was expected to emit only on the lower end of the telescope bandpass.

[2]Portal de Informacio Cientifica, the official MAGIC data repository.

### Compatible Crab dataset for cut optimization and analysis cross-check

In order to validate the analysis steps and to select an optimal set of cuts for the signal extraction, a compatible set of data from observations of the Crab Nebula ( see Appendix A) was retrieved from the database.

### Quality cuts

Some quality cuts were preliminarily applied on all the data: OJ 287 real data, Crab Nebula data, MC simulated $\gamma$-ray events. These cuts were, namely:

- SIZE $< 80$ phe
- LEAKAGE $< 0.15$
- $\mathrm{N}_{core} < 3$ pixels
- $\mathrm{N}_{islands} > 1$
- Standard spark event cut (see Section 6.6.4)

Events fulfilling one or more of the cut conditions were excluded from further analysis.

### Definition of the samples for the $\gamma$/hadron separation

Being OJ 287 a potential but not yet established VHE source, as a first step a subsample of the same real dataset was used as hadron sample for the training of the Random Forest classification algorithm used for $\gamma$/hadron separation. This was fully reasonable, as the VHE from the source could hardly be expected to be high enough (above the level of 10% of Crab) to significantly pollute the hadron sample with $\gamma$–ray events. In any case, another hadron sample of greater purity could have been searched as a further refinement, in case this assumption on the weakness of the VHE flux from the source revealed wrong.

Data from the nights 13, 14, 15, 16 and 17 of December, spanning the whole ZA range of the dataset, were therefore used as hadron sample.

Even if rather obvious, the compatibility of Hillas parameter distributions between this subset and the whole dataset was checked, and revealed optimal, as rather expected. In particular, the compatibility of the following distributions was checked: ZA, LENGHT, WIDTH, SIZE, CONC, LEAKAGE, ALPHA.

A part of the MC dataset was used as gamma–ray event sample for the training of the classification algorithm. The remaining part of the sample was left as an independent "test" sample, useful for the calculation of effective area.

### 7.3.3 Gamma/hadron separation

The multidimensional matrices needed for the calculation of the HADRONNESS of the events were optimized with the Random Forest method, by means of the `osteria` program included in the MARS package. Two different sets of matrices were produced, one for the source dependent analysis, and one for the source independent analysis. The first approach is more sensitive, exploiting the discrimination power of the source dependent parameters such as DIST; the second is free from biases introduced from the *a priori* knowledge of source position, and best suitable for tasks such as blind searches in the sky. The SIZE and ZA parameters are included in the multidimensional parameter set as scale parameters,given that the hadron sample had preliminarly been filtered to match the corresponding distributions of the MC events (RESIZING and REZENITHING procedures, see Section 6.7.3). The time parameters (see Section 6.6.3) are also included. The parameters involved in the discrimination are reported in table 7.1 for both approaches.

| Parameters used for the optimization of the $\gamma$/hadron separation | |
|---|---|
| Source Dependent | Source Independent |
| SIZE | SIZE |
| ZA | ZA |
| WIDTH | WIDTH |
| LENGTH | LENGTH |
| SIZE/ WIDTH $\times$ LENGTH | SIZE/ WIDTH $\times$ LENGTH |
| CONC | CONC |
| DIST | |
| M3LONG | M3LONG |
| RMSTIME | RMSTIME |
| P1GRAD | |

Table 7.1: Synopsis of the parameters used for the $\gamma$/hadron separation in the analysis of OJ 287. Both a source independent (left column) a the source dependent (right column) approach were used leading to two different set of classification matrices.

Based on these matrices, calculation of HADRONNESS was performed (by means of the `melibea` program included in MARS) for each event of the OJ 287 data sample and for the sample of simulated events devoted to the calculation of collection area.

### Energy Estimation

The estimation of energy of the events was performed by means of the Random Forest method, implemented in `osteria`. Two independent sets of multidimensional matrices were produced: one for the source independent approach and one for the source independent, similarly to the $\gamma$/hadron selection procedure. Based on the matrices generated at the `osteria` level, estimated energy of the primary $\gamma$ rays was calculated for the events in the OJ 287 and MC test samples.

### Optimization of the signal extraction on Crab Nebula data

The same matrices for the calculation of HADRONNESS and estimation of energy performed on the OJ 287 dataset were applied to the Crab Nebula data. Thereafter, signal extraction was performed with the ALPHA method on the Crab Nebula sample. A grid of cuts in the two–fold space of the HADRONNESS and SIZE parameters was explored in order to determine a set of cuts that maximized the $\gamma$–ray signal.

The highest significance on Crab Nebula was provided by:

- ALPHA $< 8^{\circ}$
- HADRONNESS $< 0.05$
- SIZE $> 350$ phe$^{-}$

The analysis energy threshold for this set of cuts was $E_{th} \sim 240$ GeV, measured from the peak in the *true* energy distribution of the MC simulated events surviving the cuts.
The significance of the VHE signal from the $\sim 3$ hours of Crab Nebula data analyzed, calculated according to Li&Ma (Li & Ma, 1983, see also Section 6.8.1) formula, is 26.8 $\sigma$, in agreement with the expected performance of the telescope for dark observations in wobble mode, with the 2GHz MUX FADCs and the timing cleaning and analysis methods applied.
This ensures that the $\gamma$/hadron separation has been efficiently performed and the background rejection level is good.

### Extraction of signal from the whole OJ 287 dataset

The cuts that grant optimal significance of the signal from the Crab Nebula are anyway too tight for the extraction of signal from the OJ 287 dataset, as excess events are expected to be concentrated at the low edge of the telescope energy bandpass.

Therefore, a set of looser cuts was applied to the OJ 287 dataset, namely:

- ALPHA $< 8^{\circ}$

- HADRONNESS $< 0.25$
- SIZE $> 125$ phe

This looser set of cuts halved the energy threshold of the analysis, down to $E_{th} \simeq 120$ GeV, with only a moderate ($\sim 20\%$) significance loss with respect to the optimal cuts reported in Section 7.3.3. Nevertheless, the ALPHA–plot (displayed in Figure 7.2 didn't show any excess. The number of ON and OFF events in the signal region (ALPHA $< 8°$) are reported in table 7.2: 75123 $N_{on}$ and 75272 $N_{off}$ events, from the on–source and background event histogram respectively, survived the applied cuts in HADRONNESS and SIZE. The excess event count is therefore $N_{exc} = -149$ and can be interpreted as a non significant ($\sigma_{Li\&Ma} = 0.38$) fluctuation in the background event rate.

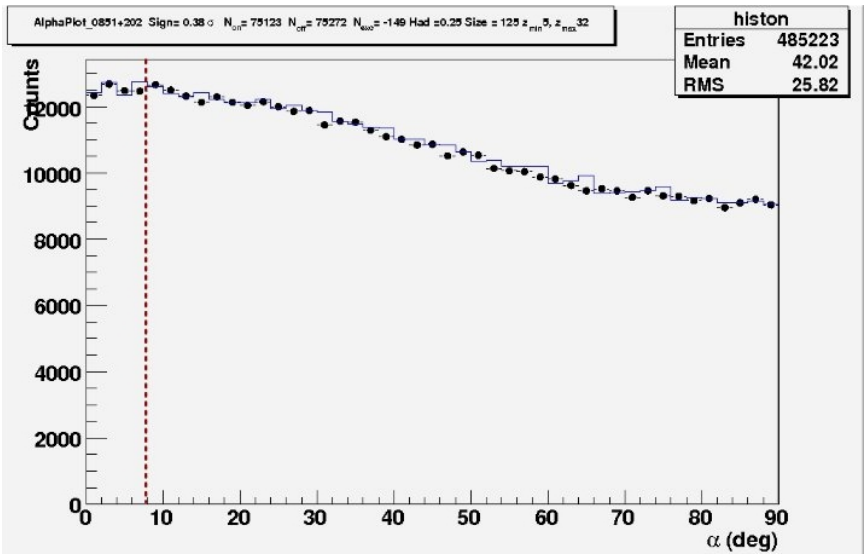


Figure 7.2: ALPHA–plot built from the full OJ 287 data sample. The cuts applied are SIZE $< 125$ phe$^-$, HADRONNESS $< 0.25$. The signal region is defined from the condition ALPHA $< 8°$. The red vertical dashed line defines the signal region on the plot. The two histograms of the OFF (blue line) and ON (black points) events are in good agreement in the background region ($30° <$ ALPHA $< 80°$). No VHE excess is found.

### Search for VHE signal in single nights

The absence of VHE signal in the whole dataset is in principle not incompatible with significant VHE flares in single nights.

| On source events $N_{on}$ | Background events $N_{off}$ | Excess count $N_{exc}$ | Excess significance ($\sigma_{Li\&Ma}$) |
|---|---|---|---|
| 75123 | 75272 | −149 | 0.38 |

Table 7.2: Result of the search for VHE signal from the OJ 287 full dataset (41.2 h of wobble observations).

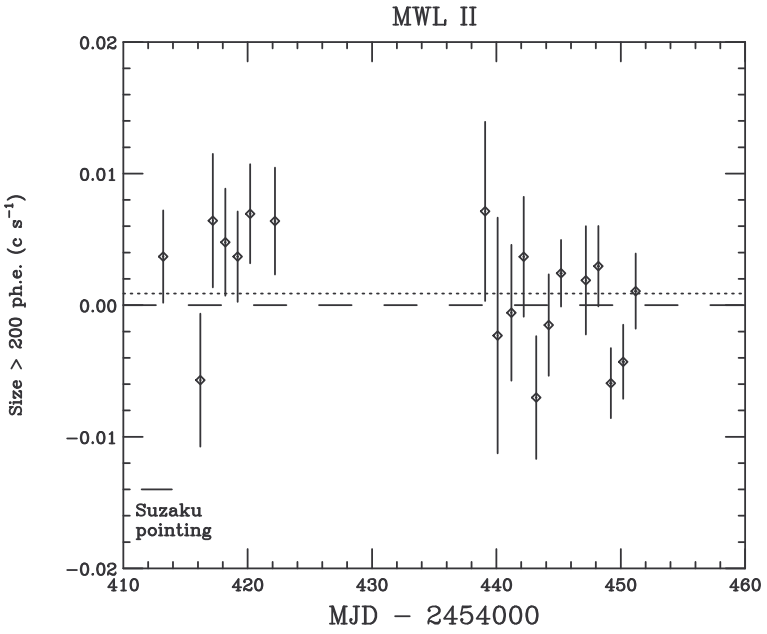


Figure 7.3: Plot of the excess count rate from OJ 287 in single nights of observation during MWL II campaign. All excesses are consistent with a null result.

The dataset was therefore split in separated subsamples, one for each single night, checking the symmetry between wobble positions, as otherwise camera inhomogeneities would bias the result at the low energies of interest.

No significant positive excess was detected in any night, and single excesses are compatible with fluctuations in the background event rate.

Figure 7.3 displays the excess count rates from each night, compatible with a constant null signal (probability of the constant fit P=11%, measured from the $\chi^2$ of the fit: $\chi^2$/dof= 22.55/18).

### Upper limits

As no VHE signal was observed neither in the whole dataset nor in single nights, the last step of the MAGIC analysis was the calculation of the upper limits for the OJ 287 observation. This was performed as described in section 6.11.2; the results are reported in the lower panel of table 7.3. The reported

| MWL I: 3 nights, 4.5 h On, 6.5 h Off | | | |
|---|---|---|---|
| Threshed Energy [GeV] | 80 | 145 | 310 |
| On events | 40056 | 1219 | 42 |
| Off events | 40397±226 | 1340±38 | 39.5±6.3 |
| Significance ($\sigma_{Li\&Ma}$) | -1.13 | -0.94 | -0.47 |
| U.L. of excess | 394 | 75.1 | 21.9 |
| $\text{Flux}_{95\%\text{U.L.}}[\times 10^{-12}$ cm$^{-2}$s$^{-1}]$ | 59.8 | 11.1 | 2.83 |
| Crab Flux (%) | 8.5 | 3.3 | 2.4 |
| MWL II: 19 nights, 41.2 h Wobble | | | |
| Threshed Energy [GeV] | 85 | 150 | 325 |
| On events | 281885 | 12582 | 578 |
| Off events | 282342±493 | 12573±65 | 576±14 |
| significance ($\sigma_{Li\&Ma}$) | -0.75 | 0.07 | 0.07 |
| U.L. of excess | 1218 | 330 | 71.6 |
| $\text{Flux}_{95\%\text{U.L.}}$ $[\times 10^{-12}$ cm$^{-2}$s$^{-1}]$ | 22.1 | 5.64 | 1.18 |
| Crab Flux (%) | 3.4 | 1.7 | 1.1 |

Table 7.3: Results of the search for VHE $\gamma$-ray emission from OJ 287, in MWL I (upper panel) and MWL II (lower panel) campaign. The threshed energy, expressed in GeV, corresponds to the peak energy of $\gamma$-ray MC samples after all cuts. The significance is calculated according to eq. 17 in Li & Ma (1983). The upper limit of the number of excess events is calculated at 95% C.L., with 30% systematic error. The flux upper limit is calculated assuming a photon index of $\Gamma = -2.6$ when convolving with the effective area in order to derive the flux. The Crab flux in percentage means the fraction of Crab flux corresponding to the U.L. in each energy range, according to the observations of the Crab Nebula performed with the MAGIC telescope (Albert et al., 2008a).

upper limits were calculated at 95% CL, assuming 30% of systematics and a a source with power law spectrum, with $\Gamma = -2.6$.

## 7.4 Multiwavelength data

In this section MWL data from the other instruments involved in the OJ 287 campaign are reported.

### 7.4.1 Radio data

Radio observations were performed since January 2007 until January 2008 at the Nobeyama Radio Observatory (NRO)

with the NMA, an array of six antennas, each 10 m wide in diameter.

Eleven measurements of the radio continuum from OJ 287 were performed, simultaneously in two bands at 86.75 GHz and 98.75 GHz, each 1 GHz wide. In each observation the on source time was $\sim$ 10 minutes. In each session, observations of the bright reference amplitude calibrators 3C 84 and 3C 435 were interleaved with the on source observations. As absolute calibrators, Uranus and Neptune were used to calculate the radio flux of OJ 287. The averaged flux levels in MWL I and MWL II are reported in table 7.4. An increase of the flux from MWL I to MWL II has been observed.

| Obs. Period | radio flux (Jy) | |
|---|---|---|
| | 86.95 GHz | 98.75 GHz |
| MWL I | $1.73 \pm 0.26$ | $1.75 \pm 0.26$ |
| MWL II | $3.04 \pm 0.46$ | $2.98 \pm 0.46$ |
| | Flux ratio | |
| MWL II/MWL I | $1.76 \pm 0.53$ | $1.70 \pm 0.52$ |

Table 7.4: Summary of the radio fluxes of OJ 287 measured by NMA during MWL I and MWL II. Both radio bands show that MWL I radio flux is roughly doubled in MWL II.

### 7.4.2 Optical data

Optical and NIR photometric observations were performed at the Higashi–Hiroshima Observatory with the KANATA (1.5 m $\varnothing$) telescope. Images of the field of OJ 287 in $V$, $J$, and $K_s$ filter were simultaneously obtained with the TRISPEC (Watanabe et al., 2005) instrument. Also the KVA telescope monitored regularly the source, in the Johnson $R$ band.

#### Optical $V$–band measurement with KANATA telescope

$V$ band measurements were taken in 53 nights between October 2006 and December 2007. In each night $\sim$ 20 images of the field were taken, with an exposure time of 108 s each. The magnitude of OJ 287 was measured by differential photometry, which means obtaining CCD images of the target and of the calibrated comparison stars (Fiorucci & Tosti, 1996) in the same field of view. A neighbor star in the field ($\alpha$, $\delta$) =($08^h54^m52^s.7$, $+20°04'46''$) with V=14.160 (Skiff, 2007) was used as comparison star. The steadiness of the comparison star was checked by another star in the field ($\alpha$, $\delta$) =($08^h54^m59^s.0$, $20°02'58''$); the fluctuations in the magnitude of the comparison star did not exceed $\Delta m$ =0.003. The whole study was performed with the aperture photometry package available in the IRAF[3] software.

[3]Image Reduction Advanced Facility

| Obs. period | Optical flux (mJy) | | | |
|---|---|---|---|---|
| | $K_s$ | $J$ | $R$ | $V$ |
| MWL I | $17.74 \pm 0.33$ | $8.82 \pm 0.03$ | $3.20 \pm 0.05$ | $3.03 \pm 0.01$ |
| MWL II | $55.98^{+7.69}_{-6.76}$ | $27.02 \pm 0.21$ | $8.70 \pm 0.14$ | $8.93 \pm 0.05$ |
| | Flux ratio | | | |
| MWL II/MWL I | $3.15 \pm 0.49$ | $3.06 \pm 0.03$ | $2.72 \pm 0.09$ | $2.95 \pm 0.03$ |

Table 7.5: Optical Fluxes of OJ 287 during MWL I and MWL II observations. The $R$–band observations were performed by Tuorla Observatory with the remotely operated KVA telescope located in Canary Island; the other bands were observed with KANATA 1.5 m telescope at Higashi-Hiroshima Observatory. In tle last row, the flux ratio of MWL II to MWL I is reported.

### $J$ and $K_s$ NIR measurements with KANATA telescope

NIR observations were taken on 2007 April 11, 12 and 13 (for MWL I) and on 2007 November 7, 8 and 9 (for MWL II) in order to be simultaneous with *Suzaku* (see 7.4.3). Exposure times of the single frames were of 15 s and 4 s for the $J$ and $K_s$ band respectively. The reduction procedure and reference and comparison stars were the same used for the V-band optical observations. The $J$ (= 12.664) and $K_s$ (= 12.090) magnitudes of the comparison star were retrieved from the 2MASS catalog (Skrutskie et al., 2006). During the observations, the comparison star magnitude was stable within $\Delta m = 0.004$ and $\Delta m = 0.012$ for $J$ and $K_s$ band respectively. The results are reported in table 7.5.

### R–band optical measurements with KVA telescope

R-band observations simultaneous to *Suzaku* time windows were performed with KVA telescope. The exposure time was 180 s for each frame. Photometric measurements were performed in differential mode. The magnitudes of the source and comparison stars were measured with aperture photometry; the color corrected zero point of the image was determined form the magnitude of the comparison star. The object magnitude was finally computed using the zero point and a filter–dependent color correction. The transformation to linear fluxes was performed with the formula

$$F = F_0 \times 10^{\frac{M}{-2.5}} \tag{7.1}$$

where $M$ is the magnitude of the object and $F_0$ is a filter–dependent zero point. For the Johnson $R$ band the value $F_0 = 3080$ Jy (Bessell, 1979).

### 7.4.3 X-ray data

#### Suzaku observations

The Suzaku satellite observed OJ 287 with two of its instruments: the *X–ray Imaging Spectrometer* (XIS), sensitive to soft X–rays, and the *Hard X–ray Detector* (HXD), sensitive up to $\sim 60$ keV.

Long ($\sim$ 100 ks), continuous exposures were taken both in April 2007 (MWL I) and in November 2007 (MWL II). The latter was the first X–ray observation during the second optical flare of the source. Details of the exposures are reported in table 7.6.

| Campaign | Start | | End | | Eff. time | |
|---|---|---|---|---|---|---|
| | Day | Time (UT) | Day | Time (UT) | XIS (ks) | HXD (ks) |
| MWL I | April 10 | 19:47:00 | April 13 | 11:10:19 | 85.3 | 93.6 |
| MWL II | November 7 | 11:24:00 | November 9 | 21:30:23 | 102.6 | 102.9 |

Table 7.6: Summary of the Suzaku exposures for MWL I and MWL II. The total observed time available for the analysis after data quality checks is reported in the last two columns for the XIS and the HXD instruments respectively.

The analysis was performed by the *Suzaku* team, with the HEADAS 6.5.1 package. The data were selected based on some conditions, either observational such as the distance from the South Atlantic Anomaly (SAA) or the elevation of the source above the rim of the bright night Earth, either operational, such absence of telemetry saturation. Thereafter, events were again filtered with data quality cuts.

#### XIS detection, light curves and spectra

The XIS imaging spectrometer identified clearly the source in the 0.5–10 keV band at the position ($\alpha$, $\delta$) =($08^h54^m48^s.87$, $20°06'30''.6$).

The source was significantly brighter in MWL II than in MWL I. Both signal and background were integrated over $3'$ radius wide circles. The light curves in a soft (0.5–2 keV) and medium (2–10 keV) bands were produced for both MWL I and II. Flux was on average steady in MWL I, and constantly decreasing of 30% in the first half of MWL II, in both bands. No variation in the hardness ratio was measured in each period, therefore no clear signal of spectral variation during each observation is detected; the ratio is actually higher in MWL II than in MWL I instead. Consequently, background–subtracted XIS spectra of OJ 287 for the whole MWL I and MWL II observations were produced. The spectra appear featureless, with no absorption or emission lines. These spectra were corrected for the absorption from Galactic HI regions, with column density $N_H < 2.56 \times 10^{20}$ cm$^{-2}$ (Kalberla et al., 2005). A fit with simple power law functions gave a photon index $\Gamma = 1.65 \pm 0.02$ for MWL I and of $\Gamma = 1.50 \pm 0.01$ for MWL II,

proving a spectral hardening during the optical flare. Even the flux density was increased of a factor $\sim 2$ in MWL II ($F = 404^{+6}_{-5}$ nJy) with respect to MWL I ($F = 215 \pm 5$ nJy), proving a high state in soft X-rays during the optical flare.

**HXD spectrum**

After accurate subtraction of the Non X–ray Background affecting (NXB) the HXD–PIN instrument and of the Cosmic X–ray Background (CXB), in MWL I no significant excess is seen in HXD. Instead, in MWL II a $5.0\sigma$ significant excess is detected in the 12–27 keV range. A count rate of $0.011 \pm 0.002$ cts s$^{-1}$ is measured, 35% lower than the extrapolation of the XIS power law spectrum up to these energies. This points to a spectral break between the XIS and HXD energy ranges.

## 7.5 Multiwavelength study

As shown in the multiwavelength light curves of OJ 287 (Figure 7.4, the optical flux of OJ 287 increased from below 3 mJy in $V$ band in 2007 April to above 7 mJy in 2007 September. The radio flux increased during the optical flare in MWL II.

From MWL I to MWL II, the flux in all the observed bands increased of a factor 2 (radio, soft X rays) or 3 (optical). The observed variability time scale in the optical was $T_{var} \sim 4$ days (Seta et al., 2009). No VHE signal was detected either in MWL I or in MWL II, while hard X–ray signal in the 12–27 keV energy range was observed in MWL II but not in MWL I.

One of the most interesting outcomes of the campaign is the soft X–ray spectral hardening associated to the flux brightening in the same band during MWL II. This is in contrast with previous soft X–ray observations of the first peak, where a spectral softening in X–rays was associated to X–ray brightening (Idesawa et al., 1997; Isobe et al., 2001).

This was interpreted as a consequence of the dominance of the IC component over the X–ray spectrum in the quiescent state. In this picture, the increase in the position of the synchrotron peak in the flaring state led to a contribution of the high energy tail of the synchrotron component to the X–ray flux thus softening the spectrum. Isobe with ASCA data of the first flare in 1994 successfully separated the X-ray spectrum in a soft component due to synchrotron and a hard one due to IC. Even the the XMM–Newton spectrum of the first optical flare in 2005 is well described by a concave broken power law; this also supports contribution from the soft component to the X–ray spectrum (Ciprini et al., 2008). To search for a similar contribution in the present *Suzaku*/XIS spectra, a steep power law spectrum, with $\Gamma = 2.62$ fixed to the best fit found by Isobe et al. (2001) for the 1994 first flare is added to the fit, leaving the normalization as a free parameter.

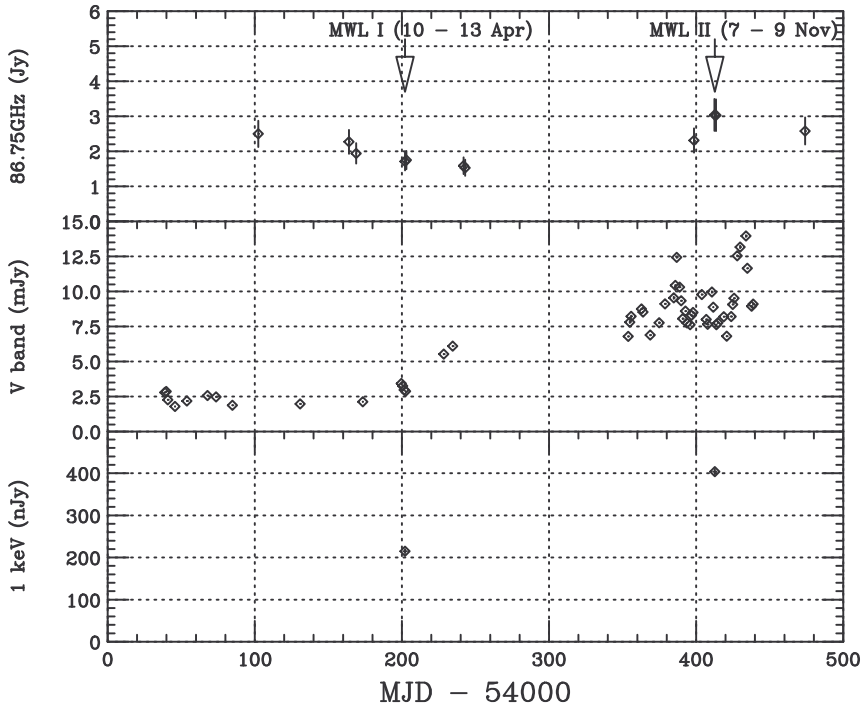


Figure 7.4: The multiwavelength light curves of OJ 287 during the 2007 campaign. Top panel: 86.75 GHz radio flux observed with NMA. Middle panel: optical $V$–band flux observed with KANATA. Bottom panel: X–ray flux density at 1 keV. The arrows indicate the time of the *Suzaku* observations in MWL I and MWL II.

In this two-component model fitting, the upper limit on the flux density at 1 keV for the additional soft spectrum is 8.7 nJy at the $3\sigma$ level, while the hard component remains consistent withe the best fit value found in the fit with simple power law. The upper limit on the flux ratio of the soft to the hard component at 1 keV is 0.022, to be compared to the $0.186 \pm 0.034$ found in the 1994 flare.

It can be stated therefore that, in contrast with the 1994 flare, negligible contribution to the X–ray spectrum comes from the synchrotron component, and the flux in the 0.5–10 keV band is dominated by the Inverse Compton bump.

### Source SSC modeling

In Figure 7.5 the broad band measurements of the SED of OJ 287 in MWL I (blue markers) and MWL II (red markers) are reported. Both the quiescent and the active state have been modeled; the expected SED are plotted with

continuous lines, cyan and magenta in color respectively.

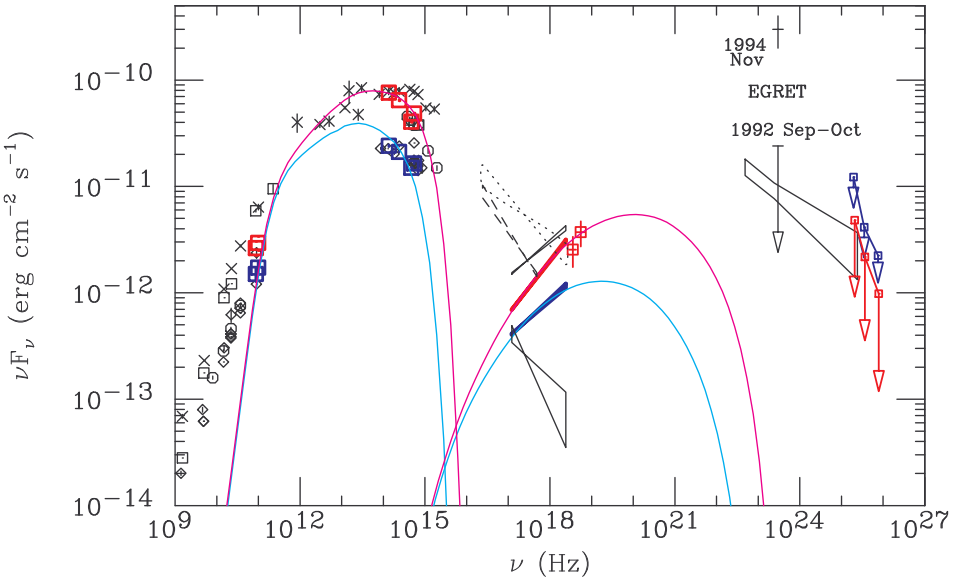


Figure 7.5: The SED of OJ 287 built with the data gathered during the 2007 multiwavelength campaign. Radio, Optical X–ray data and MAGIC upper limits are plotted; data from the April 2007 observations during quiescent state in blue, data from the 2007 December flare in red. Also some historical data are reported for reference; it is worth noticing the EGRET detection in Nov 1994 (Shrader et al., 1996), while in 1992 only an upper limit, at flux levels one decade below the 1994 detection, had been calculated from EGRET data.

The adopted model is the one–zone SSC code developed by Kataoka (2000). As a working hypothesis, it was assumed that the variation of the SED was caused by a change in the electron energy distribution, following e.g. Takahashi et al. (2000).

The electron number density spectrum was assumed to be a broken power law, as in Equation 3.3. The spectral index of electron spectrum $n$ below $\gamma_b$ was determined from the X–ray photon index as $n = (2\alpha - 1)$, obtaining $n = 2.3$ and $n = 2.0$ in MWL I and MWL II respectively.

Seven parameters were left free, to be determined from the fit to the data: the Doppler factor $\delta$. the electron energy density $K$, the magnetic field $B$, the blob radius $R$ and the minimum, break and maximum Lorentz factor of the electron distribution $\gamma_{min}$, $\gamma_b$ and $\gamma_{max}$.

For the Doppler factor a $\delta = 15$ value was assumed, typical of LBLs (see e.g. Ghisellini et al., 1998). The optical variability time scale ($T_{var} \sim 4$ days) could be used to constrain the blob radius $R$:

| Parameters | MWL I | MWL II |
|---|---|---|
| $\delta$ | 15 | |
| $R$ [cm] | $7.0 \times 10^{16}$ | |
| $B$ [G] | 0.71 | |
| $\gamma_{min}$ | 70 | |
| $\gamma_b$ | 700 | |
| $\gamma_{max}$ | 3300 | 4500 |
| $p$ | 2.3 | 2.0 |
| $u_e$ (erg cm$^{-3}$) | $1.5 \times 10^{-3}$ | $2.1 \times 10^{-3}$ |

Table 7.7: List of the parameters used in the modeling of the SED of OJ 287 as observed in MWL I and MWL II. The parameters (described in the text) were derived in the working hypothesis of explaining the different SED with a variation in the electron energy distribution.

$$R < c\frac{\delta}{1+z}T_{var} \simeq 1.2 \times 10^{17}(\frac{T_{var}}{4\,\mathrm{d}})(\frac{\delta}{15})\,\mathrm{cm} \tag{7.2}$$

The derived model parameters are listed in table 7.7. The evolution of the SED has been therefore interpreted as arising from an increase in the electro energy density during the flare.

It must be noted that in 2008 *Fermi*/LAT detected in $\gamma$ rays OJ 287, already in its quiescent state. The measured spectrum is reported in Figure 7.5 (black bow tie). This measurement significantly exceeds the $\gamma$–ray flux foreseen in the presented SSC model. This could be explained by means of a significant contribution of External Compton radiation, produced by electrons at the break frequency ($\sim 10^{22}$ Hz) scattering seed soft photons of frequency $\nu_{seed} \simeq 10^{14}$ Hz (Seta et al., 2009). Multi–wavelength broadband simultaneous observations could confirm this further hypothesis.

## 7.6 Physical interpretation of results

In the multiwavelength observation of both the quiescent and optical flaring state of OJ 287, the SED of the source is clearly *blazar*–like (see Figure 7.5), with synchrotron and Inverse Compton bump. The X–ray spectrum appears to be dominated by the Inverse Compton process, with marginal to none contribution fron synchrotron. The frequency of the synchrotron peak and the position of the cut off of its high energy tail appears to be the same in both states (Seta et al., 2009; Hayashida et al., 2009). All these feaures of the spectral behaviour are rather different from the ones reported in the first flare of November 2005, therefore pointing to a different mechanism in the source in the two optical flares. This is compatible with the interpretation (Valtaoja et al., 2000) assuming for the first optical flare

a thermal origin related to the central engine, and instead for the second outburst a non–thermal origin related to the jet and more likely producing $\gamma$ rays.

Even if in the 2007 campaign OJ 287 didn't show any measurable VHE emission, nevertheless according to many extrapolations from SSC models it is expected to be a TeV emitter, at weak flux levels but still in reach of the present generation of Cherenkov Stereo Systems (Liang & Jin-Ming, 2010). Therefore there are hopes that the MAGIC stereo system will be able to detect the source, owing to its improved performance with respect to MAGIC–I.

# Chapter 8

# The HBL *blazar* Mrk 421

Mrk 421 is a High–Peaked *blazar* (HBL) source in the Northern Sky, located within the *Ursa Maior* region. The equatorial ($J2000$) coordinates of the source are ($\alpha$, $\delta$) =($11^h4^m27.3^s$, $+38°12'31.8''$).

The name comes from the inclusion of the source in the catalog of Markarian objects (Petrosian et al., 2007). The catalogue in turn takes his name from the Armenian astronomer Benjamin Markarian (1913–1985) who worked since 1964 to the first list of these sources, comprising "*70 faint mainly spheroidal galaxies with early–type spectra, with abnormal spectra and abnormal colors in the central region*"(Markarian, 1967).

The selection criterion of the Markaryan sample was actually based on the brightness of the UV continuum emission, that was observed by means of objective prism spectroscopy. Noteworthily, 3 out of the 44 extragalactic VHE sources discovered until 2010 October are included in this sample, now counting 1544 sources. Apart from Mrk 421, also Mrk 501 (at z=0.034, discovered by Whipple Quinn et al. 1996) and the Mrk 180 discovered by MAGIC ($z = 0.045$, Albert et al. 2006). All belong to the HBL class, and Mrk 421 and Mrk 501 happen to be amongst the most bright and variable sources of the TeV sky.

## 8.1 Source overview

Mrk 421, is one of the closest ($z = 0.031$, de Vaucoleurs et al. 1991) and brightest extragalactic TeV sources; therefore the first detected (by Whipple, Punch et al., 1992) and one of the best studied. The VHE integral flux can vary from a few tenths to a few Crab Units (e.g., see Donnarumma et al. 2009; Hsu et al. 2009 or Pichel 2009), on time scales as short as 15 minutes (Gaidos et al., 1996). The $\nu F(\nu)$ distribution of the emitted photons follows the standard "double-bumped" shape, but varies significantly from low activity states to the most intense flares, on time scales that in X–rays can be of few hours (Ushio et al., 2009). The low-energy bump peaks in the

$0.1 - 10$ keV range ( see e.g. Fossati et al. 2008), as usual for HBLs; the maximum of the high energy bump is usually found below 100 GeV, but can as well move around according to the state of the source (Albert et al., 2007b).

This peculiar SED shape favors multi–wavelength studies that exploit the MAGIC sensitivity and low energy threshold at VHE combined with soft X–ray telescopes. In particular, the All–Sky Monitor (ASM) onboard the *Rossi X–ray Timing Explorer* (RXTE) can provide continuously a daily-averaged flux, while the *X–Ray Telescope* (XRT) onboard the *Swift* satellite can observe the source with far better precision and energy resolution in $\sim$ 1 ks targeted exposures. From the observation of the source spectrum in both X–ray and VHE an unique set of physical parameters that describe the source can be derived within the single–zone Synchrotron Self–Compton developed in Tavecchio et al. (1998) and briefly outlined in Section 3.5. Historically, this has been already done in the past (see e.g. Bednarek & Protheroe 1997, the same Tavecchio et al. 1998 or the more recent Fossati et al. 2008) but often the available data were not properly simultaneous, mainly because the coordination of ground-based and satellite instruments, that intrinsically cope with different overheads and schedule constraints, and work on different time scales, is a really tough task. The lack of simultaneity weakens the result for such a variable source, as possibly the two instruments have sampled different states and the spectra are not closely related to each other. Even more difficult is to observe in tight simultaneity during high states, as these are quite unpredictable in raise and duration, and, being intrinsically unsteady, call even more strongly for close simultaneity. In the case of Maraschi et al. (1999), a properly simultaneous multiwavelength observation of a flaring state of Mrk 421 was obtained, but the high threshold of the Whipple telescope (500 GeV in that observation) did not allow sampling of the IC bump close to the peak.

It must be recalled that alternative hadronic models, such as the synchrotron proton model (Mücke et al. 2003; see also Section 3.3.1) are not ruled out in this source, due to the relatively lower density of external photon fields necessary for processes such as pion photoproduction to be effective. On the contrary, a higher level of tuning is necessary to account for the highly correlated variability at X–ray and TeV energies. Amongst leptonic model, EC processes can be assumed depressed in Mrk 421 as the ratio of thermal ( i.e. produced from accretion disk or lines) to synchrotron can be constrained below the 10 % level. Multiwavelength observations in the past have been mainly devoted to month long time scales (Błażejowski et al., 2005; Rebillot et al., 2006), with rather sparse time sampling. A more dense coverage was obtained in March 2001 with Hegra, Whipple and RXTE (Fossati et al., 2008) confirming a rather tight correlation between X–ray and $\gamma$–ray flux variations. Moreover, it was pointed out that no interband lag could be evidentiated, even if the timing of the record burst was *not* consis-

tent with the simultaneity of the two bands ($\Delta T = 2.1 \pm 0.7$ ks) with the TeV peak delayed w.r.t. the one in X rays. Also, it was pointed out that the correlation is linear in the amplitudes, except for the higher isolated peaks, where $\gamma$–ray flux scaled quadratically with respect to the X–ray flux.

## 8.2 Early observations with MAGIC

Already since MAGIC commissioning phase, many observations have been devoted to Mrk 421, as its brightness and its variability make it one of the best candidate sources for precise spectrum calculation and sub–hour scale, time resolved light curves. Moreover, this specific source seems characterized by a rather dense duty cycle (even if it could be due to an observational bias related to its brightness); this intense activity grants promising chances of catching interesting transient phenomena, potentially casting forward our understanding of the mechanisms at work into its relativistic jet. The position of Markarian 421 in the sky limits the potential observational window from the MAGIC telescope site: the source is observable since early December to mid June. This is balanced from the benefit that the source, can be observed at very small zenith angle ($\approx 10^\circ$ at culmination, see Figure 8.5.2) allowing for the lowest possible energy threshold at both trigger and analysis level.

The first observations of Mrk 421 with MAGIC Telescope (Albert et al., 2007b) started shortly after the end of the commissioning phase of the instrument. Data were taken between November 2004 and April 2005, with various hardware setups.

The vast majority of observations were conducted at low Zenith Angle ($ZA \leq 30^\circ$) to achieve the lowest possible energy threshold. The total observing time was of $\sim 29$ h, that were reduced to 25.6 h after rejection of runs affected by hardware problems or unusual trigger rates, possibly due to bad weather or inconsistent telescope performance.

The integrated excess during this early observation time amounted to 700 events, significant at 49 $\sigma$ level according to Li&Ma formula (Li & Ma, 1983). The reconstructed source position from the $\gamma$–ray sky map was RA $= +11h4'19''$ DEC $= 38°11'41''$, with uncertainty dominated by systematic errors of the pointing, estimated as $2'$. The observed extension of Mrk 421 was compatible with the expectation for a point source as reproduced with Monte Carlo simulations (see Figure 8.2, right panel).

## 8.3 Observations of Mrk 421 during MAGIC Cycle III

During MAGIC Cycle III (spanning the June '07 – June '08 period) many datasets have been acquired on this source all along its observability window,

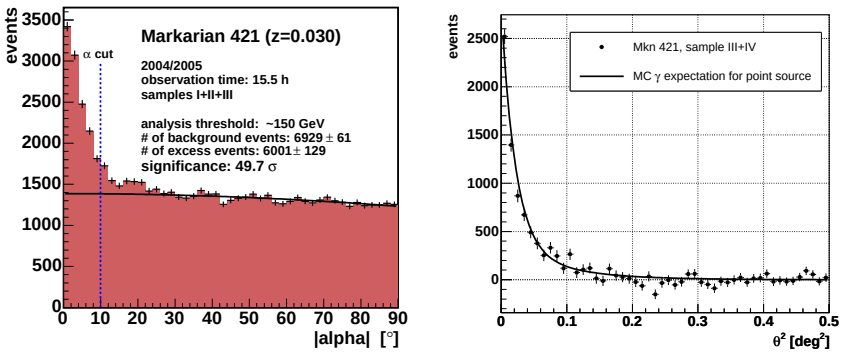


Figure 8.1: Plot of excesses agains isotropic background during Mrk 421 observations in Cycle 1. The dataset is split in two subsamples, due to different (On–Off and Wobble) observation modes. alpha–plot for the On–Off sample (left panel) and $\Theta^2$–plot (right panel) are displayed. In the right panel, the $\Theta^2$ distribution of excesses from a simulated point source is plotted for comparison. From Albert et al. (2007b)

in force of different approved proposals.

### Twilight monitoring program

MAGIC has followed a program of *twilight monitoring* of bright *blazars* (namely the HBLs Mrk 421, Mrk 501 and 1ES 1959+650) that involved routinely, untriggered snapshot observations of these sources both at sunset and sunrise.

This strategy aims to exploit either the peculiar capability of MAGIC of extending observations to partly light–polluted time windows, either the brightness of these peculiar sources, that allows MAGIC to perform a flux measurement and a rough but still significant spectral measurement within 15–20 minutes, even in such, sub–optimal observing conditions.

These observations constitute an interesting dataset by themselves, allowing for unbiased sampling of the source activity, useful for estimation of the flaring duty cycle and for the search of a possible low brightness, steady contribution to the VHE flux. Moreover, the possibility of calculation of a spectral slope, allows for interesting statistical MWL studies such as the ones reported in Satalecka et al. (2009), in spite of the low cost in terms of the valuable telescope dark time.

But the monitoring performed at sunset is also a powerful strategic tool for triggering Target of Opportunity (ToO) observations, owing to the availability since fall 2007 of the Online Analysis (see Section 6.14), a very useful automated software performing a very preliminary fast analysis whitin few

minutes after the actual acquisition. This tool applies rather blindly very standard cuts, but anyway gives important "quick and dirty" informations, to be perhaps checked later. In this context, if the source shows significant activity MAGIC observations may be extended in the night, overriding the planned schedule, provided that:

- The source is within the usual astronomical observability limits, and the conditions remain potentially fruitful (e.g source elevation within Zenith Angle $< 45°$
- No observation of higher priority (e.g. GRB alerts) is scheduled (see Section5.5.2)
- the ToO proposal has not exhausted its allocated telescope time[1];
- The PI of the observation explicitly asks for ToO extended observation, based on the expectation of the scientific outcome.

Sometimes it can happen that two or more sources, observable in the same time slots, are eligible for ToO observations at the same time. This is a complex situation, usually solved by the Time Allocation Committee.

### 8.3.1 Mrk 421 multiwavelength ToO program

Mrk 421 was also one of the most promising target of the ToO program of MAGIC, aiming to observe a list of sources following either the internal triggers coming from the aforementioned monitoring, either triggers coming from other instruments/observatories, active in the optical, radio or soft X–ray band.

#### Optical telescopes: KVA

MAGIC has continuous mutual feedback with the KVA optical telescope. This is a fully automated 35 cm reflector also located in the Roque de los Muchachos Observatory. The telescope is managed by the Finnish group of the Tuorla Observatory, that also make use of a larger (100 cm) telescope that is situated in Tuorla ($\approx$ 35 m a.s.l.), and therefore suffers from much worse sky quality. This exchange of mutual triggers has allowed important discoveries (Albert et al., 2006, 2007d) of previously unestablished VHE sources, that have been observed by MAGIC because of consistent (50%) optical flux enhancement observed by KVA.

On the other hand, KVA can easily follow MAGIC schedule, as:

[1]Director Discretionary Time (DDT) can be granted by the Spokesperson of the MAGIC Collaboration in case of very promising, extraordinary conditions.

- being located at the same observatory, it observes the same sky and under the same weather conditions;
- moreover, optical photometry requires shorter exposure times than those usually needed for TeV sources.

This grants systematic optical coverage for the sources observed by MAGIC, either scheduled at fixed time either promptly observed as ToOs.

#### X–ray telescopes

In fall 2007, MAGIC negotiated with the *Swift* team a plan of joined follow–up of active states of Mrk 421. In case of request from MAGIC, *Swift* would have allocated some targeted exposures with the XRT and UVOT telescopes, trying to match the observablilty constraints of MAGIC and informing the MAGIC contact person about the allocated time windows, so that a properly matching schedule could be prepared by MAGIC. A similar agreement was negotiated with RXTE, even if this other instruments lacks the rapid movement that is peculiar of *Swift*, and consequently follows more rigid schedules, privileging fewer, longer exposures with respect to *Swift*.

#### Other Cherenkov telescopes

MAGIC, VERITAS and HESS have an ongoing agreement regarding the exchange of prompt informations on flaring sources. This agreement has been activated various times along the past years. In particular, VERITAS and MAGIC are located at similar Northern latitudes, but separated in longitude by $\sim 8$ hours; this means that they can observe the same sources, but extending the total dark time available each night. MAGIC and HESS instead roughly share the longitude, but are separated from $\sim 60^\circ$ in latitude, with HESS located in the Southern emisphere. This allows simultaneous obervations of sources next to the celestial equator, that culminate at high elevations for both telescopes (Mazin & et al., 2005).

## 8.4 Overview of MAGIC data

All the observations of Mrk 421 considered here were made in Wobble mode, targeting two opposite positions in the sky and with the standard $0.4^\circ$ offset from the nominal position of the source. This was intended to ensure a robust background estimation from the dataset itself and the uninterrupted follow–up of the source (see Section 5.5.5).

### 8.4.1 Data taken in December–January

All along December 2007 Mrk 421 was observed as planned in the proposal regarding MAGIC monitoring of bright *blazars*. The Online Analy-

sis revealed a flux enhancement ($F \simeq 2$ C.U.) on 1 January 2008 ("Mrk 421 New Year's gift") that triggered some ToO proposals: the MAGIC–HESS–VERITAS agreement, and the MWL observation plan with *Swift* and RXTE. *Swift*/XRT covered along January some MAGIC time slots[2].

### 8.4.2 Data taken in February

Even in February in some nights the flux level of Mrk 421 triggered the conditions for extension of observations. A very high flux ($\sim 2.6$ C.U. above 200 GeV) )was detected on February the 6th, and followed continuously for $\sim 4$ hours.

### 8.4.3 April Flare

At the end of March the Online Analysis revealed a high state at VHE ($\sim 2$ C.U.) in MAGIC–I data acquired under the twilight monitoring program. Simultaneously, Mrk 421 was detected in high state by the *Burst Alert Telescope*(BAT) onboard of *Swift*, on the level of 0.05 Crab Units. This triggered both extended observations with MAGIC and targeted observations with *Swift*/XRT (*X–Ray Telescope*) during the following $\sim 10$ days. Unfortunately, the main MAGIC–I observation (2 hour long starting March the 30th around 21.00 UT) had no X–ray counterpart, as *Swift*/XRT observed the source only 14 hours later, on March the 31th around 13.00 UT. Some interesting consequences of this will be discussed in Section 8.14.1

### 8.4.4 May and June data

At the end of May, and in early June, another flaring episode was jointly followed by MAGIC, VERITAS and ohter instruments; the concerned MWL study was published on short notice (Donnarumma et al., 2009).

## 8.5 Analysis of the MAGIC data

In the following section, I summarize the relevant steps of the analysis that I performed on the whole MAGIC Cycle III data sample on Mrk 421. This analysis was cross–checked independently by Dr. Ching–Cheng Hsu.

### 8.5.1 Calibration and Image Cleaning

The starting point were the data stored in the MAGIC database located at PIC. The data were already calibrated, with application of the standard method in use for the MUX readout system (see section 6.4) and the default integration time of 7.5 ns (15 time slices). In order to exploit the improved

[2]Even VERITAS time slots were covered by *Swift*

sensitivity allowed by the availability of timing information, standard time cleaned (see section 6.5.2) data were chosen.

#### Sample of simulated $\gamma$-ray events

Along the whole observation period, the optical PSF of the telescope fluctuated around 10 mm (see Figure C.1); therefore for the analysis was selected a sample of MC simulated $\gamma$–ray events that had been produced assuming a PSF= 10.6 mm. The MC data covered the whole ZA range of the data and were simulated assuming a standard Wobble observation with 0.40° offset. The calibration and image cleaning applied were the same of the real dataset.

In addition to the simulated $\gamma$–ray sample generated with standard spectrum (photon index $\Gamma = -2.6$, see Table 6.1), also the HE sample (photon index $\Gamma = -1$) was involved in this analysis, in order to enrich the simulated $\gamma$–ray sample at high energy, where Mrk 421 is a well known emitter. Above 1 TeV this favors both a better energy estimation and a better calculation of the collection area, improving the accuracy of the spectrum calculation.

### 8.5.2 Data selection

#### Selection of the dark subsample

This analysis was done using data taken in dark conditions, because of a better control of systematics, since the treatment of light–polluted data is still not perfectly established, as no "Moon" MC simulated events are available.

The data are classified as Moon, No–Moon and Twilight depending on the astronomical times of rise and set of the Sun and Moon. Nevertheless, especially when the fraction of illuminated moon is low, conditions can be compatible with dark ones. Therefore data have also been checked for average level of Discriminator Thresholds (DT) and average value of Direct Current (DC):.

- DT $< 20$ A.U.
- DC $\lesssim 1.5$ $\mu$A

#### Quality of the observations

Information on data quality was gathered from:

- the nightly logbook of observations compiled by the shifters, that keeps track of weather evolution during the night, problems of telescope hardware, possible accidental light flashes from cars passing by or from the lasers fired by optical telescopes when testing or using adaptive optics.

- Level 1 trigger rates
- Number of recognized stars in the starguider camera FOV
- Cloudiness level reported by the pyrometer

To be included in the analysis, data had to fulfill these conditions:

- No patent hardware or weather inconvenience reported in the runbook
- Level 1 average trigger rates above 180 Hz and below 350 Hz
- Pyrometer cloudiness below 50%

**Zenith Angle of the observations**

The distribution in zenith angle of the complete sample is wide, as plotted in figure 8.5.2. A preliminary cut at ZA $< 46^{\circ}$ was applied, removing a negligibly small fraction of data, almost wholly constituted by ending tails of long exposures. These data would have required a completely independent analysis, in force of the mean ZA, significantly higher than the one of the remaining dataset. As a matter of fact, MAGIC observations at low ZA are for clear reasons privileged, and real hadronic events compatible with high ZA observations are quite rare. Therefore this dataset would have required a much more difficult analysis in spite of its expected modest relevancy and was simply dropped.

### 8.5.3 Filter cuts

The filter cuts applied to the dataset were:

- SIZE $< 80$ phe
- Standard *spark* cut (see 6.6.4)
- LEAKAGE $> 0.05 \cdot (3 + (0.5 \cdot \log(\text{SIZE})))$
- Number of core pixels $< 3$
- Number of islands $> 3$

The events fulfilling one or more of the cut conditions were excluded from the analysis.

The SIZE–dependent LEAKAGE cut, excluding events with LEAKAGE $>$ 0.2 at SIZE $= 100$ and with LEAKAGE $> 0.3$ at SIZE $= 10^6$, was intended to increase the statistics at high energies. Being the only non–standard cut applied, it was checked in the control analysis performed on Crab Nebula data (see Appendix A).

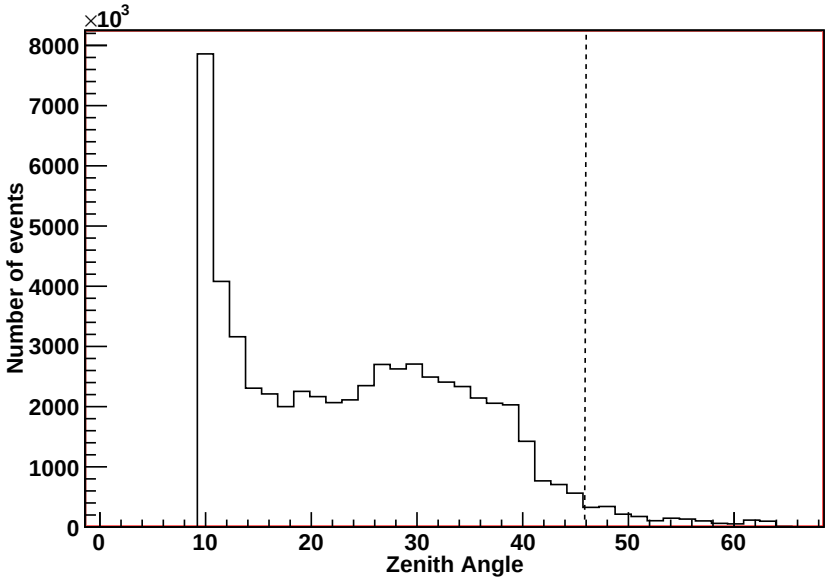


Figure 8.2: Zenith Angle distribution for the Mrk 421 event set, after exclusion of bad quality runs.

### 8.5.4 The full final dataset

Table 8.1 reports the surviving dataset analyzed. For each observation night (labeled with the civil date of the following morning), the timespan of the observation is reported, and the effective time of observation calculated from the `fluxlc` tool according to Section 6.11.

| Data Time Label | Obs. Start (U.T.) | Obs. End (U.T.) | Eff. On Time ($s$) |
|---|---|---|---|
| 20071201 | 01.12.2007 04:42 | 01.12.2007 04:43 | 43 |
| 20071202 | 02.12.2007 04:02 | 02.12.2007 04:51 | 2766 |
| 20071203 | 03.12.2007 03:53 | 03.12.2007 05:13 | 4589 |
| 20071204 | 04.12.2007 03:48 | 04.12.2007 06:49 | 6282 |
| 20071205 | 05.12.2007 04:10 | 05.12.2007 05:37 | 4995 |
| 20071207 | 07.12.2007 04:40 | 07.12.2007 05:56 | 4394 |
| 20071208 | 08.12.2007 05:06 | 08.12.2007 06:51 | 3307 |
| 20071209 | 09.12.2007 04:58 | 09.12.2007 06:51 | 3340 |
| 20071210 | 10.12.2007 05:00 | 10.12.2007 05:38 | 2257 |
| 20071211 | 11.12.2007 06:37 | 11.12.2007 06:53 | 880 |
| 20071212 | 12.12.2007 06:39 | 12.12.2007 06:55 | 887 |
| 20071213 | 13.12.2007 06:39 | 13.12.2007 06:54 | 838 |
| 20071214 | 14.12.2007 06:37 | 14.12.2007 06:56 | 1066 |

| | | | |
|---|---|---|---|
| 20071215 | 15.12.2007 06:38 | 15.12.2007 06:55 | 998 |
| 20071216 | 16.12.2007 06:39 | 16.12.2007 06:57 | 1052 |
| 20071217 | 17.12.2007 06:38 | 17.12.2007 06:56 | 1002 |
| 20071231 | 31.12.2007 02:04 | 31.12.2007 07:00 | 16609 |
| 20080101 | 01.01.2008 02:01 | 01.01.2008 07:00 | 17007 |
| 20080102 | 02.01.2008 02:57 | 02.01.2008 07:00 | 13899 |
| 20080103 | 03.01.2008 02:17 | 03.01.2008 02:40 | 1293 |
| 20080104 | 04.01.2008 02:15 | 04.01.2008 04:46 | 8511 |
| 20080105 | 05.01.2008 02:12 | 05.01.2008 03:53 | 5795 |
| 20080106 | 06.01.2008 02:05 | 06.01.2008 02:39 | 1877 |
| 20080107 | 07.01.2008 02:01 | 07.01.2008 05:56 | 6848 |
| 20080108 | 08.01.2008 01:58 | 08.01.2008 05:57 | 9273 |
| 20080109 | 09.01.2008 01:53 | 09.01.2008 06:43 | 11556 |
| 20080110 | 10.01.2008 02:23 | 10.01.2008 07:04 | 5163 |
| 20080111 | 11.01.2008 05:11 | 11.01.2008 06:17 | 2127 |
| 20080113 | 13.01.2008 05:14 | 13.01.2008 07:03 | 3740 |
| 20080114 | 14.01.2008 04:50 | 14.01.2008 05:26 | 2095 |
| 20080115 | 15.01.2008 01:33 | 15.01.2008 06:59 | 5066 |
| 20080116 | 16.01.2008 00:58 | 16.01.2008 07:03 | 12406 |
| 20080117 | 17.01.2008 03:26 | 17.01.2008 07:03 | 6563 |
| 20080118 | 18.01.2008 04:52 | 18.01.2008 07:04 | 4057 |
| 20080119 | 19.01.2008 05:17 | 19.01.2008 07:03 | 3341 |
| 20080129 | 29.01.2008 00:37 | 29.01.2008 01:46 | 4016 |
| 20080202 | 02.02.2008 00:18 | 02.02.2008 00:57 | 2259 |
| 20080204 | 04.02.2008 00:58 | 04.02.2008 01:37 | 2268 |
| 20080205 | 05.02.2008 00:29 | 05.02.2008 01:08 | 2275 |
| 20080206 | 06.02.2008 00:25 | 06.02.2008 04:18 | 13369 |
| 20080208 | 08.02.2008 00:18 | 08.02.2008 05:30 | 2276 |
| 20080211 | 11.02.2008 01:22 | 11.02.2008 03:58 | 2850 |
| 20080301 | 29.02.2008 22:50 | 29.02.2008 23:02 | 733 |
| 20080302 | 01.03.2008 22:30 | 01.03.2008 23:00 | 1735 |
| 20080305 | 04.03.2008 23:30 | 05.03.2008 00:05 | 1626 |
| 20080308 | 07.03.2008 23:18 | 07.03.2008 23:55 | 2147 |
| 20080311 | 10.03.2008 20:29 | 10.03.2008 22:26 | 3645 |
| 20080312 | 11.03.2008 20:25 | 11.03.2008 23:34 | 7511 |
| 20080313 | 12.03.2008 20:43 | 12.03.2008 23:07 | 6356 |
| 20080329 | 28.03.2008 20:28 | 28.03.2008 22:15 | 832 |
| 20080330 | 29.03.2008 20:35 | 29.03.2008 20:42 | 388 |
| 20080331 | 30.03.2008 20:30 | 30.03.2008 22:48 | 7897 |
| 20080401 | 01.04.2008 01:20 | 01.04.2008 01:27 | 407 |
| 20080402 | 01.04.2008 20:32 | 02.04.2008 01:00 | 1427 |
| 20080403 | 02.04.2008 20:35 | 03.04.2008 01:10 | 2225 |
| 20080404 | 03.04.2008 20:48 | 04.04.2008 01:08 | 2990 |
| 20080405 | 04.04.2008 20:36 | 05.04.2008 01:12 | 1328 |

| | | | |
|---|---|---|---|
| 20080406 | 05.04.2008 20:36 | 05.04.2008 23:54 | 1981 |
| 20080412 | 12.04.2008 01:40 | 12.04.2008 01:56 | 927 |
| 20080504 | 03.05.2008 20:51 | 03.05.2008 22:43 | 2840 |
| 20080505 | 04.05.2008 20:56 | 05.05.2008 00:06 | 4662 |

Table 8.1: Complete set of data from Mrk 421 observations during MAGIC CycleIII. Only data from low sky brightness time windows are considered here. For each night are reported: the time label that identifies the data files, the UT of the start and end of the Mrk 421 time window (eventually interleaved by other observations), the effective time $t_{eff}$ of the observation.

## 8.6 $\gamma$/hadron discrimination

The background discrimination was performed with the standard Random Forest method summarized in Section 6.7.2. The case of Mrk 421 is actually different from the one of OJ 287, as the source is presumably bright, so the dataset itself should be considered a sample of hadrons of questionable purity. Therefore, I browsed extensively the data archive, spanning the epoch of observations, and gathered a few samples of data, acquired in observations of potential, but not yet established sources. Some of these datasets had been already analyzed, showing no signal; other could be expected at most weak emitters (on levels below 10% the Crab Nebula) according to previous observations. This allowed to consider those observation as a trustable sample of pure hadron events. These sets had to be acquired in dark conditions, in wobble mode and with standard settings. Moreover, they had to span the whole $10^\circ < \mathrm{ZA} < 45^\circ$ range of the Mrk 421 dataset itself. This ancillary dataset was subjected to the same quality filtering of the dataset of interest. Moreover the Resizing and Rezenithing procedures were applied. Especially the latter was needed here, as the dataset spanned a large ZA range.

### 8.6.1 Choice of the parameters for the $\gamma$/hadron discrimination

For the $\gamma$–hadron separation the following image parameters were included in the decision process:

1. Size (not directly discriminant, due to Resizing of the hadron sample)
2. Zenith Agle(not directly discriminant, due to Rezenithing of the hadron sample)

3. Width
4. Length
5. Size/Width×Lenght
6. Conc
7. Dist
8. M3Long
9. RMSTime
10. Time Gradient

Figure 8.3 displays the "Gini plot" of this classification. The discriminating power is low as expected for Size and Zenith Angle, high for Width and Length. It is also very high for the source dependent parameter Dist; much of the advantage of the source dependent approach relies on it.

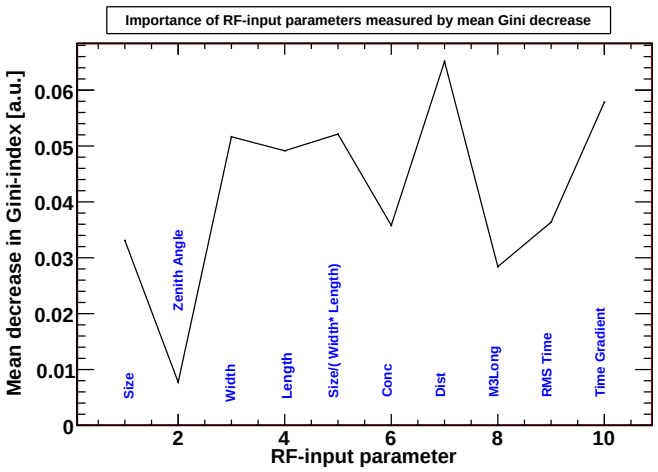


Figure 8.3: The "Gini plot", summarizing the discriminating power of the parameters involved in the Random Forest classification method applied for the analysis of Mrk 421 data.

## 8.7 Random Forest classification for the estimated energy of photons

For the $\gamma$–hadron separation the following image parameters were used as discriminants:

1. Size
2. Zenith Agle
3. Width
4. Lenght
5. Size/Width×Lenght
6. Conc
7. M3Long
8. RMSTime

In Figure 8.4 the precision of the estimation can be evaluated on the sample of Monte Carlo simulated $\gamma$–ray events. The classification method has been optimized on the minimal dispersion of the Estimated energy around the True energy of the events.

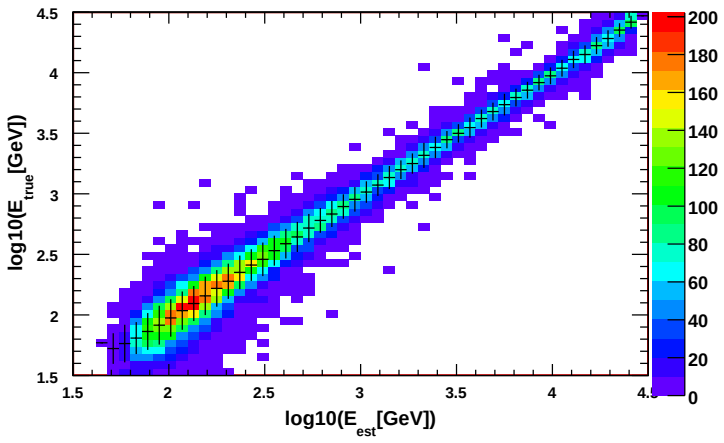


Figure 8.4: The plot displays the two–dimensional distribution of simulated $\gamma$–ray events in the Estimated vs. True energy plane.

### 8.7.1 Calculation of Hadronness and Estimated Energy for the real data

Subsequently, the classification matrices produced with the Random Forest algorithm have been applied to the data by means of the `melibea` tool included in the MARS package. For each event of the Mrk 421 dataset the value of the Hadronness and Estimated Energy parameters have been

calculated. The same procedure has been applied to the Crab Nebula sample used for checking the analysis, and to the Monte Carlo sample needed for the calculation of the effective area.

## 8.8 Excesses and fluxes

Differently from the case of OJ 287, which is not a known TeV emitter, Mrk 421 is a well known, bright source of VHE $\gamma$ rays. Therefore, there was no need in this case to optimize very selective cuts aiming to obtain a detection, that in this case is rather obvious even in few minutes of data.

The `fluxlc` sofware from the MARS package has then been used, in order to calculate

- fluxes in bin of estimated energy
- integral fluxes, either averaged on the observations of each night, either time resolved to the scale of few minutes.

The software works in bins of Estimated Energy that in this case have been chosen as 30 logarithmically evenly spaced bins between 5 and 500000 GeV The Alpha parameter has been used for signal extraction. The cuts in both the Alpha and the Hadronness parameters have been set from the efficiency on the MC $\gamma$–ray simulated events, imposing that 80 % of the events had to survive each cut. A Size excluding events with less than 150 phe of total charge have been also applied. Apart from signal extraction, `fluxlc` also calculates the effective time of the observation from the dataset itself, and the collection area of the telescope from the dedicated sample of simulated events.

## 8.9 VHE light curves

### 8.9.1 Night–averaged fluxes

The night–averaged integral flux above a conservative threshold of 200 GeV was calculated for each of the 66 nights with datasets surviving the quality cuts. The VHE light curve of Mrk 421 along the campaign is plotted in the top panel of figure 8.12. It's worth noticing that even if Mrk 421 is believed to emit a low VHE flux baseline (Schubnell et al., 1996), the flux was seldom below the Crab Unit (C.U. hereafter) level ($F_{E>200\,\mathrm{GeV}} = 1.96 \pm 0.05_{stat} \times 10^{-10}\mathrm{cm}^{-2}\mathrm{s}^{-1}$ , Albert et al. 2008a) all along the period, confirming an intense and persistent active state. The maximum observed flux ($F_{E>200\,\mathrm{GeV}} = 6.99 \pm 0.15_{stat} \times 10^{-10}\mathrm{cm}^{-2}\mathrm{s}^{-1}$) was on March 2008, the 30th.

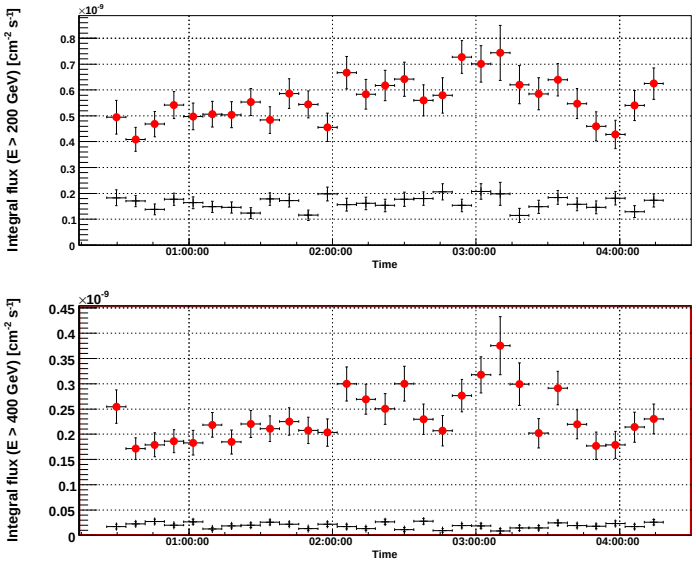


Figure 8.5: Mrk 421 VHE light curves in 8 min. time bins, from the observations taken on 2008, February the 6th. Integral flux of excess (filled circles) and background (thin crosses) events is plotted. The energy threshold is 200 GeV (upper panel) and 400 GeV (lower panel).

### 8.9.2 Time resolved VHE light curves

Due to the intrinsic VHE brightness and to the occurring active state, Mrk 421 could be detected by MAGIC–I on short timescales. This can be of the utmost interest, as the variability timescale of *blazars* decreases with increasing energy, and rapid flares can be detected, such as already happened for Mrk 421 itself (Gaidos et al., 1996)

In particular, on February the 2nd and March the 30th long ($\sim 4$ and $\sim 2$ hours respectively) and continuous observations of very high flux states could be performed, under good and stable weather conditions. Light curves in 8 min. time bins are shown for these nights (Figures 8.5 and 8.6 respectively, with a softer ($E > 200\,\mathrm{GeV}$, upper panels) and harder ($E > 400\,\mathrm{GeV}$, lower panels) energy threshold. Flux variability with doubling/halving times down to $\sim 16$ min can be seen in the first night, while in the second night no rapid evolution is visible. This is in agreement with the $\chi^2$ test performed on a linear fit to the data: in the case of February the 2nd the fit is not adequate, while in the other it is, showing that points do not over–fluctuate around the average. The fit parameters and results of the $\chi^2$ test are reported in Table 8.2.

The determination of the variability time scale is of the utmost interest for the modeling of the SED, as will be discussed in Section 8.13.1.

At higher energy the signal has higher significance, essentially due to

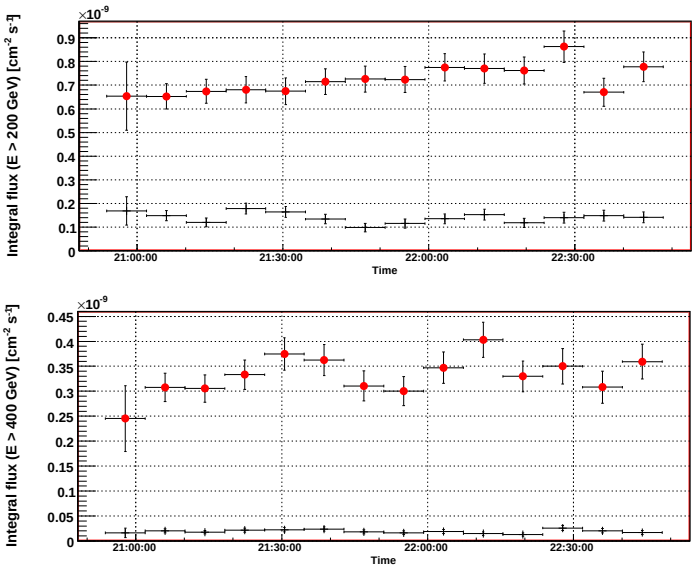


Figure 8.6: Mrk 421 VHE light curves in 8 min. time bins, from the observations taken on 2008, March the 30th. Integral flux of excess (filled circles) and background (thin crosses) events is plotted. The Energy threshold is 200 GeV (upper panel) and 400 GeV (lower panel).

| Day yyyymmdd | $E_{min}$ GeV | $p_0[\cdot 10^{-10}]$ $\mathrm{cm}^{-2}\mathrm{s}^{-1}$ | $\Delta p_0[\cdot 10^{-10}]$ $\mathrm{cm}^{-2}\mathrm{s}^{-1}$ | $\chi^2/ndf$ |
|---|---|---|---|---|
| 20080206 | 200 | 5.4 | 0.1 | 55/28 |
| 20080206 | 400 | 2.20 | 0.05 | 63/28 |
| 20080330 | 200 | 7.2 | 0.16 | 12/13 |
| 20080330 | 400 | 3.3 | 0.09 | 13/13 |

Table 8.2: The parameters of a constant fit to the VHE light curves of Mrk 421 as observed by MAGIC–I on 2008 February the 6th and on March the 30th. $E_{min}$ is the threshold energy of the light curve, $p_0$ is the constant value, and $\Delta p_0$ its uncertainty. The results of a $\chi^2$ test are reported in the last column, along with the number of degrees of freedom. The constant fit is appropriate for the night of March the 30th, but not for the night of February the 6th.

two effects:

- the performance of the $\gamma$/hadron separation is much better, providing a more efficient background suppression;
- the higher energy threshold allows for application of a tighter SIZE cut without significant signal loss; then the systematics effect of camera inhomogeneities can be neglected, and 3 OFF positions can be considered for the estimation of background, leading to a reduction in background fluctuations of the order $\sim 1/\sqrt{3}$.

Moreover, the rather different energy spectrum between such a hard source and the background also contributes to a stronger signal–to–noise ratio at high energies.

## 8.10 VHE spectra of Mrk 421

**Spectrum of March the 30th**

On March the 30th, Mrk 421 was observed with MAGIC–I continuously for two hours, as follow–up observation of the monitoring performed during twilight, that spotted a very high state of the source. In the Online Analysis Mrk 421 was detected with $15.2\sigma$ of significance; the gamma rate was $\sim 19$ $\gamma$/min at $ZA \sim 40$, against a Crab Nebula reference value of $\approx 6$ at these zenith angles. This triggered follow-up observations (the critical threshold was 2 C.U.) that were performed under good weather and instrumentale conditions and stable trigger rates.

The data was analyzed with the following cuts and setting:

- Size $> 120$ phe$^-$;
- ALPHA and HADRONNESS cuts tuned to give 80% efficiency on MC simulated events:
- 1 instead of 3 OFF position for background estimation (this choice is less prone to systematics related to camera inhomogeneity that such a low SIZE cut) can arguably be severe.

The total excess count was $N_{exc} = 3566 \pm 73$ in 120 min, with an average gamma rate of 29.7 $\gamma$/min , 4.4 times the Crab Nebula excess rate with the same analysis setting (6.7 $\gamma$/min). When divided in bins of estimated energy the excess is significant above $5\sigma$ level in the bins between 95 and 7000 GeV. The spectrum in bins of estimated energy has a slope $\Gamma = -2.08 \pm 0.09$, and is plotted in Figure 8.7.

The unfolding procedure (see Section 6.11.1) was applied, testing different methods (Berthero, Tikhonov, Schmelling) and different functions, namely power law, power law with cutoff, curved power law.

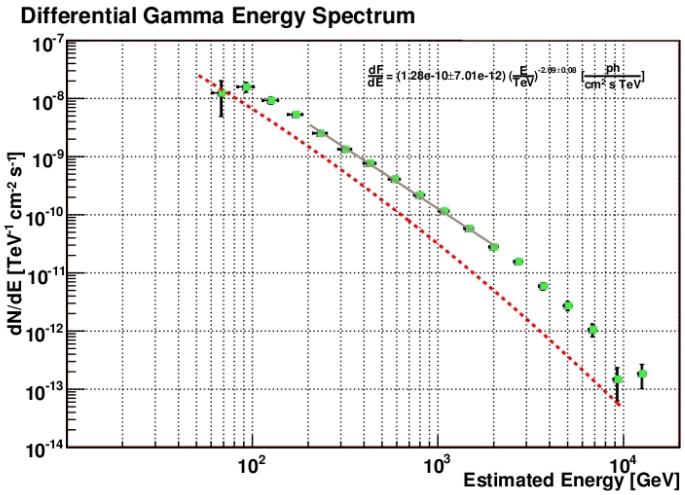


Figure 8.7: VHE Spectrum of Mrk 421 from March 30th observations. The plotted spectrum is in bins of estimated energy, before unfolding. The VHE spectrum of Crab Nebula is plotted for comparison.

A good fit and the agreement of the various unfolding methods is reached for the curved power law: the VHE spectrum of Mrk 421 in the two hours of MAGIC observations on March the 30th can be described by

$$\Phi(E) = f_0 \cdot (\frac{E}{E_0})^{(-a+b\cdot\log(\frac{E}{E_0}))} \tag{8.1}$$

where: $f_0 = (0.16\pm0.01)\times10^{-8}$ cm$^{-2}$s$^{-1}$, $a = -1.90\pm0.05$, $b = -0.32\pm0.05$.

The pivot energy $E_0$ is 300 GeV, and the $\chi^2$ test for goodness of fit gives $\chi^2$/ndf= 2.88/8.

In Figure 8.10 the VHE SED obtained from the spectrum unfolded with the Tikhonov algorithm is plotted. The lowest energy point (plotted with dashed error bars) has been excluded from the fit due to the small telescope collection area at such low energies (below 10% of the peak value). As a consequence, the result at this energy is affected by poor statistics both in real data and in simulated events, and the systematics can be poorly predicted but can be assumed as dominant and biasing the result.

### 8.10.1 Spectra of the nights with simultaneous X–ray observations

Apart from the dataset from March the 30th considered in the previous section, the study of the spectra was focused on the subset of the eight observations with a simultaneous X–ray observation performed by *Swift*/XRT. These datasets were those of interest for the modeling of the simultaneous

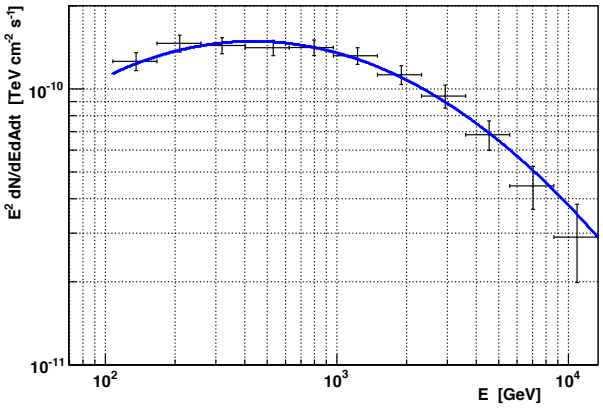


Figure 8.8: VHE SED of Mrk 421, as derived from the spectrum measured on 30th of March 2008 and unfolded with the Tikhonov method. The continuous blue line displays the curved power law fit to the data. This spectrum is the observed one, before any correction of the extinction due to EBL.

multiwavelength SED (see Section 8.13) and are listed in Table 8.5. From each observation I derived a VHE spectrum in bins of the estimated energy of the $\gamma$–ray primary events. Then I applied the Tikhonov unfolding algorithm (Albert et al., 2007c) to reconstruct the physical spectrum in terms of the true energy of the primary $\gamma$–rays. As in the previous case, the agreement among different methods was taken as a proof of the robustness of the procedure-The best fit to the data was in most cases performed assuming a log–parabolic model for the differential spectrum:

$$\frac{dN}{dE\,dA\,dt} = f_0 \times (\frac{E}{E_0})^{(a+b\cdot\log(\frac{E}{E_0}))} \tag{8.2}$$

where a *pivot* energy $E_0 = 300$ GeV has been chosen. The parameters of the fit and the $\tilde{\chi}^2$ are reported in table 8.3; quoted uncertainties are statistical only. IN the case of three nights, a simple power law model described adaequately the spectra, much probably due to lower statistics. This can be ascribed either to relatively lower state of the source (January the 1st) or to the short exposure and higher energy threshold (the reasons are explained below) adopted in the analysis (April the 2nd and the 4th).

The spectral points were hereafter corrected for EBL absorption, assuming the model by Franceschini et al. (2008), and are plotted in Figure 8.10 along with the SSC models of the SED (see Section 8.13.1) that are anticipated here only as a help to guide the eye. For comparison is also plotted, without model, the VHE SED from 2008 March the 30, deabsorbed as well). Unfortunately, this dataset could not be included in the SED study, as *Swift* could only observe with 14 hours of delay with respect to MAGIC

in this case. Anyway, the VHE spectrum derived from this observation is intriguingly hard, peaking around 500 GeV, well within the MAGIC band. In Figure 8.9 the observed SED (red filled points) is plotted together the deabsorbed one (black open triangles), that peaks above 1 TeV.

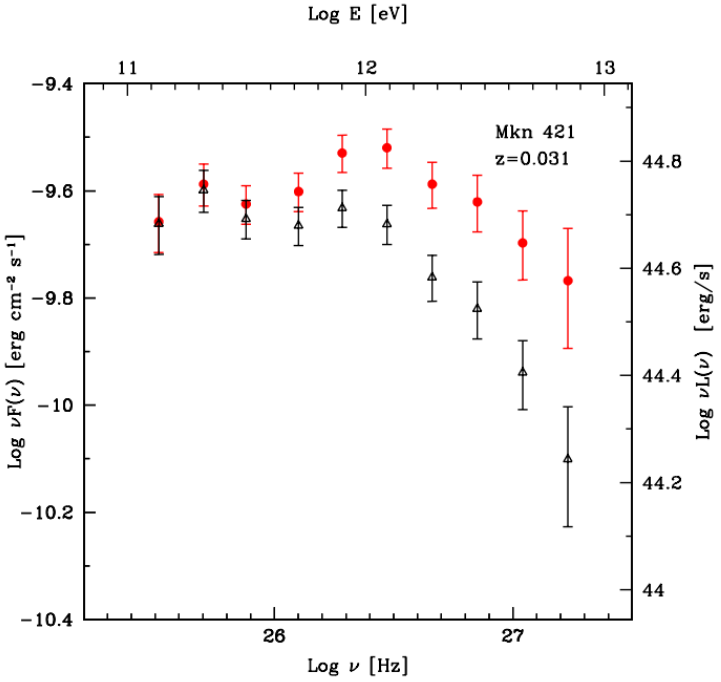


Figure 8.9: VHE SED of Mrk 421 derived from the MAGIC observations performed on March the 30th, when the flux rose up to 3.6 Crab Units. Data points before (red filled points) and after (black open triangles) applying a correction for EBL absorption following Franceschini et al. 2008 are shown. The observed position of the IC peak is evaluated at $\sim$ 500 GeV from the fit with a curved power law, and above 1 TeV after deabsorption.

A note must be added on the two spectra from April the 2nd and the 4th that were observed following the MAGIC–*Swift* MWL proposal activated after the outburst detected on 30th of March. In these night the data strictly simultaneous to *Swift*/XRT observations were taken tracking only one position of the sky, without wobbling.

The main concern with observations taken tracking only one wobble position is that camera inhomogeneity is not properly corrected by the simmetrization of the source position on the camera plane along the exposure. Therefore for these two nights only events with Size $\geq 250$ phe$^-$ were considered, as above this Size level camera inhomogeneity becomes negligibly effective. Usually such a conservative Size cut allows for considering more

| Night<br>yyyymmdd | Integral flux<br>$cm^{-2}s^{-1}$<br>$[\times 10^{-10}]$<br>($E > 200$ GeV) | $f_0$<br>$cm^{-2}s^{-1}TeV^{-1}$<br>$[\times 10^{-10}]$<br>($E_0 = 300$ GeV) | $a$ | $b$ | $\chi^2/ndf$ |
|---|---|---|---|---|---|
| 20080108 | $2.13 \pm 0.20$ | $5.9 \pm 0.7$ | $-2.72 \pm 0.12$ | – | 2.00/5 |
| 20080109 | $2.61 \pm 0.11$ | $6.3 \pm 0.3$ | $-2.50 \pm 0.07$ | $-0.44 \pm 0.15$ | 4.38/7 |
| 20080110 | $2.53 \pm 0.16$ | $7.4 \pm 0.5$ | $-2.42 \pm 0.08$ | $-0.52 \pm 0.20$ | 7.55/6 |
| 20080116 | $4.42 \pm 0.14$ | $10 \pm 1$ | $-2.25 \pm 0.07$ | $-0.33 \pm 0.10$ | 2.01/6 |
| 20080117 | $3.80 \pm 0.19$ | $9.8 \pm 1.2$ | $-2.37 \pm 0.10$ | $-0.57 \pm 0.18$ | 4.17/6 |
| 20080211 | $5.34 \pm 0.32$ | $12 \pm 1$ | $-2.11 \pm 0.14$ | $-0.44 \pm 0.24$ | 6.60/6 |
| 20080402 | $2.94 \pm 0.32$ | $7.1 \pm 0.5$ | $-2.44 \pm 0.16$ | – | 0.93/3 |
| 20080404 | $4.53 \pm 0.30$ | $11 \pm 1$ | $-2.35 \pm 0.10$ | – | 2.22/6 |

Table 8.3: Results of MAGIC VHE observations of Mrk 421 for the 8 nights with overlapping MAGIC and *Swift*/XRT data and good data quality. For each night, the integral VHE flux above 200 GeV is reported in the first column. The best fit parameters to the observed (no EBL correction) spectrum are reported, with statistical errors only. The fit function chosen is the simplest giving acceptable reduced $\chi^2$ amongst simple power law, power law with exponential cutoff and curved power law.

than one anti–source position (e.g. three) leading to a more precise measurement of the background. This could anyway introduce systematics here in case of residual camera inhomogeneities, so has been avoided.The reliability of this approach was checked *a priori*, from the Center of Gravity and "phi" plots, that showed small inhomogeneities above 250 $phe^-$. Another check was made *a posteriori*, from the compatibility within fluctuations of the background ($30° \leq$ Alpha $\leq 80°$) regions of the Alpha–plots (see Figure 8.11).

For each of these nights the differential spectra in units of estimated energy[3] have been unfolded in order to correct for the finite energy resolution of the telescope. Table 8.3 summarizes the VHE data available from MAGIC observations in these nighs: the integral flux above 200 GeV and the parameters of a fit to the experimental points in the differential flux, performed with the simplest function achieving a convincing reduced $\chi^2$, amongst PL, PL with cut off and curved PL.

## 8.11 Multiwavelength data

### 8.11.1 X-ray data from RXTE/ASM

The All–Sky Monitor (ASM) onboard of the *Rossi X-ray Timing Explorer* (RXTE, Bradt et al. 1993) is sensitive enough to set one point per day from Mrk 421.

ASM data for Mrk 421 during the MWL campaign are taken from the results provided by the ASM/RXTE teams at MIT and at the RXTE SOF

[3]Calculated by means of the `fluxlc` software included in MARS.

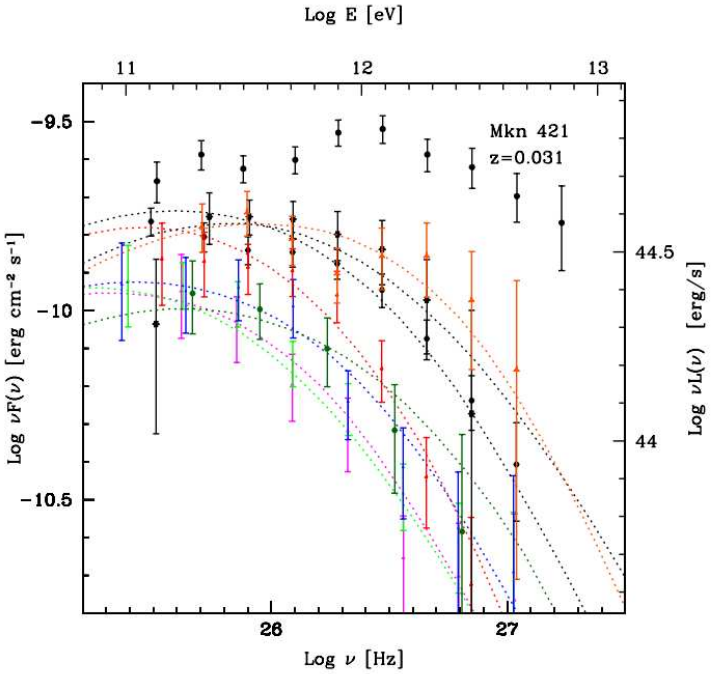


Figure 8.10: VHE SED of Mrk 421 derived from the MAGIC observations performed in the 8 timeslots with tightly simultaneous *Swift*/XRT data ( see Section 8.13). The spectra are shown after correction of the EBL absorption, following Franceschini et al. (2008). For comparison, the spectrum derived from the observation that registered the highest flux (3.6 C.U above 200 GeV) of the whole campaign, performed on 2008 March the 30th. For each night, the SSC model (see Section 8.13.1 is plotted in order to guide the eye.

and GOF at NASA's GSFC. The count rates observed in the $2-10$ keV band are shown in the middle–lower panel of Figure 8.12.

### 8.11.2 *Swift*/XRT and *Swift*/UVOT observations

The *Swift* satellite (Gehrels et al., 2004) is a NASA mission, launched in 2003, devoted to observations of fast transients, namely GRB prompt observations. These are detected with the monitoring coded mask Burst Alert Telescope (BAT, Barthelmy et al. 2005) sensitive to 15-150 keV X-rays and covering a wide FOV with a resolution of few arcminutes, and then rapidly targeted with the two co–aligned pointing instruments, X–Ray Telescope (XRT, Burrows et al. 2005) and Ultra–Violet Optical Telescope (UVOT, Roming et al. 2005).

The fast repositioning capability of the spacecraft allows snapshotting of variable sources with little overheads. In the case of Mrk 421, observa-

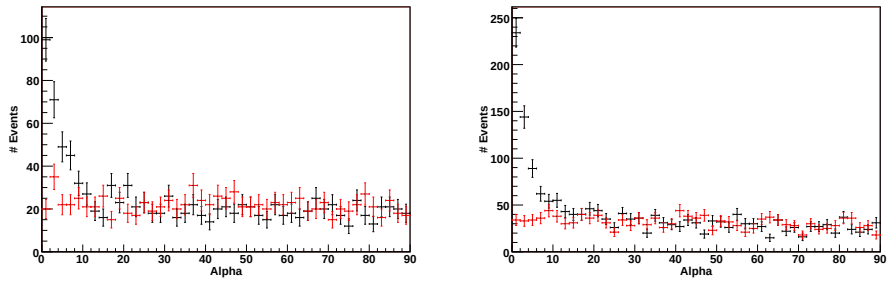


Figure 8.11: ALPHA–plot of the events survived to all cuts for the MAGIC–I observation of Mrk 421 taken on 2008, April, the 2nd (left panel) and April the 4th (right panel) and time coincident with *Swift*/XRT pointings. A SIZE $\geq$ 250 phe$^-$ cut has been applied, and only one anti–source has been considered for the estimation of background. The agreement within fluctuations of the background region in the histograms of ON (black) and OFF (red) events reassures that residual systematic discrepancies between the two event samples are negligible.

tions lasting $\sim$ 1 ks allow the derivation of a detailed X–Ray spectrum and multi–filter aptical–UV photometry due to the sensitivity of the targeted instruments and the brightness of the source.

*Swift*/XRT is a Wolter type I grazing incidence telescope, with 110 cm$^2$ effective area, 23.6' arcmin FOV and 15" angular resolution, sensitive in the 0.2–10 keV energy band. During the MAGIC campaign the instrument performed 43 targeted X-ray observations of Mrk 421 with 1–2 ks typical exposure times. Data were reduced using the software distributed with the `heasoft` 6.3.2 package by the NASA High Energy Astrophysics Archive Research Center (HEASARC). The `xrtpipeline` was set for the photon counting or window timing modes and having selected single pixel events (grade 0). The observed count rates in the $0.2 - 10$ keV band are reported in the second panel of Figure 8.12.

### Soft X–ray spectra derived from *Swift*/XRT data

In the case of the eight simultaneous observations with MAGIC listed in Table 8.5 soft X–ray spectra have been derived in order to build the MWL SED (see Section 8.13). Data were rebinned in order to have at least 30 counts per energy bin. Broken power law models have been fitted to the spectra. In Tab. 8.4 the spectral parameters used for modeling the SED are reported. The X–ray reddening due to absorbing systems along the light travel path has been corrected assuming the Galactic value for column density of neutral hydrogen $N_H = 1.6 \times 10^{20}$ cm$^{-2}$ (Lockman & Savage, 1995).

| Obs. ID | Start Time | Obs. Time ks | $F_{2-10\mathrm{keV}}$ erg/ cm$^2$ s [$\cdot 10^{-12}$] | $\alpha_1$ | $E_{break}$ keV | $\alpha_2$ | $f_0$ | $\tilde{\chi}^2$/ndf |
|---|---|---|---|---|---|---|---|---|
| 00030352041 | 2008-01-08 02:30 | 2.0 | 280 | 2.29(0.02) | 1.22(0.08) | 2.59(0.03) | 0.239(0.003) | 1.57/148 |
| 00030352042 | 2008-01-09 04:04 | 2.0 | 284 | 2.27(0.03) | 1.08(0.10) | 2.60(0.03) | 0.254(0.004) | 1.32/154 |
| 00030352044 | 2008-01-10 02:27 | 2.3 | 284 | 2.29(0.02) | 1.09(0.09) | 2.57(0.02) | 0.245(0.003) | 1.92/160 |
| 00030352053 | 2008-01-16 03:21 | 1.2 | 345 | 2.16(0.03) | 1.18(0.16) | 2.44(0.04) | 0.241(0.005) | 1.44/85 |
| 00030352055 | 2008-01-17 03:29 | 0.8 | 311 | 2.17(0.02) | 1.94(-0.8/+0.2) | 2.76(0.09) | 0.240(0.003) | 1.77/74 |
| 00030352068 | 2008-02-11 03:40 | 1.9 | 588 | 2.17(0.01) | 2.40(0.2) | 2.58(0.06) | 0.369(0.002) | 1.81/195 |
| 00030352083 | 2008-04-02 00:42 | 0.9 | 475 | 2.09(0.02) | 2.86(0.33) | 2.54(0.14) | 0.258(0.002) | 1.73/86 |
| 00030352086 | 2008-04-03 21:59 | 1.2 | 964 | 1.93(0.01) | 2.34(0.18) | 2.34(0.06) | 0.434(0.003) | 1.44/184 |

Table 8.4: Results of the best fit (assuming a broken power law model) to the X–ray spectra of Mrk 421 obtained from the eight *Swift*/XRT pointings contemporary to MAGIC observations (see Section 8.13). For each dataset are reported (with uncertainties in parentheses): the Obs-ID, the gregorian date and time at the beginning of observation, the exposure time, th integral flux in the 0.2–10 keV band, the spectral indexes and the break energy of the broken power law model assumed for the fit, and the resulting $\tilde{\chi}^2$ (reduced $\chi^2$) with the number of degrees of freedom.

**UVOT Ultra–Violet observations**

UVOT is a 30 cm diffraction limited optical–UV telescope, equipped with 6 different filters, sensitive in the 1700–6500 Å wavelength range, in a 17' × 17' FOV. Unfortunately, during the January 2008 campaign UVOT didn't observe the source, so that the UVOT datasets were fewer and, for instance, its information was missing for most of the simultaneous sets of observation (see Section 8.13). Nevertheless data in the optical band came from the ground observations performed by the KVA telescope, with far more dense coverage in time but in only one filter (see section 8.11.3. Therefore the UVOT analysis was restricted to the three observations simultaneous with MAGIC performed on February the 11th and April the 2nd and 4th, with the UV filters alone. Analysis was performed by means of the `uvotimsum` and `uvotsource` tasks with a source region of $5''$, while the background was extracted from a source–free circular region with radius equal to $50''$ (it was not possible to use an annular region, because of a nearby source). The extracted $\nu F_\nu$ magnitudes have been corrected for Galactic extinction using the values of Schlegel et al. (1998) and applying the formulae by Pei (1992) for the UV filters, and eventually have been converted into fluxes following Poole et al. (2008). The resulting flux densities have been used to build the multiwavelength SED of Mrk 421 plotted in Figure 8.15.

### 8.11.3 KVA optical observations

Along the time span of the MAGIC observations, 117 observations of Mrk 421 were performed in the Johnson $R$ band. The optical data were reduced by the Tuorla Observatory as described in Nilsson et al. (2007). The light contribution from the host galaxy and nearby companion galaxy ($F_{h+cg} = 8.07 \pm 0.47$ mJy) has been subtracted from the measured fluxes. The optical light curve is reported in the bottom panel of Figure 8.12, while the available measurements referred to the simultaneous datasets listed in Tab. 8.5 (see Section 8.13 are plotted in Figure 8.15 after correction for Galactic extinction, again applied according to the values of Schlegel et al. (1998).

## 8.12 Correlation of fluxes in the various bands

VHE fluxes have been correlated to the available data in the other bands. Due to the general lack of tightly simultaneous observations, points in the different bands taken within a time window of 0.5 days have been accepted here as matching. This is quite acceptable for the optical, where variations can be assumed small on these timescales. As far as RXTE/ASM measurements are concerned, these come from a 24–hours average, therefore the criterion can be kept also in this case.

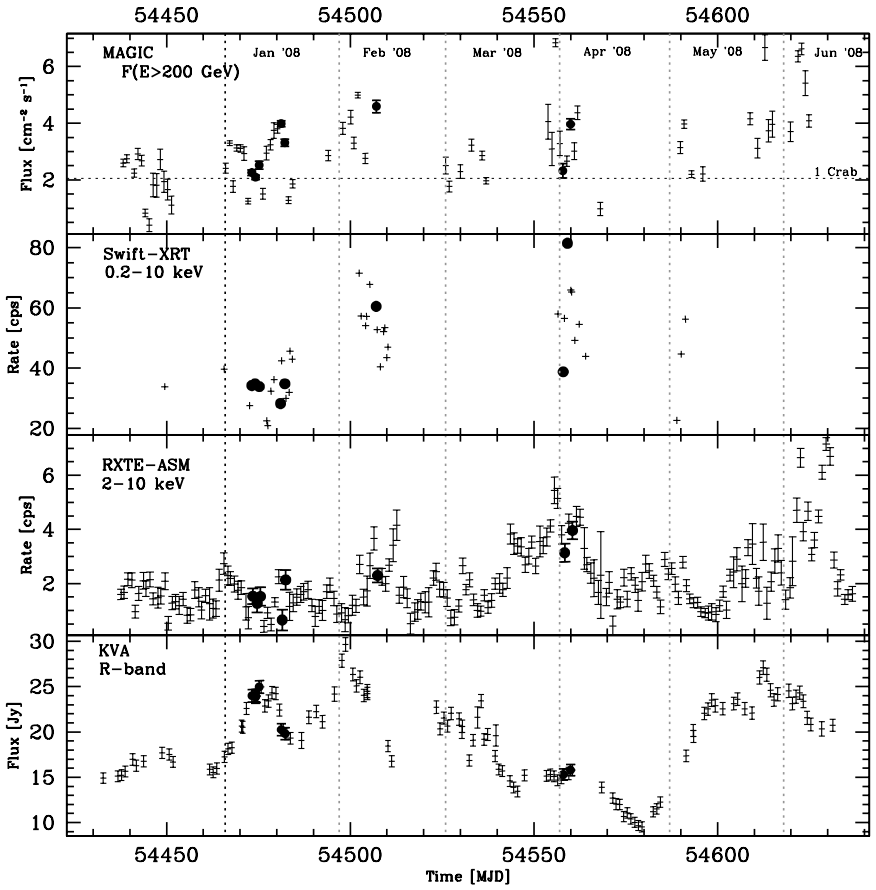


Figure 8.12: Multiwavelength light curves of Mrk 421 along the MAGIC observation period; full circles mark the fluxes observed when MAGIC and *Swift*/XRT pointed simultaneously the source. Upper panel: MAGIC VHE light curve above 200 GeV, for the 66 observation nights that passed quality cuts. MAGIC detected the source clearly in all the nights; the integral flux was below the Crab Unit (C.U., $\approx F_{E>200\,\mathrm{GeV}} = 2.0 \times 10^{-10}$ photons $\cdot$ cm$^{-2}$s$^{-1}$, represented here by the dashed horizontal line) only in a few nights. A maximum flux of $\sim 3.6$ C.U. has been observed on 2008 March the 30th (MJD=54555). Middle–upper panel: soft X–ray count rates (0.2–10 keV) measured by *swift*/XRT. Middle–lower panel: soft X–ray (2–10 keV) count rates measured by RXTE/ASM. Lower panel: Johnson R–band optical light curve from the Tuorla Observatory.

For the correlation between *Swift*/XRT and MAGIC observations, the assumption is no longer satisfactory, as lags of few hours between the two instruments are enough to make that significantly different jet states are

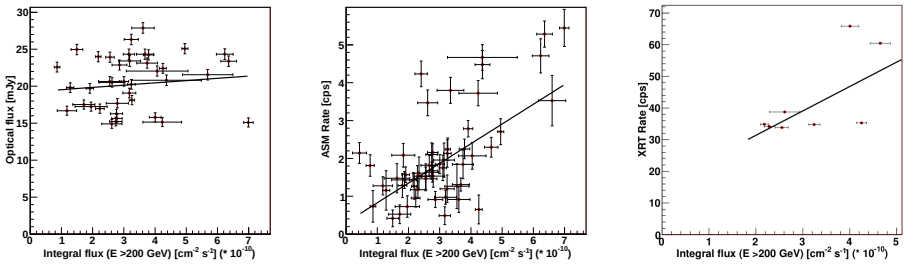


Figure 8.13: Correlation plots for the MWL observations of Mrk 421. Left panel: KVA optical (Johnson R–band) vs. MAGIC VHE data. Within a time window of 0.5 days, 48 observations have been matched. The probability that the two datasets are independent is $P(null) = 5.6\%$ ($\rho = 0.23$). Central panel: RXTE/ASM X–ray data vs. MAGIC VHE data. Within a time window of 0.5 days, 56 couples of points have been matched. The probability of independence of data is $P(null) < 0.001\%$, $\rho = 0.67$. Right panel: correlation plot for the 8 *tightly* simultaneous observations with MAGIC and *Swift*/XRT. The probability of independence is 3.1%, $\rho = 0.68$.

sampled in the two energy bands. Therefore the correlation has been restricted only to the simultaneous datasets considered in Section 8.13. The results are that optical and VHE (figure 8.13, left panel) are partially correlated (Pearson's index[4] $\rho = 0.23$, probability that the datasets are independent $P(null) = 5.6\%$) Stronger correlation is found between RXTE-ASM and MAGIC data (figure 8.13, middle panel): $\rho = 0.67$, $P(null) < 0.01\%$. Also *Swift*/XRT and MAGIC data (figure 8.13, right panel) are correlated: $\rho = 0.68$, $P(null) = 3.0\%$. This result is clearly affected by the paucity of the sample; nevertheless no significant improvement has been found relaxing the request on tight simultaneity, probably due to fact that the variation of the jet state between time-separated measurements introduces a noise that roughly counterbalances the gain in statistics. Moreover it must be noted in the correlation between MAGIC fluxes and ASM rates the data span a wider dinamic range than in the one between MAGIC and *Swift* and consequently the scatter of the points is less dominant. This is expected, as *Swift* pointings were triggered as Target of Opportunity (ToO) observations therefore are biased towards high states, while RXTE/ASM data come from a daily, unbiased monitoring that evenly sampled also lower states.

Anyway, the results confirm a positive correlation between X rays and VHE $\gamma$ rays, as already observed in this source (see e.g. Fossati et al., 2008). This is also in agreement with the predictions of one–zone leptonic models of *blazars*. The looser correlation with the optical can also be explained within this context, as at these lower frequencies larger areas of the jet not

[4]See e.g. Hollander & Wolfe (1973)

| Night | MAGIC Obs. | | | | *Swift*/XRT Obs. | | Overlap |
|---|---|---|---|---|---|---|---|
| | Start (UT) (hh.mm) | End (UT) (hh.mm) | Time ($s$) | ZA range (deg) | Start (UT) (hh.mm) | Time ($s$) | Time ($s$) |
| 20080108 | 01.58 | 02.44 | 2676 | 31-41 | 02.30 | 2006 | 800 |
| 20080109 | 03.56 | 06.19 | 8130 | 6-20 | 04.04 | 1973 | 2000 |
| 20080110 | 02.23 | 06.05 | 3493 | 10-34 | 02.27 | 2265 | 1100 |
| 20080116 | 03.17 | 05.11 | 6529 | 6-21 | 03.21 | 1248 | 1200 |
| 20080117 | 03.26 | 04.25 | 3434 | 6-18 | 03.29 | 828 | 800 |
| 20080211 | 03:33 | 03:58 | 1440 | 10-18 | 03.40 | 1868 | 1100 |
| 20080402 | 00.45 | 01.00 | 880 | 17-21 | 00.42 | 895 | 600 |
| 20080404 | 21.55 | 22.20 | 1317 | 15-23 | 21.59 | 1160 | 1100 |

Table 8.5: Summary of the 8 tightly simultaneous observations of Mrk 421 with MAGIC–I and *Swift*/XRT. For each night, the beginning (col. 1) and the end (col.2) of the MAGIC–I observation time span, the total effective time (col.3) and the ZA range (col. 4) of each observation are reported. The start time (col. 5) and duration (col. 6) of the corresponding *Swift*/XRT pointing are also reported, and the truly overlapped observed time (rounded up, col.7).

involved in the highest energy emission can contribute to the observed flux.

## 8.13 The simultaneous multiwavelength datasets

Hereafter I focus on the 8 cases for which tightly simultaneous observations in VHE with MAGIC telescope and in X–rays with *Swift*/XRT could be performed. Table 8.5 summarizes the observation logs of the two instruments for these nights.

It's worth noticing that the MAGIC data considered for each night cover in many cases a time span that is bigger than *Swift* exposures: this was necessary, as the tipical observation time of *Swift* in this campaign (1 ks) is enough for deriving a rather detailed X–ray spectrum of Mrk 421, but the significantly lower count rate available in the $\gamma$–ray domain makes such an exposure time too short for deriving a VHE spectrum detailed enough for the modeling. Therefore for each night the whole MAGIC exposure was used to derive the VHE spectrum given that the observing conditions were stable and no evidence for sharp evolution of the source arose from the VHE light curves at minute scales. For each of the eight states under study, I built the MWL SED matching the MAGIC, *Swift*/XRT and optical–UV (either R–band from KVA, or UV from*Swift*/XRT, or both) data. As an example, the SED of Mrk 421 as observed on 2008 February the 11th is plotted in Figure 8.14, compared to historical MWL data taken from Tavecchio & Ghisellini (2008). It's worth noticing that the VHE SED is high and hard, while the X–ray SED is high but rather soft w.r.t. to past states where the synchrotron peak was observed at higher energies. The wide separation of the two peaks is further discussed in Section 8.13.1

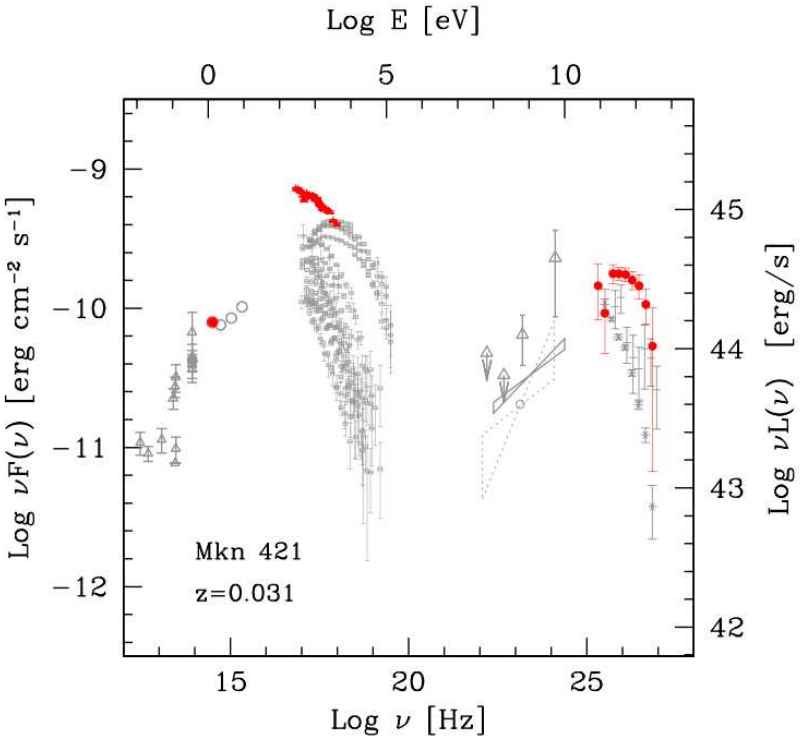


Figure 8.14: Example MWL SED of Mrk 421 as observed in tight simultaneity by *Swift*/UVOT, *Swift*/XRT and MAGIC on 2008 February the 11th (filled red circles). Historical data taken from Tavecchio et al. (2010d) are plotted for comparison, with gray open symbols.

### 8.13.1 SED modeling

For modeling the SED I adopted the simple one–zone SSC model from Tavecchio et al. (1998) summarily recalled in Section 3.5 (for further details see Tavecchio et al. (1998), Maraschi & Tavecchio (2003)). This model has the great benefit of being fully constrained if simultaneous data covering the regions near the SED peaks are available. It also has proven to describe well *blazars* in spite of the few parameters considered (see e.g. Maraschi et al. 1999 on Mrk 421 itself, Tagliaferri et al. 2008 on 1ES 1959+650 or Anderhub et al. 2009b on Mrk 501).

As detailed in Tavecchio et al. (1998), this simple model can be fully constrained by using simultaneous multiwavelength observations. Indeed, the total number of free parameter of the model is reduced to 9: the 6 parameter specifying the electron energy distribution plus the Doppler factor $\delta$, the size of the emission region $R$ and the magnetic field $B$ (see Section 3.5.1. On the other hand, from observations ideally one can derive 7 observational quantities: the slopes of the synchrotron bump before and above the peak $\alpha_{1,2}$ (uniquely connected to $n_{1,2}$), the synchrotron and SSC peak frequencies ($\nu_{\rm s,C}$) and luminosities ($L_{\rm s,C}$) and the minimum variability timescale $t_{\rm var}$, which provides an upper limit to the size of the sources through the relation $R < ct_{\rm var}\delta$.

Therefore, once all the observational quantities are known, one can derive an unique set of parameters, as $\gamma_{min}$ and $\gamma_{max}$ are not much related to the peak regions, and can be constrained by further observation such as those in the optical region for $\gamma_{min}$. In this respect, the cases studied here are rather favorable, since a rather good determination of the peak frequencies (and fluxes) of both peaks has been achieved. Indeed, although the synchrotron peak of Mrk 421 is seldom observed within the band encompassed by XRT, the joint optical–UV and X–ray data provide an excellent constraint to the position of the synchrotron peak in all the cases. The SSC peak is well determined only for the February 11 observation. In all the other cases the peak is located at energies below the MAGIC band: however, the pronounced curvature of the MAGIC spectrum at the lowest energies allows to constrain the peak at energies not much below $\approx 50$ GeV.

Unfortunately for the epochs used to derive the SEDs we do not have information on the variability timescale, $t_{\rm var}$, one of the key observational parameters needed to completely close the system and uniquely derive the parameters. In the X–ray band *Swift*/XRT observed in short ($\sim 1$ ks) snapshots, while no pressing evidence for sub–hour variability arose from the corresponding MAGIC observations. Therefore we still have some freedom in choosing the input parameters: one can obtain different sets of parameters, reproducing the spectral data equally well but differing in the predicted observed minimum variability timescale.

The model has been applied to all the eight sets of data collected when

*Swift* and MAGIC could observe simultaneously the source. UVOT and *KVA* data were also included in the SED when available. The sets of parameters obtained from the modeling are reported in Table 8.6 and the SED data and the corresponding model are plotted in Figure 8.15. It's worth noticing that no radio data have been considered for reproducing the SED, since the modeled region is opaque at these frequencies: in this framework the radio emission originates in regions of the jet farther away from the black hole, beyond the core visible at VLBI scale, thought to mark the radio "photosphere". Accordingly, the inferred source radius is well within the upper limit of 0.1 pc ($3 \times 10^{17}$ cm) imposed by Charlot et al. (2006) for the projected size of the SSC zone, based on VLBI observations of the radio core.

| Night | $\gamma_{\rm min}$ | $\gamma_{\rm b}$ | $\gamma_{\rm max}$ | $n_1$ | $n_2$ | $B$ | $K$ | $R$ | $\delta$ | $t_{var}$ |
|---|---|---|---|---|---|---|---|---|---|---|
| yyyymmdd | $[10^3]$ | $[10^4]$ | $[10^6]$ | | | $[10^{-2}$ G] | $[10^3$ cm$^{-3}]$ | $[10^{15}$ cm] | | h |
| 20080108 | 7.0 | 6.0 | 3.0 | 2.0 | 4.0 | 5.0 | 1.70 | 9.0 | 45 | 1.8 |
| 20080109 | 10 | 2.9 | 3.0 | 2.0 | 4.0 | 4.3 | 3.70 | 5.0 | 85 | 0.5 |
| 20080110 | 6.0 | 5.7 | 3.0 | 2.0 | 4.0 | 3.7 | 3.30 | 5.0 | 70 | 0.7 |
| 20080116 | 8.3 | 6.7 | 3.0 | 2.0 | 4.0 | 2.5 | 4.00 | 5.0 | 80 | 0.6 |
| 20080117 | 10 | 6.0 | 0.7 | 2.0 | 4.2 | 3.7 | 2.60 | 7.2 | 60 | 1.1 |
| 20080211 | 11 | 6.9 | 3.0 | 2.0 | 3.7 | 2.0 | 2.40 | 6.6 | 85 | 0.7 |
| 20080402 | 8.0 | 3.2 | 1.0 | 2.0 | 3.5 | 5.0 | 5.90 | 3.9 | 70 | 0.5 |
| 20080404 | 17 | 20 | 3.0 | 2.0 | 4.0 | 4.0 | 2.00 | 8.5 | 40 | 2.0 |

Table 8.6: Input model parameters for the eight nights with tightly simultaneous MAGIC and *Swift*/XRT data. For each night (identified with the civil date of the following morning) the minimum, break and maximum Lorentz factors of the electron distribution, the low and high energy slopes of the electron distribution, the magnetic field and the electron density within the emitting region, the radius of the emitting region, its Doppler factor and the resulting light crossing time are reported.

Inspection of Table 8.6 shows that the derived Doppler factors are rather large, exceeding $\delta = 40$ in all the cases and reaching values as large as 80–85 in the most extreme cases. The main reason for such large values of $\delta$ is the large separation between the two peaks, the synchrotron one located below $10^{17}$ Hz, the SSC one around $10^{25}$ Hz or above. As detailed in e.g. Tavecchio & Ghisellini (2008) a large distance between the two peaks implies a rather large value of the Lorentz factor at the peak, $\gamma_{\rm b}$, since $\gamma_{\rm b} = (\nu_{\rm C}/\nu_{\rm s})^{1/2}$, and this directly implies a low $B$ and/or a large $\delta$ to satisfy the other constraints. Another useful formula clearly showing this can be found in Fossati et al. (2008)

$$\frac{B}{\delta} \propto \frac{\nu_{\rm S}}{\nu_{\rm IC}^2} \tag{8.3}$$

However it must be recalled that, since the variability timescale in not known, we are left with some freedom in selecting the input parameters, namely we cannot remove a degeneracy in the $\log B$–$\log \delta$ diagnostic plane

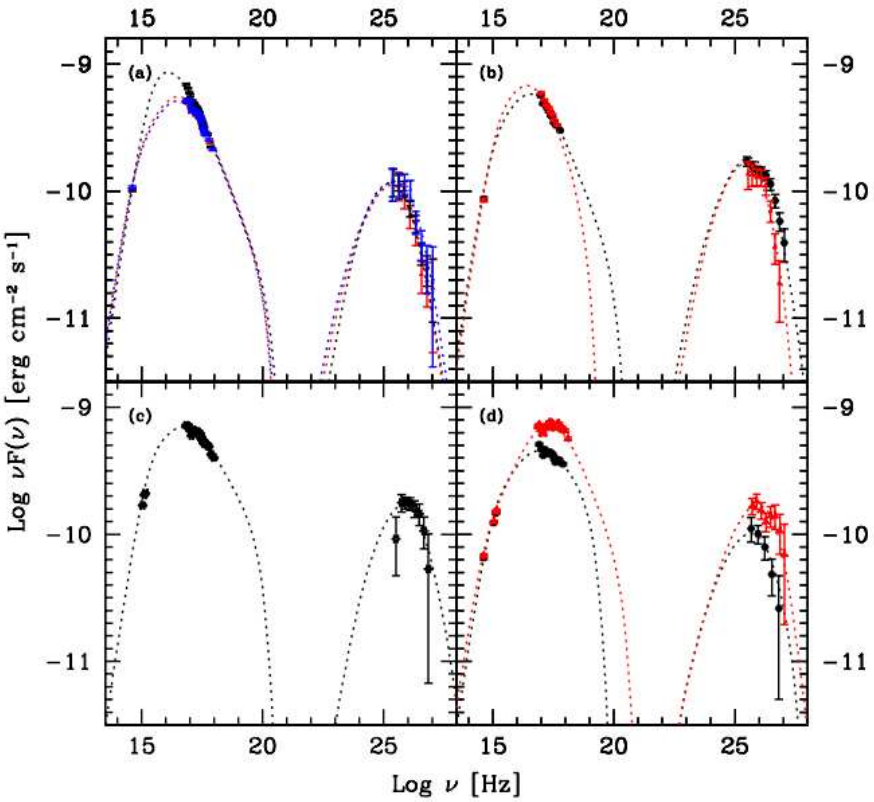


Figure 8.15: SED of Mrk 421 with overplotted SSC model for each of the eight simultaneous sets of MAGIC, *Swift*/XRT and optical–UV data obtained in the 2008 campaign. Observations date to 8,9,10 of January (a), 16 and 17 of January (b), 11 of February (c) and 2 and 4 of April (d).

(see Tavecchio et al., 1998). In the models reported in Figure 8.15 variability timescales in the range 0.5–2 hours are assumed, as typically derived for these sources (see Section 8.14). In general, the required Doppler factor roughly scales with the observed variability timescale as $\delta \propto t_{\rm var}^{-0.5}$ (e.g. Tavecchio & Ghisellini 2008). Therefore, relaxing the condition on $t_{\rm var}$, so that longer minimum variability timescales are allowed, one gets lower $\delta$.

As an example, the case for which we derive the largest $\delta$, that of February 11 requiring $\delta = 85$ can be considered. As noted above this is a case in which the determination of the peak frequencies is very robust, since the SSC peak falls in the band covered by MAGIC. Therefore this is also the best "benchmark" available to test the robustness of the derived parameters. In this case it is possible to reproduce the data with different fits basically differing only for the value of the Doppler factor, the radius of the emitting

region and the magnetic field intensity. When assuming $\delta = 85$ the variability scale is set to $t_{\rm var} = 0.7$ h ($2.5 \times 10^3$ s), while more than halving the Doppler factor $\delta = 40$ implies a rather long variability timescale, $t_{\rm var} = 5$ h ($1.8 \times 10^4$ s), already larger than the characteristic variability timescale of Mrk 421 in the X–ray band (Ushio et al., 2009). It can be concluded that for the case of February 11, although the parameters cannot be uniquely fixed, the required Doppler factor is large, at least larger than $\delta \approx 40$. All the other cases are similar.

## 8.14 Discussion of the results

During the 2008 campaign on Mrk 421 with MAGIC a very interesting dataset was gathered in VHE $\gamma$–rays, complemented by crucial data in optical–UV and soft X–rays. For the first time it was possible to collect data in these bands in close simultaneity during high states of the source, so that the derived spectra sampled the SED close to the synchro and IC peaks. In this situation the parameters describing the source in the framework of the standard one-zone leptonic model can be determined with unprecedented robustness. One of the most relevant results of our analysis is that, in order to reproduce the observed SED with this model, very large Doppler factors are required. There is some freedom in choosing the parameters, mainly due to the not known variability timescale at those epochs. In the models summarized in Table 8.6 and reported in Figure 8.15 variability timescales in the range 0.5–2 hours are assumed. This assumption is well motivated by the observed typical raising/decaying timescales of flares of Mrk 421 and similar HBLs (PKS 2155-304, Mrk 501), characterized by doubling/halving times of $\approx 10^4$ s (e.g. Fossati et al. 2008, Ravasio et al. 2004, Zhang 2002, Tanihata et al. 2000), with evidences for the occurrence of even faster events (e.g. Gaidos et al. 1996, Cui 2004). Also in this campaign, but during another night (February the 6th), a hint of fast variability was detected, down to timescales of $\sim$ 15 minutes (see section 8.9.2 and Figure 8.5). In general, the required Doppler factor roughly scales with the observed variability timescale as $\delta \propto t_{\rm var}^{-0.5}$ (e.g. Tavecchio & Ghisellini 2008). However, relaxing this assumption on the variability timescales the required Doppler factors remains large. In the case of the observations of February 11, which allows us to firmly constrain the synchrotron and SSC peak, this implies $\delta \gtrsim 45$.

Actually, such large values of inferred $\delta$ are not rare: very large Doppler factors, sometimes larger than $\delta \sim$50, for Mrk 421 and other well observed HBLs were obtained in the past, leading to the so called "$\delta$-crisis" (e.g. Krawczynski et al. 2002, Konopelko et al. 2003, Georganopoulos & Kazanas 2003). Analogously, the recent exceptional VHE flare of PKS 2155-304 Aharonian et al. (2007) seems to require extreme Doppler factors in the frame-

work of one–zone models (Begelman et al., 2008; Ghisellini & Tavecchio, 2008; Finke et al., 2008; Kusunose & Takahara, 2006). Such large values of $\delta$ (implying similarly large value of the bulk Lorentz factors) contrast with the very small jet velocities inferred at VLBI scales in this a large fraction of TeV BL Lacs (e.g., Giroletti et al., 2004; Piner & Edwards, 2004), including Mrk 421, and with the value of $\Gamma$ required from the unification of BL Lacs and FRI radiogalaxies (e.g., Urry & Padovani , 1995).

Georganopoulos & Kazanas (2003) and Ghisellini et al. (2005) propose a solution to this problem based on the possibility that the flow is characterized by portions moving at different speeds. If these regions emit, in each of them the electrons can scatter not only the locally-produced synchrotron photons, but also the soft protons produced in the other region. Moreover, the energy density of these "external" photons is amplified in the rest frame of the emitting region due to the relative speed between the two portions of the flow. The result is that the inverse Compton emission of each region is amplified with respect to the SSC emission. As a consequence, the Doppler factor required to reproduce the SED is lower than those of the one-zone model. In particular, in the "spine-layer" model of Ghisellini et al. (2005), it is assumed that the jet has a inner faster core (the spine) surrounded by a slower layer. At small angle of view, those characterizing *blazars*, the emission is dominated by the faster spine whose IC emission is a mixture of SSC and "external" Compton components.

A modeling of the SED with the more complex (and less constrained) structured–jet model is beyond the scope of this research and left to future work.

### 8.14.1 A case study: modeling of the SED observed on 2008 March the 30th

An interesting proof of the crucial role of simultaneity can be derived from the dataset of 2008 March the 30th. As far as MAGIC VHE data are concerned, this was the most intriguing night; a long observation could be performed in good conditions and the source showed the record flux of the whole campaign. Moreover, the TeV spectrum was very hard (see Figure 8.9, with the *observed* IC peak well within the MAGIC band ($\nu_{IC} \approx 500$ GeV) and the deabsorbed spectrum peaking at even harder energies ($\nu_{IC}$ above $\approx 1$ TeV). Unfortunately, the *Swift*/XRT pointing lagged the MAGIC observation by 14 hours. The observed X–ray spectrum was not particularly hard, with the syncrotron peak within the *Swift*/XRT band, at $\sim 1$ keV (see Figure 8.16).

Focusing on this night, I produced three different models of the SED. In the first case, the model reproduces the whole MWL dataset, actually neglecting the X–ray data delay. This leads to the parameters reported in the first row of Table 8.7, while the model SED is drawn in blue in Figure

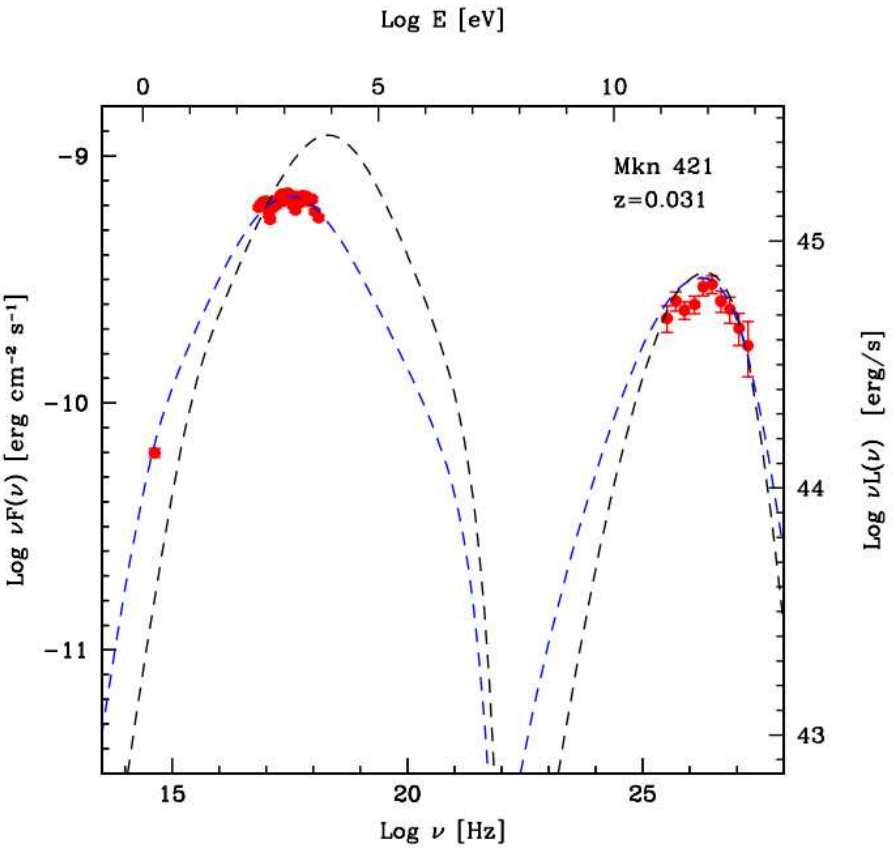


Figure 8.16: Competing models for the SED of 2008 March the 30th. A model fitting the whole MWL SED, actually neglecting the 14 h lag between VHE and X–ray observations (blue line) and a model fitting the VHE data alone and assuming $\delta = 40$ (black line) are plotted. Another model fitting the whole MWL SED but assuming a larger variability time scale and therefore lower $\delta$ is reported in Table 8.7 but is not plotted, the differences from the blue line being negligible.

8.16. Exploiting the already mentioned degeneracy in the $B$–$\delta$ plane arising from the lack of knowledge about $t_{var}$, the same MWL SED can be modeled with a lower, but still large, $\delta = 50$, but leading to a variability time scale that is at the very edge of the reasonable interval. This model is reported in the second row of the table; the plot is omitted as it would differ only minimally from the previous one. The black line in the same figure represents a model reproducing only the TeV spectrum, again assuming a less extreme Doppler factor $\delta = 40$. The parameters of this second model are also reported in Table 8.7, third row. Obviously the modeling without X–

rays has an unconstrained freedom, but from Equation 8.3 is evident that, given a fixed $\nu_{IC}$, lowering $\delta$ forces down $B$ or $\nu_S$ up, or both, as actually assumed here. It's very reasonable that the X–ray spectrum observed by *Swift*/XRT samples a different state from the VHE spectrum measured by MAGIC–I. Obviously, extreme Doppler factors are not *a priori* excluded, as I found similar ones from the tightly simultaneous datasets. Even the derived variability scale $t_{var} = 0.35$ h is short but not unconceivable in TeV *blazars*. A contemporary X–ray observation of this extreme flare would have resolved the degeneracy, allowing a robust derivation of the source parameters in this case. The lack of simultaneity weakens any conclusion that one could try to draw from the data. This casts shadows on all the modeling of variable sources in active state performed with non contemporary data; something that was acceptable years ago, but no more now, when both the greater detail requested and the instrumentation available push towards careful simultaneous observations.

The subject can be therefore summarized as such:

- without multi–wavelength data, the source model is unconstrained, even in such a simple model, based on very few parameters;
- with multiwavelength spectra, the source can be modeled, but the $B$–$\delta$ degeneracy remains if the information on the variability time scale $t_{var}$ is missing, be it either because the light curve could not be followed or because no fast transients were observed;
- if MWL spectra and a constraint on $t_{var}$ are available, the model is fully constrained; but if the observations are not simultaneous, no firm conclusion can be drawn; this problem worsens with the exceptionality of the observed transients.

| Night yyyymmdd | $\gamma_{\rm min}$ [$10^3$] | $\gamma_{\rm b}$ [$10^4$] | $\gamma_{\rm max}$ [$10^6$] | $n_1$ | $n_2$ | $B$ [$10^{-2}$ G] | $K$ [$10^3$ cm$^{-3}$] | $R$ [$10^{15}$ cm] | $\delta$ | $t_{var}$ h |
|---|---|---|---|---|---|---|---|---|---|---|
| MWL | 6 | 20 | 15 | 2.0 | 3.8 | 1.7 | 6.5 | 3.3 | 90 | 0.35 |
| MWL, low $\delta$ | 10 | 30 | 3 | 2 | 3.7 | 1.2 | 1.7 | 12.8 | 50 | 2.4 |
| only TeV | 13 | 47 | 13 | 2.0 | 4.0 | 6.0 | 10 | 3.4 | 40 | 0.8 |

Table 8.7: Input model parameters for the data from 2008 March the 30th. Three models have been produced and two of these are plotted in Figure 8.16. The first two models fit together the VHE and X–ray data, neglecting that the latter have been acquired $\sim$ 14 hours later. In the first case, an extreme Doppler factor is assumed, while in the second a lower, but still large value is considered. The last model reproduces only the TeV data, with the additional constrain of a "standard" Doppler factor ($\delta = 40$). Without the constraint set by the X–ray spectrum, significantly different parameter sets can reproduce equally well the same TeV spectrum, predicting different luminosities for the synchrotron peak. If we neglect the 14 hours delay, and consider the TeV and X–ray spectrum simultaneous, the large separation in frequency between the two peaks forces towards large $\delta$ and small $B$.

# Chapter 9

# Conclusions

The research project undertaken in this thesis dealt with the investigation of tightly simultaneous multiwavelength observations of *blazars*. The results on two different AGNs have been presented and discussed.

The first results reported have been obtained in the 2007 multiwavelength campaign on the potential VHE emitter OJ 287. I analyzed the MAGIC data collected in 2008 November and December, during the observation of the periodic flare that could be related to the relativistic jet according to some models of this peculiar source (Valtaoja et al., 2000). The MAGIC analysis did not reveal any VHE signal, but allowed to calculate upper limits to the VHE flux from this source. The upper limit on the flux above 85 GeV is $22.1 \times 10^{-12}$ ph cm$^{-2}$s$^{-1}$ (3.4 % of the Crab flux), and above 150 GeV is $5.64 \times 10^{-12}$ ph cm$^{-2}$s$^{-1}$ (1.7 % of the Crab flux). The observations confirmed that the SED in both the quiescent and flaring state followed the predictions for an LBL *blazar*, with synchrotron and Inverse Compton components. During the flaring state, the synchrotron peak and high energy tail didn't shift significantly towards higher energies with respect to the quiescent state, differently from what had been observed in previous flares. The hard X–ray spectrum could be related to a dominant contribution from the Inverse Compton process in that band. The SED was modeled within the SSC framework, interpreting the variations between the quiescent and flaring state as produced by an increase in the maximum energy of the electrons in the jet. Anyway, the incomplete knowledge of the SED prevented from deriving any firm conclusion on the inner structure of this source.

The second task accomplished was the analysis of the observations of the bright VHE emitting HBL Mrk 421, performed by MAGIC since 2007 December and until 2008 June. VHE fluxes above 200 GeV were measured for 66 nights. The whole period was characterized by intense activity of the source, that reached a record flux $F_{E>200\,\mathrm{GeV}} = 6.99 \pm 0.15_{stat} \times 10^{-10}\mathrm{cm}^{-2}\mathrm{s}^{-1}$ (corresponding to $\sim 3.6$ C.U.) on 2008 March the 30th. Also

time resolved light curves down to scales of 8 minutes were produced. A hint of fast variability to the scale of $\sim 15$ minutes was observed during the flare occurred on 2008 February the 6th. A multiwavelength study involving either MAGIC VHE data either optical (KVA,*Swift*/UVOT) and X–ray (*Swift*/XRT, RXTE/ASM) data was also performed. Correlations between MAGIC fluxes and the other bands were investigated, finding a moderate correlation (Pearson's index $\rho = 0.68$) between VHE $\gamma$ rays and X rays, a and looser one (Pearson's index $\rho = 0.23$) between VHE $\gamma$ rays and optical fluxes; results in agreement with the predictions of one–zone SSC models.

The main focus of the research was the study of the SED of Mrk 421 in active state.The observational campaign allowed to reconstruct the *simultaneous* SED of Mrk 421 with unprecedented sensitivity; moreover, the low energy threshold of the MAGIC telescope allowed direct sampling of the spectrum close to the peak of the Inverse Compton bump. Eight simultaneous MAGIC and *Swift*/XRT datasets were collected along the whole campaign, and the corresponding MWL SEDs were reconstructed by means of the derived VHE and X–ray spectra. Optical and UV data from KVA and *Swift*/UVOT were also included when available. The theoretical model of Tavecchio et al. (1998), assuming SSC emission, requires high ($\delta \gtrsim 40$) Doppler factors to explain the observed SEDs, where in general the Inverse Compton peak is shifted at high frequencies while the synchrotron peak is located around 1 keV or below. This result holds in spite of the lack of constraints on the variability time scale $t_{var}$.

## 9.1 Role and importance of the simultaneity

Both these works were carried on joining MAGIC–I observations of VHE $\gamma$ rays with contemporary observations performed by other telescopes in softer energy bands. Both campaigns were devoted to transient phenomena in variable sources; this introduced a time–criticality constraint. A careful scheduling of the observations was thus mandatory, coping on one side with the (mainly unpredictable) source evolution, on the other with the (not fully predictable) availability of the involved telescopes.

In the case of OJ 287 the constraint was less severe as:

- there were solid arguments predicting the approximate epoch of the outburst phase, even if the exact onset had to be spotted by means of a systematic monitoring that resulted in the optical trigger from KVA;
- it was expected that the outburst phase would span several weeks;
- as far as MAGIC–I is concerned, it was rather expected that OJ 287 had to be, in the most favorable case, a very dim VHE $\gamma$–ray emitter, detectable at most on very long exposures (only upper limits could be set, indeed).

For all these reasons, in this campaign the time constraint was rather loose: the primary need was to integrate observation time within the time span of the flare, i.e. within the scale of weeks, and also the epoch of observations could be planned in advance.

Completely different was the case of Mrk 421: this source is bright enough to allow time resolved observations at VHE as well, against the rather general rule that in $\gamma$ rays the scarcity of the fluxes force towards long integrations of hours and more, wasting the far better time resolution easily reached, for instance, in X–rays. Moreover, Mrk 421 has a far less predictable light curve and may vary on short timescales; so that in this campaign the density of the monitoring and the fast reaction to triggers were far more crucial than in the other one. Therefore in this case there were both the practical possibility, and the phenomenological and scientific reasons for aiming to a truly simultaneous sampling on the sub–hour scale.

This coordination amongst different instruments, all coping with different schedules, overheads and observing constraints, called for an intense cooperative effort between PIs of the various campaigns, often leading to difficult compromises and, as well, to painful sacrifices regarding the observing time allocated to the other, standalone research projects that every observatory or satellite carries on independently. As the Mrk 421 MWL campaign in 2008 testifies, the harvest in terms of truly simultaneous data was only a small fraction of the whole observing time allocated by the single instruments; due sometimes to technical troubles, sometimes to bad weather, sometimes to time conflicts regarding one or the other of the involved instruments.

This large inefficiency can be addressed only partly to the relative youth of this kind of extremely interactive observation. The ability to handle very dynamic schedules will no doubt grow with the progressive gathering of experience in the field, and with the improvement in sensitivity of detectors and in the smoothness of the data acquisition procedures of the future instruments. All these improvements can be easily foreseen, and will play a role in every instrument or observatory, irrespective of the specific observed band. But some limitations will hardly be bypassed, such as the one related to space–borne instruments, where on one side the large FOV detectors grant time dense coverage but low S/N and poor time, angular and energy resolution; on the other the high quality targeted telescopes are heavily over–booked, and therefore not easily available.

Following all this reasoning, an interesting, even if – apparently – purely practical, question that should be addressed, and answered, is:

- *Is the scientific outcome of such an observational strategy worth of the effort?*

My answer, hopefully only marginally biased by my personal involvement in this research, is positive.

To prove that, one can discuss some of the scientific outcomes of the two campaigns, and try to figure out on one side what (and how relevant) those have added to the previous knowledge of the involved sources; on the other, how much of the learning would have been spoiled if a more stand–alone approach had been assumed, instead of the "simultaneous MWL" one.

It is clear that the broad band SED allows, in principle at least, to disentangle amongst the competing models of *blazars*, as its shape and its evolution are the fingerprints of the processes involving the jet and the central engine.

Just a few examples.

In the case of OJ 287, from the comparison between these observations and previous data (see Figure 7.5) it's evident that the photon index in the soft X–ray band can vary a lot, from very soft and steep ( $\alpha \gg 2$) to very hard and steep ($\alpha \ll 2$). It is the availability of the broad band data, sampling the whole SED, that suggests that in that band the high energy tail of the synchrotron emission and the soft tail of the Inverse Compton bump are blended. The entanglement of the two processes would remain uninterpreted by means, for instance, of soft X–ray observations alone.

Again in the case of OJ 287, in the past the source has been detected by CGRO/EGRET in a high $\gamma$–ray state (see again Figure 7.5). Unfortunately EGRET was no more active in late 2007, *Fermi* was not yet, and AGILE date were proprietary. This, and the non detection at VHE, imply that the constraint on the models deriving from the shape of the IC bump is extremely loose, spoiling not only the possibility of ruling out some emission models, but also, for a given a model, of resolving unambiguously the degeneracy in the accessible parameter space. This strongly proves how the intrinsic power of the MWL approach is spoiled if a crucial portion of the SED, such as the peak of the IC bump, is not observed; as a consequence, this pushes strongly towards seeking the fullest coverage possible, in spite of the difficulty of organizing such difficult campaign.

As far as the Mrk 421 campaign is concerned, the main outcome was a small number of broad band SED involving data in the optical–UV, soft X rays and VHE $\gamma$ rays. Nevertheless, this small dataset constituted a big novelty with respect to the past. Even if Mrk 421 is one of the most observed and studied *blazars*, and its SED has been studied several times in the past, it is worth noticing that the past datasets lacked some of the interesting features that are condensed in these ones. Some were not at all contemporary, others didn't happen to sample high states. In this case, the high VHE state did not only ameliorate the S/N of the MAGIC–I observation; it allowed also to sample the IC bump very close to the peak, that instead slides to softer frequencies when the source is dimmer. This allowed an unprecedented constraint in the parameter space, as usually VHE telescopes sample the decaying tail of the IC bump, so that the position of the peak must be extrapolated and is, at best, only loosely estimated. The availability of si-

multaneous X–ray data, showed how, in spite of the very hard state at high energies, the soft X–ray spectrum, associated to the synchrotron component, was not comparably hard; this leads to a wide separation between the two peaks, that in turn pushes towards very high Doppler factors and/or small magnetic fields. Moreover, the optical–UV data from KVA and/or *Swift*/UVOT helped to constrain the shape of the synchrotron bump in the cases when the X–ray spectrum was softer and the peak lied somewhere below the *Swift*/XRT band. In the other cases, optical–UV data anyway allowed to set the value of the minimum energy of the electron population ($\gamma_{min}$), that is important for deriving further physical quantities such as the total power carried by the jet.

Another, strong proof of how simultaneity is crucial especially when dealing with extreme, unsteady conditions of the source, is well explained by Figure 8.16, where it's easily seen that the X–ray spectrum observed by *Swift*/XRT, although observed only 14 hours after the MAGIC observation, can hardly be considered simultaneous to the VHE one. Should it be simultaneous, extreme Doppler factors or suspiciously large variability scales should be invoked owing to the huge separation in frequency between the two peaks. Perhaps, even after such a small delay, the flare had already faded away and the X–ray telescope sampled a different, dimmer state of the source. Mixing data that sample different states obviously spoil the consistency of the models and the reliability of their predictions, and such an intriguing dataset is nevertheless not worth of deriving any robust conclusion.

A well defined trend is clear in the branch of High Energy Astrophysics dealing with *blazars* and AGN in general: the community is going towards more and more detailed models of the sources; on the other side, more and more refined observations will be possible, with the increased performance of the future detectors. The simultaneity of observations will become more and more mandatory, if we don't want to spoil the predictive power of those models and waste the quality of the data we will collect.

## 9.2 A glimpse on next future

### 9.2.1 MAGIC Stereo

The stronger points of MAGIC–I, clearly evident also in this research, were the low energy threshold achieved, and the high sensitivity. These properties are crucial not only when trying to discover at VHE $\gamma$ rays a distant source with presumably soft spectrum such as OJ 287, but also when observing the bright nearby HBL Mrk 421. In fact, a low threshold favors the observation of the SED next to the region of the IC peak, that can be also directly observed in high states. Moreover, a low threshold and a high sensitivity together allow to enhance the count statistic of photons, that in turn may

help to resolve the light curves on very small time scales. This is of the utmost importance, as it was seen in Section 8.13.1 that the variability time scale is crucial in order to set uniquely the parameters describing the physics of the emitting region of the *blazar* jets.

The already operating MAGIC stereo system surely embodies many significant improvements as far as the lower threshold is concerned, and not only: the background rejection, the angular resolution and the energy resolution also are much improved, so that the performance of MAGIC–I in this kind of research will be undoubtedly surpassed.

## 9.3 Improved MWL techniques

In spite of the good quality of the data obtained, in the MWL campaign conducted by MAGIC on Mrk 421 a few weaknesses emerged in the observing strategies that could be overridden in the next campaigns. For instance, even if the sampling of the MWL spectra in order to reconstruct the SED was undoubtedly careful and well performed, on the other hand the campaign lacked the determination of the variability time scale of the source, in simultaneity to the MWL spectra. As a matter of fact, *Swift*/XRT for both strategic and operational reasons cannot follow individual sources continuously for long times; MAGIC–I could observe a few times Mrk 421 for more than one hour without interruptions, but unfortunately none of the most interesting observations was contemporary to *Swift*. In order to constrain even better the model, this weak point will have to be corrected.

# Appendices

# Appendix A

# Crab Nebula: the VHE standard (?) candle

The Crab Nebula or M1 (Messier, 1781) is a planetary nebula in the Taurus constellation, with equatorial ($J2000$) coordinates ($\alpha$,$\delta$) = ($05^h34^m31.971^s$, $+22°00'52.06$").

An optical image of the Crab Nebula taken from the Hubble Space Telecope is reported in Figure A. It is the remnant of the historical galactic supernova exploded on 1054 A.D. July the 4th, (or probably earlier, see Collins et al., 1999, and references therein), and witnessed by the Chinese astronomers of the Imperial Observatory of Peking, who described it as a new star, six times brighter than Venus, abruptly appearing in the sky and fading away within few weeks. The nebula, is $\sim$ 3 pc across in size, and is located $\sim$ 2 kpc away (Trimble, 1968). The now rapidly expanding ($v \sim 1800$ km/s) gas clouds , before the explosion constituted the external layers of the massive progenitor star, that were ejected as a consequence of the core–collapse mechanism typical of the SNI class of *supernovae*. The innermost region of the Nebula hosts the Crab *pulsar* (PSR B0531+21), a rotating neutron star, relic of the core of the parent star, that emits pulsed, strictly periodic signals in all bands from radio, where it was discovered in 1968 (Staelin & Reifenstein, 1968) to optical (Cocke et al., 1969) to VHE $\gamma$ rays (Aliu et al., 2008) with $\sim$ 30 Hz frequency, and with a characteristic double–peaked phaseogram.

The pulsar radiates due to its rapid spinning movement, provoking the precession of the large magnetic field that the neutron star inherited from the progenitor. The magnetic field accelerates electrons, that heat constantly the inner region of the nebula, where intense synchrotron emission is revealed from its spectrum and polarization. Inverse Compton mechanism is responsible for emission at even higher energies (Aharonian et al., 2004). The broad band SED of Crab Nebula is reported in Figure A.

The Crab Nebula is a well known source of $\gamma$ rays, already observed

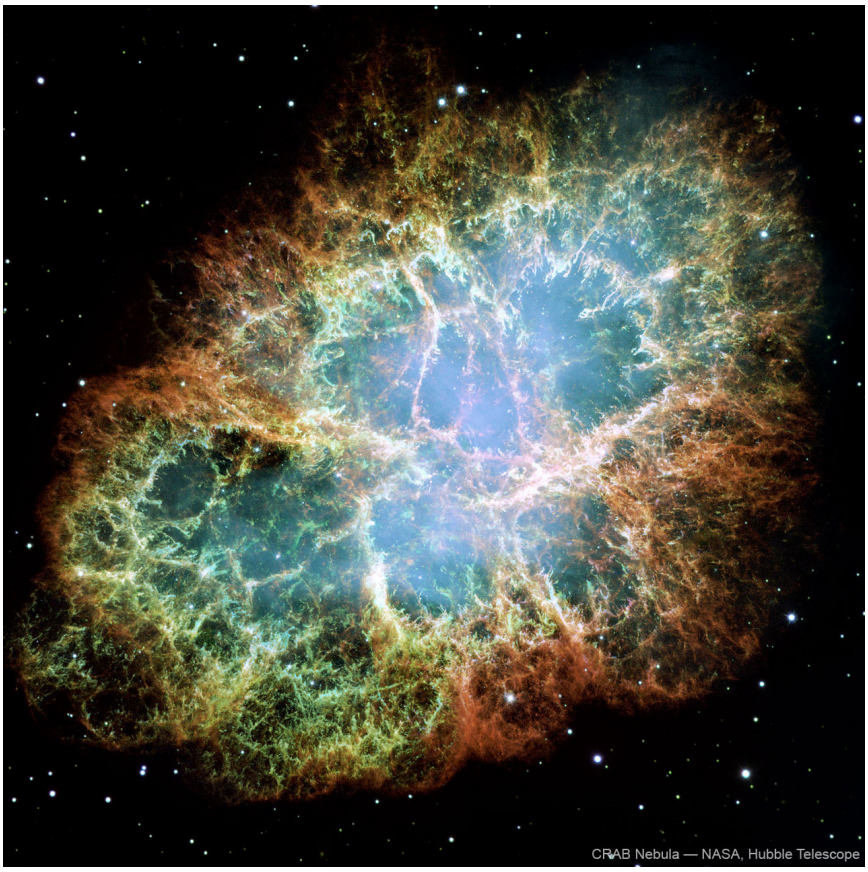


Figure A.1: A true colour optical image of the Crab Nebula taken by the Wide Field Camera onboard the Hubble Space Telescope. The nebula, which is $\sim 3$ pc across, is located $\sim 2$ kpc away in the Taurus constellation. The green, yellow and red filaments concentrated toward the edges of the nebula are remnants of the star that were ejected into space by the explosion.
At the center of the Crab Nebula, but unrevealed in this image, is hosted the Crab Pulsar, a rapidly rotating (30 Hz) neutron star.

by the pioneering observations of the Whipple Telescope (Weekes et al., 1989); as shown Figure A, Cherenkov telescopes actually sample the high energy end of the IC peak. The energy spectrum observed by MAGIC (Albert et al., 2008a) can be described by a curved power law $\mathrm{d}F/\mathrm{d}E = f_0\ (E/300\,\mathrm{GeV})^{[a+b\log_{10}(E/300\,\mathrm{GeV})]}$ with a flux normalization $f_0$ of $(6.0 \pm 0.2_{\mathrm{stat}}) \times 10^{-10}\,\mathrm{cm}^{-2}\mathrm{s}^{-1}\mathrm{TeV}^{-1}$, $a = -2.31 \pm 0.06_{\mathrm{stat}}$ and $b = -0.26 \pm 0.07_{\mathrm{stat}}$. The peak in the spectral energy distribution is estimated at $77 \pm 35\,\mathrm{GeV}$.

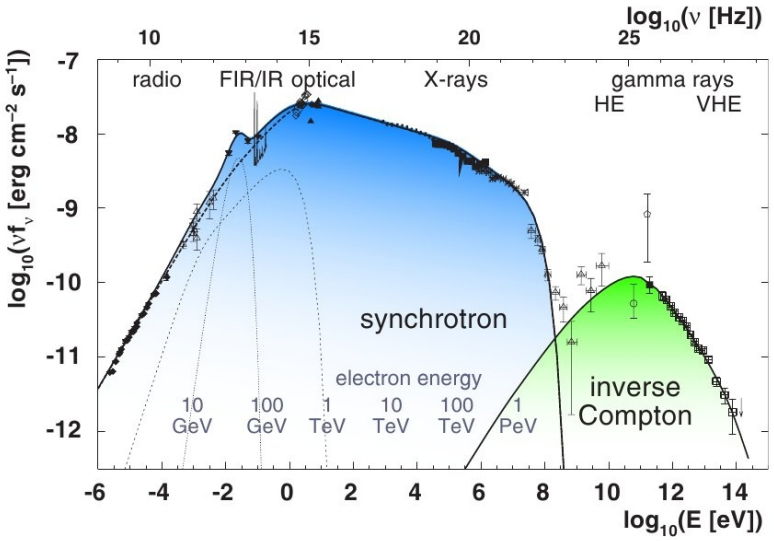


Figure A.2: The broad band SED of Crab Nebula. Two bumps are prominent; the one at lower energies is due to synchrotron emission, while the high energy one is produced by IC processes. Cherenkov telescopes sample the high energy tail of the latter. Taken from Wagner (2006).

## A.1 Crab Nebula as a standard candle for VHE astronomy

Due to its steadiness and relative brightness, Crab Nebula has been until now considered *the* reference standard candle for VHE astronomy (see e.g. Meyer et al., 2010, and references therein). Relative flux calibration is a task of the utmost subtlety in VHE astronomy. In this field, the sources are rare, generally variable to a high extent, and usually observed one at the time; all these factors prevent calibration procedures such as, for instance, those nowadays common in stellar photometry, where primary or secondary calibrators are imaged together and simultaneously to the targets, within the same exposure. Therefore, a careful and more complex procedure has to be applied, checking if the same analysis applied to the datasets of interest, produces results in agreement with the literature when applied to observations of a reference source of known properties, acquired in matching conditions and subjected to the same quality cuts.

This procedure can be accomplished rather smoothly in MAGIC, as the Crab Nebula is routinarily observed during all the MAGIC observation cycles, either due to the scientific interest in the source itself, or due to its utility as a benchmark test for the technical performance of the telescope,

or eventually due to the known need of suitable datasets for cross–checking the analyses. Therefore suitable Crab Nebula observations are usually available, at least for the most usual combinations of parameters (ZA range, cloudiness, moon phase and sky brightness, hardware setup).

## A.2 Analysis cross–checks within this work

In order to validate the quality of the analyses performed for both of the sources studied in the thesis, a sample of MAGIC data from the observations of Crab Nebula was carefully selected

- Wobble mode, as for the sources
- Same trigger setting
- Same zenith angle range
- Same period (implying also similar PSF)
- Comparable mean and variance of trigger rates

The dataset thus selected underwent the same quality cuts of the *blazar* datasets, and Hadronness and Estimated energy were calculated applying the same matrices used for the dataset of OJ 287 and Mrk 421. As a last step the flux, the steadiness of the light curve within errors, the spectrum before and after unfolding were checked, and found in agreement within the errors with the known properties of the source.

## A.3 Breaking news on the steadiness of the Crab Nebula $\gamma$–ray flux

The steadiness of the Crab Nebula has been investigated from times to times in the past years, and also questioned (see for instance Longair, 1992, pp.208–209) but never really doubted except for some episodic events (Wilson–Hodge et al., 2010). Lately some striking evidences for significant flux variations on scales of few days arose in the HE $\gamma$–ray band, discovered by AGILE/GRID (Tavani et al., 2010), and confirmed by *Fermi*/LAT (Buehler et al., 2010). The sharp and rapid flux enhancement in the band accessible to $\gamma$–ray satellites has neither shown any counterpart in the hard X rays (e.g. INTEGRAL Markwardt et al. 2010 or *Swift*/BAT Ferrigno et al. 2010)or in the soft X rays (e.g. RXTE, Shaposhnikov et al. 2010 or *Swift*/XRT Evangelista et al. 2010) or lower bands (Kanbach et al., 2010). Again, no significant variability has been observed in the VHE domain by MAGIC (Mariotti, 2010d) or VERITAS (Ong, 2010). On the contrary, the

TeV detector array ARGO–YBT (De Mitri, 2007), sensitive in the harder 0-4–10 TeV band, has claimed a contemporary rise in the flux from Crab Nebula (Aielli et al., 2010). The field remains open and intriguing, not only for its practical side effects; actually, it has been pointed out that the process producing such variations on dayscales seems unrelated to the inner pulsar (Hays et al., 2010). Therefore, some mechanism must be imagined capable of acting in some portion of the nebula, that as a whole has dimensions not compatible with such short timescales due to the light crossing time constraint.

In any case many calibration issues that affected in the past years many instruments, mainly X–ray telescopes, could be related to formerly unrecognized variability in the Crab Nebula flux, possibly on the 10–20 % level; some slight (3.5% $\mathrm{yr}^{-1}$) but steady variations over the last years have been pointed out also in X–rays, in a careful re–analysis triggered by the AGILE discovery (Wilson–Hodge et al., 2010). Even if the VHE band seems not involved in this variability episode, this pushes towards the opportunity of adding other, new standard candles, to be used as cross–checks for Crab Nebula. For instance, given the energy threshold and sensitivity of the present and, better, future generation of IACTs, the relatively bright and seemingly steady intermediate redshift ($z \simeq 0.40$ Danforth et al., 2010) HBL PG 1553+113 (jointly discovered by HESS Aharonian et al. 2006a and MAGIC Albert et al. 2007a could be reckoned a viable candidate for this task.

# Appendix B

# Camera Inhomogeneity

The term camera inhomogeneity refers to the discrepancy between the response of the actual PMT camera and an ideal camera, with acceptance described by a simple, symmetric function of the camera geometry and of the trigger region.

If we consider the distribution of the centroid of Hillas images on the camera for the events of a real dataset, it actually shows deviations from the ideal, uniform behavior, that increase at lower SIZE.

In Figure B.1 both the so–called "Center of Gravity plot" (on the left), and its projection on the azimuthal coordinate of a polar system centered at the camera center ($\phi$ plot, on the right) are displayed. From the former, it's evident that deviation from uniformity appear; the latter shows that some directions on the camera are preferred and other are depleted). The effect is more severe for low SIZE (upper panels) than for high SIZE(lower panels) events.

Factors that may contribute to camera inhomogeneity are:

- "Dead" pixels: some pixels on the camera do not show any signal, even during calibration.. This can be due to a broken PMT, poor optical link or some other defect along the acquisition stream for that channel.
- Trigger inefficiencies: the 19 macrocells of the trigger show different trigger rates
- Poor flatfielding of the camera: differences in PMTs behavior (e.g. quantum efficiency, gain) and differences in the readout chain force an individual setting of HV for each pixel to have the same signal at trigger level

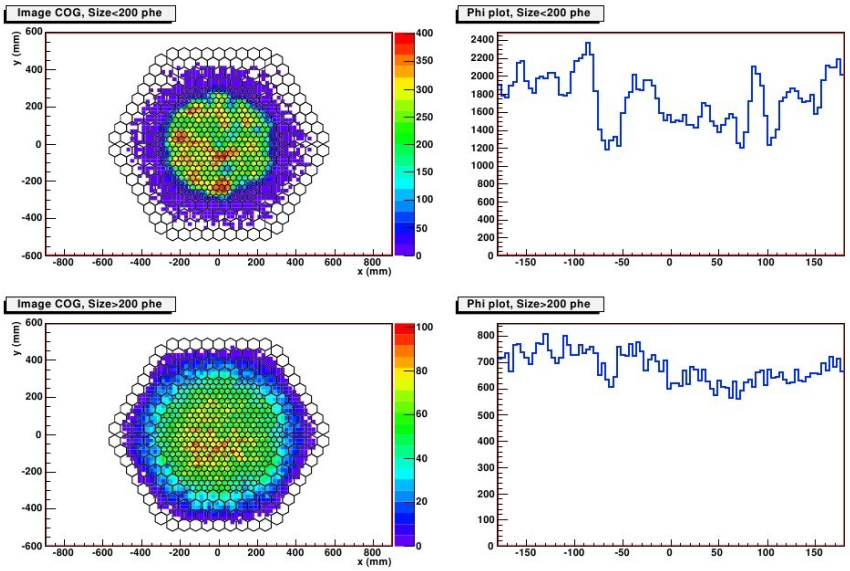


Figure B.1: Plots of the distribution of the centroids of shower images on the camera, for the Mrk 421 dataset of 2008 April the 4th. The two–dimensional distribution of centroids is plotted on the left (Center of Gravity plot), while its prjection in the azimuthal coordinate of a polar system centered on the camera center is drawn on the right. Events below and above a SIZE =200 phe$^-$ threshold populate the upper and lower panels respectively. Above 200 phe$^-$ the distribution is rather uniform and radially symmetric, while below this level the inhomogeneity is severe.

# Appendix C

# Optical Performance of the telescope

Two important parameters related to the optical performance of the telescope, and relevant for the data analysis, are the optical Point Spread Function (PSF) and the Overall Light Conversion Factor (OLCF).

The PSF is a measure of the focusing accuracy of the reflector; it can be defined as the diameter of the *Airy disk* produced on the camera plane by a point source shining the reflector.

The OLCF instead depends from the quality of the reflecting surface, and is defined as the ratio between the total light concentrated into the camera with respect and the expected light.

These two parameters can be monitored by means of a dedicated analysis of the recorded events due to background muons, as described in (Meyer, 2005).

Briefly, the analysis of the Cherenkov image of muons is performed on a set of dedicated geometric parameters, namely:

- Radius: the radius of the ring
- ArcWidth: the width of the ring
- ArcPhi: the opening angle of the ring
- MuonSize: the total light content of the ring, measured in photoelectrons

The muon events are selected by cuts in these image parameters, then the distribution of parameters for simulated muon events are confronted with the ones from real muons. A possible set of cuts to separate muon from non-muon events may be:

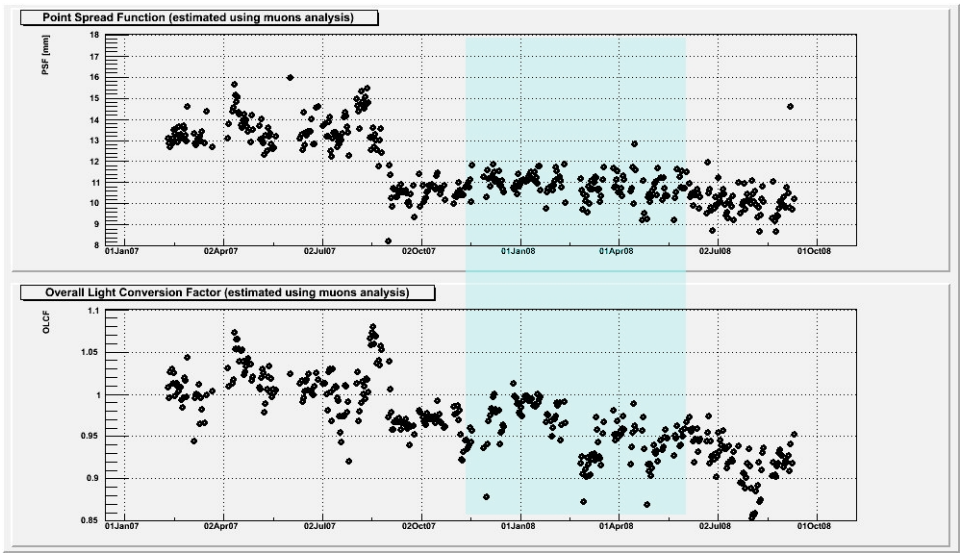


Figure C.1: **Upper panel**: daily plot of the PSF value as calculated from muon ring analysis; the improvement in the PSF in August 2007 due to a new version of the AMC is clearly visible. The PSF has remained quite constant on a value $\sim 10.5$ all along the period of the observations analyzed in this thesis, that is evidentiated by the light blue shaded region. **Lower Panel**: daily plot of the OLCF value as calculated from muon analysis. Sudden drops attribuible to calima can be seen in summer 2007.

- 180 mm $<$ Radius $<$ 400 mm ($0.61° <$ Radius $< 1.35°$)
- deviation $< 0.35$ mm
- $0.04° <$ ArcWidth $< 0.20°$
- ArcPhi $\geq 198°$

In particular, for the PSF the width of the muon rings is considered.

This analysis is performed on a routinely basis each observation night. In figure C.1 it can be noted that the optical PSF was rather constant before August 2007, and has been also rather constant after, but on a rather smaller value due to a significant improvement in the AMC.

It can be noted that along the whole period relevant for the analyses this thesis is focused on, both parameters have remained rather constant, except for fluctuations.

# Bibliography


Aarseth, S. J. 2008, IAU Symposium, 246, 437

Abdo, A. A., et al. 2010, ApJSS, 188, 405

Adelman-McCarthy, J. K., et al. 2008, ApJSS, 175, 297

Aharonian, F. A. 2000, *New Astronomy*, 5, 377

Aharonian, F., et al. 2004, ApJ, 614, 897

Aharonian, F., et al. 2006a, A&A, 448, L19

Aharonian, F., et al. 2006b, Physical Review Letters, 97, 221102

Aharonian, F., et al. 2007, ApJL, 664, L71

Aielli, G., et al. 2010, The Astronomer's Telegram, 2921, 1

Albert, J., et al. 2006, ApJL, 648, L105

Albert, J., et al. 2007a, ApJL, 654, L119

Albert, J., et al. (the MAGIC Collaboration) 2007b, ApJ, 663, 125

Albert, J., et al. 2007c, Nuclear Instruments and Methods in Physics Research A, 583, 494

Albert, J., et al. 2007d, ApJL, 666, L17

Albert, J., et al. 2007e, ApJ, 667, 358

Albert, J., et al. 2007f, ApJ, 669, 862

Albert, J. et al. (the MAGIC Collaboration) 2008a, ApJ, 674, 1037

Albert, J. et al. (the MAGIC Collaboration), 2008b, Nucl. Instr. Meth. A, 588, 424

Aliu, E., et al. 2008, Science, 322, 1221

Aliu, E. et al. (the MAGIC Collaboration), 2009a, Astropart. Phys., 30, 293

Aliu, E., et al. 2009b, ApJL, 692, L29

Anderhub, H., et al. 2009a, ApJL, 704, L129

Anderhub, H., et al. 2009b, ApJ, 705, 1624

Antonucci, R. 1993, ARA&A, 31, 473

Antonucci, R. R. J., & Miller, J. S. 1985, ApJ, 297, 621

Anykeyev, V. B., Spiridonov, A. A., & Zhigunov, V. P. 1991, Nuclear Instruments and Methods in Physics Research A, 303, 350

Atwood, W. B., et al. 2009, ApJ, 697, 1071

Bahcall, J. N., Kirhakos, S., & Schneider, D. P. 1994, ApJL, 435, L11

Barthelmy, S. D., et al. 2005, Space Sci.Rev., 120, 143

Beatty, J. 1999, International Cosmic Ray Conference, 5, 61

Bednarek, W. 1998, A&A, 336, 123

Bednarek, W., & Protheroe, R. J. 1997, MNRAS, 292, 646

Begelman, M. C., Blandford, R. D., & Rees, M. J. 1984, Reviews of Modern Physics, 56, 255

Begelman, M. C., Fabian, A. C., & Rees, M. J. 2008, MNRAS, 384, L19

Bell, A. R. 1978, MNRAS, 182, 147

Bennett, A. S. 1962, MmRAS, 68, 163

Bernlohr, K. 2000, Astroparticle Physics, 12, 255

Bertero, M., 1988, INFN/TC-88/2

Bessell, M. S. 1979, *PASP*, 91, 589

Binette, L., Dopita, M. A., & Tuohy, I. R. 1985, ApJ, 297, 476

Blackett, P. M. S. 1948, *The Emission Spectra of the Night Sky and Aurorae*, 34

Blandford, R. 2005, Growing Black Holes: Accretion in a Cosmological Context, 477

Blandford, R. D., & Ostriker, J. P. 1978, ApJL, 221, L29

Blandford, R. D., & Payne, D. G. 1982, MNRAS, 199, 883

Blandford, R. D., & Znajek, R. L. 1977, MNRAS, 179, 433

Błażejowski, M., Sikora, M., Moderski, R., & Madejski, G. M. 2000, ApJ, 545, 107

Błażejowski, M., et al. 2005, ApJ, 630, 130

Bloom, S. D. & Marscher, A. P. 1996, ApJ, 461, 657

Bonnoli, G., Ghisellini, G., Foschini, L., Tavecchio, F., & Ghirlanda, G. 2010, MNRAS, 1476

Boettcher, M., & Dermer, C. D. 1998, ApJL, 501, L51

Böttcher, M. 2005, ApJ, 621, 176

Bradt, H. V., Rothschild, R. E., & Swank, J. H. 1993, A&AS, 97, 355

Breiman, L., 2001, Machine Learning, 45, 4

Buckley, J. H. 1999, Astroparticle Physics, 11, 119

Buehler, R., D'Ammando, F., & Hays, E. 2010, The Astronomer's Telegram, 2861, 1

Burrows, D. N., et al. 2005, Space Sci.Rev., 120, 165

Caraveo, P., et al. 2010, The Astronomer's Telegram, 2903, 1

Casandjian, J.-M., & Grenier, I. A. 2008a, A&A, 489, 849

Casandjian, J.-M., & Grenier, I. A. 2008b, VizieR Online Data Catalog, 348, 90849

Chantell, M. C., et al. 1998, Nuclear Instruments and Methods in Physics Research A, 408, 468

Charlot, P., Gabuzda, D. C., Sol, H., Degrange, B., & Piron, F. 2006, A&A, 457, 455

Chung, C. H., & AMS Collaboration 2006, ESA Special Publication, 637,

Ciprini, S., et al. 2008, Blazar Variability across the Electromagnetic Spectrum,

Cocke, W. J., Disney, M. J., & Taylor, D. J. 1969, Nature, 221, 525

Collins, G. W., II, Claspy, W. P., & Martin, J. C. 1999, *PASP*, 111, 871

Cortina, J., et al. 2005, International Cosmic Ray Conference, 5, 359

Costamante, L., et al. 2001, A&A, 371, 512

Cronin, J. W., Gaisser, T. K., & Swordy, S. P. 1997, Scientific American, 276, 32

CTA Consortium, T. 2010, arXiv:1008.3703

Cui, W. 2004, ApJ, 605, 662

Danaher, S., Fegan, D. J., Porter, N. A., Weekes, T. C., & Cole, T. 1982, Solar Energy, 28, 335

Danforth, C. W., Keeney, B. A.,Stocke, J. T., Shull, J. M., & Yao, Y. 2010, ApJ, 720, 976

Daum, A., et al. 1997, Astroparticle Physics, 8, 1

De Mitri, I., & ARGO-YBJ Collaboration 2007, Nuclear Physics B Proceedings Supplements, 165, 66

de Vaucouleurs, G., de Vaucouleurs, A., Corwin, H. G., Jr., Buta, R. J., Paturel, G., & Fouque, P. 1991, Volume 1-3, XII, 2069 pp. 7 figs.. Springer-Verlag Berlin Heidelberg New York,

Dermer, C. D. & Schlickeiser, R. 1993, ApJ, 416, 458

Dermer, C. D., Sturner, S. J., & Schlickeiser, R. 1997, ApJSS, 109, 103

Domingo-Santamaria, E., Flix, J., Rico, J., Scalzotto, V., & Wittek, W. 2005, International Cosmic Ray Conference, 5, 363

Domínguez, A., et al. 2010, MNRAS, 1665

Donato, D., Ghisellini, G., Tagliaferri, G., & Fossati, G. 2001, A&A, 375, 739

Donnarumma, I., et al. 2009, ApJL, 691, L13

Dunlop, J. S., McLure, R. J., Kukula, M. J., Baum, S. A., O'Dea, C. P., & Hughes, D. H. 2003, MNRAS, 340, 1095

Elterman, L. 1951, *J. Geophys. Res.*, 56, 509

Evangelista, Y., et al. 2010, The Astronomer's Telegram, 2866, 1

Falomo, R., Kotilainen, J. K., Pagani, C., Scarpa, R., & Treves, A. 2005, *Multiwavelength Mapping of Galaxy Formation and Evolution*, 380

Fan, X., et al. 1999, Astronom. Journal, 118, 1

Fanaroff, B. L., & Riley, J. M. 1974, MNRAS, 167, 31P

Fegan, D. J. 1997, Journal of Physics G Nuclear Physics, 23, 1013

Fermi, E. 1954, ApJ, 119, 1

Ferrarese, L., & Ford, H. 2005, Space Sci.Rev., 116, 523

Ferrigno, C., Walter, R., Bozzo, E., & Bordas, P. 2010, The Astronomer's Telegram, 2856, 1

Finke, J. D., Dermer, C. D., Böttcher, M. 2008, ApJ, 686, 181

Fiorucci, M., & Tosti, G. 1996, A&AS, 116, 403

Fomin, V. P., Stepanian, A. A., Lamb, R. C., Lewis, D. A., Punch, M., & Weekes, T. C. 1994, Astroparticle Physics, 2, 137

Foschini, L., Tagliaferri, G., Ghisellini, G., Ghirlanda, G., Tavecchio, F., & Bonnoli, G. 2010, MNRAS, 408, 448

Fossati, G., Maraschi, L., Celotti, A., Comastri, A., & Ghisellini, G. 1998, MNRAS, 299, 433

Fossati, G., et al. 2008, ApJ, 677, 906

Franceschini, A., Rodighiero, G., & Vaccari, M. 2008, A&A, 487, 837

Funk, S. 2005, International Cosmic Ray Conference, 4, 123

Gaidos, J. A., et al. 1996, *Nature*, 383, 319

Gaug, M., Bartko, H., Cortina, J., & Rico, J. 2005, International Cosmic Ray Conference, 5, 375

Gehrels, N., Chipman, E., & Kniffen, D. 1994, ApJSS, 92, 351

Gehrels, N., et al. 2004, ApJ, 611, 1005

Gehrels, N., & Michelson, P. 1999, Astroparticle Physics, 11, 277

Georganopoulos, M., & Kazanas, D. 2003, ApJL, 594, L27

Ghisellini, G., Celotti, A., Fossati, G., Maraschi, L., & Comastri, A. 1998, MNRAS, 301, 451

Ghisellini, G., & Celotti, A. 2001, A&A, 379, L1

Ghisellini, G., & Madau, P. 1996, MNRAS, 280, 67

Ghisellini, G., Maraschi, L., & Dondi, L. 1996, A&AS, 120, 503

Ghisellini, G., & Tavecchio, F. 2008, MNRAS, 386, L28

Ghisellini, G., Tavecchio, F., & Chiaberge, M. 2005, A&A, 432, 401

Giacconi, R., & Rossi, B. 1960, *J. Geophys. Res.*, 65, 773

Gilmore, R. C., Madau, P., Primack, J. R., Somerville, R. S., & Haardt, F. 2009, MNRAS, 399, 1694

Giommi, P., & Padovani, P. 1994, MNRAS, 268, L51

Giroletti, M., Giovannini, G., Taylor, G. B., & Falomo, R. 2004, ApJ, 613, 752

Goebel, F., Bartko, H., Carmona, E., & et al. 2008, International Cosmic Ray Conference, 3, 1481

Goodman, J., et al. 1993, BAAS, 25, 921

Goulding, A. D., Alexander, D. M., Lehmer, B. D., & Mullaney, J. R. 2010, MNRAS, 406, 597

Guzik, T. G., et al. 2004, Advances in Space Research, 33, 1763

Hartman, R. C., et al. 1999a, ApJSS, 123, 79

Hartman, R. C., et al. 1999b, VizieR Online Data Catalog, 212, 30079

Hayashida, M., et al. 2009, arXiv:0907.1343

Hays, E., Buehler, R., D'Ammando, F., Grove, J. E., & Ray, P. S. 2010, The Astronomer's Telegram, 2879, 1

Hazard, C., Mackey, M. B., & Shimmins, A. J. 1963, Nature, 197, 1037

Heck, D., Knapp, J., Capdevielle, J. N., Schatz, G., & Thouw, T. 1998, *CORSIKA: a Monte Carlo code to simulate extensive air showers.*, 1998

Hess. V., 1913, Phys. Zeit. 13, 1084

HESS Collaboration 2000, American Institute of Physics Conference Series, 515, 500

Hewitt, A., & Burbidge, G. 1989a, A new optical catalog of QSO (1989), 0

Hewitt, A., & Burbidge, G. 1989b, ApJSS, 69, 1

Hillas, A. M. 1985, International Cosmic Ray Conference, 3, 445

Hogg, D. W. 1999, arXiv:astro-ph/9905116

Hollander, M., Wolfe, D. A., *Nonparametric statistical methods*, Wiley (1973)

Hsu, C. C., et al. 2009, arXiv:0907.0893

Hubble, E. P. 1926, ApJ, 63, 236

Hubble, E. P. 1929a, ApJ, 69, 103

Hubble, E. 1929b, Proceedings of the National Academy of Science, 15, 168

Hughes, P. A., Aller, H. D., & Aller, M. F. 1998, ApJ, 503, 662

Idesawa, E., et al. 1997, PASJ, 49, 631

Igumenshchev, I. V., & Abramowicz, M. A. 1999, MNRAS, 303, 309

Isobe, N., Tashiro, M., Sugiho, M., & Makishima, K. 2001, PASJ, 53, 79

Johnston, K. J., et al. 1995, Astronom. Journal, 110, 880

Kanbach, G., et al. 1988, Space Sci.Rev., 49, 69

Kanbach, G., Kruehler, T., Steiakaki, A., & Mignani, R. 2010, The Astronomer's Telegram, 2867, 1

Kalberla, P. M. W., Burton, W. B., Hartmann, D., Arnal, E. M., Bajaja, E., Morras, R., Pöppel, W. G. L. 2005, A&A, 440, 775

Karlsson, N., for the VERITAS collaboration 2009, arXiv:0912.3807

Kataoka, J., *Ph. D. Thesis*, 2000, Univ. of Tokyo

Katz, J. I. 1997, ApJ, 478, 527

Kellermann, K. I., Sramek, R., Schmidt, M., Shaffer, D. B., & Green, R. 1989, Astronom. Journal, 98, 1195

Kinney, A. L., Calzetti,D., Bohlin, R. C., McQuade, K., Storchi-Bergmann, T., & Schmitt, H. R. 1996, ApJ, 467, 38

Kneiske, T. M., & Dole, H. 2010, A&A, 515, A19

Konopelko, A., Mastichiadis, A., Kirk, J., de Jager, O. C., & Stecker, F. W. 2003, ApJ, 597, 851

Kormendy, J., & Gebhardt, K. 2001, 20th Texas Symposium on relativistic astrophysics, 586, 363

Kounine, A. 2010, arXiv:1009.5349

Krawczynski, H., et al. 2004, ApJ, 601, 151

Krawczynski, H., Coppi, P. S., & Aharonian, F. 2002, MNRAS, 336, 721

Krennrich, F., et al. 2004, *New Astronomy Review*, 48, 345

Kusunose, M., & Takahara, F. 2006, ApJ, 651, 113

Laor, A. 2000, ApJL, 543, L111

Lehto, H. J., & Valtonen, M. J. 1996, ApJ, 460, 207

Lessard, R. W., Buckley, J. H., Connaughton, V., & Le Bohec, S. 2001, Astroparticle Physics, 15, 1

Li, T.-P., & Ma, Y.-Q. 1983, ApJ, 272, 317

Liang, C., & Jin-Ming, B. 2010, arXiv:1009.2321

Liu, F. K., Liu, B. F., & Xie, G. Z. 1997, A&AS, 123, 569

Lockman, F. J., & Savage, B. D. 1995, ApJSS, 97, 1

Longair, M. S. 1992, High Energy Astrophysics,Vol. 1:*Particles, photons and their detection* Cambridge University Press, 1992

Madau, P., & Pozzetti, L. 2000, MNRAS, 312, L9

MAGIC Collaboration, et al. 2008, Science, 320, 1752

MAGIC Collaboration, et al. 2010, arXiv:1004.1093

Majumdar, P., Moralejo, A., Bigongiari, C., Blanch, O., & Sobczynska, D. 2005, International Cosmic Ray Conference, 5, 203

Mannheim, K., Biermann, P. L., & Kruells, W. M. 1991, A&A, 251, 723

Mannheim, K. 1993, A&A, 269, 67

Maraschi, L., et al. 1999, ApJL, 526, L81

Maraschi, L., Ghisellini, G., & Celotti, A. 1992, ApJL, 397, L5

Maraschi, L., & Tavecchio, F. 2003, ApJ, 593, 667

Mariotti, M. 2010a, The Astronomer's Telegram, 2510, 1

Mariotti, M. 2010b, The Astronomer's Telegram, 2684, 1

Mariotti, M., 2010c, The Astronomer's Telegram, 2916, 1

Mariotti, M., 2010d, The Astronomer's Telegram, 2967, 1

Markarian, B. E. 1967, Astrofizika, 3, 55

Markwardt, C. B., Barthelmy, S. D., & Baumgartner, W. H. 2010, The Astronomer's Telegram, 2858, 1

Marscher, A. P., et al. 2008, Nature, 452, 966

Marziani, P., Sulentic, J. W., Dultzin-Hacyan, D., Calvani, M., & Moles, M. 1996, ApJSS, 104, 37

Mazin, D., & et al. 2005, International Cosmic Ray Conference, 4, 331

Mazin, D., PhD Thesis, Technische Universität, Munchen, 2007

Mazin, D., & Raue, M. 2007, A&A, 471, 439

Messier, C., *Catalogue des nebuleuses et des amas d'etoiles*, 1781

Meyer, M., MAGIC Internal Note, TDAS 05–10, 2005

Meyer, M., Horns, D., & Zechlin, H. -. 2010, arXiv:1008.4524

Mirzoyan, R., et al. 1994, Nuclear Instruments and Methods in Physics Research A, 351, 513

Mirzoyan, R., Sobczynska, D., Lorenz, E., & Teshima, M. 2006, Astroparticle Physics, 25, 342

Misner, C. W., Thorne, K. S., & Wheeler, J. A., *Gravitation*, 1973, San Francisco: W.H. Freeman and Co.

Mücke, A. et al. 2003, APh, 18, 593

Neronov, A., & Semikoz, D. V. 2009, *Phys. Rev.* D, 80, 123012

Neronov, A., & Vovk, I. 2010, Science, 328, 73

Nilsson, K., Pasanen, M., Takalo, L. O., Lindfors, E., Berdyugin, A., Ciprini, S., & Pforr, J. 2007, A&A, 475, 199

Ong, R. A., 2010, The Astronomer's Telegram, 2968, 1

Orienti, M., Migliori, G., Siemiginowska, A., & Celotti, A. 2010, arXiv:1006.5296

Osterbrock, D. E., & Ferland, G. J. 2006, *Astrophysics of gaseous nebulae and active galactic nuclei*, 2nd. ed. by D.E. Osterbrock and G.J. Ferland. Sausalito, CA: University Science Books, 2006,

Pacini, D., 1912, D. Nuovo Cimento VI/3, 93

Pacini, D., & De Angelis, c. b. A. 2010, arXiv:1002.1810

Padovani, P., & Giommi, P. 1995, ApJ, 444, 567

Padovani, P. 2007, Ap&SS, 309, 63

PAMELA Collaboration 1999, International Cosmic Ray Conference, 5, 96

Peebles, P. J. E.*Principles of physical cosmology*, 1993, Princeton Series in Physics, Princeton, NJ

Pei, Y. C. 1992, ApJ, 395, 130

Perola, G. C. 1969, A&A, 3, 481

Petrosian, A. McLean, B., Allen, R. J., & MacKenty, J. W. 2007, ApJSS, 170, 33

Pichel, A., & for the VERITAS Collaboration 2009, arXiv:0908.0010

Piner, B. G., & Edwards, P. G. 2004, ApJ, 600, 115

Poole, T. S., et al. 2008, MNRAS, 383, 627

Prandini, E., Bonnoli, G., Maraschi, L., Mariotti, M., & Tavecchio, F. 2010, MNRAS, 405, L76

Primack, J. R., Bullock, J. S., & Somerville, R. S. 2005, High Energy Gamma-Ray Astronomy, 745, 23

Pühlhofer, G., et al. 2003, Astroparticle Physics, 20, 267

Punch, M., et al. 1992, *Nature*, 358, 477

Pursimo, T., et al. 2000, A&AS, 146, 141

Quinn, J., et al. 1996, ApJL, 456, L83

Ravasio, M., Tagliaferri, G., Ghisellini, G., & Tavecchio, F. 2004, A&A, 424, 841

Rebillot, P. F., et al. 2006, ApJ, 641, 740

Rees, M. J. 1966, Nature, 211, 468

Rees, M. J. 1984, ARA&A, 22, 471

Rieger, F. M., Bosch-Ramon, V., & Duffy, P. 2007, Ap&SS, 309, 119

Rolke, W. A., López, A. M., & Conrad, J. 2005, Nuclear Instruments and Methods in Physics Research A, 551, 493

Roming, P. W. A., et al. 2005, Space Sci.Rev., 120, 95

Roncadelli, M., de Angelis, A., & Mansutti, O. 2009, Nuclear Physics B Proceedings Supplements, 188, 49

Rybicki, G. B., & Lightman, A. P. 1986, *Radiative Processes in Astrophysics*, Wiley-VCH

Satalecka, K., et al. 2009, American Institute of Physics Conference Series, 1112, 223

Schlegel, D. J., Finkbeiner, D. P., & Davis, M. 1998, ApJ, 500, 525

Schmelling, M. 1994, Nuclear Instruments and Methods in Physics Research A, 340, 400

Schmidt, M. 1963, Nature, 197, 1040

Schönfelder, V., et al. 1984, IEEE Transactions on Nuclear Science, 31, 766

Schubnell, M. S., et al. 1996, ApJ, 460, 644

Seta, H., et al. 2009, PASJ, 61, 1011

Shakura, N. I., & Sunyaev, R. A. 1973, A&A, 24, 337

Shaposhnikov, N., Jahoda, K., Swank, J., Strohmayer, T., Markwardt, C., & Weisskopf, M. 2010, The Astronomer's Telegram, 2872, 1

Shrader, C. R., Hartman, R. C., & Webb, J. R. 1996, A&AS, 120, 599

Skiff, B. A. 2007, VizieR Online Data Catalog, 2277, 0

Skrutskie, M. F., et al. 2006, Astronom. Journal, 131, 1163

Sikora, M., Moderski, R., & Madejski, G. M. 2008, ApJ, 675, 71

Sikora, M., Stawarz, Ł., Moderski, R., Nalewajko, K., & Madejski, G. M. 2009, ApJ, 704, 38

Sillanpaa, A., Haarala, S., Valtonen, M. J., Sundelius, B., & Byrd, G. G. 1988, ApJ, 325, 628

Sillanpaa, A., et al. 1996a, A&A, 305, L17

Sillanpaa, A., et al. 1996b, A&A, 315, L13

Smith, D. A. 2006, arXiv:astro-ph/0608251

Staelin, D. H., & Reifenstein, E. C., III 1968, Science, 162, 1481

Stecker, F. W., de Jager, O. C., & Salamon, M. H. 1992, ApJL, 390, L49

Stecker, F. W., Malkan, M. A., & Scully, S. T. 2006, ApJ, 648, 774

Stickel, M., Fried, J. W., & Kuehr, H. 1989, A&AS, 80, 103

Sundelius, B., Wahde, M., Lehto, H. J., & Valtonen, M. J. 1997, ApJ, 484, 180

Tagliaferri, G., et al. 2008, ApJ, 679, 1029

Takahashi, T., et al. 2000, ApJL, 542, L105

Tanihata, C., et al. 2000, ApJ, 543, 124

Tavani, M., et al. 2008, Nuclear Instruments and Methods in Physics Research A, 588, 52

Tavani, M., et al. 2010, The Astronomer's Telegram, 2855, 1

Tavecchio, F., & Ghisellini, G. 2008, MNRAS, 385, L98

Tavecchio, F., Ghisellini, G., Bonnoli, G., & Ghirlanda, G. 2010a, MNRAS, 405, L94

Tavecchio, F., Ghisellini, G., Bonnoli, G., & Foschini, L. 2010b, arXiv:1009.1048

Tavecchio, F., Ghisellini, G., Foschini, L., Bonnoli, G., Ghirlanda, G., & Coppi, P. 2010c, MNRAS, 406, L70

Tavecchio, F., Ghisellini, G., Ghirlanda, G., Foschini, L., & Maraschi, L. 2010d, MNRAS, 401, 1570

Tavecchio, F., Maraschi, L., & Ghisellini, G. 1998, ApJ, 509, 608

Tescaro, D., Bartko, H., Galante, N., & et al. 2008, International Cosmic Ray Conference, 3, 1393

Tikhonov, A. N., & Arsenin, V. Ja., 1979, *Methods of Solution of Ill–posed Problem – M*, Nauka

Torres, D. F. 2003, arXiv:astro-ph/0308069

Torres, D. F. 2009, arXiv:0909.4999

Treves, A., Falomo, R., & Uslenghi, M. 2007, A&A, 473, L17

Trimble, V. 1968, Astronom. Journal, 73, 535

Urry, C. M., & Padovani, P. 1995, *PASP*, 107, 803

Ushio, M., et al. 2009, ApJ, 699, 1964

Valtaoja, E., Teräsranta, H., Tornikoski, M., Sillanpää, A., Aller, M. F., Aller, H. D., & Hughes, P. A. 2000, ApJ, 531, 744

Valtonen, M. J., et al. 2006, ApJL, 643, L9

Valtonen, M. J., et al. 2006b, ApJ, 646, 36

Valtonen, M. J. 2007, ApJ, 659, 1074

Valtonen, M. J., et al. 2008, Nature, 452, 851

van den Bergh, S. 1998, Galaxy morphology and classification, Cambridge University Press, 1998

Vanden Berk, D. E., et al. 2001, Astronom. Journal, 122, 549

Vanden Berk, D., Wilhite, B., Kron, R., Ivezic, Z., Pereyra, N., & SDSS 2004, Bulletin of the American Astronomical Society, 36, 1548

Véron-Cetty, M.-P., & Véron, P. 2006, A&A, 455, 773

Vestergaard, M., Fan, X., Tremonti, C. A., Osmer, P. S., & Richards, G. T. 2008, ApJL, 674, L1

Vietri, M. *Astrofisica delle alte energie*, 2006, Bollati Boringhieri

Vincent, P. 2005, International Cosmic Ray Conference, 5, 163

Wagner, R. M., PhD Thesis, Technische Universität, Munchen, 2006

Watanabe, M., et al. 2005, *PASP*, 117, 870

Weekes, T. C., & Turver, K. E. 1977, Recent Advances in Gamma-Ray Astronomy, 124, 279

Weekes, T. C., et al. 1989, ApJ, 342, 379

Weekes, T. C. 2005, arXiv:astro-ph/0508253

Wilson-Hodge, C. A., et al. 2010, arXiv:1010.2679

Wolter, H. 1952, Annalen der Physik, 445, 94

Yodh, G. B. 1996, Space Sci.Rev., 75, 199

Zavrtanik, D. 2000, Nuclear Physics B Proceedings Supplements, 85, 324

Zeldovich, I. B., Ruzmaikin, A. A., & Sokolov, D. D. 1983, *The Fluid Mechanics of Astrophysics and Geophysics*, Volume 3

Zhang, Y. H. 2002, MNRAS, 337, 609

# List of Figures

# List of Tables

# Glossary

**a.s.l.** above sea level, 61
**AGN** Active Galactic Nucleus, 18
**ASI** Agenzia Spaziale Italiana [Italian Space Agency], 7

**BAT** Burst Alert Telescope, 138
**BH** Black Hole, 23
**BLR** Broad Line Region, 19

**C.U.** Crab Units, 101
**CGRO** Compton Gamma–Ray Observatory, 6
**CL** Confidence Level, 107
**CMB** Cosmic Microwave Background, 48

**DT** Discriminator Threshold, 68

**EAS** Extended Air Shower, 50
**EBL** Extragalactic Background Light, 45
**EC** External Compton, 35
**EGRET** Energetic Gamma–Ray Experiment, 7
**EW** Equivalent Width, 21

**FADC** Fast Analog to Digital Converter, 67
**FOV** Field Of View, 8
**FRI** Fanaroff–Riley I, 20
**FRII** Fanaroff–Riley II, 20
**FSRQ** Flat Spectrum Radio *Quasar*, 21

**GBM** Gamma–ray Burst Monitor, 7
**GLAST** Gamma–Ray Large Area Space Telescope, 6
**GLAST** Gamma–ray Large Area Space Telescope, 7
**GLIMOS** Group Leader In Matter of Safety, 71
**GRB** Gamma–Ray Bursts, 6

**HBL** High–peaked BL Lac, 29
**HE** High Energy, 2
**HEGRA** High Energy Gamma Ray Astronomy, 10
**HESS** High Energy Stereoscopic System, 10
**HXD** Hard X–ray Detector, 125

**IACT** Imaging Air Cherenkov Telescope, 9
**IC** Inverse Compton, 33
**IGMF** Inter–Galactic Magnetic Field, 47
**INFN** Istituto Nazionale di Astrofisica [National Institute of Nuclear Physics], 7
**IPRC** Individual Pixel Rate Control, 68
**IR** InfraRed, 2
**IRAF** Image Reduction Advanced Facility, 125

**LAT** Large Area Telescope, 7
**LBL** Low–peaked BL Lac, 29
**LE** Low Energy, 2
**LONS** Light Of the Night Sky, 55

**MAGIC** Major Air Gamma–ray Imaging Cherenkov, 10
**MARS** MAGIC Analysis and Reconstruction Software, 77

**NLR** Narrow Line Region, 19
**NMA** Nobeyama Millimeter Array, 114
**NRO** Nobeyama Radio Observatory, 124
**NSB** Night Sky Background, 50

**OVV** Optically Violent Variable, 113

**PI** Principal Investigator, 72
**PIC** Portal de Informacio Cientifica., 117
**PIC** Proton Initiated Cascade, 33
**PMT** PhotoMultiplier Tube, 65

**QSO** Quasi–Stellar Object, 25

**RF** Random Forests, 78

**S/N** Signal to Noise ratio, 64

**SAL** Saharan Air Layer, 73
**SED** Spectral Energy Distribution, 26
**SMBH** Super–Massive Black Hole, 21
**SSC** Synchrotron Self–Compton, 35
**SSRQ** Steep Spectrum Radio *Quasar*, 21

**TAC** Time Allocation Committee, 71
**ToO** Target of Opportunity, 71

**UHE** Ultra High Energy, 2
**UV** Ultra–Violet, 2
**UVOT** Ultra–Violet Optical Telescope, 154

**VERITAS** Very Energetic Radiation Imaging Telescope Array System, 10
**VHE** Very High Energy, 2

**XIS** X–ray Imaging Spectrometer, 125
**XRT** X–Ray Telescope, 138

# Acknowledgments

It's hard to remember everybody I should, and I'd better apologize from the very beginning for the omissions I'll not be able to avoid.

First of all, I want to thank Dr. Antonio Stamerra and Prof. Riccardo Paoletti for their kind and invaluable support, both scientific and personal. A very special thank to Dr. Fabrizio Tavecchio, who had a major role in helping me with this work and in general in my scientific growth.

Obviously, thanks to all the colleagues and friends of the Siena–Pisa group, including the ones that work somewhere else now, like Nicola, Martina, Elvira, Alessio and again Nicola.

Then, I want to thank the other MAGICians that in many, many occasions helped me so much in getting acquainted with this stimulating experiment and the physics we can explore with it: Juan, Roberta, Abelardo, Diego, Pratik, Daniel, Ching Cheng, Robert, Julian, Pierre, Pol, Saverio, Elisa, Marcos, Konstancja, Alessandro and who knows how many I forgot ...

A very special thought goes to our friend Florian, who left us sadly and unexpectedly while working at the MAGIC–II Telescope construction. Florian was so expert, so clever, so well trained that nobody could suspect that something alike could happen. But life is cruel, and in subtle and unpredictable ways; from times to times this comes out strikingly and suddenly, and we only have to surrender, sad with our powerlessness.

I want to mention all the good friend that shared with me these years in the Department of Physics, such as Eraldo, Mirko, Claudio and Jacopo. And, outside the Department of Physics: Luca, Boris, Andrea, Gregorio, Elisabetta ...

The most special and warm thought can go to nobody else than my mother and my poor, beloved father, who left us two years ago. I would have never gone so far without their help, support, love, and all the important things I learned from them.